AN ABSTRACT OF A DISSERTATION

MULTIPORT HIGH FREQUENCY TRANSFORMER COUPLED BIDIRECTIONAL DC-DC CONVERTERS FOR HYBRID RENEWABLE ENERGY SYSTEM

Jianfu Fu

Doctor of Philosophy in Engineering

This dissertation proposes a new approach Harmonic Balance Technique (HBT) using converter switching functions to the modeling and analysis of the bidirectional actively controlled dc-dc converters. This modeling technique aims to effectively obtain the dynamic equations of the converter system and study the steady state performance of the converter. Also the minimization of the reactive power flow of the converter system based on the HBT is clearly discussed.

The full mathematical model of bidirectional dual active bridge (DAB) converter system using state space method is presented first. A complete insight of dynamic characteristics of the proposed converter system is given. The influence of the mutual inductance is analyzed. The state space method allows a switched nonlinear system to be approximated as a linear system after linearization by classifying in several time intervals. The power flow expressions of the DAB system based on different switching modes are also derived. The loss caused by semiconductor voltage drop is taken into account in the modeling of the DAB system. Also, the effect of dead time on the system under certain operation mode is studied and computer simulation results are given.

The complex closed form expressions gotten by state space method are not easily used to study the steady state performance of the DAB converter system. A novel approach HBT is used in which the linear and nonlinear components are decomposed. The time invariant components are extracted to study the steady state performance of the DAB system. The study of ripple quantities of the state variables can be used to the filter design of the system. Compared with the well-known averaging technique, HBT has a greater advantage when multiport bidirectional dc-dc converter system is studied.

A new control strategy aiming to minimize the system losses from a macroscopic point of view is presented. It is based on the state variables derived from the HBT. In order to minimize the system power losses caused by reactive current flowing inside the DAB converter system, the proposed control strategy can be used to determine the reference switching function command to achieve a high power efficiency. The prototype of the proposed system is designed and experimental results are discussed.

MULTIPORT HIGH FREQUENCY TRANSFORMER COUPLED BIDIRECTIONAL DC-DC CONVERTERS FOR HYBRID RENEWABLE ENERGY SYSTEM

A Dissertation

Presented to

the Faculty of the Graduate School

Tennessee Technological University

by

Jianfu Fu

In Partial Fulfillment

of the Requirements for the Degree

DOCTOR OF PHILOSOPHY

Engineering

May 2012

CERTIFICATE OF APPROVAL OF DISSERTATION

MULTIPORT HIGH FREQUENCY TRANSFORMER COUPLED BIDIRECTIONAL DC-DC CONVERTERS FOR HYBRID RENEWABLE ENERGY SYSTEM

By

Jianfu Fu

Graduate Advisory Committee:

_____	_____
Joseph Olorunfemi Ojo, Chairperson	Date
_____	_____
Ghadir Radman	Date
_____	_____
Ahmed Kamal	Date
_____	_____
Brian O'Connor	Date
_____	_____
Hwan-Sik Yoon	Date
_____	_____
Omar Elkeelany	Date

Approved for the Faculty:

_____
Francis Otuonye
Associate Vice President
for Research and Graduate Studies

_____
Date

DEDICATION

This dissertation is dedicated to my dearest parents who never stop supporting me and encouraging me throughout my life.

ACKNOWLEDGEMENTS

I cordially express my appreciation to my professor and chairperson of the advisory committee, Dr. Joseph Olorunfemi Ojo, for his encouragement and guidance during my research work. I would like to take this opportunity to thank Dr. Gadir Radman, Dr. Kamal Ahmed, Dr. Brian M. O'Connor, Dr. Hwan-Sik Yoon, and Dr. Omar Elkeelany for their advice and support as my committee members.

I gratefully acknowledge the Center for Manufacturing Research for the financial support without which this work would not have been possible.

I would like to thank all my colleagues of Power Electronics and Drives Lab for their constant support and encouragement; especially to Sosthenes, Kenedy, Mehari, Will, Charles, Melaku, Bijaya, Amrit, Hossein, and Bule for their continuous support and precious friendship during my study. I would also like to appreciate Mr. Conard Murray, Mr. Robert Peterson, and Mr. Tony Greenway for their help with computer assistance and experimental hardware supply.

Last, but not least, I am grateful for my parents, especially my mom, for their lifetime support, generous love, and spiritual encouragement which made it possible to finish the work.

TABLE OF CONTENTS

Page

Page

Page

LIST OF FIGURES

Page

Page

Page

Page

Page

LIST OF TABLES

Page

CHAPTER 1

INTRODUCTION

1.1 Research Background

During the last two centuries, human beings exploited traditional energy sources such as coal, petroleum, and other fossil fuel reserves. Electric power energy has been one of the major forms of energy delivery. This brought industrialization and economic development all over the world [1]. However, as well as the electric power is generated by the original energy sources, it also comes with undesirable side effects such as air pollution and other damage to the natural environment. The global air temperature is likely to increase 1.5°C during the 21st century. Furthermore, the increasing threat of the exhaustion of the resources such as petroleum, coal, and natural gas compels people to seek alternate regenerative energy sources. Hence, with the increasing concern about over-consumption of non-renewable resources, the development of renewable energy sources has taken on an accelerated pace. Today, in the field of power electronics, electric motor drive and electric power system, much of the research efforts have been put into the development of alternative electricity generation systems. So far the most exploited renewable energy sources are fuel cell, wind generation, photovoltaic (PV), wave energy and hydro-electric generation [2,5]. After many years of research and development, recently the renewable energy resources have experienced a faster growth in percentage. So far 19% of world's electrical energy is generated by renewable energy

sources. The following alternative energy sources introduced are widely developed clean electricity generation systems.

1.1.1 Hydro Energy

Over the last 100 years, hydro power has been the most mature renewable energy source generating electricity around the world [3,4]. The hydroelectric energy takes a large amount and is still being exploited. Hydro power generation using rivers and dams has been recognized as an excellent source of renewable energy source. Hydro power depends on the kinetic energy of a flowing fluid to generate electricity. The structure of a micro-hydro generation system is shown in Fig. 1.1. There is an increase of interest in the U.S.A. to harness the main rivers such as the Mississippi River. However, considering the environmental damage and risk of relocation of human beings, it becomes more difficult to be constructed due to the political issues. After that it comes with the wind energy, solar energy, and fuel cells. Hence, these areas will take a greater amount of the electricity generation mix to break the dependence on oil and coals.

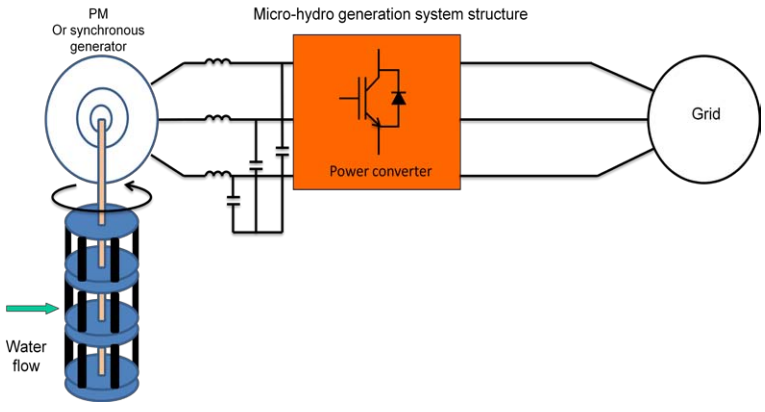

Fig. 1.1 System structure for a micro-hydro generation system

1.1.2 Wind Energy

The amount of the wind energy is infinite. It is clean, renewable, and widely distributed. Wind energy is the next most popular source of green energy around the world. The wind electricity has been commercialized for the last decades [3]. The wind energy production forecast by 2011 is more than 200 GW. The European Wind Energy Association (EWEA) projects 150,000 MW by 2020. The United States holds the second largest share of wind power in the world followed by China and India where the wind industry is also booming. Wind turbines are widely used to convert the kinetic wind aerodynamic energy into electricity. Different scales of the wind turbines can be utilized from a few hundred watts residential use to several megawatt electric grid utility. The structure of power conditioning for wind generation system is shown in Fig. 1.2. Due to instability of the wind energy, the output power of a stand-alone wind generator needs to be backed up by some other types of energy storage.

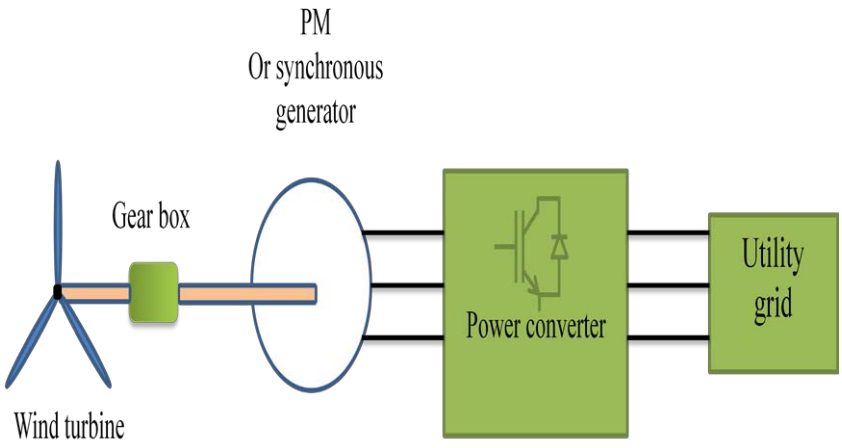

Fig. 1.2 System structure for a power conditioning for wind generation system

1.1.3 Solar Energy

Solar energy, heat coming from the sun, has been harnessed by human beings and considered a truly renewable energy source. By using photovoltaic and heat engine, sunlight can be converted into electricity. The conventional PV with power conditioning system is shown in Fig. 1.3. This green energy-solar photovoltaic is growing rapidly, even though in a small base, to a total global capacity of 40,000 MW at the end of 2010. The simplicity of the technology and flexibility of installation make PV a greater potential for worldwide growth. So far substantial research and development (R&D) investments have been made these years to achieve parity with retail electricity costs in the near future [6,7]. Right now more than 100 countries have been using PV to generate electricity. Besides, more and more PVs will be installed in developing nations where the sunlight is rich and solar-electric power is feasible. At the same time, importing PV product to the market can significantly create more jobs in the job market and spur the consumers to use the less expensive electricity generated by the PVs. Therefore the interest in PV applications has grown exponentially and PV will make an important component of the renewable energy future.

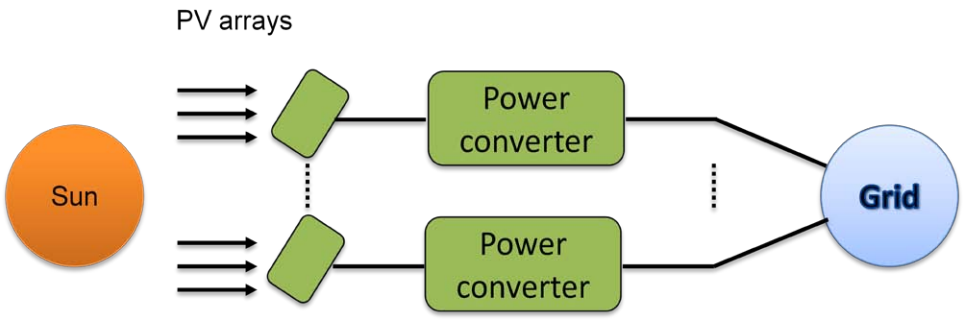

Fig. 1.3 Photovoltaic power conditioning system

1.1.4 Fuel Cell Energy

Fuel cells are also a clean, high-efficiency source for electricity generation. A typical fuel cell is comprised of two cell electrodes which can produce dc current between them. It is an environmental friendly electrochemical device converting the chemical reaction energy of hydrogen and oxygen to useful energy electricity as well as the production of water which is harmless to the environment [8]. Hence in recent years, fuel cell R&D has received much attention for its clean efficient energy conversion and lower greenhouse gas emission.

Different types of the fuel cell can be configured in a system that matches its characteristics most favorably. They can be found in wide potential applications from hybrid electric vehicles, stationary power generation, down to portable energy supplies. These applications can be as small as cell phone power supplies, or military wireless communication system. The mobile applications can be found in the energy generation system of hybrid electric vehicles. The stationary fuel cell electricity generating systems are being installed in the area of residential and industrial applications all around the world. Fig. 1.4 shows various system structures for a fuel cell and battery generation.

In summary, all kinds of the renewable energy sources discussed cannot be utilized directly. The original power sources from water, wind, sunlight and fuel cells need power conditioning systems to regulate dc or ac power appropriate for the application. Most of the renewable sources need to be regulated to the dc voltage source and further converted to either dc or ac voltage sources due to the different applications. They need to interface different energy sources with the load.

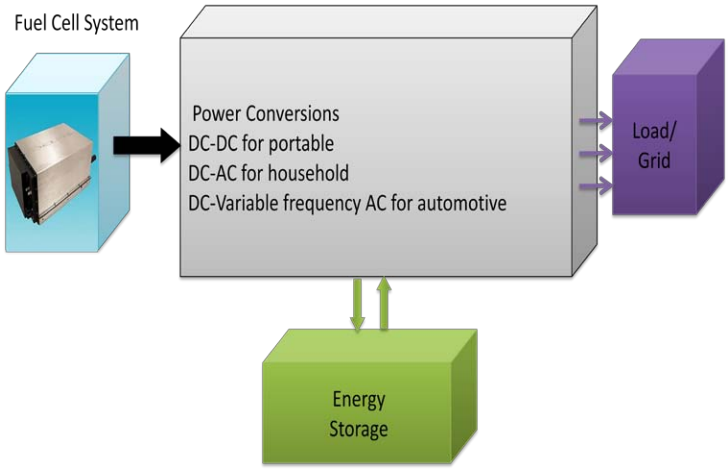

Fig. 1.4 Photovoltaic power conditioning system

Due to the dynamic characteristic of the wind speed, mechanical gear box and electrical power converters must be inserted to interface between generator and grid. The electric output can be either dc or ac. Power converters can also be used to track the maximum output power operating point based on the blade cutting speed.

Energy sources such as PV modules generate dc energy that has to be changed to another level of dc voltage and then converted to ac energy of utility grid. Like wind energy, solar energy also depends highly on the weather and needs to be backed up by some other energy storages. These tasks have to be done by the power converters.

For fuel cell systems, the output of the fuel cell is unregulated dc voltage and power converters play a significant role in converting to regulated voltage which can be utilized based on the different requirement of the terminal needs such as compact, portable, harmonic maintenance, frequency regulation, and so on. Also, more often than not, the incorporated storage such as battery and supercapacitors can increase the performance of the system. Therefore, power converters are one of the most essential components in the renewable energy systems.

In conclusion, dc-dc converters play a very important role in the application of renewable energy system and it's practically utilization. They ensure the efficient and flexible interconnection of different energy storage systems and loads. In the following study, the focus is on the dc-dc converter systems.

1.2 Literature Review

With the increasing concern about over-consumption of non-renewable resources, the development of renewable energy sources has taken on an accelerated pace. The main advantages of using renewable energy sources are the low harmful emissions such as CO_2, high operation efficiencie,s and inexhaustible resources. However, some issues such as high costs, uncontrollability, and uncertain availability need to be considered [2]. Hence, the renewable energy sources rely heavily on daily weather and the power demand by consumers which varies. To control these resources, it is necessary to introduce power electronics as an interface to keep high operation efficiency.

Most of the renewable energy sources result in variable output voltage and power such that power converters are required within the renewable generation systems for effect control. It is one of the key factors interfacing the energy sources, energy storage, grid connection, and various kinds of loads. Most of the time, for safety issues of the practical applications, electrical isolation is necessary. Normally, a high frequency transformer is connected among the converters. In the following discussion, only isolated dc-dc converter systems are studied.

1.2.1 Topology Review for DC-DC Converters

Recently the dc-dc converter has emerged as an important energy conversion system in the application of renewable energy generating systems such as fuel cells and photovoltaic (PV) array [9,14,29,30]. Applications such as unidirectional, bidirectional power conversion, high power isolated, single-phase half-bridge, and full dual-active-bridge (DAB) dc-dc converters have received more and more attention. They have merits of compact size and light weight, electrical isolation between source and load, bidirectional power flow for charging and discharging the battery system. The use of a high frequency transformer offers a large step up or step down conversion ratio and better converter utilization.

1.2.1.1 Single-phase half-bridge dc-dc converter. The single-phase unidirectional half-bridge dc-dc converter circuit topology is illustrated in Fig. 1.5. In this topology, the power is transferred from the primary side to the load. A half-bridge circuit

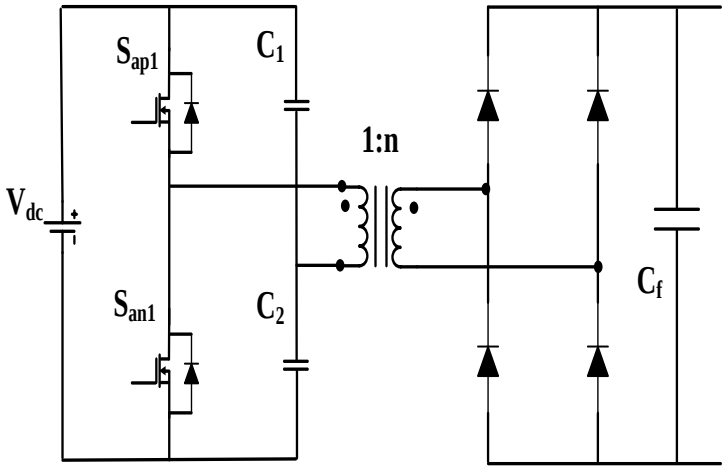

Fig. 1.5 A typical single-phase unidirectional half-bridge dc-dc converter

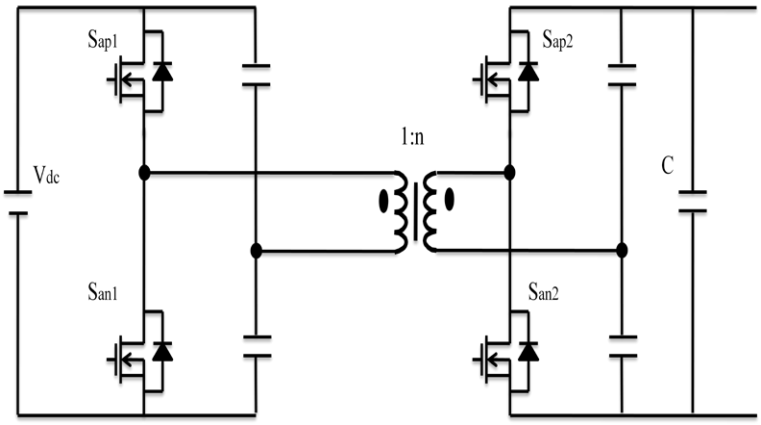

Fig. 1.6 A typical single-phase bidirectional half-bridge dc-dc converter

has the advantage of low device voltage and low device count; however, it may not be good choice because of the double current going through the semiconductor device and the split capacitors with potential unbalanced voltage issues.

By replacing the diodes of the secondary rectifier stage in the unidirectional topology of Fig. 1.5, bidirectional power flow can be achieved as shown in Fig. 1.6. It enables the charging and discharging by phase shifting the voltages operated on the primary and secondary side. Still, this topology is intended for the low power applications due to the low count of the semiconductor devices.

1.2.1.2 Single-phase full-bridge dc-dc converter. Some primary sources like fuel cells cannot absorb power. Hence the converter does not need to be bidirectional for this case. The single-phase unidirectional full bridge dc-dc converter is illustrated in Fig. 1.7. It can be operated by both phase shift and duty ratio control signals to acquire the reasonable voltage. Also, zero voltage switching (ZVS) can be realized in a limited load and input voltage range [10].

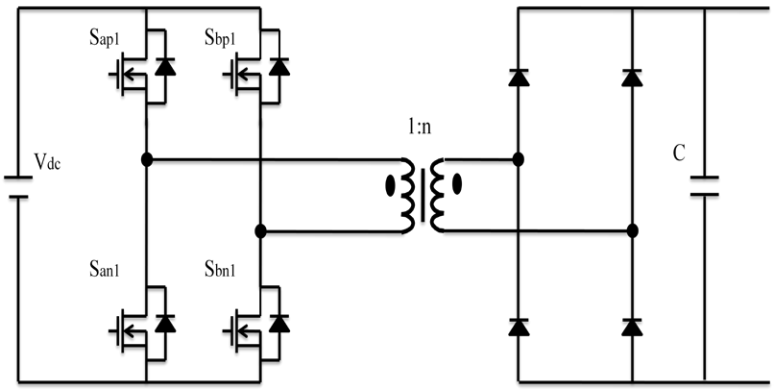

Fig. 1.7 A typical single-phase unidirectional full bridge dc-dc converter

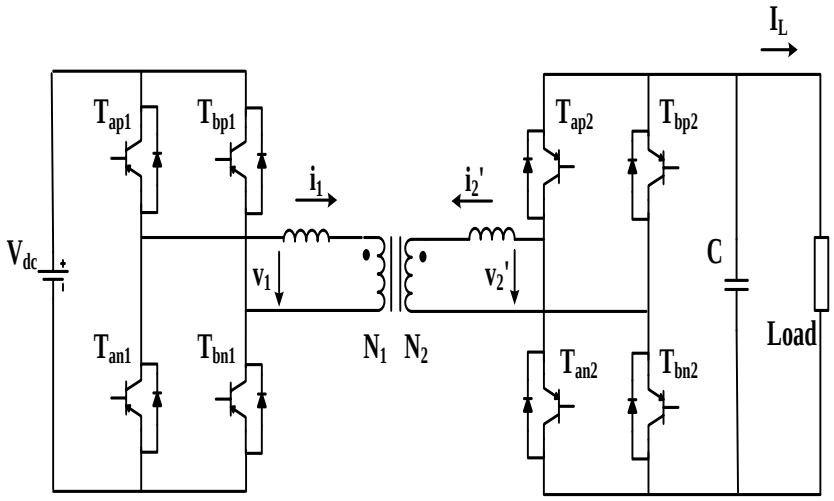

Figure 1.8 Single-phase dual active bridge (DAB) dc-dc converter topology

Single-phase bidirectional dc-dc converter topology shown in Fig. 1.8 is possibly the most popular topology for bidirectional applications. It was first proposed in [30]. This topology is also studied in [10] and called dual-active-bridge (DAB) dc-dc converter.

The two individual single-phase converters are coupled as the primary and secondary side of a high frequency transformer with a turn ratio of N_1/N_2. The ac voltage v_1 and v_2' are across the primary and secondary sides of the transformer. The single-phase

converters located at each side are all composed of full H-bridges which can decrease the current stress compared to the half-bridge configuration, where T_{ap1}, T_{an1}, T_{bp1} and T_{bn1} are the corresponding switches for primary side converter, and T_{ap2}, T_{an2}, T_{bp2} and T_{bn2} are power switches for secondary side converter. The Capacitor C is connected with the load to hold the voltage and reduce the ripple voltage. Both H-bridge converters can be operated at variable duty ratios and phase shift angles based on the need of power flow between the source and the load. The transformer leakage inductance is utilized as the energy transfer device. The high frequency transformer not only provides the electrical isolation between two converter ports, but also reduces the size of both converters which operate at a relatively high frequency.

1.2.1.3 Three-port active bridge dc-dc converter. The three-port active bridge converter topology shown in Fig. 1.9 is an extension of two-port active bridge converter topology. With the renewable energy supplied by either solar panel or fuel cell, the output power is not constant but intermittent. With a third port of full bridge, it is necessary that energy storage such as battery type or supercapacitor is used to store excess power and as

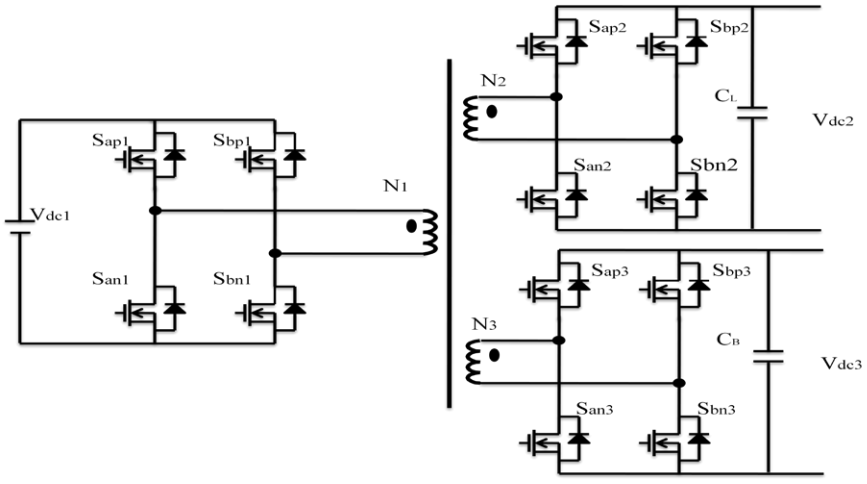

Fig. 1.9 Three-port active bridge (DAB) dc-dc converter topology

a backup component to supply peak power requirement. Hence, with an extra auxiliary power supply, the dynamics of the system can be improved and it increases the fault tolerant capability. In this regard, derived from traditional bidirectional dc-dc converter structure, the three-port bidirectional dc-dc converters have been reported in [21-26].

1.2.1.4 Multiport active bridge dc-dc converter. Recently, future energy systems have needed to interface various energy sources such as fuel cells and photovoltaic (PV) with various loads. Multiport active bridge dc-dc converters shown in Fig. 1.10 can be used to interface multiple power sources and multiple loads [35]. Due to the intermittent nature of solar and wind energy and slow dynamic response of fuel cell, the battery type backup is necessary and capable of long-term storing of energy.

Each single port of DAB is connected by an isolated high frequency transformer. Hence, developing multiport dc-dc converters is a new trend and gaining concerns in sustainable energy system and hybrid electric vehicles.

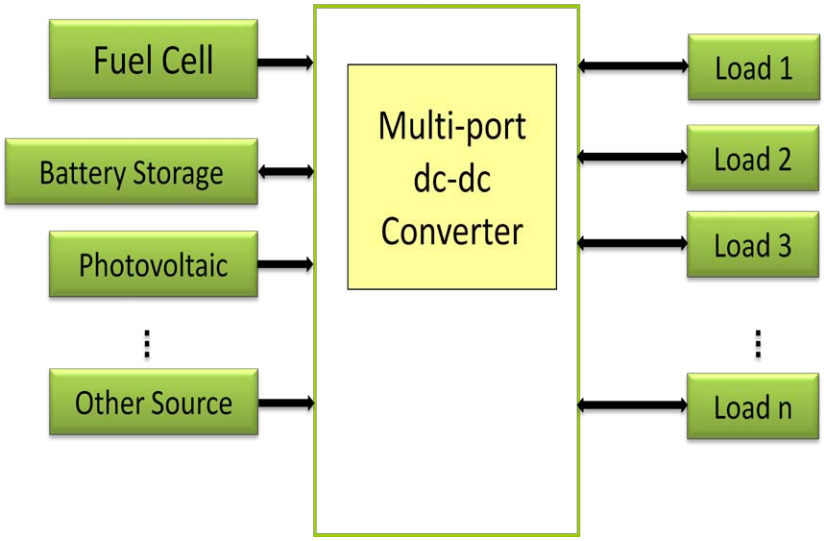

Fig. 1.10 Block diagram of multiport DAB converter system

1.2.2 State of the Art Bidirectional DC-DC Converters

In the literature, the isolated dual active bridge converter was originally studied in [29]. It is a galvanic buck and boost bidirectional dc-dc converter with a high frequency transformer. The two individual single-phase converters are operated with phase shift PWM waveforms which enable the bidirectional power flow. It has the advantage of low device stress, small filter components, and high power density. The DAB converter has been studied by the researcher from the improvement of hardware design down to the new proposed control scheme. Additionally, multiport structure also derives from this basic DAB converter system.

The zero voltage switching (ZVS) technique has been proposed [17,32]. Soft switching helps to improve the system efficiency by eliminating the power semiconductor's switching losses. A unique soft-commutating method is proposed to implement dual operation of soft-switching full bridge dc-dc converter. Another full order model has been studied taking into account the leakage inductance current and the resonant transition intervals in order to realize the ZVS condition. The method based on the discrete-time modeling and z transform is used to study the resonant transition intervals of ZVS condition. Also, in the application of three-port active bridge dc-dc converter system, much literature is available on this subject [9-10,12-14,23-24,62].

To understand the dynamic performance of the dual active bridge converter, the short time scale transient process in DAB converter is discussed [20]. Dead band time and phase shift error are two important factors which can affect the desired output voltage and power delivery. The "energy dead band" concept is defined first to describe the

condition where there is no power flow among the ports. A proportional multi-resonant controller has been designed in three-phase four wire inverter system. The phase shift PWM generation method used considered the dead time effect.

For the research of new control strategy, a model predictive control-based method has been proposed in [37-38]. The optimal control is realized using integrated perturbation analysis and sequential quadratic programming method. It can improve computational efficiency in the real time control for nonlinear system. Also, the power flow model is presented to explain the observed internal power transfer and phase drift phenomena which are vital to the phase shift control of DAB converter system. The phase shift method has been improved in [18-19]. The control technique combines the self-sustained oscillation mode with phase shift modulation technique that can significantly improve the stability of the system.

Minimization problem of converter losses enable more efficient converter utilization [27]. A switching control strategy has been proposed. It brings one more control freedom of variable duty ratio control. By doing this, it can regulate the desired power flow and minimize the total power losses at the same time. Also, the power loss model for DAB converter is presented in [31]. Calculated results are verified by the experimental results to show the accuracy of the power loss model. Loss minimizing control of permanent magnet synchronous motors is studied in [43]. It gives the insight of the using polynomials to solve the problem when the system goes to multiport structure. The optimization of the performance of the proposed strategy is studied using trapezoidal modulation method in [57]. A novel buck-boost type of DAB system is introduced and the power flow is discussed as well in [58]. An active clamp was added to the DAB

converter system and soft switching operation is used in [59,70]. The DAB system can also be applied in the hybrid electric vehicles in [60]. The DAB system can be also applied in the dc UPS system based on fuel cell and supercapacitor [72]. The light load problem of DAB system exists. Using dual leakage transformer and variable frequency can improve the overall efficiency of the system [61]. A solid state transformer and variable inductor are used as a novel DAB converter topology; it can be operated at zero switching operation at light load situation [63]. The single-phase DAB system can be extended into three-phase DAB system with enhanced current sharing capability [65]. A nanocrystalline transformer is designed and used in DAB system to minimize the transformer loss [71].

A novel nonlinear control strategy of DAB system is addressed and validated by the simulation and experimental results [67]. Another new adaptive dynamic control of the DAB system is used to study the dynamic response of the converter based on the harmonics of the phase shifted waves [68] The saturation issue of the transformer is discussed and the proposed control method is used to prevent the saturation and eliminate the dc currents in both sides of the DAB system [69].

Multiple port dc-dc converter systems are promising in renewable energy generation system [16,22,25,34]. A buck-boost startup operation of a three-port DAB system is stated and used in electric vehicle application [64]. Multimode operations and multi-loop design are vital for the multiport converters [66]. A family of the multiport bidirectional dc-dc converter has been presented. The topology is based on the DAB converter to use one magnetic component to couple the different ports. By doing this, it

has minimum conversion steps, low cost, and compact packaging. The dynamic characteristics are also clarified.

1.3. Motivation and Objectives

Recent studies have initialized the interest of bidirectional dc-dc converter system in the application of renewable energy generations. The future energy generation will not only depend on the traditional, centralized generation but also on the various alternative green energy generations. The latest revolution of energy conversions is occurring now. Power converters will be the essential components to interface for the integration of renewable energy sources. Multiport bidirectional converters are gaining popularity in this field because of the need of connecting several distributed power sources. As stated in the literature review, researchers pursue high efficiency of the power converters. Conduction loss is a major efficiency killer in the dc-dc converter system. Their improvement on conduction losses would be the major concern of this research.

First of all, to fulfill the desired objectives, a number of modeling techniques have appeared in the literatures especially based on developing equations for feasible modes of operations in which assumptions are made about the output voltages and currents are generally predicated on steady state operations. Firstly, the state space method would be implemented to study the dynamic performance of the system. Dead time effect of the switching functions can be discussed using the full mathematical model. The derivation of mathematical model of the system is shown step by step.

Secondly, when using the state space method, it may lead to a complicated matrix that is more difficult to solve and analyze. To overcome this problem, even though the system can be studied using state space method in micro time intervals, no study has discussed the steady state performance and dynamic characteristics from a macro perspective. Therefore, there is the need for dynamic and steady state converter models that can be effectually used for controller design, system optimization, and steady state performance calculations. The aim of this dissertation is to explore a new switching function based modeling method which will present the steady state performance and dynamic characteristics for DAB and even multiple DAB dc-dc converter systems.

Furthermore, harmonic balance technique (HBT) is applied to the nonlinear model with switching functions to study dynamic equations of the system. It can predict input current, output voltage, and even ripple quantities. Compared with the wellknown averaging technique, it has a greater advantage when multiport bidirectional dc-dc systems are studied in that it can predict the ripple variables. More over it yields equations with average and ripple components separately. Another advantage of the HBT methods is that the separate components of state variables can be used to study the loss minimization of the DAB dc-dc converter system. The problem of minimization of reactive power can be analyzed using separate components derived from HBT method.

Also, when it goes to the multiport DAB system, HBT would make the best use of superiority. When facing the nonlinear optimization with inequality constraints, Gröbner basis is considered a powerful mathematical tool to solve the nonlinear polynomial equations. The pro and cons of the classical iterative method and Gröbner basis are discussed and tested.

Last, but not the least, the preliminary laboratory prototype is built up with the rating of 1 kW at 20 kHz. Some of the components need to be designed after the specifications of the converter are obtained. Hence, high frequency transformer, auxiliary inductor, current sensor circuit, and controller circuit and gate drive circuit are designed and tested.

1.4 Outline of Dissertation

The dissertation is organized in seven chapters as follows. Chapter 1 outlines the background of renewable energy sources and bidirectional dc-dc converter system in the application of renewable energy generation systems are briefly introduced. An overview of recent studies on dual active bridge converters and multiport active bridge converters are conducted and the objectives of the research are proposed.

Chapter 2 presents the full mathematical model of bidirectional dual active bridge converter system using state space method. It gives a complete insight of studying the proposed converter system. The influence with and without mutual inductance has been studied. The state space method allows a switched nonlinear system to be approximated as a linear system after linearization by classifying in several time intervals.

Chapter 3 investigates the influence of the dead time effect on the DAB system. The operation stages are laid out to study the voltage change of the device. Furthermore the small signal analysis of the DAB converter and three-port DAB converter system are derived clearly to be used in the future controller design.

Chapter 4 illustrates the proposed approach using the converter switching functions and harmonic balance technique (HBT) to modeling and analyzing the DAB system. The separate state variable equations generated using HBT are used to determine the minimum loss operation of proposed system.

Chapter 5 extends the HBT method into the multiport DAB converter system. When it goes to multiport system modeling, it would be different to analyze the steady state performance of the proposed system by using the traditional state space method. The state variable matrix would be too complex to solve. HBT is a powerful method used in the analysis of multiple DAB converter system. Also, for the minimization of the reactive power, a mathematical tool, Gröbner basis, is introduced to solve the Lagrange multiplier problem with equality and inequality constraints. The proposed approach is compared with numerical iterative method using optimization tool box from software MATLAB.

Chapter 6 covers the hardware design of the proposed DAB and multiple DAB converter system. The design of the high frequency transformer and auxiliary inductor is carried out. The schematic and PCB layout of the driver circuit and power stage of single full bridge converter are addressed. Also, the implementation of PWM phase shift waveforms are included using the digital signal processor (DSP).

Chapter 7 focuses on the preliminary experimental results of the proposed system.

Chapter 8 summarizes the most important results and conclusions of the research work. Suggestions for the future work are also given last.

CHAPTER 2

ANALYSIS OF BIDIRECTIONAL DUAL ACTIVE BRIDGE CONVERTER

In this chapter, the topology of single-phase bidirectional dual active bridge (DAB) dc-dc converter is reviewed as first. This topology has been widely used in the applications such as auxiliary power supply of hybrid electric vehicles, uninterruptible power supplies, and battery management system. The following topology variations such as multiple DAB dc-dc converter derive from the traditional two-port DAB.

This topology has become the subject of research concern in recent years. The interests have arisen because the converter system has higher power density and lower weight. The overall size is reduced resulting from integration of the energy-transfer extra inductor into high frequency transformer which is also the core component to transfer the power between two bridges. In the DAB converter, each single-phase full bridge generates rectangular-wave voltages, v_1 and v_2, with controllable duty ratios, D_1 and D_2. They are phase shifted with respect to each other to realize the optional bidirectional power flow based on either leading or lagging between each other. When the state space method is used to analyze the system, the complicated algebraic equations of the proposed system result in difficulties. The objective of this chapter is to ease the problem by simplifying the equations and giving closed form solutions based on different modes of operation. Results of the analysis are also given in this chapter so that the closed form solutions can be used in future for some other researchers. Also, this method is applicable to the entire class of two-port dc-dc converters.

2.1 Introduction of State Space Technique

Among a number of ac converter modeling techniques, the state space averaging method is always the principal choice. It is the first step to study the model of the various converter topologies. The state space description is a canonical form that describes differential equations of a dynamic system [44]. It is composed of the first order differential equations in the vector value state of the system. The solutions are also expressed as a trajectory of this state vector in the space. The advantage of state space method is that the compact general models can be obtained and the small signal averaged model can also be developed.

For the linear network of the system, the derivatives of the state variables can be expressed as linear combination of the system state variables and independent system input and output. For the typical power converter systems, they are composed of resistors, capacitors, inductors, and semi conductor devices. The physical state variables are usually related with the energy storage components and are therefore chosen as inductor currents and capacitor voltages. The total number of the storage elements determines the order of the system. Most of the converter systems are operating as nonlinear systems. State space methods can allow a switched converter system to be approximated as a continuous nonlinear system. Moreover, at a small scale of time interval the nonlinear system can be considered as linear system which is called linearization.

At a given initial time, the values of the state variables depend on the parameters of the energy storage components and the previous history of the system. Hence to solve the differential equations of the system, the initial values of the state variables must be

specified. Also the parameters of the system state variables are set as well as the input energy source is given. Then, the state equations to analyze the characteristics of the state variables can be solved.

The state equations can be written as

$$\begin{cases} \dot{Kx} = Ax + Bu \\ y = Cx + Eu \end{cases} \tag{2.1}$$

where K is the matrix of the parameters of capacitance, inductance and mutual inductance. A, B, C and E are the matrix of constant values. All state variables and their derivatives must be continuous. For any time intervals, all the matrix A, B, C, and E must be constant to ensure the continuity of the nonlinear model of the converter system. Therefore, the solving equations are a set of linear equations which describe the system at each switching state. The vector y is the physical output vector and vector u is the switching input vector. The output vector can also be expressed as a linear combination of the x and u.

The general solution of the Equation (2.1) is of the form [33]:

$$x[t] = e^{At}x[0] + \int_0^t e^{A(t-\tau)}Bu(\tau)d\tau \tag{2.2}$$

where $x[0]$ is the initial value of the matrix of state variables when the system goes to steady state status.

2.2 DAB Converter Topology and System Description

Two-port DAB converter topology is the basis structure of the family DAB system. First review this topology briefly by using state space method. The proposed

converter topology analyzed in this section is as shown in Fig. 2.1. It has attractive advantages such as low switching losses, optimal bidirectional power flow and galvanic isolation between source and load. It shows two single-phase full bridge converters on the two sides of a transformer.

The two rectangular wave voltages, v_1 and v_2, can be regulated by varying duty ratio and phase shift to transfer the required power. The inductor L representing the sum of the primary-referred leakage inductance and external inductor is used as energy storage and transfer component.

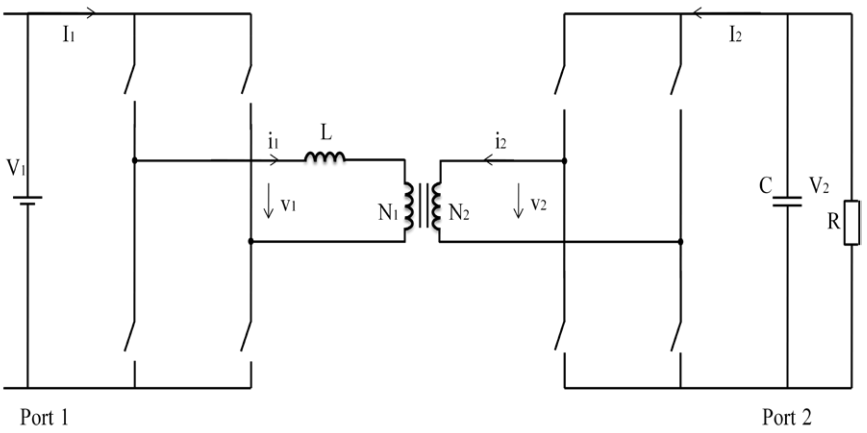

Fig. 2.1 Simplified single-phase DAB converter

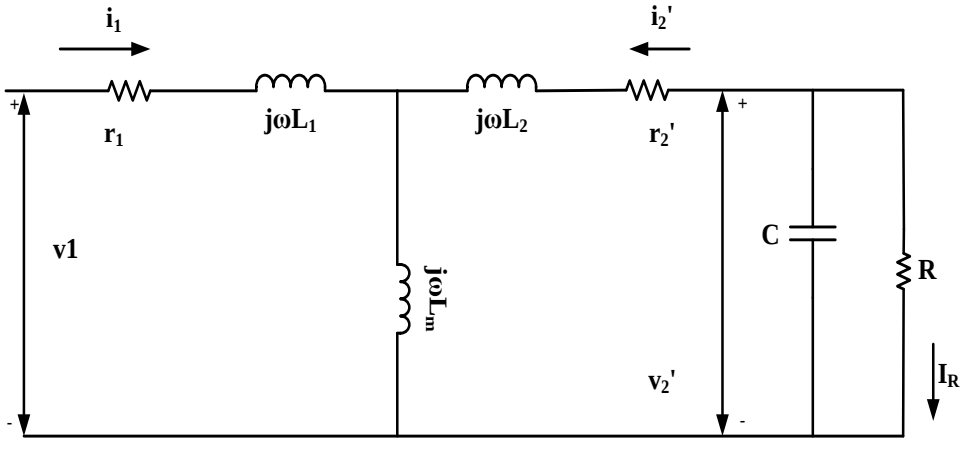

Fig. 2.2 Equivalent circuit of DAB converter

The equivalent circuit of DAB converter is shown in Figure 2.2. Considering the linear time invariant elements in the converter, the continuous time state space mathematical model that describes the converter is derived as below:

$$(L_1 + L_m)pi_1 + L_m pi_2^{'} + r_1 i_1 = v_1 \tag{2.3}$$

$$(L_2^{'} + L_m)pi_2^{'} + L_m pi_1 + r_2 i_2^{'} = v_2^{'} \tag{2.4}$$

The capacitor and load model is represented by

$$CpV_{dcL} = -i_2^{'} s_2 - \frac{V_{dcL}}{R} \tag{2.5}$$

The input and output voltage is given by

$$v_1 = V_{dc} s_1 \tag{2.6}$$

$$v_2^{'} = V_{dcL} s_2 \tag{2.7}$$

The switching functions are represented as

$$s_1 = S_{ap1} - S_{bp1} \tag{2.8}$$

$$s_2 = S_{ap2} - S_{bp2} \tag{2.9}$$

where $i_1$and $i_2^{'}$ are input and output currents, r_1 and r_2 are transformer resistances, L_1 and $L_2^{'}$ are transformer leakage inductances, L_m are transformer mutual inductance, C is output capacitance, R is the output resistive load, V_{dc} and V_{dcL} are input and output dc voltage, respectively. The switching functions S_{ap1}, S_{an1}, S_{bp1}, $S_{bn1,}$ S_{ap2}, S_{an2}, S_{bp2} and S_{bn2} define the states of the controllable switches. When the switch is on, the value of switching function is one. When it is off, the value is zero.

In order to gain more degrees of freedom to achieve the optimal real power, the full bridge converters use two rectangular voltage pulses shown in Fig. 2.3 on a high

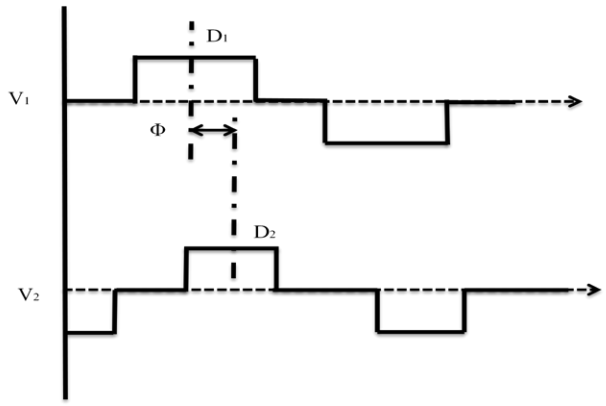

Fig. 2.3 Operation mode of two rectangular waveforms

frequency transformer. The method of state space solution is carried out as below. Closed form expression for the inductor current is derived and the real time value of the system has been calculated when the magnetizing inductance L_m either included or ignored in the analysis.

Firstly, based on the system with mutual inductance, using the dynamic Equations (2.3) and (2.4), the output voltage can be expressed in terms of resistive load and switching function:

$$v_2 = -i_2 s_2^2 R \tag{2.10}$$

where, s_2 is the switching function in Equation (2.9).

From Equation (2.3),

$$pi_1 = \frac{1}{L_1 + L_m}(v_1 - r_1 i_1 - L_m pi_2^{'}) \tag{2.11}$$

From (2.4),

$$pi_2^{'} = -\frac{1}{L_2 + L_m}(r_2 + s_2^2 R) i_2 - \frac{L_m}{L_2 + L_m} pi_1) \tag{2.12}$$

Substitute $pi_2{}'$ of (2.12) into (2.11), the expression pi_1 is as follows:

$$pi_1 = \frac{-r_1}{L_m + L_1 - \dfrac{L_m^2}{L_m + L_2}} i_1 + \frac{L_m (r_2 + s_2^2 R)}{(L_m + L_2)(L_m + L_1) - L_m^2} i_2^{'} + \frac{1}{L_m + L_1 - \dfrac{L_m^2}{L_m + L_2}} v_1 \qquad (2.13)$$

The expression for $pi_2{}'$ can be found as follows:

$$pi_2^{'} = \frac{L_m r_1}{(L_m + L_2)(L_m + L_1) - L_m^2} i_1 + \frac{(s_2^2 R + r_2)(L_m + L_1)}{(L_m + L_2)(L_m + L_1) - L_m^2} i_2^{'} - \frac{L_m}{(L_m + L_2)(L_m + L_1) - L_m^2} v_1 \qquad (2.14)$$

The state variable representation of the DAB converter is given by equation

$$\begin{bmatrix} pi_1 \\ pi_2^{'} \end{bmatrix} = \begin{bmatrix} \dfrac{-r_1}{L_m + L_1 - \dfrac{L_m^2}{L_m + L_2}} & \dfrac{L_m (r_2 + s_2^2 R)}{(L_m + L_2)(L_m + L_1) - L_m^2} \\ \dfrac{L_m r_1}{(L_m + L_2)(L_m + L_1) - L_m^2} & \dfrac{(s_2^2 R + r_2)(L_m + L_1)}{(L_m + L_2)(L_m + L_1) - L_m^2} \end{bmatrix} \begin{bmatrix} i_1 \\ i_2^{'} \end{bmatrix} + \begin{bmatrix} \dfrac{1}{L_m + L_1 - \dfrac{L_m^2}{L_m + L_2}} \\ \dfrac{-L_m}{(L_m + L_2)(L_m + L_1) - L_m^2} \end{bmatrix} v_1 \qquad (2.15)$$

By using state space general solution below [33]:

$$X[t] = e^{A(t-t_o)} X_o + \int_{t_o}^{t} e^{A(t-\tau)} B u(\tau) d\tau \qquad (2.16)$$

Both voltages are operated with two rectangular waveforms. To analyze the state space model of the proposed system, the operation is subdivided into three modes: Mode A, B, and C. To simplify the situation, it is assumed that $D_1 > D_2$, $\varphi > 0 (lagging)$.

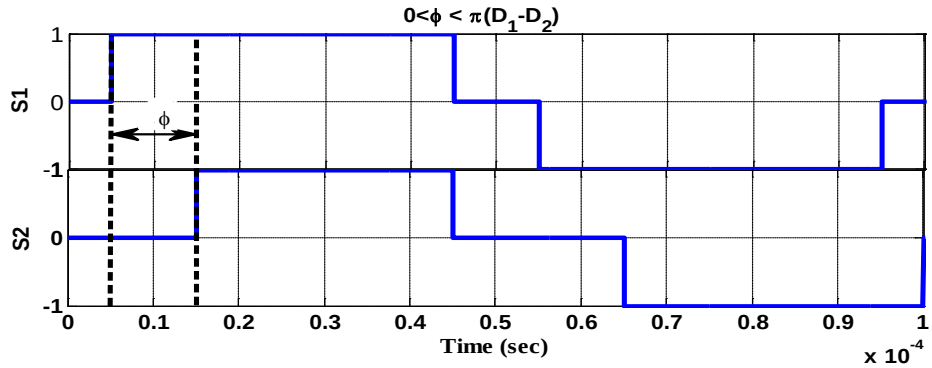

Fig. 2.4 Ideal waveform of operation Mode A

Mode A (see Fig. 2.4) $\varphi \le \frac{\pi}{2}(D_1 - D_2)$. This can be separated into four states which can make this nonlinear system into four linear systems with each state space equation.

1) At the time interval 0 to t_1 $\quad \theta_1 : V_1 = V_{dc}, s_2 = 0$ the time is t_{10}

2) At the time interval t_1 to t_2 $\quad \theta_2 : V_1 = V_{dc}, s_2 = 1$ the time is t_{21}

3) At the time interval t_2 to t_3 $\quad \theta_3 : V_1 = V_{dc}, s_2 = 0$ the time is t_{32}

4) At the time interval t_3 to t_4 $\quad \theta_4 : V_1 = V_{dc}, s_2 = 0$ the time is t_{43}

At the half-cycle of period the value of the state vector at the end t_4 is negatively equal to the one at the beginning of t_0. The solution of Equation (2.15) using formula (2.16) is given by

$$X[t] = \begin{bmatrix} e^{k(t-t_o)}[\cos(\omega_r(t-t_o)) + a\sin((\omega_r(t-t_o))] & ce^{k(t-t_o)}\sin((\omega_r(t-t_o)) \\ de^{k(t-t_o)}\sin((\omega_r(t-t_o)) & e^{k(t-t_o)}[\cos(\omega_r(t-t_o)) + b\sin((\omega_r(t-t_o))] \end{bmatrix} X_{to}$$

$$- \begin{bmatrix} B_1[\frac{\omega_r}{k^2+\omega_r^2}e^{k(t-\tau)}\sin((\omega_r(t-\tau)) + \frac{k}{k^2+\omega_r^2}e^{k(t-\tau)}\cos((\omega_r(t-\tau))]\Big|_{t_o}^{t} \\ + (B_1a + B_2c)[\frac{-\omega_r}{k^2+\omega_r^2}e^{k(t-\tau)}\cos((\omega_r(t-\tau)) + \frac{k}{k^2+\omega_r^2}e^{k(t-\tau)}\sin((\omega_r(t-\tau))]\Big|_{t_o}^{t} \\ B_2[\frac{\omega_r}{k^2+\omega_r^2}e^{k(t-\tau)}\sin((\omega_r(t-\tau)) + \frac{k}{k^2+\omega_r^2}e^{k(t-\tau)}\cos((\omega_r(t-\tau))]\Big|_{t_o}^{t} \\ + (B_2b + B_1d)[\frac{-\omega_r}{k^2+\omega_r^2}e^{k(t-\tau)}\cos((\omega_r(t-\tau)) + \frac{k}{k^2+\omega_r^2}e^{k(t-\tau)}\sin((\omega_r(t-\tau))]\Big|_{t_o}^{t} \end{bmatrix} \tag{2.17}$$

where

$$k=\frac{M}{2},\omega_r=\sqrt{N-\frac{M^2}{4}},a=\frac{\frac{M}{2}-a_{22}}{\omega_r},b=\frac{\frac{M}{2}-a_{11}}{\omega_r},c=\frac{a_{12}}{\omega_r},d=\frac{a_{21}}{\omega_r} \tag{2.18}$$

$$M=a_{11}+a_{22} \tag{2.19}$$

$$N=a_{11}a_{22}-a_{12}a_{21} \tag{2.20}$$

$$A=\begin{bmatrix} a_{11} & a_{12} \\ a_{21} & a_{22} \end{bmatrix} \tag{2.21}$$

$$a_{11}=\frac{-r_1}{L_m+L_1-\frac{L_m^{\ 2}}{L_m+L_2}} \tag{2.22}$$

$$a_{12}=\frac{L_m(r_2-s_2R)}{(L_m+L_2)(L_m+L_1)-L_m^{\ 2}} \tag{2.23}$$

$$a_{21}=\frac{L_m r_1}{(L_m+L_2)(L_m+L_1)-L_m^{\ 2}} \tag{2.24}$$

$$a_{22}=\frac{(s_2R-r_2)(L_m+L_1)}{(L_m+L_2)(L_m+L_1)-L_m^{\ 2}} \tag{2.25}$$

$$B=\begin{bmatrix} B_1 \\ B_2 \end{bmatrix}=\begin{bmatrix} \frac{1}{L_m+L_1-\frac{L_m^{\ 2}}{L_m+L_2}} \\ \frac{-L_m}{(L_m+L_2)(L_m+L_1)-L_m^{\ 2}} \end{bmatrix}V \tag{2.26}$$

Substitute the values of input vectors s_2 and V_1 for each time interval, calculate the integral parts and rearrange the equation as following:

1) At the time interval 0 to t_1 $\theta_1: V_1=V_{dc}, s_2=0$ the time is t_{10}

It is known $X[0]=-X[t_4]$ and $t_{10}=t_1-t_o=\frac{\varphi+\frac{\pi}{2}(D_1-D_2)}{\pi}\cdot\frac{T}{2}$

The $X[t_1]$ can be expressed in terms of $X[t_0]$:

$$X[t_1]=\begin{bmatrix} e^{kt_{10}}[\cos(\omega_r t_{10})+a\sin(\omega_r t_{10})] & ce^{kt_{10}}\sin(\omega_r t_{10}) \\ de^{kt_{10}}\sin(\omega_r t_{10}) & e^{kt_{10}}[\cos(\omega_r t_{10})+b\sin(\omega_r t_{10})] \end{bmatrix} X[0]$$

$$-\begin{bmatrix} B_1[\frac{k}{k^2+\omega_r{}^2}-\frac{\omega_r}{k^2+\omega_r{}^2}e^{kt_{10}}\sin(\omega_r t_{10})-\frac{k}{k^2+\omega_r{}^2}e^{kt_{10}}\cos(\omega_r t_{10})] \\ +(B_1a+B_2c)[-\frac{\omega_r}{k^2+\omega_r{}^2}+\frac{\omega_r}{k^2+\omega_r{}^2}e^{kt_{10}}\cos(\omega_r t_{10})-\frac{k}{k^2+\omega_r{}^2}e^{kt_{10}}\sin(\omega_r t_{10})] \\ B_2[\frac{k}{k^2+\omega_r{}^2}-\frac{\omega_r}{k^2+\omega_r{}^2}e^{kt_{10}}\sin(\omega_r t_{10})-\frac{k}{k^2+\omega_r{}^2}e^{kt_{10}}\cos(\omega_r t_{10})] \\ +(B_2b+B_1d)[-\frac{\omega_r}{k^2+\omega_r{}^2}+\frac{\omega_r}{k^2+\omega_r{}^2}e^{kt_{10}}\cos(\omega_r t_{10})-\frac{k}{k^2+\omega_r{}^2}e^{kt_{10}}\sin(\omega_r t_{10})] \end{bmatrix} \quad (2.27)$$

2) At the time interval t_1 to t_2 $\quad \theta_2: V_1=V_{dc}, s_2=1$ the time is t_{21}

It is known $X[t_2]_0=X[t_1]$ and $t_{21}=t_2-t_1=\frac{\pi D_2}{\pi}\cdot\frac{T}{2}$

The $X[t_2]$ can be expressed in terms of $X[t_1]$:

$$X[t_2]=\begin{bmatrix} e^{kt_{21}}[\cos(\omega_r t_{21})+a\sin(\omega_r t_{21})] & ce^{kt_{21}}\sin(\omega_r t_{21}) \\ de^{kt_{21}}\sin(\omega_r t_{21}) & e^{kt_{21}}[\cos(\omega_r t_{21})+b\sin(\omega_r t_{21})] \end{bmatrix} X[t_1]$$

$$-\begin{bmatrix} B_1[\frac{k}{k^2+\omega_r{}^2}-\frac{\omega_r}{k^2+\omega_r{}^2}e^{kt_{21}}\sin(\omega_r t_{21})-\frac{k}{k^2+\omega_r{}^2}e^{kt_{21}}\cos(\omega_r t_{21})] \\ +(B_1a+B_2c)[-\frac{\omega_r}{k^2+\omega_r{}^2}+\frac{\omega_r}{k^2+\omega_r{}^2}e^{kt_{21}}\cos(\omega_r t_{21})-\frac{k}{k^2+\omega_r{}^2}e^{kt_{21}}\sin(\omega_r t_{21})] \\ B_2[\frac{k}{k^2+\omega_r{}^2}-\frac{\omega_r}{k^2+\omega_r{}^2}e^{kt_{21}}\sin(\omega_r t_{21})-\frac{k}{k^2+\omega_r{}^2}e^{kt_{21}}\cos(\omega_r t_{21})] \\ +(B_2b+B_1d)[-\frac{\omega_r}{k^2+\omega_r{}^2}+\frac{\omega_r}{k^2+\omega_r{}^2}e^{kt_{21}}\cos(\omega_r t_{21})-\frac{k}{k^2+\omega_r{}^2}e^{kt_{21}}\sin(\omega_r t_{21})] \end{bmatrix} \quad (2.28)$$

3) At the time interval t_2 to t_3 $\quad \theta_3: V_1=V_{dc}, s_2=0$ the time is t_{32}

It is known $X[t_3]_o = X[t_2]$ and $t_{32} = t_3 - t_2 = [-\varphi + \frac{\pi}{2}(D_1 - D_2)] \cdot \frac{T}{2\pi}$

The $X[t_3]$ can be expressed in terms of $X[t_2]$:

$$X[t_3] = \begin{bmatrix} e^{kt_{32}}[\cos(\omega_r t_{32}) + a\sin(\omega_r t_{32})] & ce^{kt_{32}}\sin(\omega_r t_{32}) \\ de^{kt_{32}}\sin(\omega_r t_{32}) & e^{kt_{32}}[\cos(\omega_r t_{32}) + b\sin(\omega_r t_{32})] \end{bmatrix} X[t_2]$$

$$- \begin{bmatrix} B_1[\frac{k}{k^2+\omega_r{}^2} - \frac{\omega_r}{k^2+\omega_r{}^2}e^{kt_{32}}\sin(\omega_r t_{32}) - \frac{k}{k^2+\omega_r{}^2}e^{kt_{32}}\cos(\omega_r t_{32})] \\ +(B_1 a + B_2 c)[-\frac{\omega_r}{k^2+\omega_r{}^2} + \frac{\omega_r}{k^2+\omega_r{}^2}e^{kt_{32}}\cos(\omega_r t_{32}) - \frac{k}{k^2+\omega_r{}^2}e^{kt_{32}}\sin(\omega_r t_{32})] \\ B_2[\frac{k}{k^2+\omega_r{}^2} - \frac{\omega_r}{k^2+\omega_r{}^2}e^{kt_{32}}\sin(\omega_r t_{32}) - \frac{k}{k^2+\omega_r{}^2}e^{kt_{32}}\cos(\omega_r t_{32})] \\ +(B_2 b + B_1 d)[-\frac{\omega_r}{k^2+\omega_r{}^2} + \frac{\omega_r}{k^2+\omega_r{}^2}e^{kt_{32}}\cos(\omega_r t_{32}) - \frac{k}{k^2+\omega_r{}^2}e^{kt_{32}}\sin(\omega_r t_{32})] \end{bmatrix} \quad (2.29)$$

4) At the time interval t_3 to t_4 $\quad \theta_4 : V_1 = V_{dc}, s_2 = 0$ the time is t_{43}

It is known $X[t_4]_0 = X[t_3]$ and $t_{43} = t_4 - t_3 = \frac{\pi(1-D_1)}{\pi} \cdot \frac{T}{2}$

The $X[t_4]$ can be expressed in terms of $X[t_3]$:

$$X[t_4] = \begin{bmatrix} e^{kt_{43}}[\cos(\omega_r t_{43}) + a\sin(\omega_r t_{43})] & ce^{kt_{43}}\sin(\omega_r t_{43}) \\ de^{kt_{43}}\sin(\omega_r t_{43}) & e^{kt_{43}}[\cos(\omega_r t_{43}) + b\sin(\omega_r t_{43})] \end{bmatrix} X[t_3]$$

$$- \begin{bmatrix} B_1[\frac{k}{k^2+\omega_r{}^2} - \frac{\omega_r}{k^2+\omega_r{}^2}e^{kt_{43}}\sin(\omega_r t_{43}) - \frac{k}{k^2+\omega_r{}^2}e^{kt_{43}}\cos(\omega_r t_{43})] \\ +(B_1 a + B_2 c)[-\frac{\omega_r}{k^2+\omega_r{}^2} + \frac{\omega_r}{k^2+\omega_r{}^2}e^{kt_{43}}\cos(\omega_r t_{43}) - \frac{k}{k^2+\omega_r{}^2}e^{kt_{43}}\sin(\omega_r t_{43})] \\ B_2[\frac{k}{k^2+\omega_r{}^2} - \frac{\omega_r}{k^2+\omega_r{}^2}e^{kt_{43}}\sin(\omega_r t_{43}) - \frac{k}{k^2+\omega_r{}^2}e^{kt_{43}}\cos(\omega_r t_{43})] \\ +(B_2 b + B_1 d)[-\frac{\omega_r}{k^2+\omega_r{}^2} + \frac{\omega_r}{k^2+\omega_r{}^2}e^{kt_{43}}\cos(\omega_r t_{43}) - \frac{k}{k^2+\omega_r{}^2}e^{kt_{43}}\sin(\omega_r t_{43})] \end{bmatrix} \quad (2.30)$$

Set

$$P_1 = \begin{bmatrix} e^{kt_{10}}[\cos(\omega_r t_{10}) + a\sin(\omega_r t_{10})] & ce^{kt_{10}}\sin(\omega_r t_{10}) \\ de^{kt_{10}}\sin(\omega_r t_{10}) & e^{kt_{10}}[\cos(\omega_r t_{10}) + b\sin(\omega_r t_{10})] \end{bmatrix}$$

$$Q_1 = \begin{bmatrix} B_1[\frac{k}{k^2+\omega_r{}^2} - \frac{\omega_r}{k^2+\omega_r{}^2}e^{kt_{10}}\sin(\omega_r t_{10}) - \frac{k}{k^2+\omega_r{}^2}e^{kt_{10}}\cos(\omega_r t_{10})] \\ +(B_1a + B_2c)[-\frac{\omega_r}{k^2+\omega_r{}^2} + \frac{\omega_r}{k^2+\omega_r{}^2}e^{kt_{10}}\cos(\omega_r t_{10}) - \frac{k}{k^2+\omega_r{}^2}e^{kt_{10}}\sin(\omega_r t_{10})] \\ B_2[\frac{k}{k^2+\omega_r{}^2} - \frac{\omega_r}{k^2+\omega_r{}^2}e^{kt_{10}}\sin(\omega_r t_{10}) - \frac{k}{k^2+\omega_r{}^2}e^{kt_{10}}\cos(\omega_r t_{10})] \\ +(B_2b + B_1d)[-\frac{\omega_r}{k^2+\omega_r{}^2} + \frac{\omega_r}{k^2+\omega_r{}^2}e^{kt_{10}}\cos(\omega_r t_{10}) - \frac{k}{k^2+\omega_r{}^2}e^{kt_{10}}\sin(\omega_r t_{10})] \end{bmatrix} \quad (2.31)$$

$$P_2 = \begin{bmatrix} e^{kt_{21}}[\cos(\omega_r t_{21}) + a\sin(\omega_r t_{21})] & ce^{kt_{21}}\sin(\omega_r t_{21}) \\ de^{kt_{21}}\sin(\omega_r t_{21}) & e^{kt_{21}}[\cos(\omega_r t_{21}) + b\sin(\omega_r t_{21})] \end{bmatrix}$$

$$Q_2 = \begin{bmatrix} B_1[\frac{k}{k^2+\omega_r{}^2} - \frac{\omega_r}{k^2+\omega_r{}^2}e^{kt_{21}}\sin(\omega_r t_{21}) - \frac{k}{k^2+\omega_r{}^2}e^{kt_{21}}\cos(\omega_r t_{21})] \\ +(B_1a + B_2c)[-\frac{\omega_r}{k^2+\omega_r{}^2} + \frac{\omega_r}{k^2+\omega_r{}^2}e^{kt_{21}}\cos(\omega_r t_{21}) - \frac{k}{k^2+\omega_r{}^2}e^{kt_{21}}\sin(\omega_r t_{21})] \\ B_2[\frac{k}{k^2+\omega_r{}^2} - \frac{\omega_r}{k^2+\omega_r{}^2}e^{kt_{21}}\sin(\omega_r t_{21}) - \frac{k}{k^2+\omega_r{}^2}e^{kt_{21}}\cos(\omega_r t_{21})] \\ +(B_2b + B_1d)[-\frac{\omega_r}{k^2+\omega_r{}^2} + \frac{\omega_r}{k^2+\omega_r{}^2}e^{kt_{21}}\cos(\omega_r t_{21}) - \frac{k}{k^2+\omega_r{}^2}e^{kt_{21}}\sin(\omega_r t_{21})] \end{bmatrix} \quad (2.32)$$

$$P_3 = \begin{bmatrix} e^{kt_{32}}[\cos(\omega_r t_{32}) + a\sin(\omega_r t_{32})] & ce^{kt_{32}}\sin(\omega_r t_{32}) \\ de^{kt_{32}}\sin(\omega_r t_{32}) & e^{kt_{32}}[\cos(\omega_r t_{32}) + b\sin(\omega_r t_{32})] \end{bmatrix}$$

$$Q_3 = \begin{bmatrix} B_1[\frac{k}{k^2+\omega_r{}^2} - \frac{\omega_r}{k^2+\omega_r{}^2}e^{kt_{32}}\sin(\omega_r t_{32}) - \frac{k}{k^2+\omega_r{}^2}e^{kt_{32}}\cos(\omega_r t_{32})] \\ +(B_1a + B_2c)[-\frac{\omega_r}{k^2+\omega_r{}^2} + \frac{\omega_r}{k^2+\omega_r{}^2}e^{kt_{32}}\cos(\omega_r t_{32}) - \frac{k}{k^2+\omega_r{}^2}e^{kt_{32}}\sin(\omega_r t_{32})] \\ B_2[\frac{k}{k^2+\omega_r{}^2} - \frac{\omega_r}{k^2+\omega_r{}^2}e^{kt_{32}}\sin(\omega_r t_{32}) - \frac{k}{k^2+\omega_r{}^2}e^{kt_{32}}\cos(\omega_r t_{32})] \\ +(B_2b + B_1d)[-\frac{\omega_r}{k^2+\omega_r{}^2} + \frac{\omega_r}{k^2+\omega_r{}^2}e^{kt_{32}}\cos(\omega_r t_{32}) - \frac{k}{k^2+\omega_r{}^2}e^{kt_{32}}\sin(\omega_r t_{32})] \end{bmatrix} \quad (2.33)$$

$$P_4 = \begin{bmatrix} e^{kt_{43}}[\cos(\omega_r t_{43}) + a\sin(\omega_r t_{43})] & ce^{kt_{43}}\sin(\omega_r t_{43}) \\ de^{kt_{43}}\sin(\omega_r t_{43}) & e^{kt_{43}}[\cos(\omega_r t_{43}) + b\sin(\omega_r t_{43})] \end{bmatrix}$$

$$Q_4 = \begin{bmatrix} B_1[\frac{k}{k^2+\omega_r{}^2} - \frac{\omega_r}{k^2+\omega_r{}^2}e^{kt_{43}}\sin(\omega_r t_{43}) - \frac{k}{k^2+\omega_r{}^2}e^{kt_{43}}\cos(\omega_r t_{43})] \\ +(B_1 a + B_2 c)[-\frac{\omega_r}{k^2+\omega_r{}^2} + \frac{\omega_r}{k^2+\omega_r{}^2}e^{kt_{43}}\cos(\omega_r t_{43}) - \frac{k}{k^2+\omega_r{}^2}e^{kt_{43}}\sin(\omega_r t_{43})] \\ B_2[\frac{k}{k^2+\omega_r{}^2} - \frac{\omega_r}{k^2+\omega_r{}^2}e^{kt_{43}}\sin(\omega_r t_{43}) - \frac{k}{k^2+\omega_r{}^2}e^{kt_{43}}\cos(\omega_r t_{43})] \\ +(B_2 b + B_1 d)[-\frac{\omega_r}{k^2+\omega_r{}^2} + \frac{\omega_r}{k^2+\omega_r{}^2}e^{kt_{43}}\cos(\omega_r t_{43}) - \frac{k}{k^2+\omega_r{}^2}e^{kt_{43}}\sin(\omega_r t_{43})] \end{bmatrix} \quad (2.34)$$

By simplifying the expressions of the state variables equation at each time interval,

$$X[t_1] = P_1 X[0] - Q_1 \quad (2.35)$$

$$X[t_2] = P_2[P_1 X[0] - Q_1] - Q_2 \quad (2.36)$$

$$X[t_3] = P_3[P_2[P_1 X[0] - Q_1] - Q_2] - Q_3 \quad (2.37)$$

$$X[t_4] = P_4[P_3[P_2[P_1 X[0] - Q_1] - Q_2] - Q_3] - Q_4 \quad (2.38)$$

At steady state, due to the symmetry conditions, at the end of the half switching cycle, the values of state variables satisfy the condition $X[t_4] = -X[t_0]$, resulting in $X[t_0]$

$$X[t_0] = (1 + P_4 P_3 P_2 P_1)^{-1} \cdot (P_4 P_3 P_2 Q_1 + P_4 P_3 Q_2 + P_4 Q_3 + Q_4) \quad (2.39)$$

Hence the complete solution can be achieved by (2.17) and (2.39) if given the parameters such as duty ratios, phase angles, leakage inductance, capacitance, load resistance and input voltage.

Mode B (see Fig. 2.5) $\pi(D_1 - D_2) \le \varphi \le \frac{\pi}{2}(2 - D_1 - D_2)$. This can be separated into four states which can make this nonlinear system into four linear systems with each state space equation.

1) At the time interval 0 to t_1 $\theta_1 : V_1 = V_{dc}, s_2 = 0$ the time is t_{10}

2) At the time interval t_1 to t_2 $\theta_2 : V_1 = V_{dc}, s_2 = 1$ the time is t_{21}

3) At the time interval t_2 to t_3 $\theta_3 : V_1 = 0, s_2 = 1$ the time is t_{32}

4) At the time interval t_3 to t_4 $\theta_4 : V_1 = 0, s_2 = 0$ the time is t_{43}

Similarly the steps of calculation is are like the ones in Mode A. Substitute the values of input vectors s_2 and V_1 for each time interval, calculate the integral parts and rearrange the equation as follows:

1) At the time interval 0 to t_1 $\theta_1 : V_1 = V_{dc}, s_2 = 0$ the time is t_{10}

It is known $X[0] = -X[t_4]$ and $t_{10} = t_1 - t_0 = \dfrac{\varphi + \dfrac{\pi}{2}(D_1 - D_2)}{\pi} \cdot \dfrac{T}{2}$

The $X[t_1]$ can be expressed in terms of $X[t_0]$ which is same as the Equation (2.27).

2) At the time interval t_1 to t_2 $\theta_2 : V_1 = V_{dc}, s_2 = 1$ the time is t_{21}

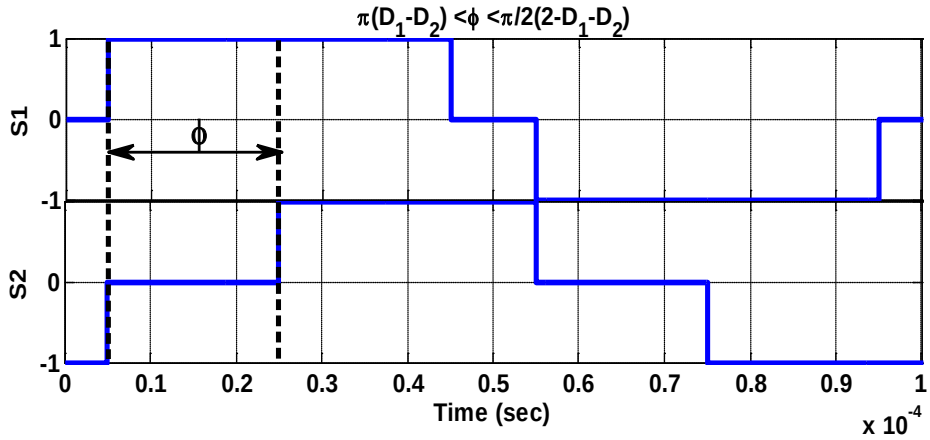

Fig. 2.5 Ideal waveform of operation Mode B

It is known $X[t_2]_0 = X[t_1]$ and $t_{21} = t_2 - t_1 = \dfrac{-\varphi + \dfrac{\pi}{2}(D_1 + D_2)}{\pi} \cdot \dfrac{T}{2}$

The $X[t_2]$ can be expressed in terms of $X[t_1]$ which is same as the Equation (2.28).

3) At the time interval t_2 to t_3 $\quad \theta_3 : V_1 = 0, s_2 = 1$ the time is t_{32}

It is known $X[t_3]_o = X[t_2]$ and $t_{32} = t_3 - t_2 = \dfrac{\varphi - \dfrac{\pi}{2}(D_1 - D_2)}{\pi} \cdot \dfrac{T}{2}$

As the input voltage $V_{dc} = 0$

$$B = \begin{bmatrix} B_1 \\ B_2 \end{bmatrix} = \begin{bmatrix} \dfrac{1}{L_m + L_1 - \dfrac{L_m{}^2}{L_m + L_2}} \\ \dfrac{-L_m}{(L_m + L_2)(L_m + L_1) - L_m{}^2} \end{bmatrix} \cdot 0 \Rightarrow \begin{bmatrix} B_1 \\ B_2 \end{bmatrix} = 0 \qquad (2.40)$$

The $X[t_3]$ can be expressed in terms of $X[t_2]$:

$$X[t_3] = \begin{bmatrix} e^{kt_{32}}[\cos(\omega_r t_{32}) + a\sin(\omega_r t_{32})] & ce^{kt_{32}}\sin(\omega_r t_{32}) \\ de^{kt_{32}}\sin(\omega_r t_{32}) & e^{kt_{32}}[\cos(\omega_r t_{32}) + b\sin(\omega_r t_{32})] \end{bmatrix} X[t_2] - 0 \qquad (2.41)$$

4) At the time interval t_3 to t_4 $\quad \theta_4 : V_1 = 0, \quad s_2 = 0$ the time is t_{43}

It is known $X[t_4]_0 = X[t_3]$ and $t_{43} = t_4 - t_3 = \dfrac{\pi(1 - D_1)}{\pi} \cdot \dfrac{T}{2}$

The $X[t_4]$ can be expressed in terms of $X[t_3]$:

$$X[t_4] = \begin{bmatrix} e^{kt_{43}}[\cos(\omega_r t_{43}) + a\sin(\omega_r t_{43})] & ce^{kt_{43}}\sin(\omega_r t_{43}) \\ de^{kt_{43}}\sin(\omega_r t_{43}) & e^{kt_{43}}[\cos(\omega_r t_{43}) + b\sin(\omega_r t_{43})] \end{bmatrix} X[t_3] - 0 \qquad (2.42)$$

Using the same simplified Equations (2.35)-(2.38) and the condition $X[t_4] = -X[t_0]$, the state space equations can be solved.

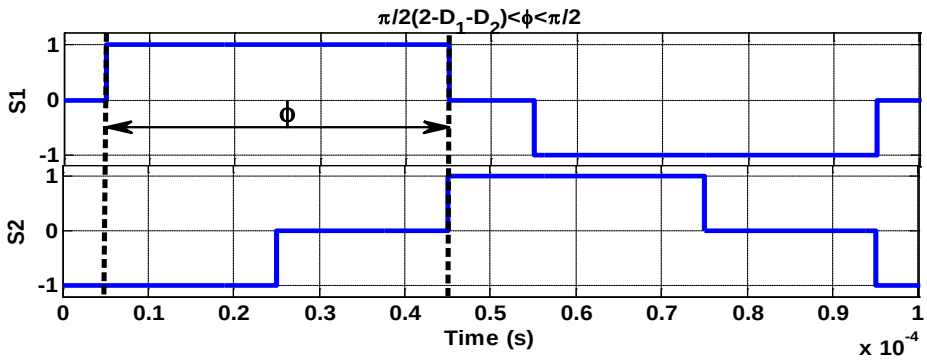

Fig. 2.6 Ideal waveform of operation Mode C

Mode C (see Fig. 2.6) $\pi(D_1 - D_2) \le \varphi \le \frac{\pi}{2}(2 - D_1 - D_2)$. This can be separated into four states which can make this nonlinear system into four linear systems with each state space equation.

1) At the time interval 0 to t_1 $\theta_1 : V_1 = V_{dc}, s_2 = -1$ the time is t_{10}

2) At the time interval t_1 to t_2 $\theta_2 : V_1 = V_{dc}, s_2 = 0$ the time is t_{21}

3) At the time interval t_2 to t_3 $\theta_3 : V_1 = V_{dc}, s_2 = 1$ the time is t_{32}

4) At the time interval t_3 to t_4 $\theta_4 : V_1 = 0, s_2 = 1$ the time is t_{43}

Similarly the steps of calculation are like the ones in Modes A and B. Substitute the values of input vectors s_2 and V_1 for each time interval, calculate the integral parts and rearrange the equation as follows:

1) At the time interval 0 to t_1 $\theta_1 : V_1 = V_{dc}, s_2 = -1$ the time is t_{10}

It is known $X[0] = -X[t_4]$ and $t_{10} = t_1 - t_o = \dfrac{\varphi + \frac{\pi}{2}(D_1 - D_2)}{\pi} \cdot \dfrac{T}{2}$

The $X[t_1]$ can be expressed in terms of $X[t_0]$ which is same as the Equation (2.27).

$$X[t_1]=\begin{bmatrix} e^{kt_{10}}[\cos(\omega_r t_{10})+a\sin(\omega_r t_{10})] & ce^{kt_{10}}\sin(\omega_r t_{10}) \\ de^{kt_{10}}\sin(\omega_r t_{10}) & e^{kt_{10}}[\cos(\omega_r t_{10})+b\sin(\omega_r t_{10})] \end{bmatrix} X[0]$$

$$-\begin{bmatrix} B_1[\frac{k}{k^2+\omega_r{}^2}-\frac{\omega_r}{k^2+\omega_r{}^2}e^{kt_{10}}\sin(\omega_r t_{10})-\frac{k}{k^2+\omega_r{}^2}e^{kt_{10}}\cos(\omega_r t_{10})] \\ +(B_1a+B_2c)[-\frac{\omega_r}{k^2+\omega_r{}^2}+\frac{\omega_r}{k^2+\omega_r{}^2}e^{kt_{10}}\cos(\omega_r t_{10})-\frac{k}{k^2+\omega_r{}^2}e^{kt_{10}}\sin(\omega_r t_{10})] \\ B_2[\frac{k}{k^2+\omega_r{}^2}-\frac{\omega_r}{k^2+\omega_r{}^2}e^{kt_{10}}\sin(\omega_r t_{10})-\frac{k}{k^2+\omega_r{}^2}e^{kt_{10}}\cos(\omega_r t_{10})] \\ +(B_2b+B_1d)[-\frac{\omega_r}{k^2+\omega_r{}^2}+\frac{\omega_r}{k^2+\omega_r{}^2}e^{kt_{10}}\cos(\omega_r t_{10})-\frac{k}{k^2+\omega_r{}^2}e^{kt_{10}}\sin(\omega_r t_{10})] \end{bmatrix} \quad (2.43)$$

2) At the time interval t_1 to t_2 $\quad \theta_2 : V_1 = V_{dc}, s_2 = 0$ the time is t_{21}

It is known $X[t_2]_0 = X[t_1]$ and $t_{21} = t_2 - t_1 = \dfrac{-\varphi + \frac{\pi}{2}(D_1 + D_2)}{\pi} \cdot \dfrac{T}{2}$

The $X[t_2]$ can be expressed in terms of $X[t_1]$ which is same as the Equation (2.28).

$$X[t_2]=\begin{bmatrix} e^{kt_{21}}[\cos(\omega_r t_{21})+a\sin(\omega_r t_{21})] & ce^{kt_{21}}\sin(\omega_r t_{21}) \\ de^{kt_{21}}\sin(\omega_r t_{21}) & e^{kt_{21}}[\cos(\omega_r t_{21})+b\sin(\omega_r t_{21})] \end{bmatrix} X[t_1]$$

$$-\begin{bmatrix} B_1[\frac{k}{k^2+\omega_r{}^2}-\frac{\omega_r}{k^2+\omega_r{}^2}e^{kt_{21}}\sin(\omega_r t_{21})-\frac{k}{k^2+\omega_r{}^2}e^{kt_{21}}\cos(\omega_r t_{21})] \\ +(B_1a+B_2c)[-\frac{\omega_r}{k^2+\omega_r{}^2}+\frac{\omega_r}{k^2+\omega_r{}^2}e^{kt_{21}}\cos(\omega_r t_{21})-\frac{k}{k^2+\omega_r{}^2}e^{kt_{21}}\sin(\omega_r t_{21})] \\ B_2[\frac{k}{k^2+\omega_r{}^2}-\frac{\omega_r}{k^2+\omega_r{}^2}e^{kt_{21}}\sin(\omega_r t_{21})-\frac{k}{k^2+\omega_r{}^2}e^{kt_{21}}\cos(\omega_r t_{21})] \\ +(B_2b+B_1d)[-\frac{\omega_r}{k^2+\omega_r{}^2}+\frac{\omega_r}{k^2+\omega_r{}^2}e^{kt_{21}}\cos(\omega_r t_{21})-\frac{k}{k^2+\omega_r{}^2}e^{kt_{21}}\sin(\omega_r t_{21})] \end{bmatrix} \quad (2.44)$$

3) At the time interval t_2 to t_3 $\quad \theta_3 : V_1 = V_{dc}, s_2 = 1$ the time is t_{32}

It is known $X[t_3]_o = X[t_2]$ and $t_{32} = t_3 - t_2 = \dfrac{\varphi - \frac{\pi}{2}(D_1 - D_2)}{\pi} \cdot \dfrac{T}{2}$

$$X[t_3]=\begin{bmatrix} e^{kt_{32}}[\cos(\omega_r t_{32})+a\sin(\omega_r t_{32})] & ce^{kt_{32}}\sin(\omega_r t_{32}) \\ de^{kt_{32}}\sin(\omega_r t_{32}) & e^{kt_{32}}[\cos(\omega_r t_{32})+b\sin(\omega_r t_{32})] \end{bmatrix} X[t_2]$$

$$-\begin{bmatrix} B_1[\frac{k}{k^2+\omega_r{}^2}-\frac{\omega_r}{k^2+\omega_r{}^2}e^{kt_{32}}\sin(\omega_r t_{32})-\frac{k}{k^2+\omega_r{}^2}e^{kt_{32}}\cos(\omega_r t_{32})] \\ +(B_1a+B_2c)[-\frac{\omega_r}{k^2+\omega_r{}^2}+\frac{\omega_r}{k^2+\omega_r{}^2}e^{kt_{32}}\cos(\omega_r t_{32})-\frac{k}{k^2+\omega_r{}^2}e^{kt_{32}}\sin(\omega_r t_{32})] \\ B_2[\frac{k}{k^2+\omega_r{}^2}-\frac{\omega_r}{k^2+\omega_r{}^2}e^{kt_{32}}\sin(\omega_r t_{32})-\frac{k}{k^2+\omega_r{}^2}e^{kt_{32}}\cos(\omega_r t_{32})] \\ +(B_2b+B_1d)[-\frac{\omega_r}{k^2+\omega_r{}^2}+\frac{\omega_r}{k^2+\omega_r{}^2}e^{kt_{32}}\cos(\omega_r t_{32})-\frac{k}{k^2+\omega_r{}^2}e^{kt_{32}}\sin(\omega_r t_{32})] \end{bmatrix} \quad (2.45)$$

4) At the time interval t_3 to t_4 $\quad \theta_4 : V_1 = 0, \quad s_2 = 1$ the time is t_{43}

It is known $X[t_4]_0 = X[t_3]$ and $t_{43} = t_4 - t_3 = \frac{\pi(1-D_1)}{\pi}\cdot\frac{T}{2}$

The $X[t_4]$ can be expressed in terms of $X[t_3]$:

$$X[t_4]=\begin{bmatrix} e^{kt_{43}}[\cos(\omega_r t_{43})+a\sin(\omega_r t_{43})] & ce^{kt_{43}}\sin(\omega_r t_{43}) \\ de^{kt_{43}}\sin(\omega_r t_{43}) & e^{kt_{43}}[\cos(\omega_r t_{43})+b\sin(\omega_r t_{43})] \end{bmatrix} X[t_3]-0 \quad (2.46)$$

Using the same simplified Equations (2.35)-(2.38) and the condition $X[t_4]=-X[t_0]$, the state space equations can be solved.

Thusfar Modes A, B, and C are calculated using state space method. One can summarize the procedure of the analysis and generalize all the conditions into one formula. First, the half time period can be separated into four states which can make this nonlinear system into four linear systems with their own state space equation. For any time interval, the time $t_{i(i-1)}$, the input voltage $V_1 = \beta_i V_{dc}, \beta_i = (0\ or 1)$, and output voltage waveforms $s_2 = (-1, 0\ or 1)$ are constant at each time interval, hence the linear system can be solved by the Equation (2.16).

The system is generalized in terms of state space equation at any time interval for each mode:

$$X[t]=\begin{bmatrix} X_1 e^{kw_1(t-t_{i-1})}-Y_1 e^{kw_1(t-t_{i-1})} & Z_1 e^{kw_1(t-t_{i-1})}-Z_1 e^{kw_2(t-t_{i-1})} \\ Z_1 e^{kw_1(t-t_{i-1})}-Z_1 e^{kw_2(t-t_{i-1})} & X_2 e^{kw_1(t-t_{i-1})}-Y_2 e^{kw_2(t-t_{i-1})} \end{bmatrix} X[t_{i-1}]$$
$$-\begin{bmatrix} \frac{B_1X_1+B_2Z_1}{kw_1}(1-e^{kw_1(t-t_{i-1})})-\frac{B_1Y_1+B_2Z_1}{kw_2}(1-e^{kw_2(t-t_{i-1})}) \\ \frac{B_1Z_2+B_2X_2}{kw_1}(1-e^{kw_1(t-t_{i-1})})-\frac{B_1Z_2+B_2Y_2}{kw_2}(1-e^{kw_2(t-t_{i-1})}) \end{bmatrix} \quad (2.47)$$

where

$$a_{11}=\frac{-r_1}{L_m+L_1-\frac{L_m^2}{L_m+L_2}} \quad (2.48)$$

$$a_{12}=\frac{L_m(r_2+s_2{}^2R)}{(L_m+L_2)(L_m+L_1)-L_m^2} \quad (2.49)$$

$$a_{21}=\frac{L_m r_1}{(L_m+L_2)(L_m+L_1)-L_m^2} \quad (2.50)$$

$$a_{22}=\frac{(s_2{}^2R+r_2)(L_m+L_1)_1}{(L_m+L_2)(L_m+L_1)-L_m^2} \quad (2.51)$$

$$A=\begin{bmatrix} a_{11} & a_{12} \\ a_{21} & a_{22} \end{bmatrix} \quad (2.52)$$

$$B=\begin{bmatrix} B_1 \\ B_2 \end{bmatrix}=\begin{bmatrix} \frac{1}{L_m+L_1-\frac{L_m{}^2}{L_m+L_2}} \\ \frac{-L_m}{(L_m+L_2)(L_m+L_1)-\frac{L_m{}^2}{L_m+L_2}} \end{bmatrix} v_1 \quad (2.53)$$

$$k=\frac{a_{11}+a_{22}}{2} \quad (2.54)$$

$$\omega_r = \sqrt{a_{11}a_{22} - a_{12}a_{21} - 0.25k^2} \tag{2.55}$$

$$X_1 = 1 + \frac{k - \omega_r - a_{22}}{2\omega_r} \tag{2.56}$$

$$Y_1 = \frac{k - \omega_r - a_{22}}{2\omega_r} \tag{2.57}$$

$$Z_1 = \frac{a_{12}}{2\omega_r} \tag{2.58}$$

$$X_2 = 1 + \frac{k - \omega_r - a_{11}}{2\omega_r} \tag{2.59}$$

$$Y_2 = \frac{k - \omega_r - a_{11}}{2\omega_r} \tag{2.60}$$

$$Z_2 = \frac{a_{21}}{2\omega_r} \tag{2.61}$$

$$kw_1 = k + \omega_r \tag{2.62}$$

$$kw_2 = k - \omega_r \tag{2.63}$$

2.3. Simulation of System with Mutual Inductance Lm and Without Lm

The analysis of an isolated dual active bridge dc-dc converter (DAB) connected by a fuel cell dc source and resistive load is studied in this section. The state space method has been used to analyze the converter for the prediction of performance. Closed form expressions of the states of the converter at specific modes are derived and the predicted results are compared with those obtained with a fundamental component model.

When the source side converter impresses two rectangular voltage pulses on the high frequency transformer, then there are three feasible modes of operation [45]. To simplify the analysis it is assumed that the duty ratio of source-side converter is greater than that of the load side converter, $D_1>D_2$, and variable phase shift angle between the converters $\Phi>0$. For this presentation, Mode B operation is selected where $\pi(D_1-D_2)/2<\Phi<\pi(2-D_1-D_2)/2$. The parameters of the converters used are given as follows: resistance $r_1=0.03\Omega$, $r_2=0.005\Omega$, leakage inductance $L_1=21\mu H$, $L_2=495nH$, mutual inductance Lm=1mH, R=40 Ω, D1=0.8, D2=0.6, Vdc1=80 V, phase shift angle $\Phi=30°$.So the generalized solution with mutual inductance can be expressed in Equation (2.45).

Secondly, based on the system without L_m, the equivalent circuit of the two-port DAB converter system is shown in Fig. 2.7.

The dynamic equations are

$$L_1 p i_1 - L_2 p i_2^{'} + r_1 i_1 - r_2 i_2^{'} - s_2^2 R i_2^{'} = v_1 \tag{2.64}$$

$$i_2^{'} = -i_1 \tag{2.65}$$

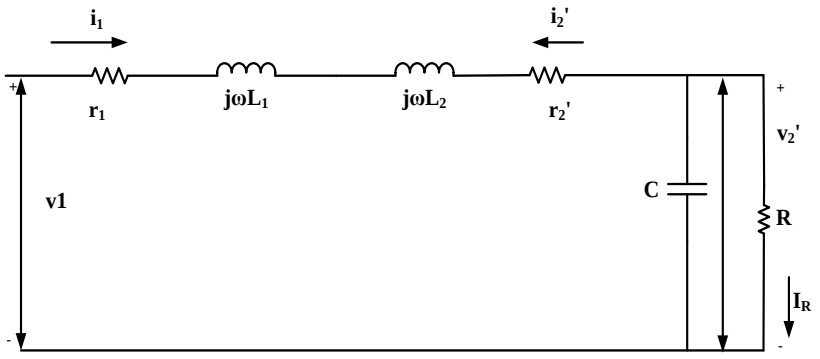

Fig. 2.7 Equivalent circuit of DAB converter without mutual inductance L_m

After the calculation, the general solution of the system without mutual inductance can be expressed as follows:

$$i_1[t]_i = e^{-\frac{r1+r_2+s_2^2R}{L_1+L_2}t} \cdot i_1[t]_{i-1} + \frac{v_1}{r_1+r_2+s_2^2R}[1-e^{-\frac{r1+r_2+s_2^2R}{L_1+L_2}t}] \tag{2.66}$$

The converter currents and input source power are calculated and compared under situations with and without the transformer mutual inductance. As is shown in Fig. 2.8 and Fig. 2.9, a slight difference between two situations is recorded. However the influence of the mutual inductance L_m on the current and power is not significant simply because the value of mutual inductance L_m is much bigger than the sum of the leakage inductances. Hence, L_m can be ignored in the analysis of the bidirectional dc-dc converter system.

A full order model of the converter including the switching functions is simulated using MATLAB/SIMULINK and the corresponding results are shown in Fig. 2.10 and Fig. 2. 11. Because of the good comparison of the two results using the analytic based on state space model and the computed simulated full order model, the mathematically analytic model obtained by using state space method can be used to study the performance of the DAB converter system.

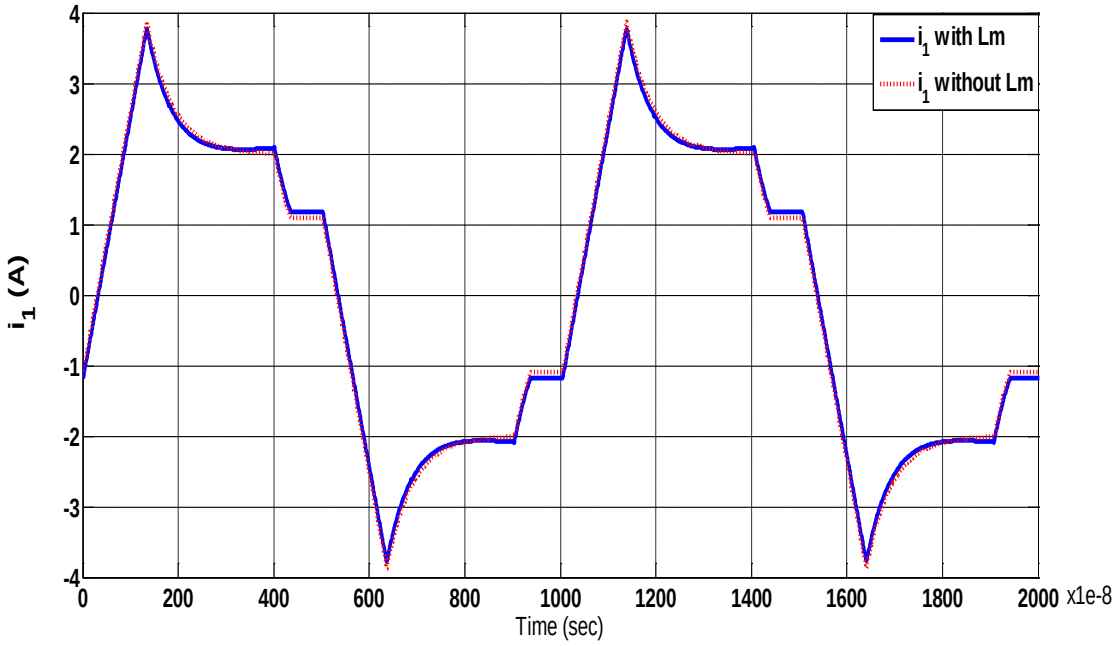

Fig. 2.8 Comparison of the instantaneous input current i_1 with and without L_m

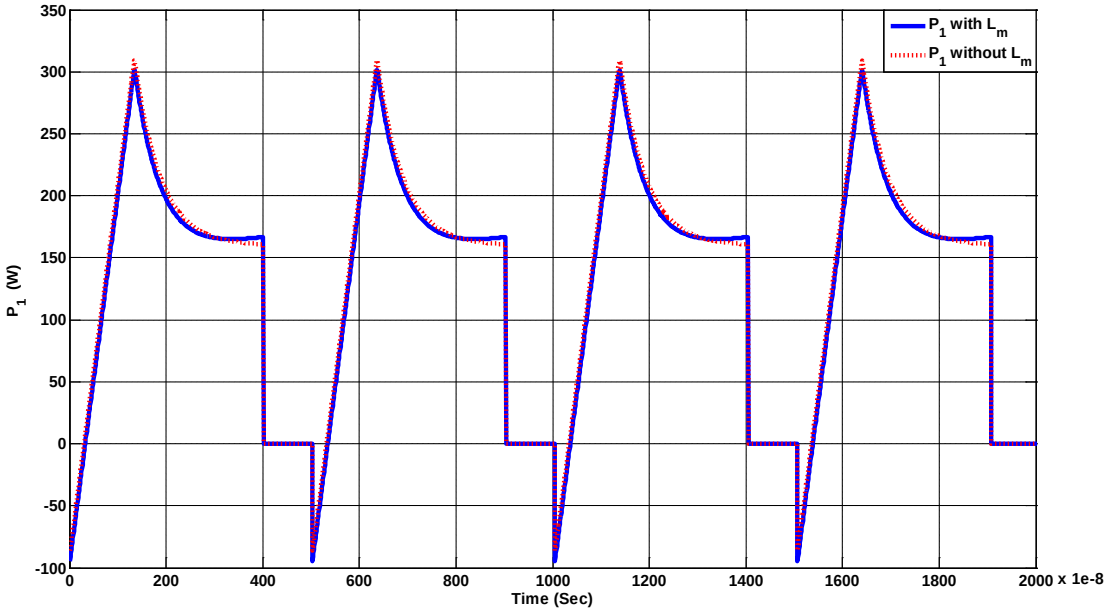

Fig. 2.9 Comparison of the instantaneous input power P_1 with and without L_m

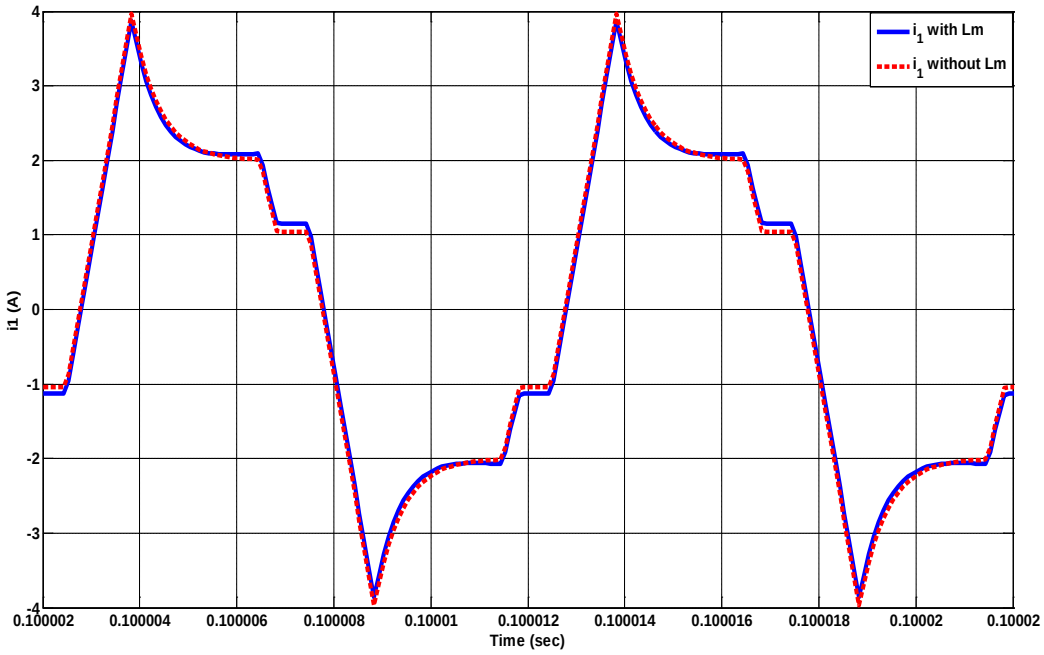

Fig. 2.10 The input current i_1 with L_m and without using L_m Simulink

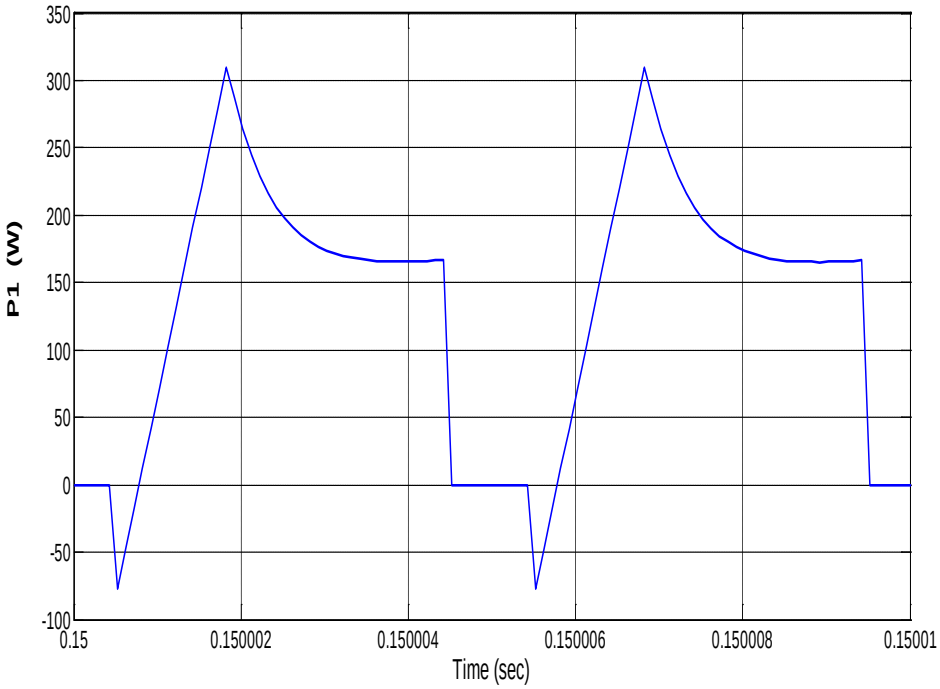

Fig. 2.11 The input power P_1 using Simulink

CHAPTER 3

POWER FLOW MANAGEMENT AND CONVERTER DYNAMICS OF THE DAB SYSTEM

3.1 Introduction

The operation of the two-port DAB converter system is classified into three modes. In the present chapter, the derivation of the power flow analysis is thoroughly studied. Key expression of the voltage imposed on the inductance, input instantaneous currents, and real power are derived by using half-cycle symmetry since the power delivered by the source to the load during the positive half-cycle is equal to the power delivered by the negative half-cycle. Additionally, in a later section, the small signal analysis of the two-port DAB converter system is presented analytically and the losses of semiconductors including power MOSFETs and diodes are added to the circuit resulting in a new state space model of non-ideal DAB system. The results derived from the small signal analysis can be used to study the dynamic behavior of the converter system.

3.2 Power Flow of the Proposed DAB System

The operation of dual active bridge converter with two rectangular waveforms can be classified into three modes. These modes are acquired by shifting one waveform while keeping the other one unchanged. Then, based on these three different modes, the power flow equations are determind as shown in the following passage. First, with the

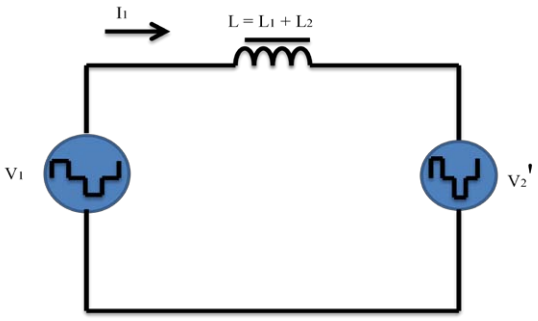

Fig. 3.1 Ideal equivalent circuit of two-port DAB converter system

assumption of two voltage sources, the mutual inductance of high frequency transformer is ignored and the equivalent is shown in Fig. 3.1. Based on the study of Chapter 2, the mutual inductance has a minor effect on the dynamic performance of the DAB system.

In this operation mode, both voltages are rectangular pulse waveforms. Assume two voltage sources as V_1 and V_2', $L = L_1 + L_2$, ignore the resistance $R = r_1 + r_2$

$$V_1 - V_2' = Lpi_1 \tag{3.1}$$

In the same way, place the derivative part on the left side:

$$pi_1 = \frac{1}{L}(V_1 - V_2') = 0 \cdot i_1 + B \cdot u \tag{3.2}$$

where, $B = \frac{1}{L}$, $u = V_1 - V_2'$

The solution of current as i_1 can be determined as follows:

$$i_1 = i_1(t_o) + \frac{1}{L}u(t - t_o) \tag{3.3}$$

The voltage can be expressed as the function of switching pulse and dc voltage:

$$V_1 - V_2' = S_1 V_{dc1} - S_2 V_{dc2} = V^* \tag{3.4}$$

The operation situation of the bidirectional dc-dc converter system based on two rectangular waveform pulses can be divided into three modes [45]. Hence, input and output ac voltages are all rectangular pulse waveforms. To simplify the operation situations, an assumption is made that $D_1 > D_2$ and the phase shift angle compared with the input rectangular waveform $\phi > 0$, which means that output rectangular waveform is lagging to the input rectangular waveform. The three operation modes are shown in Fig. 3.2.

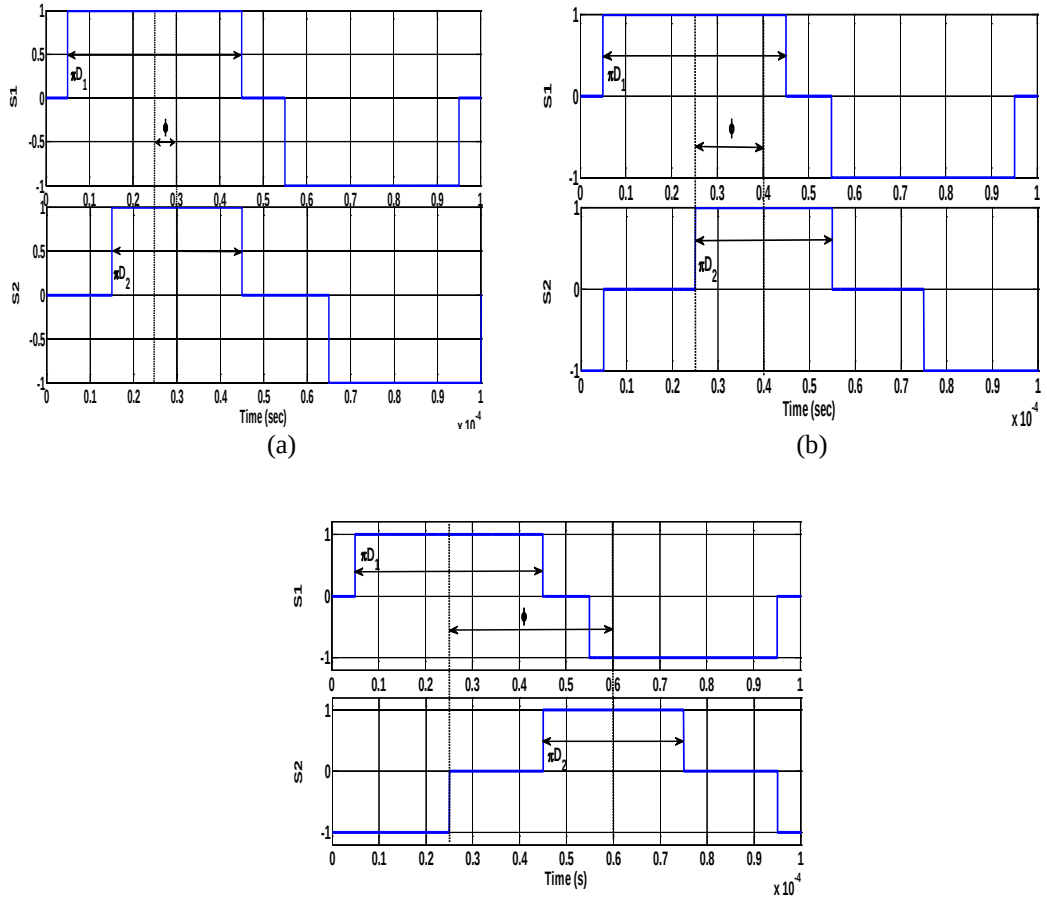

Fig. 3.2 Possible operation modes of two rectangular waveforms: (a) Mode A, when $\phi \le \frac{\pi}{2}(D_1 - D_2)$;

(b) Mode B, when $\frac{\pi}{2}(D_1 - D_2) < \phi \le \frac{\pi}{2}(2 - D_1 - D_2)$; (c) Mode C, when $\frac{\pi}{2}(2 - D_1 - D_2) < \phi \le \frac{\pi}{2}$

For any Mode A, B, and C, the time instants can be generalized as below:

$$\begin{cases} 1.\ t_o \sim t_1 \quad t_{10} \quad \begin{matrix} S_{11} \\ S_{21} \end{matrix} \\ 2.\ t_1 \sim t_2 \quad t_{12} \quad \begin{matrix} S_{12} \\ S_{22} \end{matrix} \\ 3.\ t_2 \sim t_3 \quad t_{23} \quad \begin{matrix} S_{13} \\ S_{23} \end{matrix} \\ 4.\ t_3 \sim t_4 \quad t_{34} \quad \begin{matrix} S_{14} \\ S_{24} \end{matrix} \end{cases} \tag{3.5}$$

The average power of Port 1 can be expressed as below:

$$P_1 = \frac{2}{T}[\int_{t_o}^{t_1} V_{11}{}^* I_1 dt + \int_{t_1}^{t_2} V_{12}{}^* I_2 dt + \int_{t_2}^{t_3} V_{13}{}^* I_3 dt + \int_{t_3}^{t_4} V_{14}{}^* I_4 dt] \tag{3.6}$$

where the V_{1i} is the voltage operating in the specific time intervals and the I_i is the input current operating in the specific time intervals.

During the time instant $t_o \sim t_1, V_{11}{}^* I_1$ can be expressed as

$$V_{11}{}^* I_1 = (S_{11} V_{dc1})[i_1(t_o) + \frac{1}{L}(S_{11} V_{dc1} - S_{21} V_{dc2})(t - t_o)] \tag{3.7}$$

During the time instants $t_1 \sim t_2, V_{12}{}^* I_2$ and current can be expressed as

$$V_{12}{}^* I_2 = (S_{12} V_{dc1})[i_1(t_1) + \frac{1}{L}(S_{12} V_{dc1} - S_{22} V_{dc2})(t - t_1)] \tag{3.8}$$

$$i_1(t_1) = i_1(t_o) + \frac{1}{L}(S_{11} V_{dc1} - S_{21} V_{dc2}) t_{10} \tag{3.9}$$

During the time instants $t_2 \sim t_3, V_{13}{}^* I_3$ and current can be expressed as

$$V_{13}{}^* I_3 = (S_{13} V_{dc1})[i_1(t_2) + \frac{1}{L}(S_{13} V_{dc1} - S_{23} V_{dc2})(t - t_2)] \tag{3.10}$$

$$i_1(t_2) = i_1(t_1) + \frac{1}{L}(S_{12}V_{dc1} - S_{22}V_{dc2})t_{12} = i_1(t_o) + \frac{1}{L}(S_{11}V_{dc1} - S_{21}V_{dc2})t_{10} + \frac{1}{L}(S_{12}V_{dc1} - S_{22}V_{dc2})t_{12} \tag{3.11}$$

During the time instants $t_3 \sim t_4$, $V_{14}{}^{*}I_4$ and current can be expressed as

$$V_{14}{}^{*}I_4 = (S_{14}V_{dc1})[i_1(t_3) + \frac{1}{L}(S_{14}V_{dc1} - S_{24}V_{dc2})(t - t_3)] \tag{3.12}$$

$$i_1(t_3) = i_1(t_o) + \frac{1}{L}(S_{11}V_{dc1} - S_{21}V_{dc2})t_{10} + \frac{1}{L}(S_{12}V_{dc1} - S_{22}V_{dc2})t_{12} + \frac{1}{L}(S_{13}V_{dc1} - S_{23}V_{dc2})t_{23} \tag{3.13}$$

Then bring (3.10) – (3.13) into the average power Equation (3.6), the general power flow equations can be given as

$$\begin{aligned} P = \frac{2}{T}[&V_{11}{}^{*}(i_1(t_o) + (V_{11}{}^{*} - V_{21}{}^{*})\frac{1}{L}\frac{1}{2}t_{10})t_{10} + V_{12}{}^{*}(i_1(t_o) + \frac{1}{L}(V_{11}{}^{*} - V_{21}{}^{*})t_{10} + \frac{1}{L}\frac{1}{2}(V_{12}{}^{*} - V_{22}{}^{*})t_{12})t_{12} \\ &+ V_{13}{}^{*}(i_1(t_o) + \frac{1}{L}(V_{11}{}^{*} - V_{21}{}^{*})t_{10} + \frac{1}{L}(V_{12}{}^{*} - V_{22}{}^{*})t_{12} + \frac{1}{L}(V_{13}{}^{*} - V_{23}{}^{*})\frac{1}{2}t_{23})t_{23} \\ &+ V_{14}{}^{*}(i_1(t_o) + \frac{1}{L}(V_{11}{}^{*} - V_{21}{}^{*})t_{10} + \frac{1}{L}(V_{12}{}^{*} - V_{22}{}^{*})t_{12} + \frac{1}{L}(V_{13}{}^{*} - V_{23}{}^{*})t_{23} + \frac{1}{L}(V_{14}{}^{*} - V_{24}{}^{*})\frac{1}{2}t_{34})t_{34}] \end{aligned} \tag{3.14}$$

Mode A (see Fig. 3.2 (a) shows the values of time intervals and state of switching functions by

$$t_o \sim t_1 \qquad t_{10} = [\frac{\varphi}{\pi} + \frac{1}{2}(D_1 - D_2)] \cdot T/2 \quad \begin{cases} S_{11} = 1 \\ S_{21} = 0 \end{cases} \tag{3.15}$$

$$t_1 \sim t_2 \qquad t_{12} = D_2 \cdot T/2 \quad \begin{cases} S_{12} = 1 \\ S_{22} = 1 \end{cases} \tag{3.16}$$

$$t_2 \sim t_3 \qquad t_{23} = [-\frac{\varphi}{\pi} + \frac{1}{2}(D_1 - D_2)] \cdot T/2 \quad \begin{cases} S_{13} = 1 \\ S_{23} = 0 \end{cases} \tag{3.17}$$

$$t_3 \sim t_4 \qquad t_{34} = (1 - D_1) \cdot T/2 \quad \begin{cases} S_{14} = 0 \\ S_{24} = 0 \end{cases} \tag{3.18}$$

For the initial value $i_1(t_o)$, known that $i_1(t_o) = -i_1(t_4)$, the expression can be

$$i_1(t_o) = -\frac{1}{2}\left\{\frac{\pi}{\omega L}V_{dc1}\left(\frac{\varphi}{\pi}+\frac{1}{2}(D_1-D_2)\right)+\frac{\pi}{\omega L}(V_{dc1}-V_{dc2})D_2+\frac{\pi}{\omega L}V_{dc1}\left(-\frac{\varphi}{\pi}+\frac{1}{2}(D_1-D_2)\right)\right\} \quad (3.19)$$

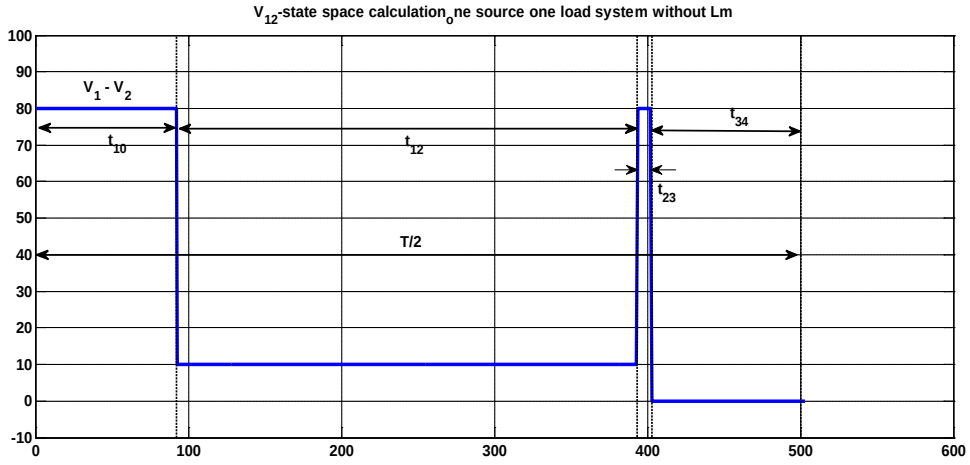

Fig. 3.3 The difference between V_1 and V_2 waveform over a half time period

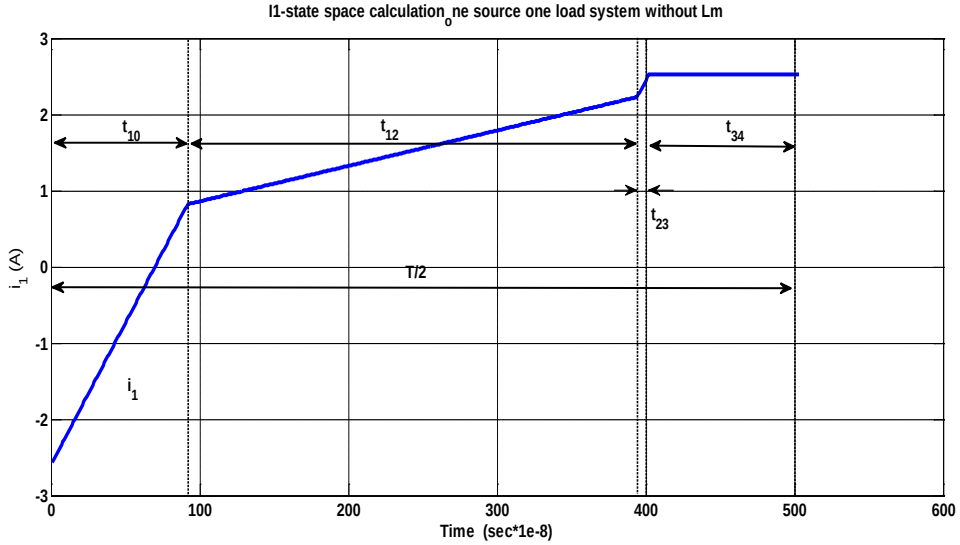

Fig. 3.4 The input current I_1 waveform over a half time period

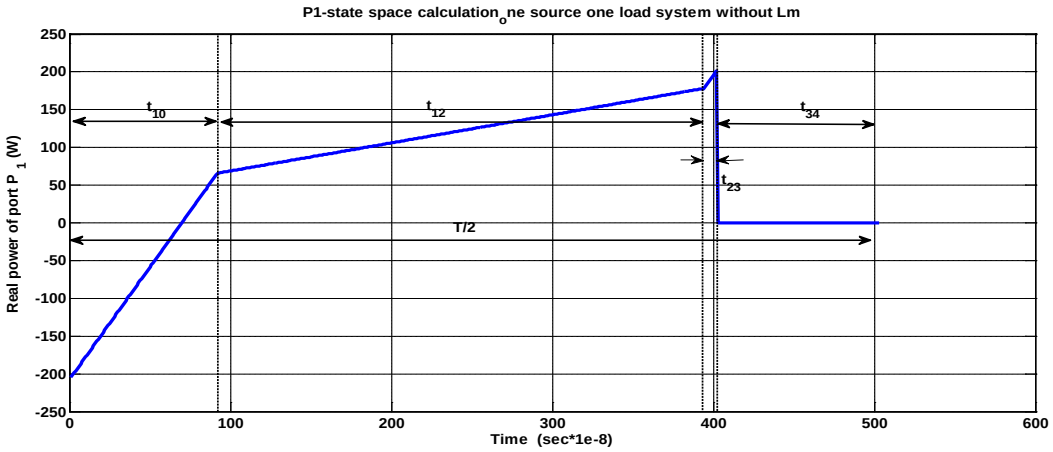

Fig. 3.5 The real power P_1 waveform over a half time period

Hence, the power flow equation for Mode A is given by

$$P_1 = V_{dc1} V_{dc2} \frac{\varphi}{\omega L} D_2 \tag{3.20}$$

The dynamic performance of the voltage drop on leakage inductance, input current, and real power between two ports is shown in Fig. 3.3 – Fig. 3.5.

Mode B (see Fig. 3.2 (b)) shows the values of time intervals and state of switching functions by

$$t_o \sim t_1 \qquad t_{10} = [\frac{\varphi}{\pi} + \frac{1}{2}(D_1 - D_2)] \cdot T/2 \quad \begin{cases} S_{11} = 1 \\ S_{21} = 0 \end{cases} \tag{3.21}$$

$$t_1 \sim t_2 \qquad t_{12} = [-\frac{\varphi}{\pi} + \frac{1}{2}(D_1 + D_2)] \cdot T/2 \quad \begin{cases} S_{12} = 1 \\ S_{22} = 1 \end{cases} \tag{3.22}$$

$$t_2 \sim t_3 \qquad t_{23} = [\frac{\varphi}{\pi} - \frac{1}{2}(D_1 - D_2)] \cdot T/2 \quad \begin{cases} S_{13} = 0 \\ S_{23} = 1 \end{cases} \tag{3.23}$$

$$t_3 \sim t_4 \qquad t_{34} = [-\frac{\varphi}{\pi} + \frac{1}{2}(2 - D_1 - D_2)] \cdot T/2 \quad \begin{cases} S_{14} = 0 \\ S_{24} = 0 \end{cases} \tag{3.24}$$

For the initial value $i_1(t_o)$, its known that $i_1(t_o) = -i_1(t_4)$, the expression can be

$$i_1(t_o) = -\left\{ V_{dc1} \frac{\pi}{2\omega L} \left(\frac{\varphi}{\pi} + \frac{1}{2}(D_1 - D_2) \right) + \frac{\pi}{2\omega L} (V_{dc1} - V_{dc2}) \left(-\frac{\varphi}{\pi} + \frac{1}{2}(D_1 + D_2) \right) - \frac{\pi}{2\omega L} V_{dc2} \left(\frac{\varphi}{\pi} - \frac{1}{2}(D_1 - D_2) \right) \right\} \quad (3.25)$$

Hence, the power flow equation for Mode B is given by

$$P_1 = V_{dc1} V_{dc2} \frac{\pi}{2\omega L} \left[\frac{\varphi}{\pi} D_2 + \frac{1}{2} D_1 D_2 - \frac{1}{2} D_2^{\,2} - \left(\frac{\varphi}{\pi} \right)^2 + \frac{\varphi}{\pi} D_1 - \frac{1}{4} (D_1^{\,2} - D_2^{\,2}) \right] \quad (3.26)$$

The dynamic performance of the voltage drop on leakage inductance, input current, and real power between two ports is shown in Fig. 3.6 – Fig. 3.8.

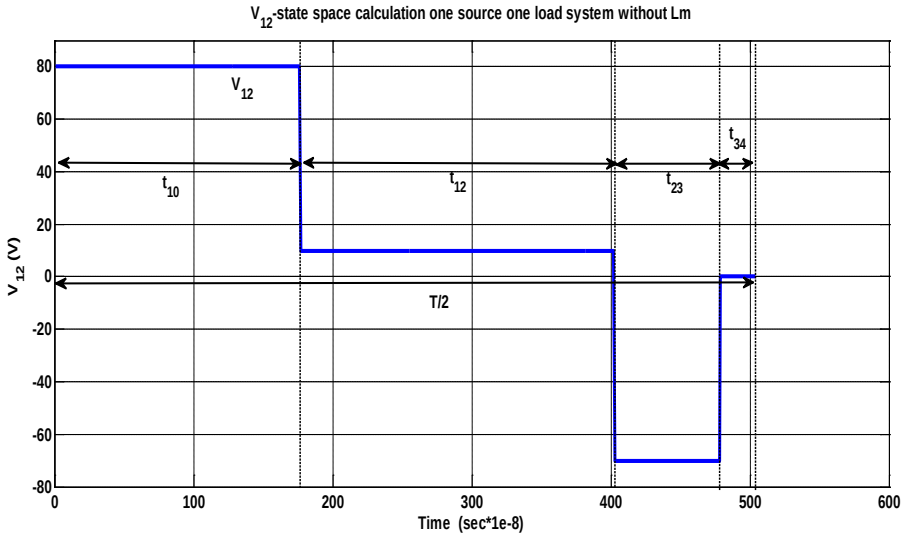

Fig. 3.6 The difference between V_1 and V_2 waveform over a half time period

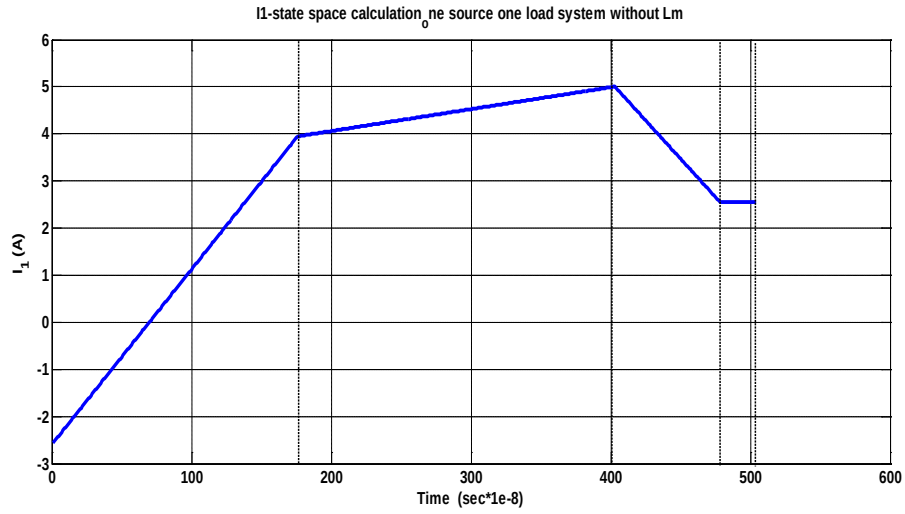

Fig. 3.7 The input current I_1 waveform over a half time period

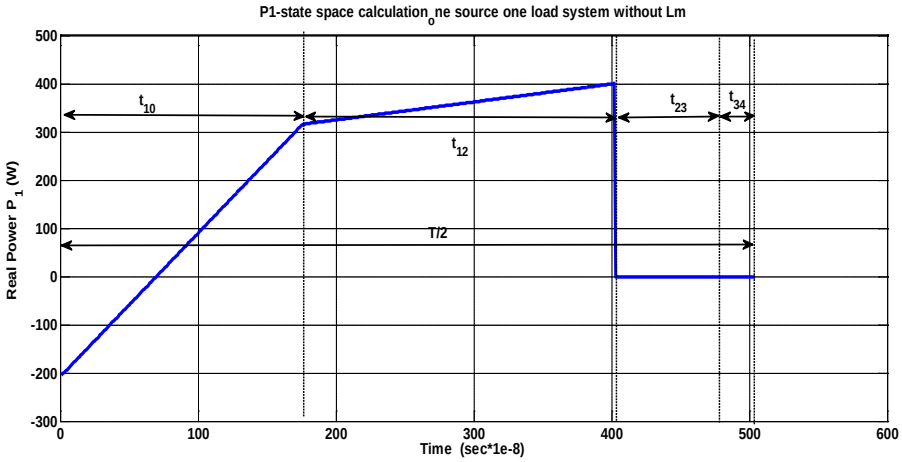

Fig. 3.8 The real power P_1 waveform over a half time period

Mode C (see Fig. 3.2 (c)) shows the values of time intervals and state of switching functions are given by

$$\frac{t_{10}}{T/2}=\frac{\varphi}{\pi}-\frac{1}{2}(2-D_1-D_2),\ \frac{t_{12}}{T/2}=1-D_2,\ \frac{t_{23}}{T/2}=-\frac{\varphi}{\pi}+\frac{1}{2}(D_1+D_2),\ \frac{t_{34}}{T/2}=1-D_1$$

$$t_o \sim t_1 \qquad t_{10}=[\frac{\varphi}{\pi}-\frac{1}{2}(2-D_1-D_2)]\cdot T/2 \quad \begin{cases} S_{11}=1 \\ S_{21}=-1 \end{cases} \tag{3.27}$$

$$t_1 \sim t_2 \qquad t_{12}=[1-D_2]\cdot T/2 \quad \begin{cases} S_{12}=1 \\ S_{22}=0 \end{cases} \tag{3.28}$$

$$t_2 \sim t_3 \qquad t_{23}=[-\frac{\varphi}{\pi}+\frac{1}{2}(D_1+D_2)]\cdot T/2 \quad \begin{cases} S_{13}=1 \\ S_{23}=1 \end{cases} \tag{3.29}$$

$$t_3 \sim t_4 \qquad t_{34}=[1-D_1]\cdot T/2 \quad \begin{cases} S_{14}=0 \\ S_{24}=1 \end{cases} \tag{3.30}$$

For the initial value $i_1(t_o)$, it is known from $i_1(t_o)=-i_1(t_4)$, the expression can be gotten,

$$i_1(t_o)=\begin{Bmatrix} -\frac{\pi}{2\omega L}(V_{dc1}+V_{dc2})(\frac{\varphi}{\pi}-\frac{1}{2}(2-D_1-D_2))-\frac{\pi}{2\omega L}V_{dc1}(1-D_2)) \\ -\frac{\pi}{2\omega L}(V_{dc1}-V_{dc2})(-\frac{\varphi}{\pi}+\frac{1}{2}(D_1+D_2))+\frac{\pi}{2\omega L}V_{dc2}(1-D_1)) \end{Bmatrix} \tag{3.31}$$

Hence the power flow equation for Mode C is given by

$$P_1 = V_{dc1}V_{dc2}\frac{\pi}{2\omega L}\left\{-2(\frac{\varphi}{\pi})^2 + \frac{\varphi}{\pi}2 - \frac{1}{4}(2(D_1-1)^2 + 2(D_2-1)^2\right\} \tag{3.32}$$

The dynamic performance of the voltage drop on leakage inductance, input current and real power between two ports is shown in Fig. 3.9 – Fig. 3.11.

So far, the calculation assumes that D_1 is greater than D_2 and the phase shift angle is greater than zero, the power flow equations can be generalized as follows:

Mode A: $P_1 = V_{dc1}V_{dc2}\frac{\varphi}{\omega L}D_2$ (3.33)

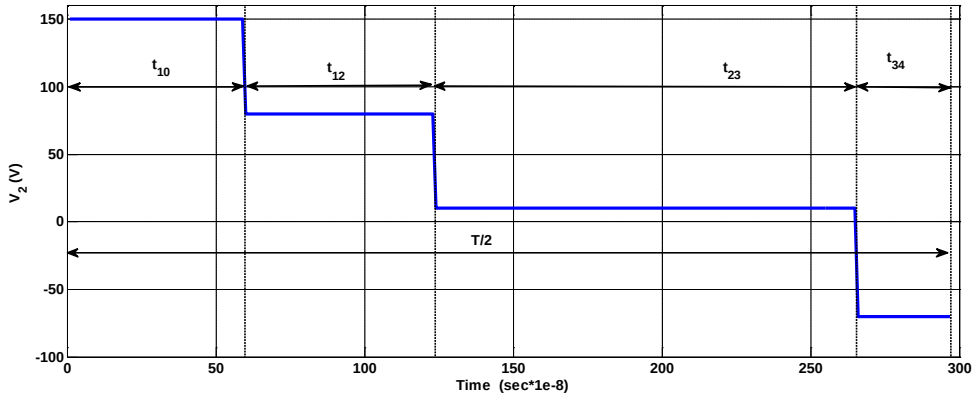

Fig. 3.9 The difference between V_1 and V_2 waveform over a half time period

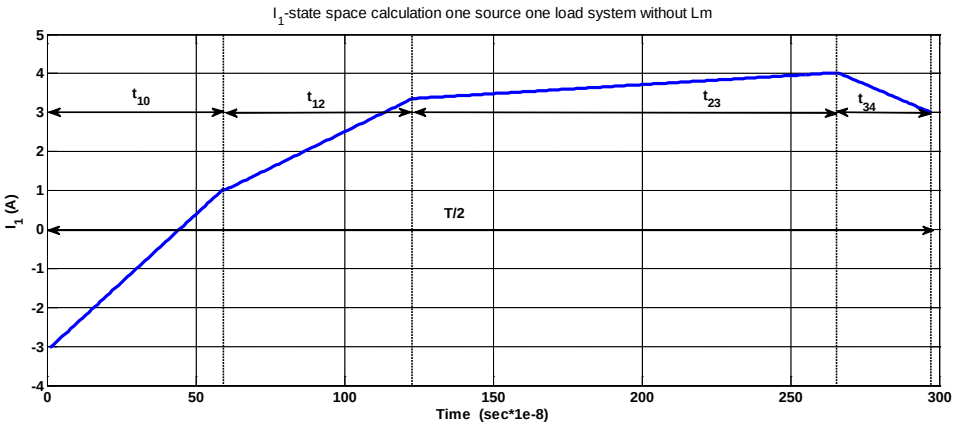

Fig. 3.10 The input current I_1 waveform over a half time period

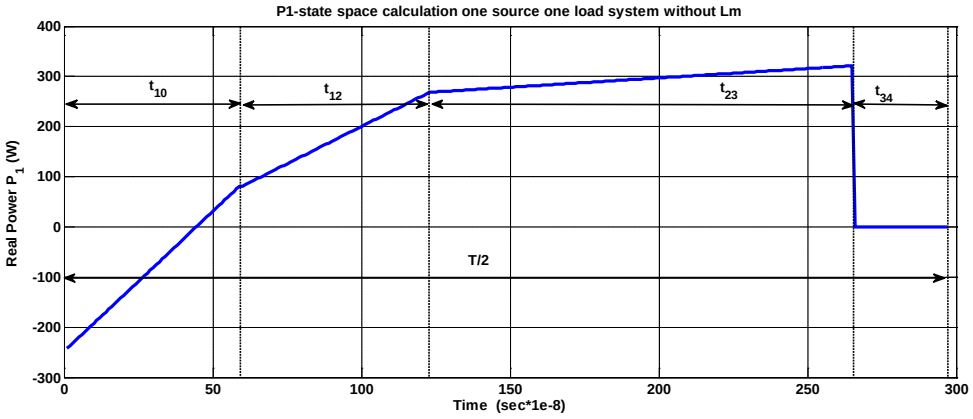

Fig. 3.11 The real power P_1 waveform over a half time period

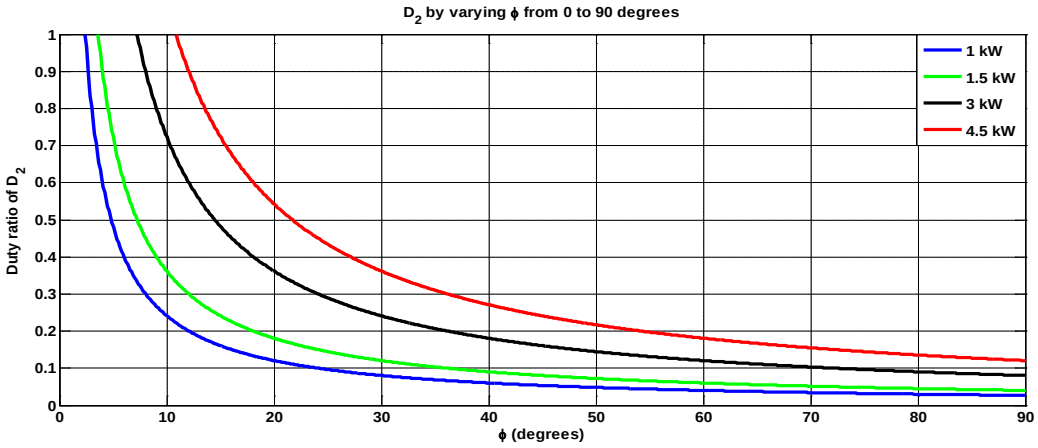

Fig. 3.12 Φ vs. D_2 as power is fixed

By varying the phase angle shift Φ from 0 to 90 degrees, the relationship between D_2 and Φ can be shown in Fig. 3.12.

Mode B:
$$P_1 = V_{dc1}V_{dc2}\frac{\pi}{2\omega L}[(\frac{\varphi}{\pi}+\frac{1}{2}(D_1-D_2))D_2+(\frac{\varphi}{\pi}-\frac{1}{2}(D_1-D_2))\cdot(-\frac{\varphi}{\pi}+\frac{1}{2}(D_1+D_2))] \quad (3.34)$$
$$= V_{dc1}V_{dc2}\frac{1}{2\omega L}[-\frac{\varphi}{\pi}^2+\varphi(D_1+D_2)-\frac{\pi}{4}(D_1-D_2)^2)]$$

A quadratic equation based on the power equation above can be generated:

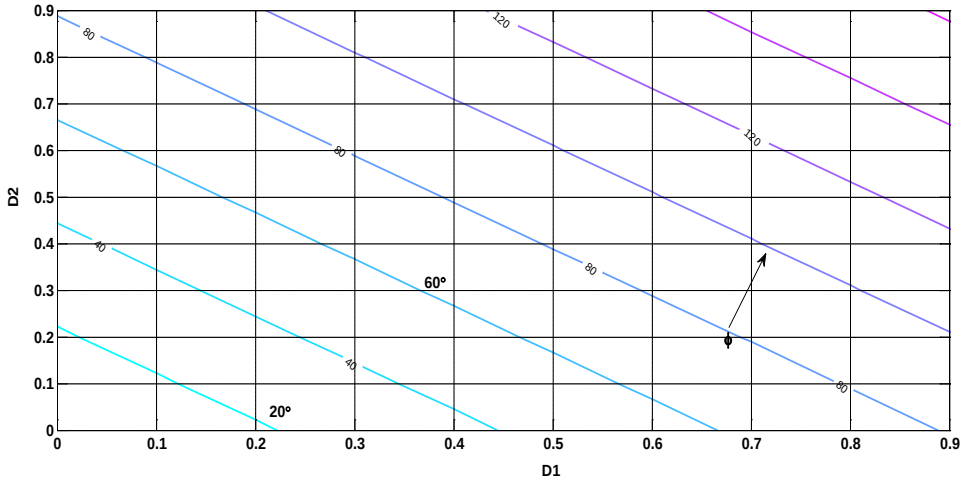

Fig. 3.13 Φ vs. D_1 and D_2 as power is fixed

$$\varphi^2 - \pi\varphi(D_1 + D_2) + \frac{\pi^2}{4}(D_1 - D_2)^2 + P_1 2\omega L\pi / V_{dc1}V_{dc2} = 0 \tag{3.35}$$

The power flows versus three control variables are shown in Fig. 3.13.

Mode C, the power equation for Mode C is expressed as follows:

$$P_1 = V_{dc1}V_{dc2}\frac{\pi}{2\omega L}\left\{-2(\frac{\varphi}{\pi})^2 + \frac{\varphi}{\pi}2 - \frac{1}{4}(2(D_1 - 1)^2 + 2(D_2 - 1)^2\right\} \tag{3.36}$$

It can be expressed in the quadratic function in terms of duty ratio D_1 and D_2:

$$\varphi^2 - \varphi\pi + \frac{\pi}{4}((D_1 - 1)^2 + (D_2 - 1)^2) + \frac{P_1\omega L\pi}{V_{dc1}V_{dc2}} = 0 \tag{3.37}$$

3.3 Voltage Loss Effect of the Semiconductor Devices of the DAB System

As known, the voltage loss caused by semiconductor loss is not trivial and needs to be studied well [38]. To illustrate the voltage loss effect with the existence of dead

time, the system under Mode B is studied. Based on each time switching state in half time period, the possibility and number of semiconductors turning on are laid out clearly as below. The MOSFET conduction model is simply a resistive drop with mΩ level. The resistive value of power MOSFET STP40NF10 is about 25 mΩ and body anti diode typically is 1 V forward voltage drop. Therefore, when the system is operating at a high frequency and high current situation, the power losses of the semiconductors are not trivial. In the following section, based on the analysis on specific Mode B, the total conduction voltage loss can be calculated as below. Circuit Modes regarding the dead time effect for two rectangular waveforms are studied.

Table 3.1 Resulting voltage drops during the time intervals in half switching cycle

Intervals	Current Direction	Output voltage V_1	Output voltage V_2
t_o–t_1	$i_L < 0$	$V_1 := V_{dc1}/2 + V_D + IR_d$	$V_2 := 2IR_d$
	$i_L > 0$	$V_1 := V_{dc1}/2 - V_D - IR_d$	$V_2 := -2IR_d$
t_1–t_2	$i_L < 0$	$V_1 := V_{dc1} + 2IR_d$	$V_2 := 2IR_d$
	$i_L > 0$	$V_1 := V_{dc1} - 2IR_d$	$V_2 := -2IR_d$
t_2–t_3	$i_L < 0$	$V_1 := V_{dc1} + 2IR_d$	$V_2 := V_{dc2}/2 + V_D + IR_d$
	$i_L > 0$	$V_1 := V_{dc1} - 2IR_d$	$V_2 := V_{dc2}/2 - V_D - IR_d$
t_3–t_4	$i_L < 0$	$V_1 := V_{dc1} + 2IR_d$	$V_2 := V_{dc2} + 2IR_d$
	$i_L > 0$	$V_1 := V_{dc1} - 2IR_d$	$V_2 := V_{dc2} - 2IR_d$
t_4–t_5	$i_L < 0$	$V_1 := V_{dc1}/2 + V_D + IR_d$	$V_2 := V_{dc2} + 2IR_d$
	$i_L > 0$	$V_1 := V_{dc1}/2 - V_D - IR_d$	$V_2 := V_{dc2} - 2IR_d$
t_5–t_6	$i_L < 0$	$V_1 := 2IR_d$	$V_2 := V_{dc2} + 2IR_d$
	$i_L > 0$	$V_1 := -2IR_d$	$V_2 := V_{dc2} - 2IR_d$
t_6–t_7	$i_L < 0$	$V_1 := 2IR_d$	$V_2 := V_{dc2}/2 + V_D + IR_d$
	$i_L > 0$	$V_1 := -2IR_d$	$V_2 := V_{dc2}/2 - V_D - IR_d$
t_7–t_8	$i_L < 0$	$V_1 := 2IR_d$	$V_2 := 2IR_d$
	$i_L > 0$	$V_1 := -2IR_d$	$V_2 := -2IR_d$

For Mode B, in Fig. 3.2 (b), considering the dead time effect for both switching pulses, there are eight switching states at each half switching period shown in Fig. 3. 14. Given the symmetric structure of the topology, the average current value should be 0. Hence the initial current should meet the following limit $i_L(t_o) = -i_L(t_o + \frac{T}{2})$.

The switching operations at each time instant are shown in Fig. 3.14; the number of semiconductor devices can be found based on the current direction. All the switching operations and possible resulting voltage drops on input voltage v_1 and output voltage v_2 are shown in Table 3.1

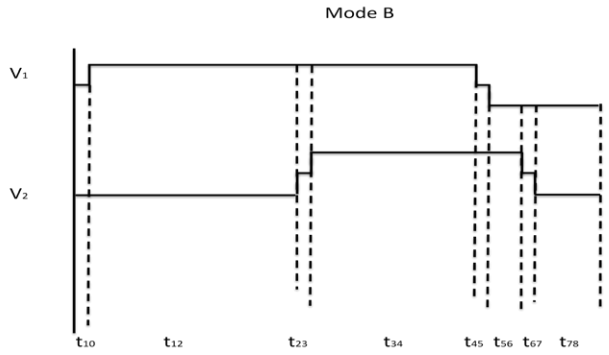

Fig. 3. 14 Operating Mode B considering the dead time effect

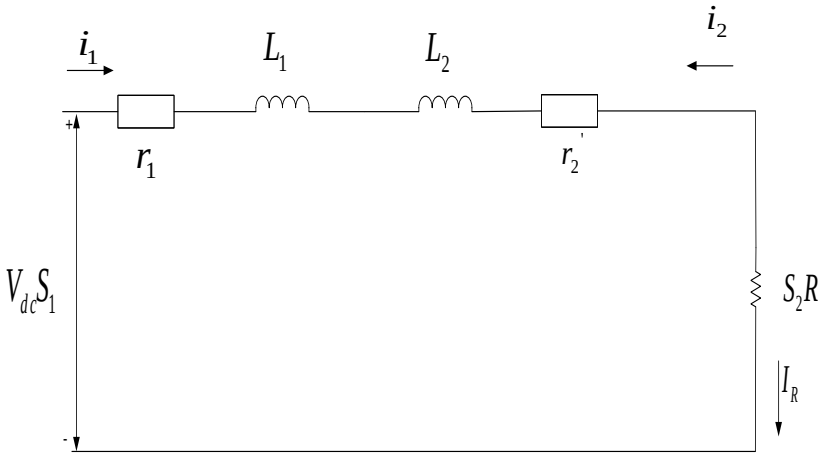

Fig. 3.15 Equivalent circuit with voltage drop model for two-port DAB converter system

3.4 State Space Analysis Considering Dead Time Effect

In the previous section, the table of voltage drop possibilities has been given. In this section, state space method considering voltage drop of semiconductor devices is carried out. Closed form expressions for the inductor current are derived and the real time value of the system has been calculated based on the equivalent circuit of two-port DAB converter system (ignoring mutual inductance L_m) shown in Fig. 3.15.

The resistive value r_1 is semiconductor's equivalent resistive value of Port 1 and r_2 is semiconductor's equivalent resistive value of Port 2. L_1 is the Port 1's equivalent inductance including primary side leakage inductance and extra inductance if required. Similarly, L_2 is Port 2's equivalent inductance including secondary leakage inductance and extra inductance if required. The input voltage is V_1. The DAB System is connected to the resistive load R. S_1 and S_2 are switching pulses shown in Fig. 3.14.

The system is expressed in following:

$$V_1 = L_1 pI_1 + r_1 I_1 - r_2 I_2 - L_2 pI_2 - S_2{}^2 RI_2 \tag{3.38}$$

$$I_1 = -I_2 \tag{3.39}$$

Substitute (3.39) into (3.38) and

$$pI_1 = -\frac{r_1 + r_2 + S_2{}^2}{L_1 + L_2} I_1 + \frac{1}{L_1 + L_2} S_1 V_{dc} \tag{3.40}$$

The solution is acquired as

$$I_1(t)_i = e^{-\frac{r_1+r_2+S_2{}^2}{L_1+L_2}t} I_1(t)_{i-1} + \frac{S_1 V_{dc}}{L_1 + L_2}[1 - e^{-\frac{r_1+r_2+S_2{}^2}{L_1+L_2}t}] \tag{3.41}$$

After considering the dead time effect, the original four states in half switching cycle have been changed to eight states. The calculation in each time interval can make this nonlinear system into eight linear systems with each state space equation.

1) At the time interval 0 to t_1 $\theta_1 : V_1 = V_{dc}/2, s_2 = 0$ the time is t_{10}

2) At the time interval t_1 to t_2 $\theta_2 : V_1 = V_{dc}, s_2 = 0$ the time is t_{21}

3) At the time interval t_2 to t_3 $\theta_3 : V_1 = V_{dc}, s_2 = 0.5$ the time is t_{32}

4) At the time interval t_3 to t_4 $\theta_4 : V_1 = V_{dc}, s_2 = 1$ the time is t_{43}

5) At the time interval t_4 to t_5 $\theta_5 : V_1 = V_{dc}/2, s_2 = 1$ the time is t_{54}

6) At the time interval t_5 to t_6 $\theta_6 : V_1 = 0, s_2 = 1$ the time is t_{65}

7) At the time interval t_6 to t_7 $\theta_7 : V_1 = 0, s_2 = 0.5$ the time is t_{76}

8) At the time interval t_7 to t_8 $\theta_8 : V_1 = 0, s_2 = 0$ the time is t_{87}

The waveform of input current i_1 from state space method is shown in Fig. 3. 16.

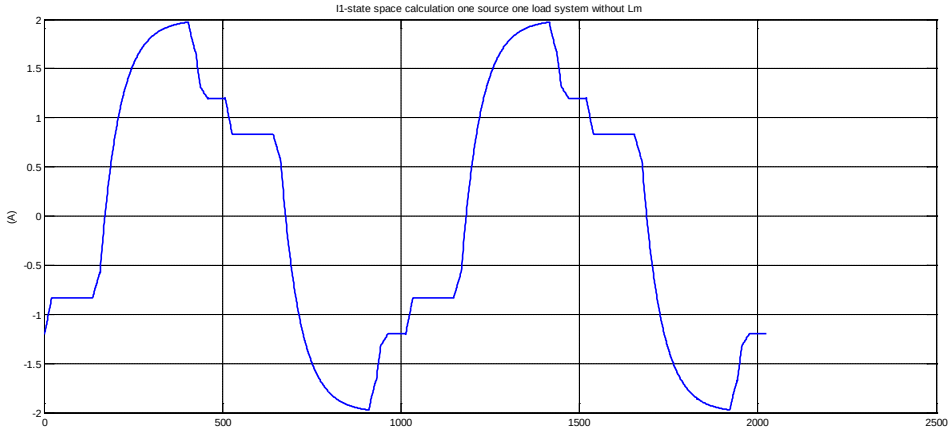

Fig. 3.16 Input current i_1 considering the voltage drop effect of Mode B mode

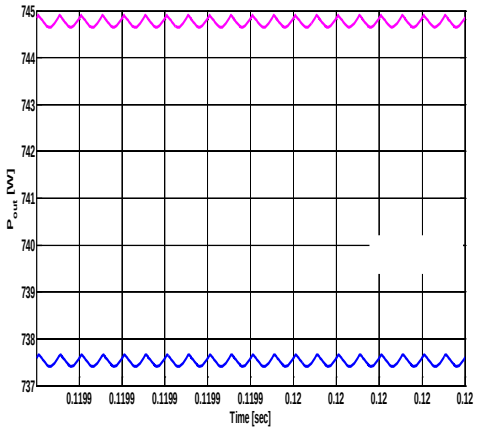

(a)

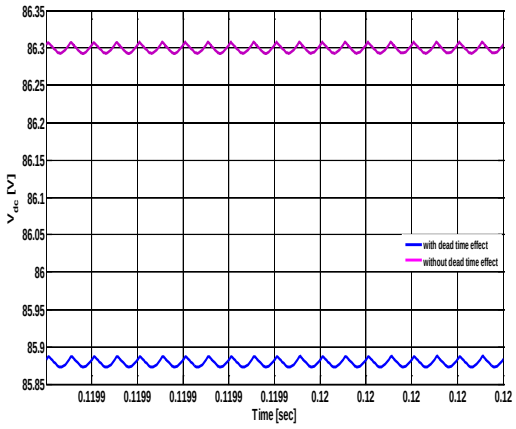

(b)

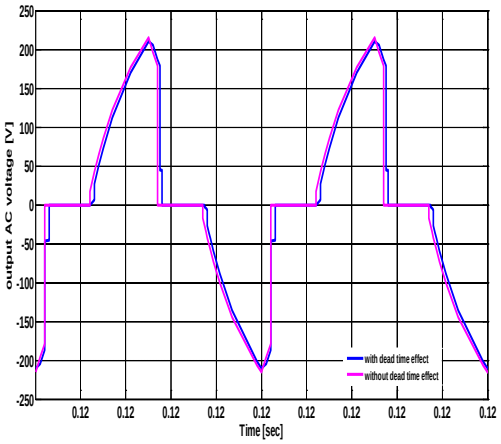

(c)

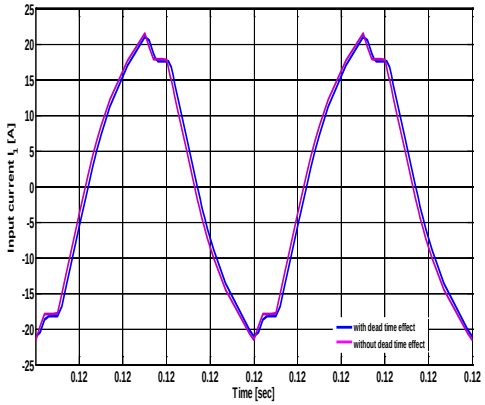

(d)

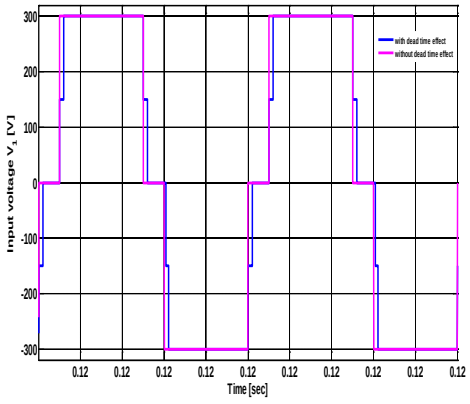

(e)

Fig. 3.17 Simulated waveforms: (a) Output dc power, (b) Output dc voltage V_{dc}, (c) Output ac voltage V_2, (d) Input current I_1, (e) Input voltage V_1 when $\Phi = 15°$

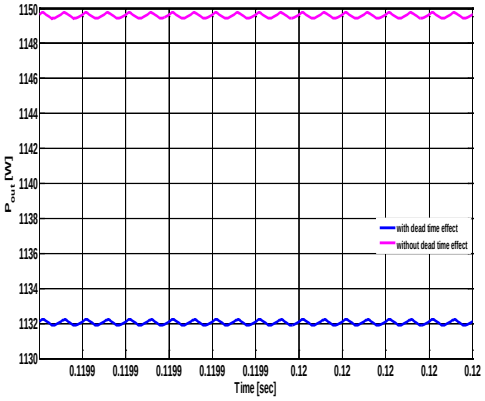

(a) Output dc power

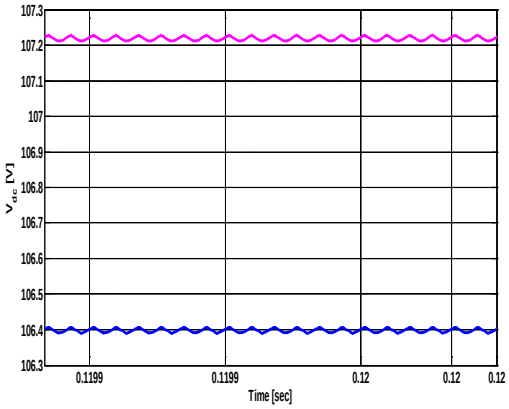

(b) Output dc voltage V_{dc}

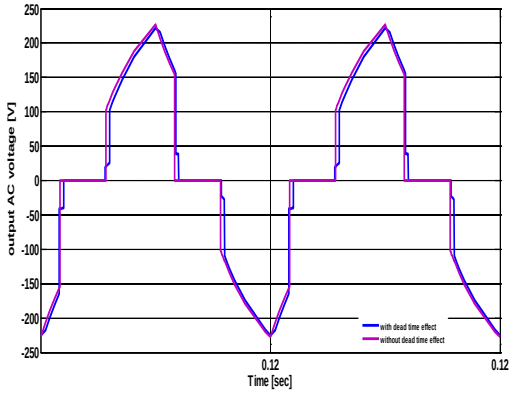

(c) Output ac voltage V_2

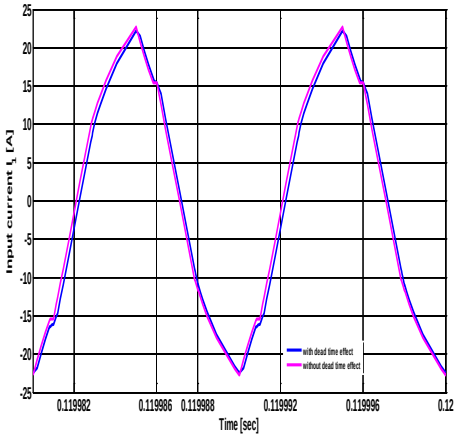

(d) Input current I_1

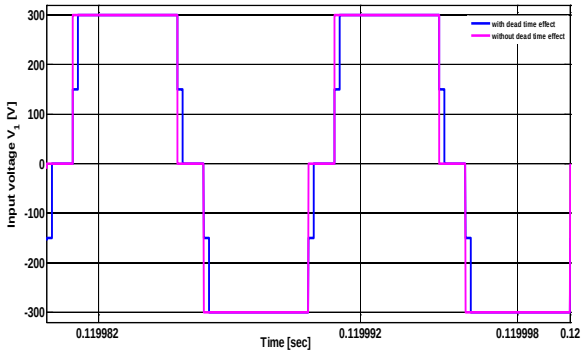

(e) Input voltage V_1

Fig. 3.18 Simulated waveforms: (a) Output dc power, (b) Output dc voltage V_{dc}, (c) Output ac voltage V_2, (d) Input current I_1, (e) Input voltage V_1 when $\Phi = 30°$

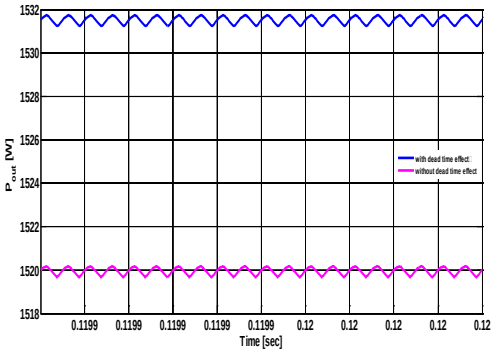

(a) Output dc power

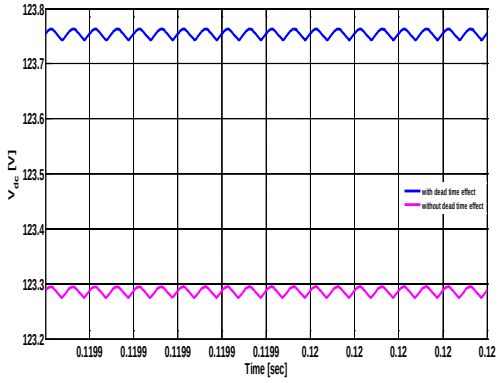

(b) Output dc voltage V_{dc}

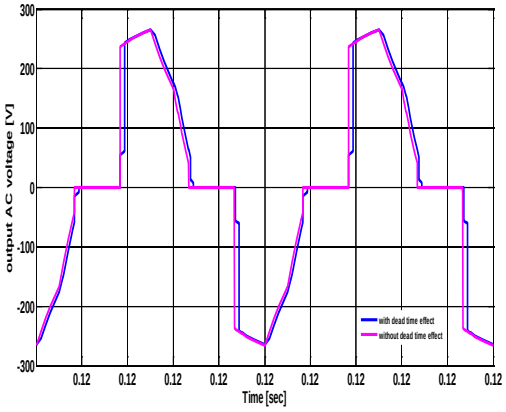

(c) Output ac voltage V_2

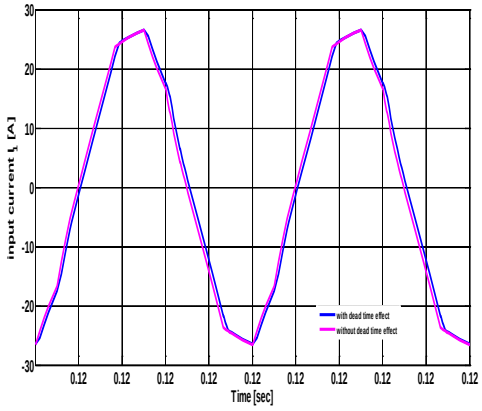

(d) Input current I_1

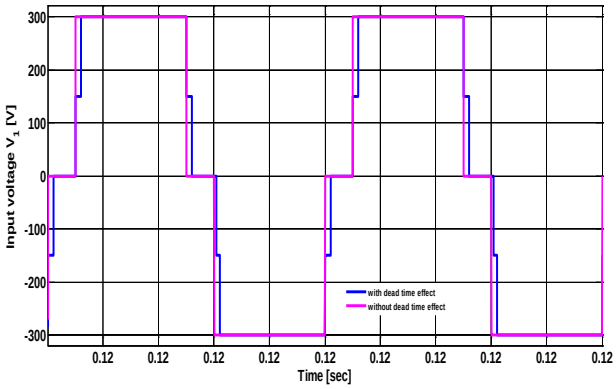

(e) Input voltage V_1

Fig. 3.19 Simulated waveforms: (a) Output dc power, (b) Output dc voltage V_{dc}, (c) Output ac voltage V_2, (d) Input current I_1, (e) Input voltage V_1 when $\Phi = 60°$

A full order model of the converter including the dead time switching functions is simulated using MATLAB/SIMULINK. As a proof of difference between the situations of state space model considering voltage drop and the simulation model without semiconductors voltage drop. The study case in the following part is studied. The duty ratios $D_1 = 0.8$ and $D_2 = 0.6$, phase shift angle is chosen as different cases $\Phi = 15°$, 30° and 60°.

To illustrate how the short time scale factors affect the output power, output dc voltage V_{dc}, output ac voltage V_{ac}, input current I_1 and input voltage V_1 by varying the phase shift angle Φ from 15°, 30°, and 60°, the minor parameters in DAB converter system such as dead time effect and semiconductor voltage drop have been discussed and the switching functions are revised considering the dead band and current waveform is studied (see Fig. 3. 17 – Fig. 3.19).

The simulation results show the effect of output power P, output dc voltage V_{dc}, output ac voltage V_{ac}, input current I_1, and input voltage V_1 by varying the phase shift angle Φ from 15°, 30° and 60° distorted by dead band and semiconductor voltage drop. They are compared and different from the ones derived from idealized lossless circuit. It can be seen that when the dead time is added, the steady state value and dynamic response of output power, output dc voltage and output ac voltage and voltage are all deteriorated.

CHAPTER 4

HARMONIC BALANCE TECHNIQUE FOR THE ANALYSIS OF THE DAB CONVERTER SYSTEM

Different from the state space method presented in Chapter 2, this chapter proposes a new switching function based modeling method-harmonic balance technique of the bidirectional dc-dc converter system. The state space method can be used to study the dynamic performance of the DAB converter system. However, the matrix of closed formed solutions is so complex that it may not be easier to study and analyze the steady state characteristics and ripple quantities. Harmonic balance technique (HBT) is a promising method that is applied to the nonlinear DAB model with switching functions to study the dynamics equations of the system. It can predict the input current, output voltage, and even ripple quantities. Compared with the well-known averaging technique, it has a greater advantage when multiport bidirectional dc-dc converter system is studied. After, a traditional two-port DAB system is studied. HBT will be used to study the three-port DAB system to show its advantage. The results derived from HBT can be combined with small signal analysis to study the dynamic behavior of the converter system.

4.1 Introduction

The definition and application of HBT was presented in the early 1937 and named by the Ukrainian scientists Kryloff and Bogoliuboff [46]. E. M. Baily developed the HBT into the application of nonlinear circuits in the 1960s [47]. J. C. Lindenlaub

presented a new approach of using HBT to acquire the sinusoidal steady state response of nonlinear system [48]. A more advanced and improved HBT was introduced by M. S. Nakhla and J. Vlach [49].

HBT is a technique for the numerical solution of nonlinear analog circuits operating in the periodic regime. It is an efficient method for the simulation of the steady state response. HBT (also called the describing function method) is critical for the application of frequency response of nonlinear system. The method uses frequency domain (Fourier series) techniques to decompose the system into two separate subsystems, a linear and a nonlinear part.

Mathematically the simplified equations are of the form as below:

$$\dot{x} = f(x,u,t) \tag{4.1}$$

$$y = g(x,u,t) \tag{4.2}$$

The steady state solutions of the defined system are dependent on *x* and *t*. However the solution of interest is the time invariant component. It is known that the system is periodic because of the sinusoidal input in the system. Moreover the system excited with an input of a particular frequency ω responds with a same frequency output.

If

$$x(t) = \sum_{k=1}^{\infty} C_k e^{(jk\omega t)} \tag{4.3}$$

Then

$$\dot{x}(t) = \sum_{k=1}^{\infty} jk\omega t C_k \, e^{(jk\omega t)} + \sum_{k=1}^{\infty} \frac{d}{dt} C_k \, e^{(jk\omega t)} \tag{4.4}$$

It can be seen from the (3.37) and (3.38) that the term $e^{(jk\omega t)}$ is common to both sides of the equation; hence, it can be inferred that the constant coefficients on both sides are equal with the same effect of time variant variable $e^{(jk\omega t)}$. It can be represented as

$$f(x,u) = \sum_{k=1}^{\infty} jk\omega t C_k + \sum_{k=1}^{\infty} \frac{d}{dt} C_k \tag{4.5}$$

From Equation (4.5), the first part -a time invariant system is obtained from a time variant system.

4.2 Simplified Analysis Using Harmonic Balance Technique for Bidirectional DC-DC Converter

HBT has emerged as a practical and efficient method to study the performance of steady state ac circuits [50]. Not only can it be used to analyze nonlinear circuits at steady state, it is useful to derive models used to design the controllers and predict the ripple quantities. The purpose in this section is to provide the detailed HBT derivation of two-port DAB converter. The equivalent circuit is shown in Fig. 4. 1.

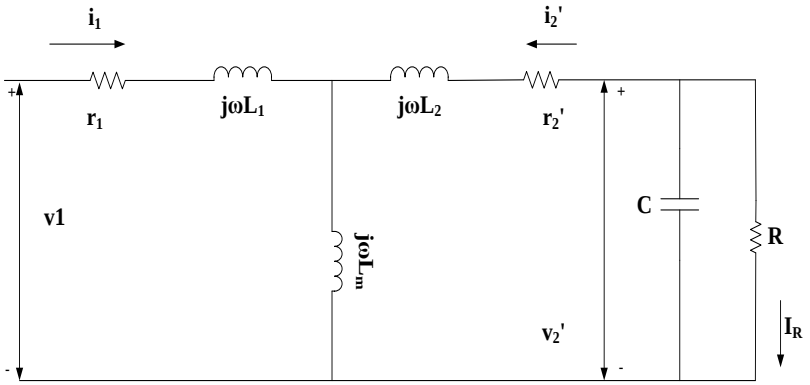

Fig. 4.1 Equivalent circuit of DAB converter system

4.2.1 Fourier Analysis of the Switching Functions

By using the harmonic balance technique in Equations (2.1) – (2.5), the state variables and switching functions are assumed to have average components and ripple quantities individually as below:

$$i_1 = I_{10} + \mathrm{Re}[I_1 e^{j\theta}] \tag{4.6}$$

$$i_2^{'} = I_{20} + \mathrm{Re}[I_2 e^{j\theta}] \tag{4.7}$$

$$V_{dcL} = V_{dc0} + \mathrm{Re}[V_{dc1} e^{j2\theta}] \tag{4.8}$$

$$s_1 = S_{10} + \mathrm{Re}[S_1 e^{j\theta}] \tag{4.9}$$

$$s_2 = S_{20} + \mathrm{Re}[S_2 e^{j\theta}] \tag{4.10}$$

The rectangular waveform of switching function is shown in Fig. 4.2. Performing Fourier analysis on the rectangular pulse, the results are

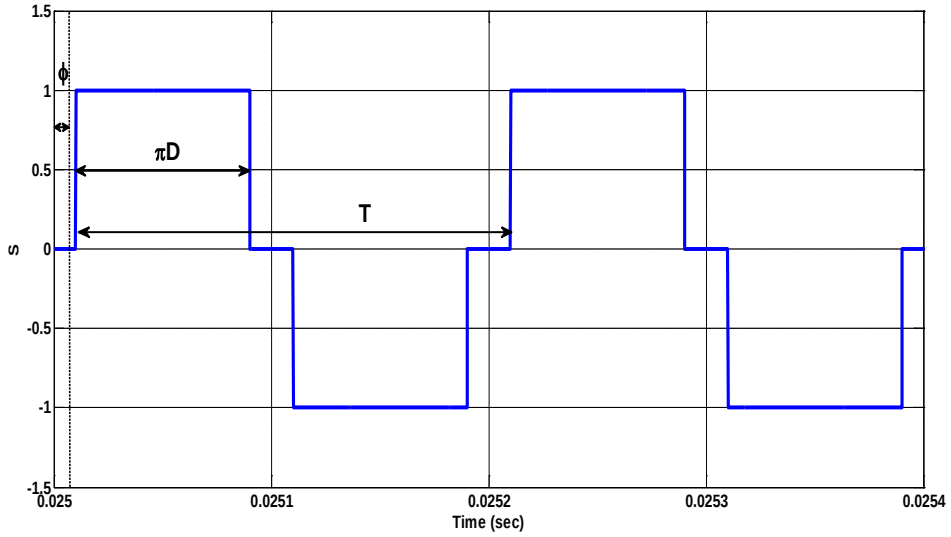

Figure 4.2 Waveform of the rectangular pulse

In general, a repetitive non sinusoidal waveform f(t) repeating with an constant frequency ω can be expressed as [51]

$$f(t) = F_o + \sum_{h=1}^{\infty} f_h(t) = \frac{1}{2}a_o + \sum_{h=1}^{\infty}\{a_h \cos(h\omega t) + b_h \sin(h\omega t)\} \tag{4.11}$$

where $F_o = \frac{1}{2}a_o$ is the average value,

$$a_h = \frac{1}{\pi}\int_0^{2\pi} f(t)\cos(h\omega t)d(\omega t) \qquad h = 0,...,\infty \tag{4.12}$$

$$b_h = \frac{1}{\pi}\int_0^{2\pi} f(t)\sin(h\omega t)d(\omega t) \qquad h = 0,...,\infty \tag{4.13}$$

where the RMS magnitude

$$F_h = \frac{\sqrt{{a_h}^2 + {b_h}^2}}{\sqrt{2}} \tag{4.14}$$

and phase ϕ_h is given by

$$\tan(\phi_h) = \frac{b_h}{a_h} \tag{4.15}$$

The Fourier analysis for switching function is shown as below:

for a_h

$$a_h = \frac{1}{\pi h}\left[\sin\left(\frac{1}{2}h(-2\phi - \pi + D\pi)\right) + \sin\left(\frac{1}{2}h(2\phi + \pi + D\pi)\right) - \sin\left(\frac{1}{2}h(-2\phi - 3\pi + D\pi)\right) - \sin\left(\frac{1}{2}h(2\phi + 3\pi + D\pi)\right)\right] \tag{4.16}$$

when *h* is odd:

$$a_h = \frac{1}{\pi h}\left[\sin\left(-\frac{h\pi}{2}\right)\cos\left(\frac{1}{2}h(D\pi - 2\phi)\right) + \sin\left(\frac{h\pi}{2}\right)\cos\left(\frac{1}{2}h(2\phi + D\pi)\right) - \sin\left(-\frac{3h\pi}{2}\right)\cos\left(\frac{1}{2}h(D\pi - 2\phi)\right) - \sin\left(\frac{3h\pi}{2}\right)\cos\left(\frac{1}{2}h(2\phi + D\pi)\right)\right] \tag{4.17}$$

when *h* is even:

$$a_h = \frac{1}{\pi h}\left[\cos\left(-\frac{h\pi}{2}\right)\sin\left(\frac{1}{2}h(D\pi - 2\phi)\right) + \cos\left(\frac{h\pi}{2}\right)\sin\left(\frac{1}{2}h(2\phi + D\pi)\right) - \cos\left(-\frac{3h\pi}{2}\right)\sin\left(\frac{1}{2}h(D\pi - 2\phi)\right) - \cos\left(\frac{3h\pi}{2}\right)\sin\left(\frac{1}{2}h(2\phi + D\pi)\right)\right] \tag{4.18}$$

Further,

when *h* is odd:

$$a_h = \frac{2}{\pi h}\left(-\sin\frac{h\pi}{2} - \sin\frac{h\pi}{2}\right)\sin\frac{hD\pi}{2}\sin h\phi \tag{4.19}$$

When *h* is even:

$$a_h = \frac{2}{\pi h}\left(\cos\frac{h\pi}{2} - \cos\frac{h\pi}{2}\right)\sin\frac{hD\pi}{2}\cosh\phi \tag{4.20}$$

Therefore,

$$a_h = \begin{cases} -\frac{4}{\pi h}\sin\frac{h\pi}{2}\sin\frac{hD\pi}{2}\sin h\phi, & for\ h = 1,3,5,7,\cdots \\ 0, & for\ h = 2,4,6,8,\cdots \end{cases} \tag{4.21}$$

Similarly, derived is the expression of b_h

$$b_h = \frac{1}{\pi h}\left[\cos\left(\frac{1}{2}h(-2\phi - \pi + D\pi)\right) - \cos\left(\frac{1}{2}h(2\phi + \pi + D\pi)\right) - \cos\left(\frac{1}{2}h(-2\phi - 3\pi + D\pi)\right) + \cos\left(\frac{1}{2}h(2\phi + 3\pi + D\pi)\right)\right] \tag{4.22}$$

when *h* is even

$$b_h = \frac{1}{\pi h}\left[\left(\cos\left(\frac{h\pi}{2}\right) - \cos\left(\frac{3h\pi}{2}\right)\right)\left(\cos\left(\frac{1}{2}h(D\pi - 2\phi)\right) - \cos\left(\frac{1}{2}h(2\phi + D\pi)\right)\right)\right] \tag{4.23}$$

when *h* is odd

$$b_h = \frac{1}{\pi h}\left[\left(\sin\frac{h\pi}{2} - \sin\frac{3h\pi}{2}\right)\left(\sin\left(\frac{1}{2}h(D\pi - 2\phi)\right) + \sin\left(\frac{1}{2}h(2\phi + D\pi)\right)\right)\right] \tag{4.24}$$

when *h* is odd

$$b_h = \frac{4}{\pi h}\sin\frac{h\pi}{2}\sin\frac{1}{2}hD\pi\cos h\phi \tag{4.25}$$

when *h* is even

$$b_h = 0 \tag{4.26}$$

Therefore,

$$b_h = \begin{cases} \frac{4}{\pi h} \sin\frac{h\pi}{2} \sin\frac{1}{2} hD\pi \cos h\phi, & h = 1,3,5,7,\cdots \\ 0, & h = 2,4,6,8,\cdots \end{cases} \tag{4.27}$$

Thus the components of the Fourier analysis are expressed as below:

$$a_0 = 0 \tag{4.28}$$

$$a_h = \begin{cases} -\frac{4}{\pi h} \sin\frac{h\pi}{2} \sin\frac{hD\pi}{2} \sin h\phi, & for\ h = 1,3,5,7,\cdots \\ 0, & for\ h = 2,4,6,8,\cdots \end{cases} \tag{4.29}$$

$$b_h = \begin{cases} \frac{4}{\pi h} \sin\frac{h\pi}{2} \sin\frac{1}{2} hD\pi \cos h\phi, & h = 1,3,5,7,\cdots \\ 0, & h = 2,4,6,8,\cdots \end{cases} \tag{4.30}$$

Therefore the general expression can be written by

$$c_h = \frac{4}{\pi} \sum_{h=1}^{n} \left[\frac{1}{h} \sin\left(\frac{h\pi}{2}\right) \sin\left(\frac{1}{2} hD\pi\right) \cos(h\phi) \sin(h\theta) - \sin\left(\frac{h\pi}{2}\right) \sin\left(\frac{hD\pi}{2}\right) \sin(h\phi) \cos(h\theta) \right] \tag{4.31}$$
$$h = 1,3,5,7,\cdots$$

where the RMS magnitude is

$$\overline{F_h} = \frac{\sqrt{a_1^{\,2} + b_1^{\,2}}}{\sqrt{2}} = \frac{1}{\sqrt{2}} \frac{4}{\pi h} \sin\frac{hD\pi}{2} \tag{4.32}$$

and phase ϕ_h is given by

$$\begin{aligned} &\tan(\phi_h) = c\tan(\frac{\pi}{2} - h\phi) \\ &\phi_h = \frac{\pi}{2} - h\phi \end{aligned} \tag{4.33}$$

For the first fundamental component, it can be represented as

$$\begin{aligned} \mathrm{F}_1 &= a_1 \cosh\theta + b_1 \sinh\theta \\ \mathrm{a}_1 &= \frac{4}{\pi}\sin\left(\frac{\pi}{2}\right)\sin\left(\frac{1}{2}\mathrm{D}\pi\right)\cos(\phi) \\ b_1 &= \frac{4}{\pi}\sin\left(\frac{\pi}{2}\right)\sin\left(\frac{\mathrm{D}\pi}{2}\right)\sin(\phi) \end{aligned} \tag{4.34}$$

Hence the complex form is shown as below:

$$\mathrm{F}_1 = \mathrm{F}_\mathrm{f} e^{j\phi_f} \tag{4.35}$$

$$\begin{aligned} \mathrm{F}_\mathrm{f} &= \frac{1}{\sqrt{2}}\sqrt{a_1{}^2 + b_1{}^2} = \frac{1}{\sqrt{2}}\frac{4}{\pi}\sin(\frac{\pi}{2})\sin(\frac{D\pi}{2}) \\ \tan(\phi_f) &= \frac{b_h}{-a_h} = c\tan\phi = \tan(\frac{\pi}{2} - \phi) \end{aligned} \tag{4.36}$$

Therefore, the switching functions of fundamental component can be represented as

$$S_{qi} = \frac{4}{\pi}\sin(\frac{D_i}{2}\pi)\sin(\phi_i) \;\; i = 1,2 \tag{4.37}$$

$$S_{di} = \frac{4}{\pi}\sin(\frac{D_i}{2}\pi)\cos(\phi_i) \;\; i = 1,2 \tag{4.38}$$

where D_i is the duty ratio and Φ_i is phase shift angle.

4.2.2 Steady State Model Equations Arising from HBT

As the switching functions can be acquired in Fourier series in terms of time variant components and time invariant components, all the other remaining state variables can also be expressed in the similar way due to the input sinusoidal source.

Substitute the equations above into dynamic Equations (2.1)–(2.5) to get

$$(L_1 + L_m + r_1)p(I_{10} + \mathrm{Re}[I_1 e^{j\theta}]) + L_m p(I_{20} + \mathrm{Re}[I_2 e^{j\theta}]) = V_{dcs}(S_{10} + \mathrm{Re}[S_1 e^{j\theta}]) \tag{4.39}$$

$$(L_2{}' + L_m + r_2)p(I_{20} + \mathrm{Re}[I_2 e^{j\theta}]) + L_m p(I_{10} + \mathrm{Re}[I_1 e^{j\theta}]) = V_{dcL0}(S_{20} + \mathrm{Re}[S_2 e^{j\theta}]) \tag{4.40}$$

The capacitor and load model is represented by the following current equation:

$$Cp(V_{dc0} + \mathrm{Re}[V_{dc1}e^{j2\theta}]) = -(I_{20} + \mathrm{Re}[I_2 e^{j\theta}]) \cdot (S_{20} + \mathrm{Re}[S_2 e^{j\theta}]) - (V_{dc0} + \mathrm{Re}[V_{dc1}e^{j2\theta}])/R \quad (4.41)$$

The input voltage can be determined by

$$v_1 = V_{dcs}(S_{10} + \mathrm{Re}[S_1 e^{j\theta}]) \quad (4.42)$$

When the system comes into steady state, the derivatives of the state variables are all equal to zero. Also the average components of $I_{10}, I_{20}, S_{10}, S_{20}$ are all equal to 0.The peak value of fundamental components from ripple equations can be used to study the characteristic and performance of the system. Hence the peak fundamental component equations are used as below:

At steady state, $pI_1, pI_2', pV_{dcL} = 0$

$$(r_1 + j\omega L_1)I_1 + j\omega L_m(I_1 + I_2') = V_{dcs}S_1 \quad (4.43)$$

$$(r_2 + j\omega L_2')I_2 + j\omega L_m(I_1 + I_2') = V_{dc0}S_2 \quad (4.44)$$

$$V_{dc0} = -R \cdot \mathrm{Re}[I_2' S_2^*] \quad (4.45)$$

Because out ac voltage V_2' contains the real value of the multiplication by two complex parts, it is feasible to separate into q and d axis variables which can make equations of state variables in the linear way.

Set

$$I_1 = I_{q1} + jI_{d1} \quad (4.46)$$

$$I_2' = I_{q2} + jI_{d2} \quad (4.47)$$

$$S_1 = S_{q1} + jS_{d1} \quad (4.48)$$

$$S_2 = S_{q2} + jS_{d2} \quad (4.49)$$

Bring the complex expressions into the matrix above and separate them into real and imaginary part, rearrange the equations:

$$r_1 I_{q1} - \omega(L_1 + L_m) I_{d1} - \omega L_m I_{d2} = V_{dc} S_{q1} \tag{4.50}$$

$$r_1 I_{d1} + \omega(L_1 + L_m) I_{q1} + \omega L_m I_{q2} = V_{dc} S_{d1} \tag{4.51}$$

$$r_2' I_{q2} - \omega(L_2' + L_m) I_{d2} - \omega L_m I_{d1} = -\frac{1}{2} R[I_{q2} S_{q2} + I_{d2} S_{d2}] S_{q2} \tag{4.52}$$

$$r_2' I_{d2} + \omega(L_2' + L_m) I_{q2} + \omega L_m I_{q1} = -\frac{1}{2} R[I_{q2} S_{q2} + I_{d2} S_{d2}] S_{d2} \tag{4.53}$$

The matrix can be as follows:

$$\begin{bmatrix} r_1 & -\omega(L_1 + L_m) & 0 & -\omega L_m \\ \omega(L_1 + L_m) & r_1 & \omega L_m & 0 \\ 0 & -\omega L_m & 0.5R S_{q2}^{\,2} + r_2 & 0.5R S_{q2} S_{d2} - \omega(L_2' + L_m) \\ \omega L_m & 0 & \omega(L_2' + L_m) + 0.5R S_{q2} S_{d2} & 0.5R S_{d2}^{\,2} + r_2 \end{bmatrix} \begin{bmatrix} I_{q1} \\ I_{d1} \\ I_{q2} \\ I_{d2} \end{bmatrix} = \begin{bmatrix} V_{dc} S_{q1} \\ V_{dc} S_{d1} \\ 0 \\ 0 \end{bmatrix} \tag{4.54}$$

Compared with the fundamental component of the system, the high order harmonic ripple components of the system can be calculated by the equations below:

For the high order ripple components of capacitor side:

$$Cp(V_{dc0} + \mathrm{Re}[V_{dc1} e^{j2\theta}]) = -\mathrm{Re}[I_2 e^{j\theta}] * \mathrm{Re}[S_2 e^{j\theta}] - \frac{V_{dc0} + \mathrm{Re}[V_{dc1} e^{j2\theta}]}{R_l} \tag{4.55}$$

The ripple can be found by

$$CpV_{dc1} + 2C * j\omega V_{dc1} = -\frac{1}{2} I_2 S_2 - \frac{V_{dc1}}{R_l} \tag{4.56}$$

For the high order ripple components of input inductor side:

$$\mathrm{Re}[I_1 e^{j\theta}] * \mathrm{Re}[S_1 e^{j\theta} + S_{13}^{\,j3\theta}] = I_{dc0} + \mathrm{Re}[I_{dc2} e^{j2\theta}] \tag{4.57}$$

The ripple can be gotten as below:

$$\frac{1}{2}\mathrm{Re}[I_1 S_1 e^{j2\theta}] + \frac{1}{2}\mathrm{Re}[S_{13} I_1^{*} e^{j2\theta}] = \mathrm{Re}[I_{dc2} e^{j2\theta}] \tag{4.58}$$

$$I_{dc2} = \frac{1}{2}(I_1 S_1 + S_{13} I_1^{*}) \tag{4.59}$$

The steady state characteristics based on the input current I_1, input voltage V_1, output current I_2', output load voltage V_{dc2}, real input and output power P_1, P_2 and reactive power Q are studied and shown in Fig. 4.3.

The results are obtained by fixing $D_1 = 0.8$ and $\Phi_1 = 0$ while varying the phase angle Φ_2 at D_2 is equal to 0.2, 0.4, 0.6 and 0.8. The parameters used are from a prototype transformer and given as follows: $r_1 = 0.03\Omega$, $L_1 = 5.85\mu H$, $r_2 = 0.005\Omega$, $L_2 = 1.35\mu H$, $L_m = 185\mu H$, f = 10k Hz, R = 2.5 Ω.

The input, output power, reactive power and output dc voltage are plotted versus phase shift at different duty ratios in Fig. 4.3 (a), (b), (c) and (d). From Fig. 4.3 (b), the real power flow is increased as phase shift angle increases. When duty ratio is decreased, less power is transferred at a given phase shift compared with the traditional only phase shift control. It also clearly shows that the system can draw more reactive power when phase shift angle is leading. As Fig. 4.3 (c) shows, to minimize the reactive power, it is better to set a constraint region of phase shift angle for minimum loss. Therefore limiting the phase angle range, it can increase the overall system efficiency.

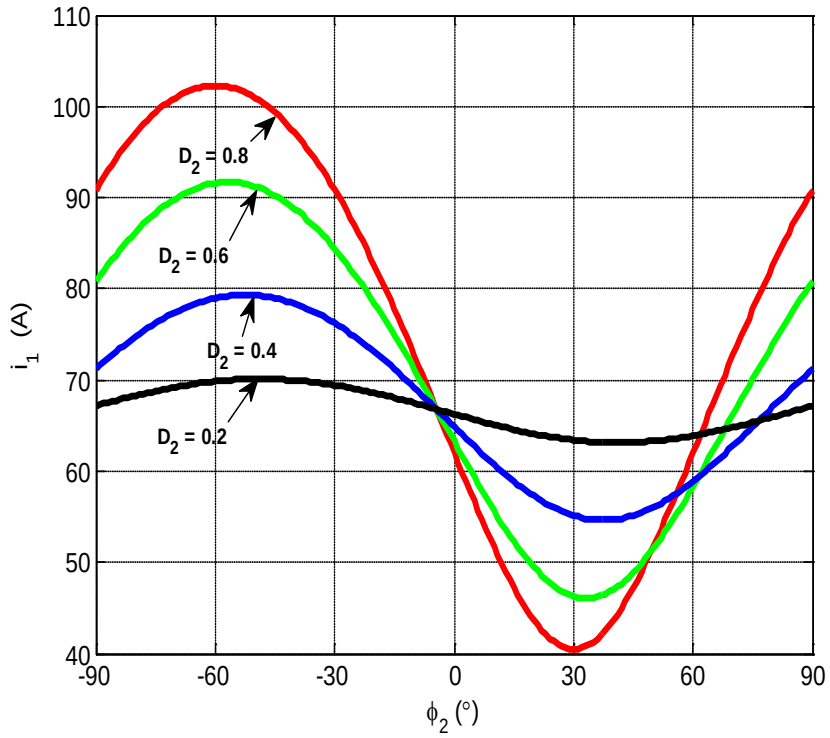
110
100
90
80
70
60
50
40
-90
-60
-30
0
30
60
90
i_1 (A)
ϕ_2 (°)
D_2 = 0.8
D_2 = 0.6
D_2 = 0.4
D_2 = 0.2

(a)

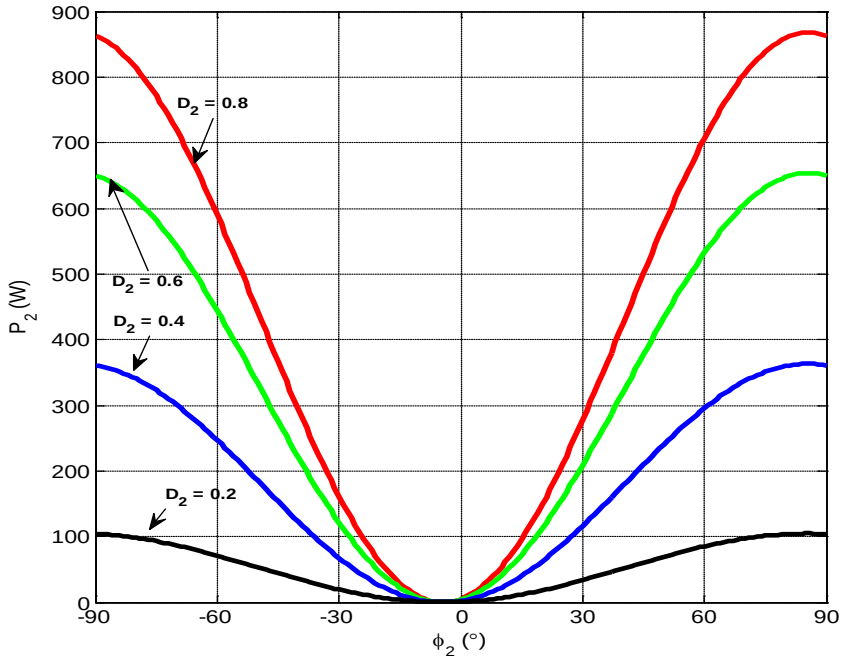
900
800
700
600
500
400
300
200
100
0
-90
-60
-30
0
30
60
90
P_2 (W)
ϕ_2 (°)
D_2 = 0.8
D_2 = 0.6
D_2 = 0.4
D_2 = 0.2

(b)

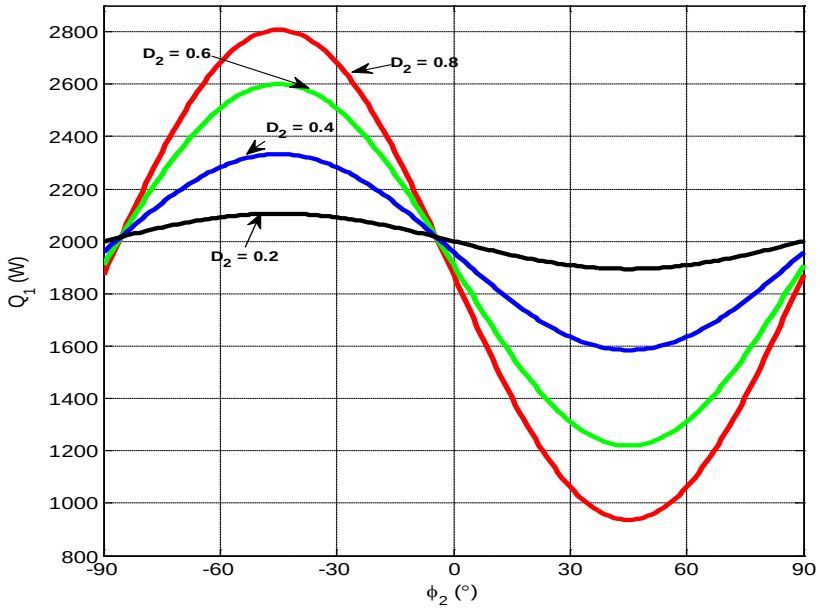

(c)

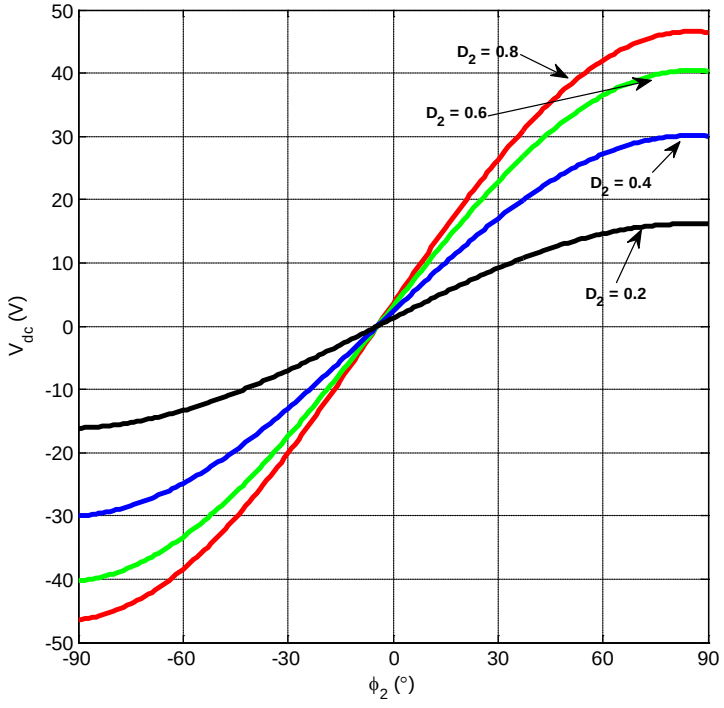

(d)

Fig. 4.3 Steady state performance: (a) I_1 (b) P_2 (c) Q_1 (d) V_{dc}

4.2.3 Verification of Steady State Results by HBT

To verify the steady state results predicted by the harmonic balance technique, the simulation results using the dynamic equations of the proposed system generated using MATLAB/SIMULINK/Simulink are compared with them and are shown from Fig. 4.4 to Fig. 4.15. The harmonic balance technique largely predicts the performance of the converter very well with discrepancies observed only when operating close to the peak current region.

The steady state analysis based on the input current I_1, input voltage V_1, output current I_2', output load voltage V_{dc2}, real input and output power P_1, P_2 and reactive power Q are studied and shown in the figures below. Fix duty ratio (1) D_1 = 1, D_2 =1, (2) D_1 = 0.8, D_2 =0.8, (3) D_1 = 1, D_2 =0.8 and (4) D_1 = 0.8, D_2 =0.6. Vary the phase angle Φ_2 from -90° to 90°when fixing Φ_1 at 0.

The parameters are listed: Input resistance r_1 = 0.03Ω, input leakage inductance L_1 = 5.85 μH, output resistance r_2 = 0.005Ω, output leakage inductance L_2 = 1.35 μH, mutual inductance L_m = 185μH, f = 10k Hz, R = 2.5 Ω. The input voltage is 25 V, output voltage is 50 V.

In Study Case 1:

D_1 = 1, D_2 =1 $\phi = -90^{\circ}, -75^{\circ}, -60^{\circ}, -45^{\circ}, -30^{\circ}, -15^{\circ}, 0^{\circ}, 15^{\circ}, 30^{\circ}, 45^{\circ}, 60^{\circ}, 75^{\circ}, 90^{\circ}$

Steady State Results vs. simulation results

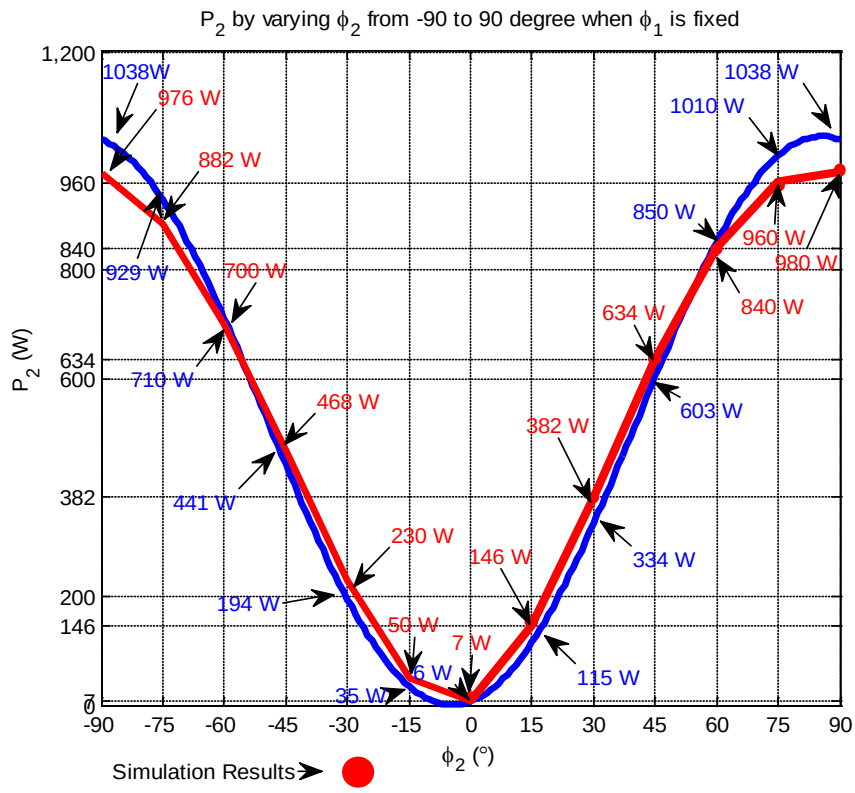

Fig. 4.4 Output Power P_2

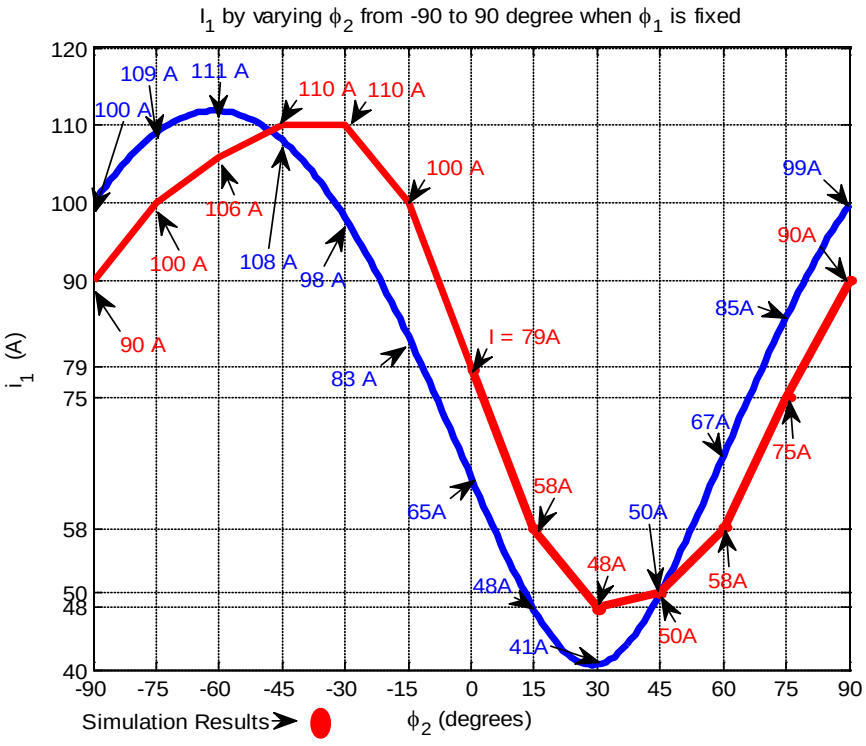

Fig. 4.5 Input current I_1

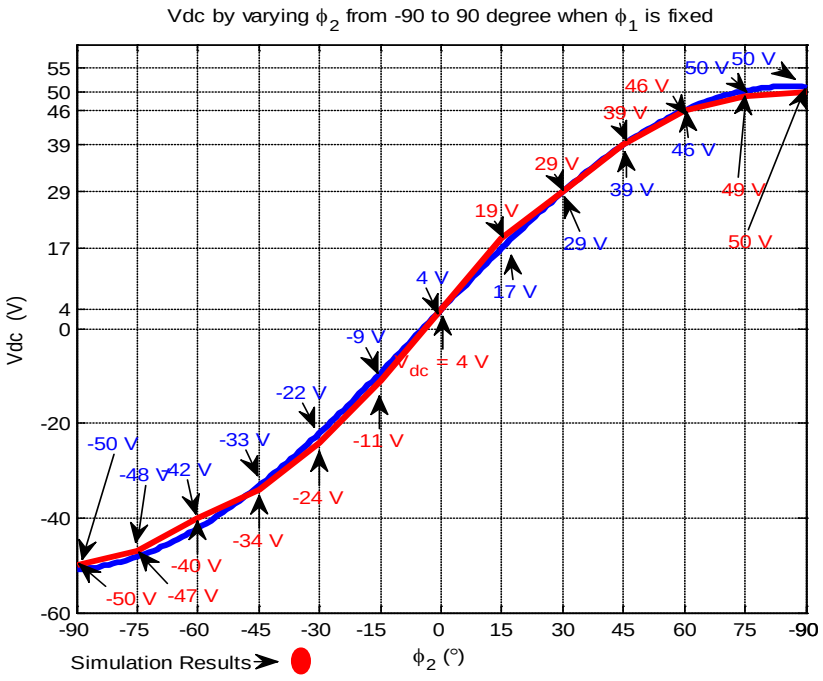

Fig. 4.6 Output dc voltage V_{dc}

In Study Case (2):

$D_1 = 0.8$, $D_2 = 0.8$ $\phi = -90^{\circ}, -75^{\circ}, -60^{\circ}, -45^{\circ}, -30^{\circ}, -15^{\circ}, 0^{\circ}, 15^{\circ}, 30^{\circ}, 45^{\circ}, 60^{\circ}, 75^{\circ}, 90^{\circ}$

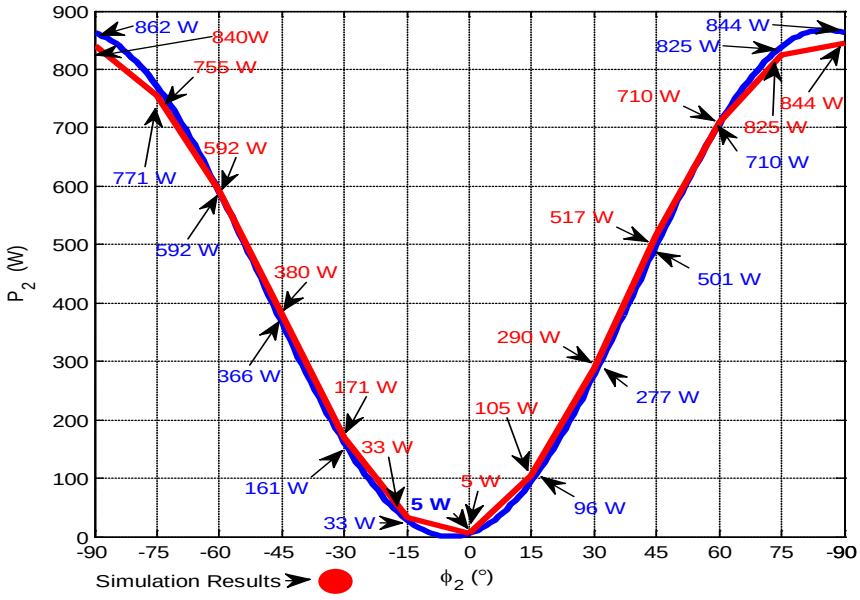

Fig. 4.7 Output Power P_2

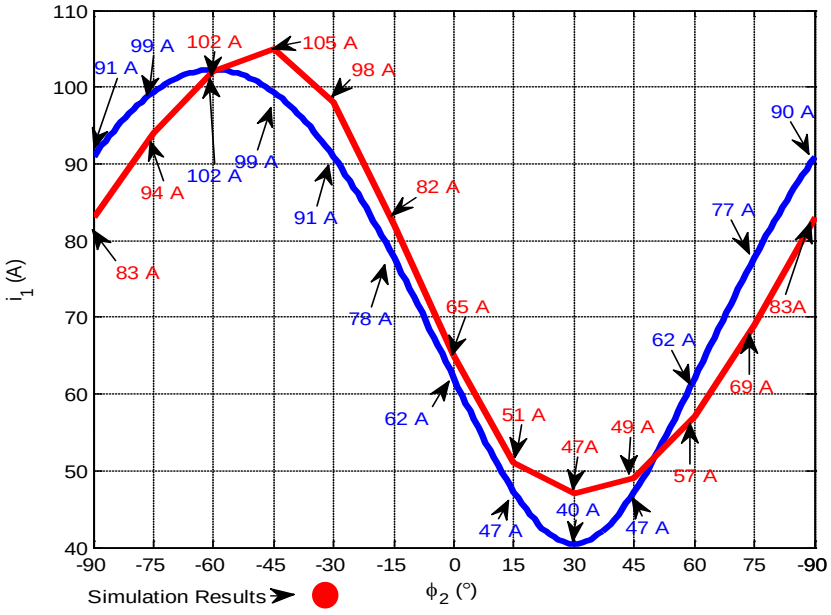

Fig. 4.8 Input current I_1

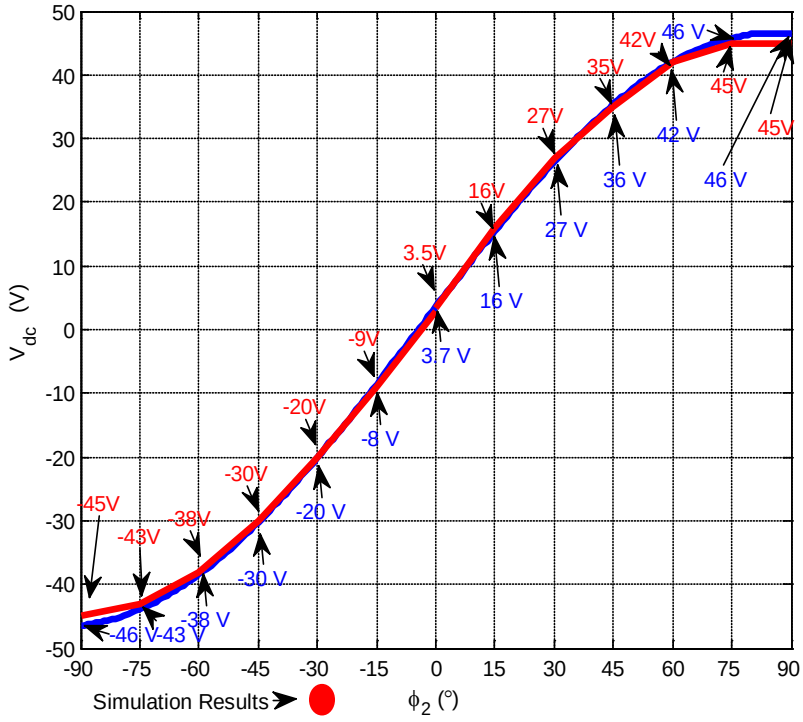

Fig. 4.9 Output dc voltage V_{dc}

In Study Case (3):

$D_1 = 1,\ D_2 = 0.8\ \phi = -90^\circ, -75^\circ, -60^\circ, -45^\circ, -30^\circ, -15^\circ, 0^\circ, 15^\circ, 30^\circ, 45^\circ, 60^\circ, 75^\circ, 90^\circ$

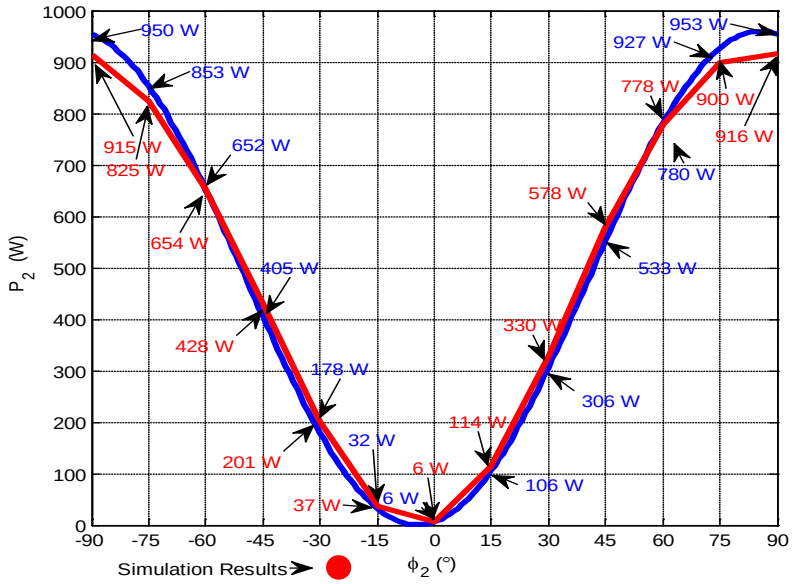

Fig. 4.10 Output Power P_2

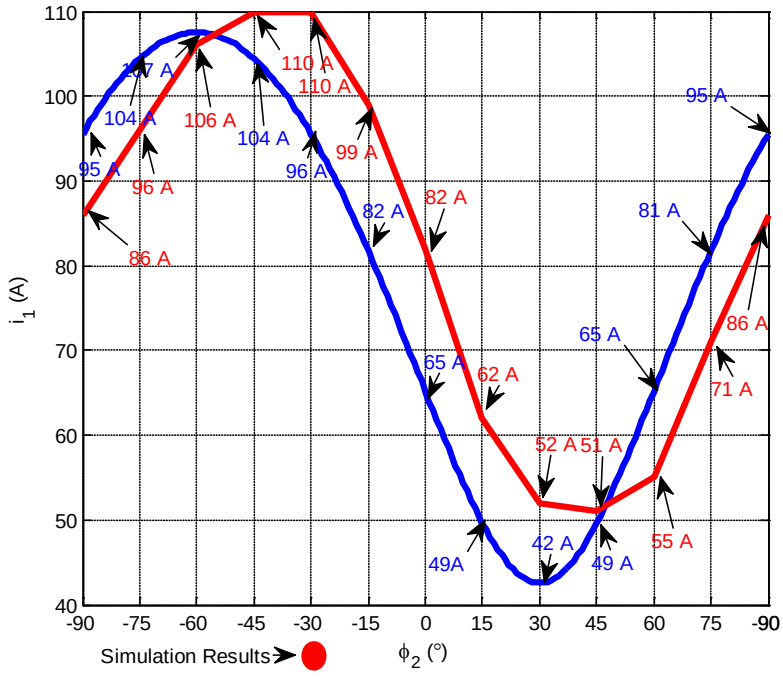

Fig. 4.11 Input current I_1

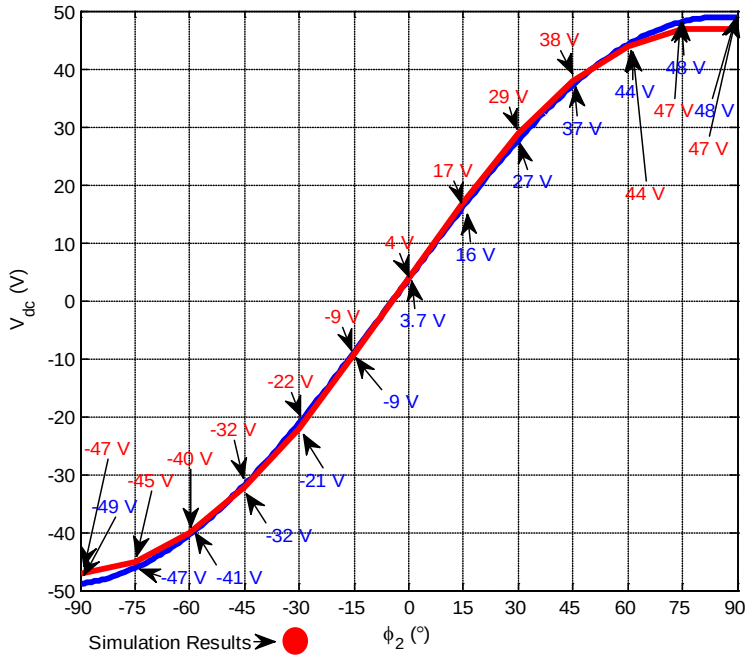

Fig. 4.12 Output dc voltage V_{dc}

In Study Case (4):

$D_1 = 0.8,\ D_2 = 0.6\ \phi = -90^{\circ}, -75^{\circ}, -60^{\circ}, -45^{\circ}, -30^{\circ}, -15^{\circ}, 0^{\circ}, 15^{\circ}, 30^{\circ}, 45^{\circ}, 60^{\circ}, 75^{\circ}, 90^{\circ}$

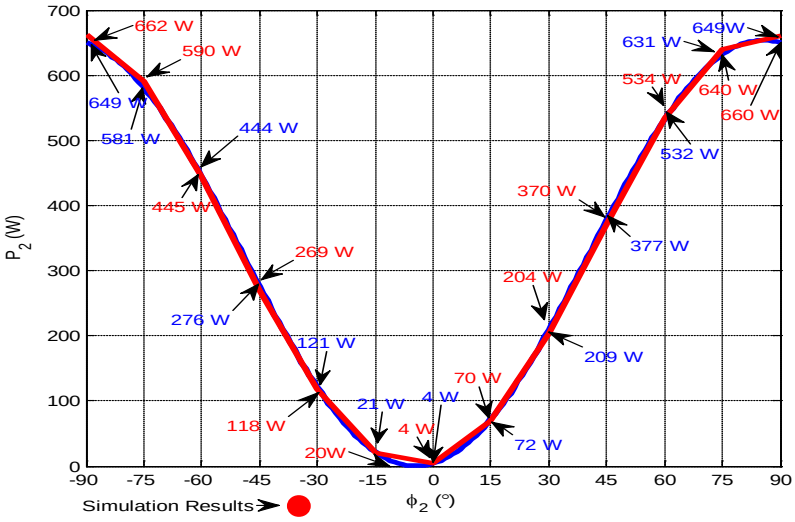

Fig. 4.13 Output Power P_2

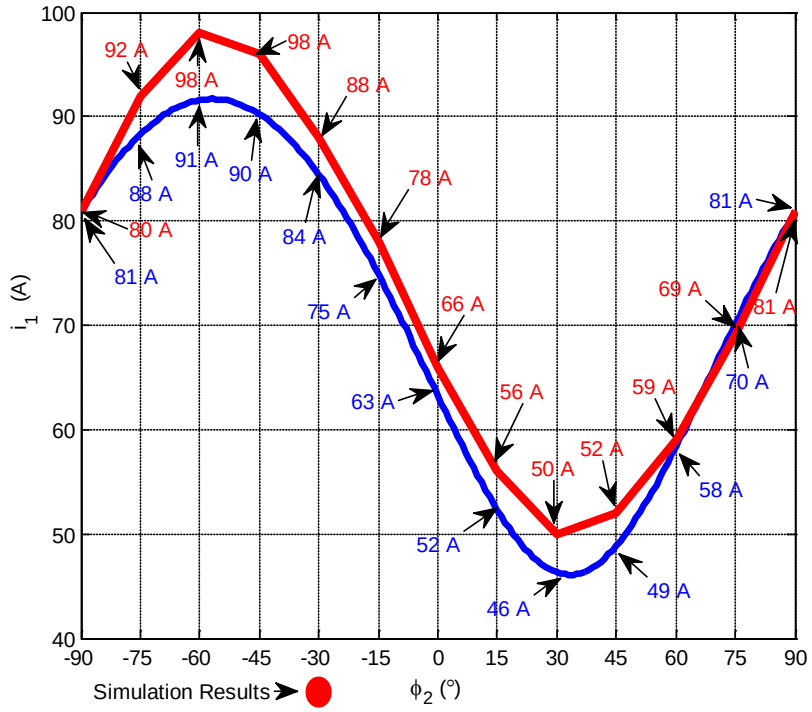

Fig. 4.14 Input current I_1

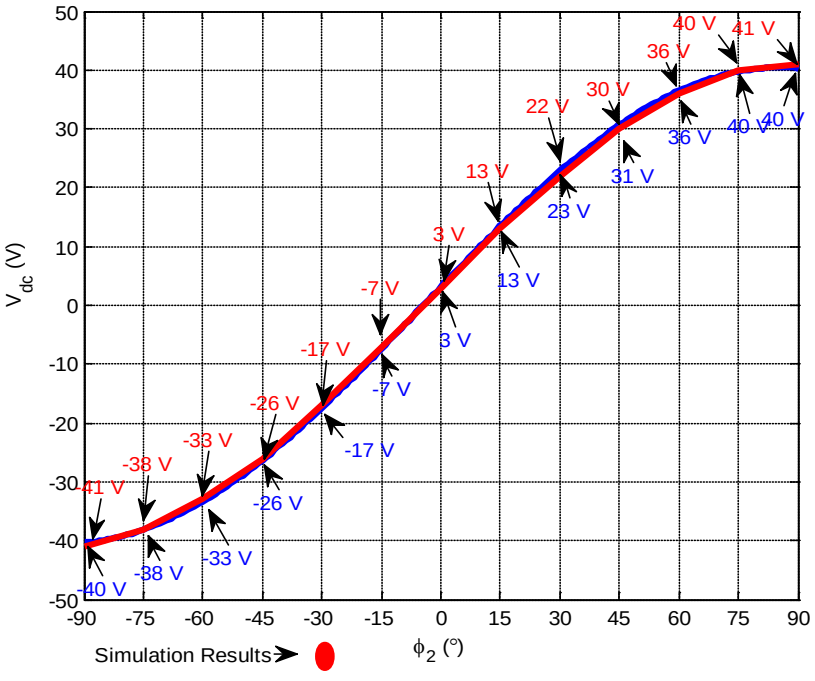

Fig. 4.15 Output dc voltage V_{dc}

The previous waveforms show that the simulation results are in agreement with harmonic balance technique. When phase angle Φ_2 is equal to 30° and duty ratio $D_1 = 0.8$, $D_2 = 0.8$, the input current obtained from the simulation of the full order converter is shown in Fig. 4.16. It is observed that the waveform is not sinusoidal, with polluting higher order components. The presence of strong higher order harmonic currents which are not accounted in the HBT suggests an explanation for the lack of excellent correlation between the two results especially at relatively higher input and output currents.

4.3 Analysis of Third and Fifth Ripple Quantities

As mentioned in the former section, HBT can yield the equations with average and ripple components. Compared with the state space averaging method, it would be

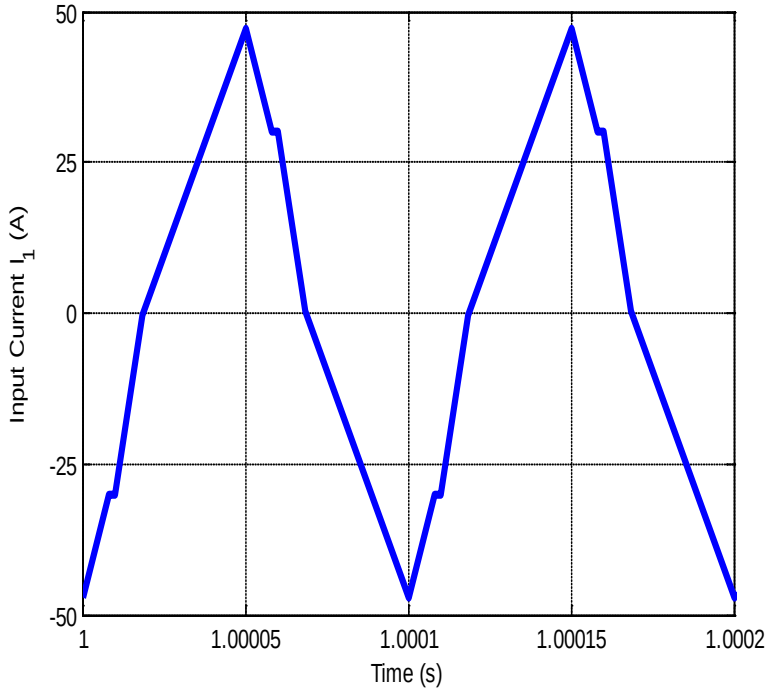

Fig. 4.16 Instantaneous input current i_1

easier to analyze and predict the characteristics of the higher order harmonic components.The ripple capabilities of filter capacitor and inductor design can be calculated. Therefore, the size and cost will be reduced due to the more precise selection of the components. In the following part, the third and fifth harmonic components will be discussed.

The derivations of the third harmonic ripples are shown as below. By using harmonic balance technique, the state variables and switching functions are assumed to have average components and third ripple quantities individually:

$$i_1 = I_{10} + \mathrm{Re}[I_{13}e^{j3\theta}] \tag{4.60}$$

$$i_2' = I_{20} + \mathrm{Re}[I_{23}e^{j3\theta}] \tag{4.61}$$

$$V_{dcL} = V_{dc3} + \mathrm{Re}[V_{dc3}e^{j6\theta}] \tag{4.62}$$

$$S_1 = S_{10} + \mathrm{Re}[S_{13}e^{j3\theta}] \tag{4.63}$$

$$S_2 = S_{20} + \mathrm{Re}[S_{23}e^{j3\theta}] \tag{4.64}$$

Substituting Equations (4.60) – (4.64) above into dynamic Equations (2.1)–(2.5), under steady state conditions, the average components of I_{10}, I_{20}, S_{10} and S_{20} are obtained as 0. The peak value of fundamental components can be used to study the characteristic and performance of the system. Because all the items contain $\mathrm{Re}[e^{j3\theta}]$, hence they can be simplified as follows:

$$(L_1 + L_m)pI_{13} + 3j\omega(L_1 + L_m)I_1 + L_m pI_{23} + 3j\omega L_m I_{23} + r_1 I_{13} = V_{dcs}S_{13} \tag{4.65}$$

$$(L_2' + L_m)pI_{23} + 3j\omega(L_2' + L_m)I_{23} + L_m pI_{13} + 3j\omega L_m I_{13} + r_2 I_{23} = V_{dc3}S_{23} \tag{4.66}$$

The dc component of capacitor is shown as below:

$$CpV_{dc3} = -\mathrm{Re}[I_{23}S_{23}^{*}]/2 - V_{dc3}/R \tag{4.67}$$

At steady state, from (4.65) – (4.67), the derivatives $pI_{13}, pI_{23}, pV_{dc3} = 0$

$$(r_1 + 3j\omega L_1)I_{13} + 3j\omega L_m(I_{13} + I_{23}) = V_{dcs}S_{13} \tag{4.68}$$

$$(r_2 + 3j\omega L_2')I_{23}' + 3j\omega L_m(I_{13} + I_{23}) = V_{dc3}S_{23} \tag{4.69}$$

$$V_{dc3} = -R \cdot \mathrm{Re}[I_{23}S_{23}^{*}]/2 \tag{4.70}$$

It is possible to decompose the state variables above into *q* and *d* components, which can linearize the equations above. If it is assumed that

$$I_{13} = I_{q13} + jI_{d13} \tag{4.71}$$

$$I_{23}' = I_{q23} + jI_{d23} \tag{4.72}$$

$$S_{13} = S_{q13} + jS_{d13} \tag{4.73}$$

$$S_{23} = S_{q23} + jS_{d23} \tag{4.74}$$

Making appropriate substitution into Equations (4.68) – (4.70) and separating them into real and imaginary parts, the third ripple component steady state variables matrix by HBT evolves as follows:

$$\begin{bmatrix} r_1 & -3\omega(L_1+L_m) & 0 & -3\omega L_m \\ 3\omega(L_1+L_m) & r_1 & 3\omega L_m & 0 \\ 0 & -3\omega L_m & 0.5RS_{q23}^{\ 2} + r_2 & 0.5RS_{q23}S_{d23} - 3\omega(L_2^{'} + L_m) \\ 3\omega L_m & 0 & 3\omega(L_2^{'} + L_m) + 0.5RS_{q23}S_{d23} & 0.5RS_{d23}^{\ 2} + r_2 \end{bmatrix} \begin{bmatrix} I_{q13} \\ I_{d13} \\ I_{q23} \\ I_{d23} \end{bmatrix} = \begin{bmatrix} V_{dc}S_{q13} \\ V_{dc}S_{d13} \\ 0 \\ 0 \end{bmatrix} \tag{4.75}$$

The steps of getting the fifth harmonic component are similar, after the derivations of the fifth ripple components, the fifth harmonic steady state variables matrix by HBT is given.

$$\begin{bmatrix} r_1 & -5\omega(L_1+L_m) & 0 & -5\omega L_m \\ 5\omega(L_1+L_m) & r_1 & 5\omega L_m & 0 \\ 0 & -5\omega L_m & 0.5RS_{q2}^{\ 2}+r_2 & 0.5RS_{q25}S_{d25}-5\omega(L_2^{'}+L_m) \\ 5\omega L_m & 0 & 5\omega(L_2^{'}+L_m)+0.5RS_{q25}S_{d25} & 0.5RS_{d25}^{\ 2}+r_2 \end{bmatrix} \begin{bmatrix} I_{q15} \\ I_{d15} \\ I_{q25} \\ I_{d25} \end{bmatrix} = \begin{bmatrix} V_{dc}S_{q15} \\ V_{dc}S_{d15} \\ 0 \\ 0 \end{bmatrix} \quad (4.76)$$

The Fig. 4.17–Fig. 4.23 show the characteristics of third harmonic components of state variables.

As can be seen from the previous figures, the output dc voltage ripple component can be used to design the corresponding value of the capacitor based on the voltage-second rule. The input ripple current can be regulated based on the right selection of the inductor. Hence, due to the prediction of ripple quantities of HBT, it can be a powerful tool to design the filter components

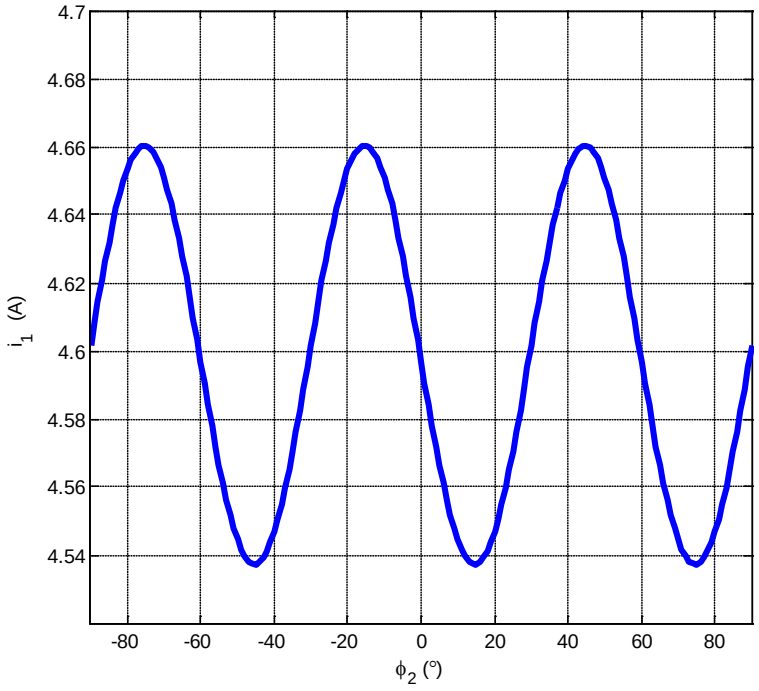

Fig. 4.17 Input ac current I_1

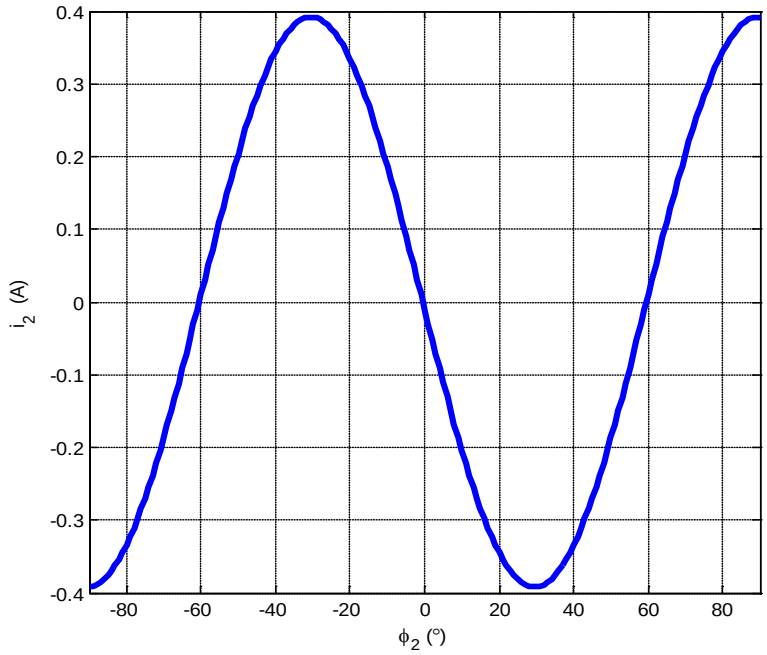

Fig. 4.18 Output ac current I_2

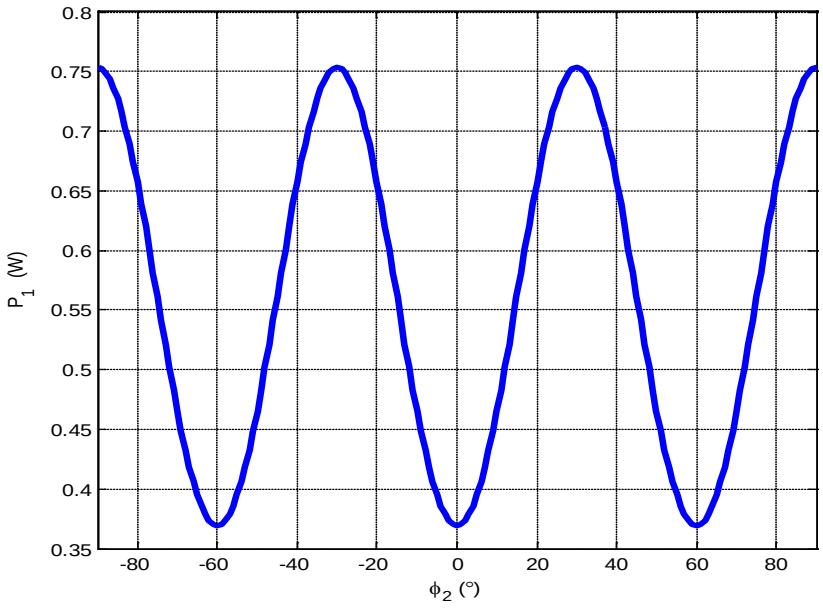

Fig. 4.19 Input power P_1

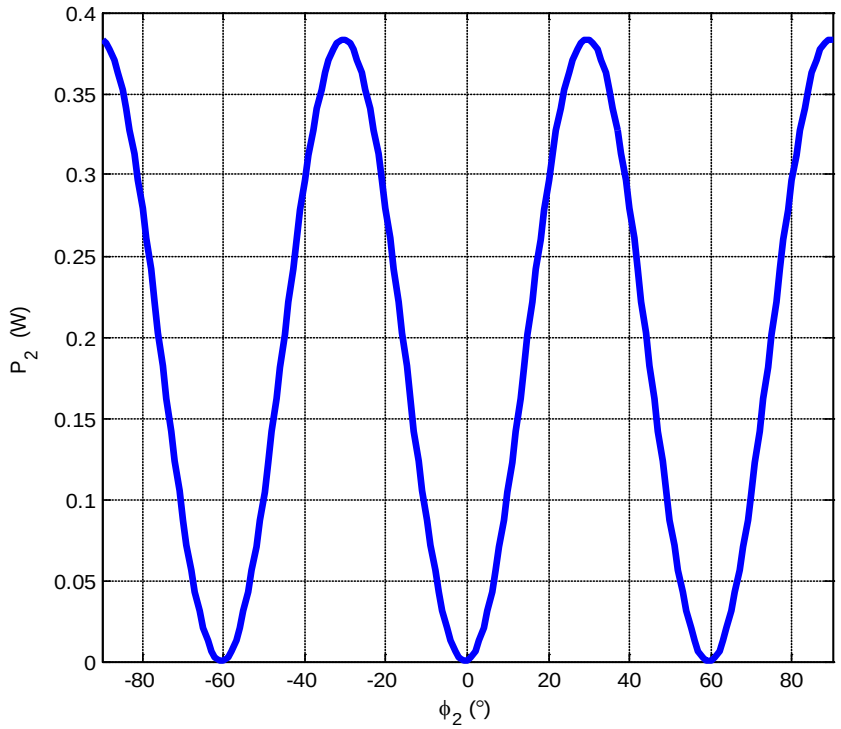

Fig. 4.20 Output power P_2

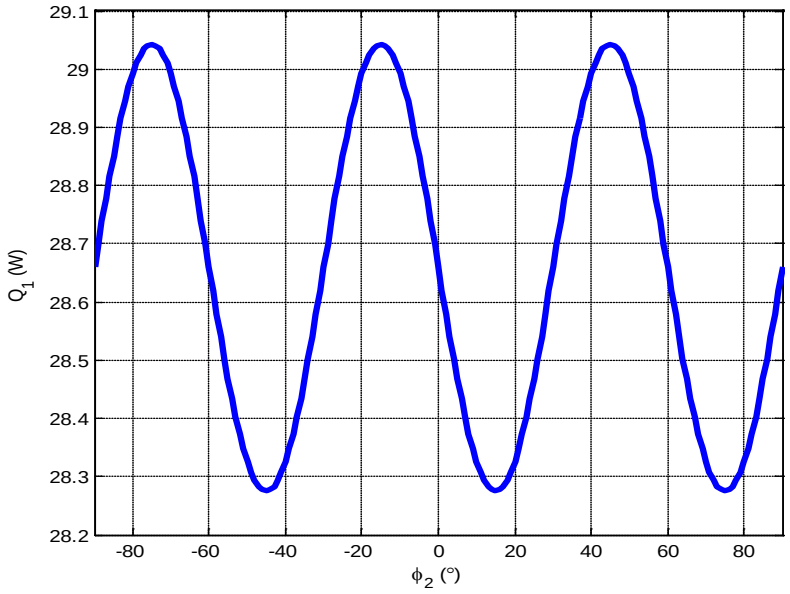

Fig. 4.21 Reactive power Q_1

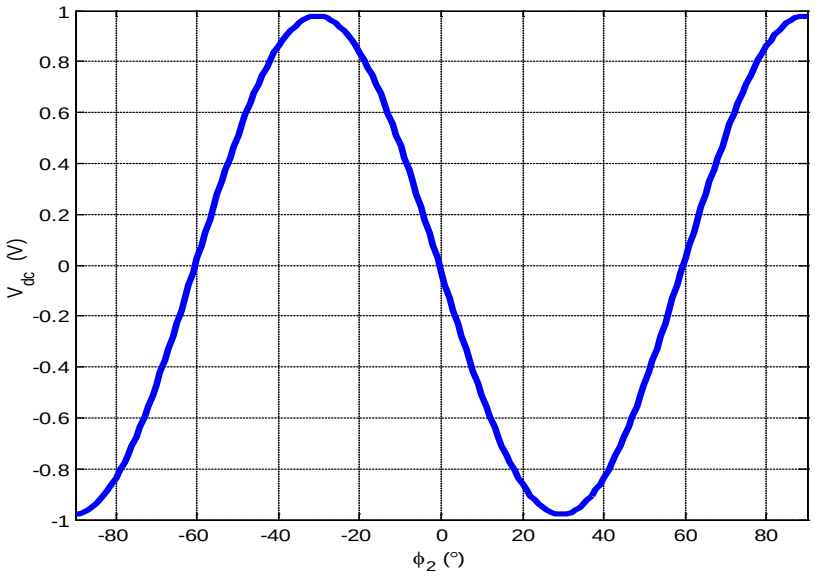

Fig. 4.22 Output dc voltage V_{dc}

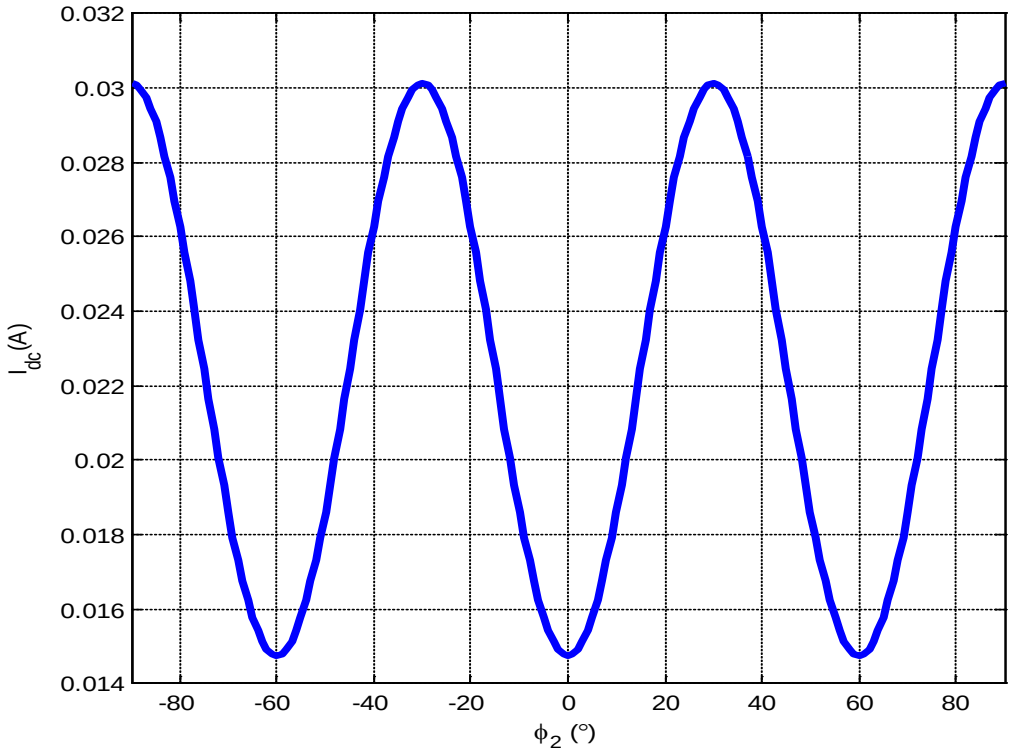

Fig. 4.23 Input dc current I_{dc}

4.4 Control Strategy of Reactive Power Minimization

Previous works are focused on small time scale control strategies. This section will present a new control strategy from the macroscopic perspective. It is based on the state variables derived from the HBT. In order to minimize the system power losses caused by reactive current flowing between the primary and the secondary converters, an optimization control strategy that dynamically determines the reference switching function command S_q and S_d required to achieve a high power efficiency (minimum peak current) is investigated.

This method uses a Lagrange multiplier to minimize the objective function which is the least summation of the squares of the currents. Hence, if the magnitude of the input ac current can be minimized for the given input dc voltage, the input real power can be optimized. From Equations (4.43) – (4.44) the current I_{qd1} can be expressed as follows:

$$I_{qd1} = \frac{V_{dc1}S_{qd1} - V_{dc2}S_{qd2}}{-j\omega L} \tag{4.77}$$

The q and d axis currents I_{q1} and I_{d1} are expressed as

$$I_{q1} = \frac{1}{\omega L}(V_{dc2}S_{d2} - V_{dc1}S_{d1}) \tag{4.78}$$

$$I_{d1} = \frac{1}{\omega L}(V_{dc2}S_{q1} - V_{dc1}S_{q2}) \tag{4.79}$$

The magnitude of current is calculated as

$$I^2 = \frac{1}{(\omega L)^2}[(V_{dc2}S_{d2} - V_{dc1}S_{d1})^2 + (V_{dc1}S_{q1} - V_{dc2}S_{q2})^2] \tag{4.80}$$

The input real power is given by

$$P_1 = \frac{1}{\omega L}[V_{dc1}S_{q1}(V_{dc2}S_{d2} - V_{dc1}S_{d1}) + V_{dc1}S_{d1}(V_{dc1}S_{q1} - V_{dc2}S_{q2})^2] \tag{4.81}$$

Using the Lagrange multipliers optimization method, it can be shown that the input current is minimized for a given input power when the determinant is zero::

$$\Delta = \begin{vmatrix} \frac{\partial P_1}{\partial S_{q2}} & \frac{\partial P_1}{\partial S_{d2}} \\ \frac{\partial I^2}{\partial S_{q2}} & \frac{\partial I^2}{\partial S_{d2}} \end{vmatrix} = 0 \tag{4.82}$$

Solving the determinant of (4.82) and simplify the equation gives the defining equation as

$$\frac{V_{dc1}({S_{q1}}^2 + {S_{d1}}^2)}{V_{dc2}} = (S_{q1}S_{q2} + S_{d1}S_{d2}) \tag{4.83}$$

By setting V_{dc1} = 25V, V_{dc2} = 60V, D_1 = 0.8 and $\Phi_1 = \pi/12$, Fig. 4.17 is obtained. It is clearly seen that as the output switching function S_{qd2} is varied, the maximum real power operating point is acquired at the lowest input current point indicated in Fig. 4.24. This means that the reactive power is minimized. Then, the correspondent input current is also minimized. Hence, the system operates at its maximum efficiency. It is therefore evident that to achieve the maximum power transfer efficiency, the correspondent S_{q2} and S_{d2} can be chosen based on the constraint established by (4.83). Also the duty ratio D_2 can be calculated from S_{q2} and S_{d2} using (4.37) – (4.38).

When varying the output voltage V_{dc2} while keeping the input voltage V_{dc1} constant for the same power level, the input current is minimized according to the curves shown in Fig. 4.25.

4.5 State Space Analysis Considering Dead Time Effect

Small signal analysis is well-known for studying the converter equivalent circuits. The converter characteristics can be analyzed in a linear way. This technique can be used in many different kinds of converters and switching elements, including phase controlled DAB converter system. For a proposed continuous nonlinear system, it can be approximated as a linear system within the vicinity of its dc operating point. The state

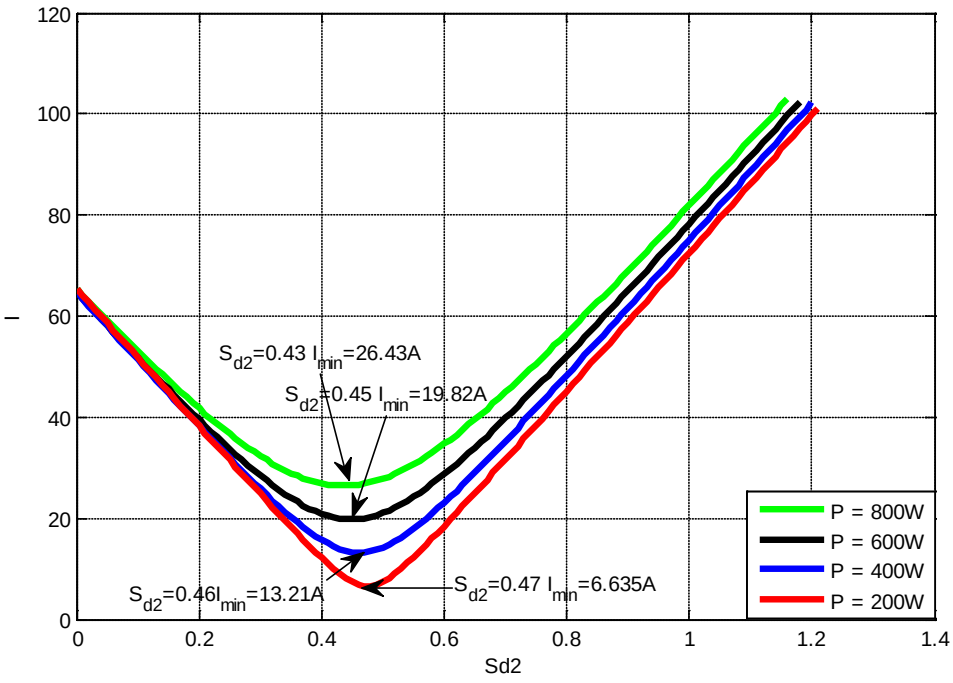

(a)

Fig. 4.24 Operating points: (a) input current I vs. S_{d2}; (b) S_{d2} vs. S_{q2} (c) D_2 vs. Φ_2;

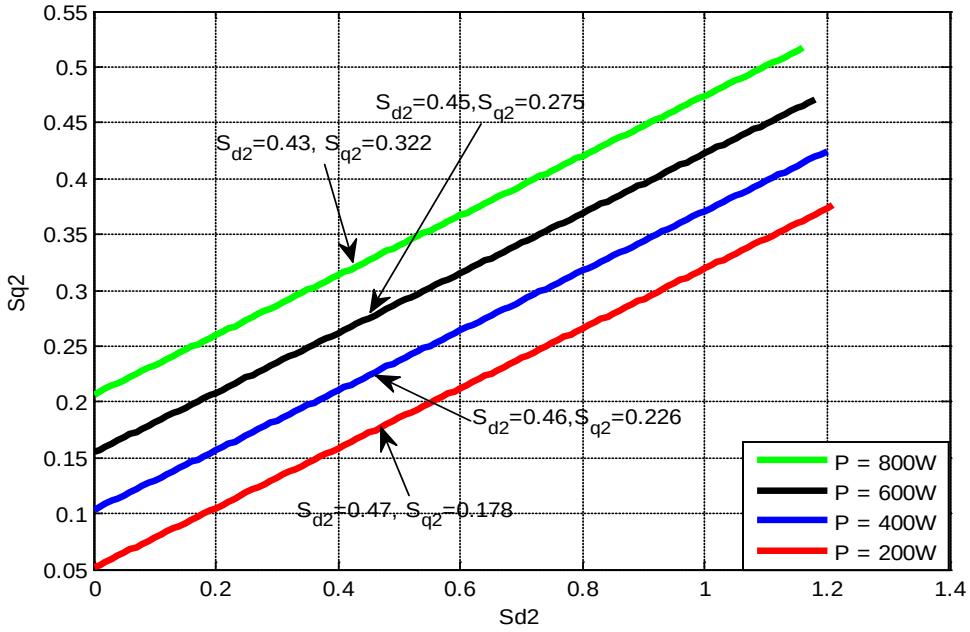

(b)

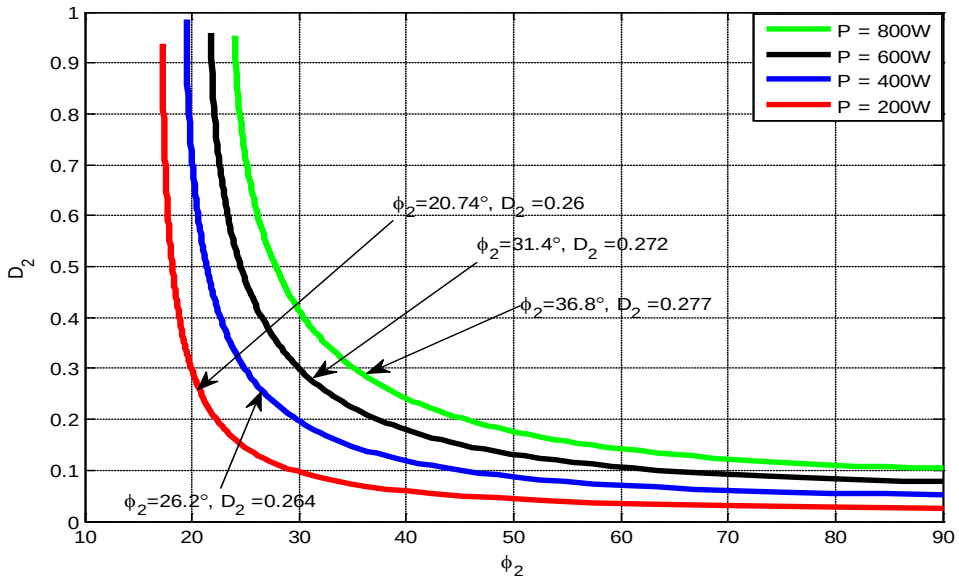

(c)

Fig. 4.24 Operating points: (a) input current I vs. S_{d2}; (b) S_{d2} vs. S_{q2} (c) D_2 vs. Φ_2;

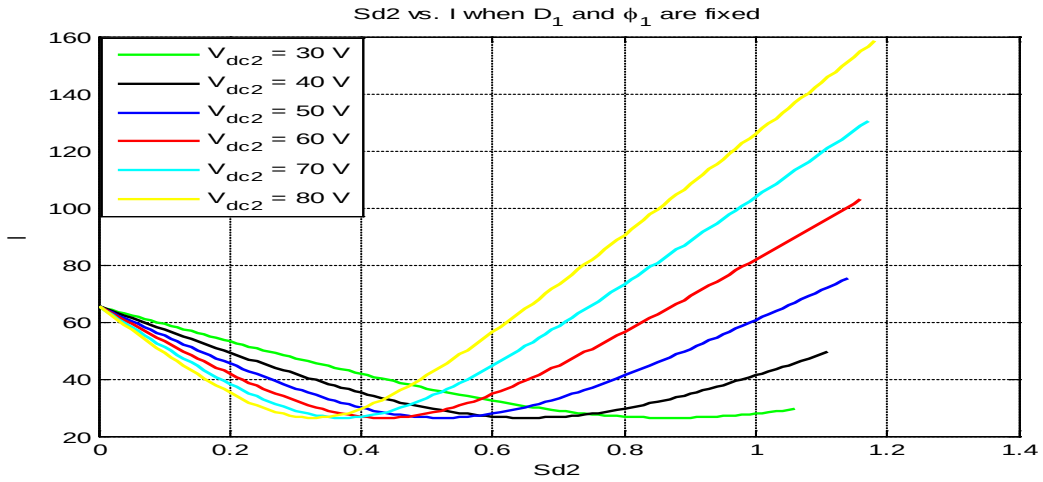

Fig. 4.25 Input current I vs. S_{d2} for obtaining minimum input current

variables can be separated in the dc terms and ac frequency terms. It can be described as

$$x = x_0 + \Delta x \tag{4.84}$$

where x_0 is the dc term, and Δx is the signal frequency term

The key theory is to replace the converter circuits with voltage and current sources to obtain a linear circuit. The initial waveforms of the voltage, current, duty ratio, and phase angle of the current state can be identical to the last value from last circuit state. By using this technique, the converter waveforms can be averaged over a small time instant. Hence any nonlinear elements can be linearized and perturbed.

In this section the proposed DAB system by using small signal analysis is studied. Perturbation method can be derived the circuit model equations. The q and d axis dynamic equations of the system are described in Equations (4.50) – (4.55). Hence, all the state variables can be redefined as

$$D_1 = D_{10} + \Delta D_1 \tag{4.85}$$

$$\phi_1 = \phi_{10} + \Delta\phi_1 \tag{4.86}$$

$$D_1 = D_{20} + \Delta D_2 \tag{4.87}$$

$$\phi_2 = \phi_{20} + \Delta\phi_2 \tag{4.88}$$

$$I_{q1} = I_{q10} + \Delta I_{q1} \tag{4.89}$$

$$I_{d1} = I_{d10} + \Delta I_{d1} \tag{4.90}$$

$$I_{q2} = I_{q20} + \Delta I_{q2} \tag{4.91}$$

$$I_{d2} = I_{d20} + \Delta I_{d2} \tag{4.92}$$

$$V_{dc0} = V_{dc00} + \Delta V_{dc0} \tag{4.93}$$

Substitute the Equations (4.85) – (4.93) into the Equations (4.50) – (4.55), the small signal model can be expressed as

$$\begin{aligned}&(L_1 + L_m)p(I_{q10} + \Delta I_{q1}) + L_m p(I_{q20} + \Delta I_{q2}) + r_1(I_{q10} + \Delta I_{q1}) \\ &- \omega(L_1 + L_m)(I_{d10} + \Delta I_{d1}) - \omega L_m(I_{d20} + \Delta I_{d2}) = V_{dc}\frac{4}{\pi}\sin[\frac{\pi}{2}(D_{10} + \Delta D_1)]\sin[\phi_{10} + \Delta\phi_1]\end{aligned} \tag{4.94}$$

$$\begin{aligned}&(L_1 + L_m)p(I_{d10} + \Delta I_{d1}) + L_m p(I_{d20} + \Delta I_{d2}) + r_1(I_{d10} + \Delta I_{d1}) \\ &+ \omega(L_1 + L_m)(I_{q10} + \Delta I_{q1}) + \omega L_m(I_{q20} + \Delta I_{q2}) = V_{dc}\frac{4}{\pi}\sin[(\frac{\pi}{2}(D_{10} + \Delta D_1)]\cos[\phi_{10} + \Delta\phi_1]\end{aligned} \tag{4.95}$$

$$\begin{aligned}&(L_2 + L_m)p(I_{q20} + \Delta I_{q2}) + L_m p(I_{q10} + \Delta I_{q1}) + r_2(I_{q20} + \Delta I_{q2}) \\ &- \omega(L_2 + L_m)(I_{d20} + \Delta I_{d2}) - \omega L_m(I_{d10} + \Delta I_{d1}) \\ &= -\frac{R}{2}\frac{16}{\pi^2}\sin^2[\frac{\pi}{2}(D_{20} + \Delta D_2)]\sin^2(\phi_{20} + \Delta\phi_2)(I_{q20} + \Delta I_{q2}) \\ &-\frac{R}{2}\frac{16}{\pi^2}\sin^2[\frac{\pi}{2}(D_{20} + \Delta D_2)]\sin(\phi_{20} + \Delta\phi_2)\cos(\phi_{20} + \Delta\phi_2)(I_{d20} + \Delta I_{d2})\end{aligned} \tag{4.96}$$

$$
\begin{aligned}
&(L_2+L_m)\,p(I_{d20}+\Delta I_{d2})+L_m\,p(I_{d10}+\Delta I_{d1})\\
&+r_2(I_{d20}+\Delta I_{d2})+\omega(L_2+L_m)(I_{q20}+\Delta I_{q2})+\omega L_m(I_{q10}+\Delta I_{q1})\\
&=-\frac{R}{2}\frac{16}{\pi^2}\sin^2[\frac{\pi}{2}(D_{20}+\Delta D_2)]\sin(\phi_{20}+\Delta\phi_2)\cos(\phi_{20}+\Delta\phi_2)(I_{q20}+\Delta I_{q2})\\
&-\frac{R}{2}\frac{16}{\pi^2}\sin^2[\frac{\pi}{2}(D_{20}+\Delta D_2)]\cos^2(\phi_{20}+\Delta\phi_2)(I_{d20}+\Delta I_{d2})
\end{aligned}
\tag{4.97}
$$

For higher order components $\Delta D_2\Delta\phi_2$ is high order component compared with ΔD_2 an $\Delta\phi_2$, hence it can be ignored. Assume $\cos(\pi\Delta D_i)\approx 1,\cos 2\Delta\phi_i\approx 1,\sin(\pi\Delta D_i)\approx\Delta D_i\pi,\sin 2\Delta\phi_i\approx 2\Delta\phi_i$.

Simplify the equations as

$$
\begin{aligned}
&(L_1+L_m)\,p\Delta I_{q1}+L_m\,p\Delta I_{q2}+r_1\Delta I_{q1}-\omega(L_1+L_m)\Delta I_{d1}-\omega L_m\Delta I_{d2}\\
&=\frac{4}{\pi}[V_{dc0}\sin(\frac{\pi}{2}D_{10})\cos\phi_{10}\Delta\phi_1+V_{dc0}\cos(\frac{\pi}{2}D_{10})\frac{\pi}{2}\Delta D_1\sin\phi_{10}+\sin(\frac{\pi}{2}D_{10})\sin\phi_{10}\Delta V_{dc}]
\end{aligned}
\tag{4.98}
$$

$$
\begin{aligned}
&(L_1+L_m)\,p\Delta I_{d1}+L_m\,p\Delta I_{d2}+r_1\Delta I_{d1}+\omega(L_1+L_m)\Delta I_{q1}+\omega L_m\Delta I_{q2}\\
&=\frac{4}{\pi}[-V_{dc0}\sin(\frac{\pi}{2}D_{10})\sin\phi_{10}\Delta\phi+V_{dc0}\cos(\frac{\pi}{2}D_{10})\frac{\pi}{2}\cos\phi_{10}\Delta D_1+\sin(\frac{\pi}{2}D_{10})\cos\phi_{10}\Delta V_{dc}]
\end{aligned}
\tag{4.99}
$$

$$
\begin{aligned}
&(L_2+L_m)\,p\Delta I_{q2}+L_m\,p\Delta I_{q1}+r_2\Delta I_{q2}-\omega(L_2+L_m)\Delta I_{d2}-\omega L_m\Delta I_{d1}=-\frac{R}{2}\frac{16}{\pi^2}[\Delta I_{q2}(\sin^2(\frac{\pi}{2}D_{20})\sin^2\phi_{20})\\
&+\frac{1}{2}\Delta I_{d2}(\sin^2(\frac{\pi}{2}D_{20})\sin 2\phi_{20})+\frac{1}{4}\Delta D_2(\pi I_{q20}\sin\pi D_{20}2\sin^2\phi_{20}+\pi I_{d20}\sin 2\phi_{20}\sin\pi D_{20})\\
&\frac{1}{4}\Delta\phi_2(4I_{q20}\sin 2\phi_{20}\sin^2(\frac{\pi}{2}D_{20})+4I_{d20}\cos 2\phi_{20}\sin^2(\frac{\pi}{2}D_{20}))]
\end{aligned}
\tag{4.100}
$$

$$
\begin{aligned}
&(L_2+L_m)\,p\Delta I_{d2}+L_m\,p\Delta I_{d1}+r_2\Delta I_{d2}+\omega(L_2+L_m)\Delta I_{q2}+\omega L_m\Delta I_{q1}\\
&=-\frac{R}{2}\frac{16}{\pi^2}[\frac{1}{2}\Delta I_{q2}\sin 2\phi_{20}\sin^2(\frac{\pi}{2}D_{20})+\Delta I_{d2}(\cos^2\phi_{20}\sin^2(\frac{\pi}{2}D_{20})\\
&+\frac{\pi}{2}\Delta D_2(\frac{1}{2}\sin\pi D_{20}\sin 2\phi_{20}I_{q20}+\sin\pi D_{20}\cos^2\phi_{20}I_{d20})\\
&+\Delta\phi_2(\sin^2(\frac{\pi}{2}D_{20})\cos 2\phi_{20}I_{q20}-\sin^2(\frac{\pi}{2}D_{20})\sin 2\phi_{20}I_{d20})
\end{aligned}
\tag{4.101}
$$

$$Cp\Delta V_{dc2}+\frac{\Delta V_{dc2}}{R}=-\frac{1}{2}\frac{4}{\pi}[\Delta I_{q2}\sin\frac{\pi}{2}D_{20}\sin\phi_{20}+\Delta I_{d2}\sin\frac{\pi}{2}D_{20}\cos\phi_{20}$$
$$+\Delta D_2\frac{\pi}{2}\cos\frac{\pi}{2}D_{20}(\sin\phi_{20}I_{q20}+\cos\phi_{20}I_{d20})+\Delta\phi_2\sin\frac{\pi}{2}D_{20}(\cos\phi_{20}I_{q20}-\sin\phi_{20}I_{d20}) \quad (4.102)$$

Combining the Equations (4.98) –(4.102), the linear small signal model of equations above can be written as

$$A\begin{bmatrix}p\Delta I_{q1}\\ p\Delta I_{d1}\\ p\Delta I_{q2}\\ p\Delta I_{d2}\\ p\Delta V_{dc20}\end{bmatrix}=-B\begin{bmatrix}\Delta I_{q1}\\ \Delta I_{d1}\\ \Delta I_{q2}\\ \Delta I_{d2}\\ \Delta V_{dc20}\end{bmatrix}-C\begin{bmatrix}\Delta V_{dc1}\\ \Delta D_1\\ \Delta\phi_1\\ \Delta D_2\\ \Delta\phi_2\end{bmatrix} \quad (4.103)$$

where

$$A=\begin{bmatrix}L_1+L_m & 0 & L_m & 0 & 0\\ 0 & L_1+L_m & 0 & L_m & 0\\ L_m & 0 & L_2+L_m & 0 & 0\\ 0 & L_m & 0 & L_2+L_m & 0\\ 0 & 0 & 0 & 0 & C\end{bmatrix} \quad (4.104)$$

$$B=\begin{bmatrix} r_1 & -\omega(L_1+L_m) & 0 & -\omega L_m & 0\\ \omega(L_1+L_m) & r_1 & \omega L_m & 0 & 0\\ 0 & -\omega L_m & r_2+\frac{16R}{2\pi^2}\sin^2(\frac{\pi D_2}{2})\sin^2\phi_2 & -\omega(L_2+L_m)+\frac{16R}{4\pi^2}\sin^2(\frac{\pi D_2}{2})\sin 2\phi_2 & 0\\ \omega L_m & 0 & \omega(L_2+L_m)+\frac{16R}{4\pi^2}\sin^2(\frac{\pi D_2}{2})\sin 2\phi_2 & r_2+\frac{16R}{2\pi^2}\sin^2(\frac{\pi D_2}{2})\cos^2\phi_2 & 0\\ 0 & 0 & \frac{1}{2}\frac{4}{\pi}\sin(\frac{\pi D_2}{2})\sin\phi_2 & \frac{1}{2}\frac{4}{\pi}\sin(\frac{\pi D_2}{2})\cos\phi_2 & \frac{1}{R}\end{bmatrix} \quad (4.105)$$

$$C=\begin{bmatrix} -\frac{4}{\pi}\sin(\frac{\pi D_1}{2})\sin\phi_1, & \frac{-4V_{dc}}{\pi}\sin\phi_1\cos(\frac{\pi D_1}{2})\frac{\pi}{2} & \frac{-4V_{dc}}{\pi}\sin(\frac{\pi D_1}{2})\cos\phi_1, & 0, & 0 \\ -\frac{4}{\pi}\sin(\frac{\pi D_1}{2})\cos\phi_1, & \frac{-4V_{dc}}{\pi}\cos\phi_1\cos(\frac{\pi D_1}{2})\frac{\pi}{2} & \frac{4V_{dc}}{\pi}\sin(\frac{\pi D_1}{2})\sin\phi_1 \ , & 0, & 0 \\ 0, & 0, & 0, & \frac{16R}{2\pi^2}\sin(\pi D_2)\frac{\pi}{2}(I_{q2}\sin^2\phi_2+I_{d2}\frac{\sin 2\phi_2}{2}), & \frac{16R}{2\pi^2}\sin^2(\frac{\pi D_2}{2})(I_{q2}\sin 2\phi_2+I_{d2}\cos 2\phi_2) \\ 0, & 0, & 0, & \frac{16R}{2\pi^2}\sin(\pi D_2)\frac{\pi}{2}(I_{q2}\frac{\sin 2\phi_2}{2}+I_{d2}\cos^2\phi_2), & \frac{16R}{2\pi^2}\sin^2(\frac{\pi D_2}{2})(I_{q2}\cos 2\phi_2-I_{d2}\sin 2\phi_2) \\ 0, & 0, & 0, & \frac{1}{2}\frac{4}{\pi}\cos(\frac{\pi D_2}{2})\frac{\pi}{2}(I_{q2}\sin\phi_2+I_{d2}\cos\phi_2) & ,\frac{1}{2}\frac{4}{\pi}\sin(\frac{\pi D_2}{2})(I_{q2}\cos\phi_2-I_{d2}\sin\phi_2) \end{bmatrix} \tag{4.106}$$

Rearrange the Equation (4.104) into state space model,

$$\begin{bmatrix} p\Delta I_{q1} \\ p\Delta I_{d1} \\ p\Delta I_{q2} \\ p\Delta I_{d2} \\ p\Delta V_{dc20} \end{bmatrix} = -A^{-1}B\begin{bmatrix} \Delta I_{q1} \\ \Delta I_{d1} \\ \Delta I_{q2} \\ \Delta I_{d2} \\ \Delta V_{dc20} \end{bmatrix} - A^{-1}C\begin{bmatrix} \Delta V_{dc1} \\ \Delta D_1 \\ \Delta\phi_1 \\ \Delta D_2 \\ \Delta\phi_2 \end{bmatrix} \tag{4.107}$$

When the Equation (4.107) is gotten, the key transfer function can be derived based on it.

CHAPTER 5

MULTIPORT BIDIRECTIONAL DC-DC CONVERTER SYSTEM

5.1 Introduction

Recent development in renewable energy system needs to interface a variety of alternative power sources such as solar panels, fuel cells, and wind turbines. Meanwhile the supplementary energy storages such as supercapacitors and batteries need to back up due to the intermittent nature of renewable sources. The design of power conversion system faces the challenge to interact different renewable energy sources with different voltage levels. The multiport dc-dc converters are gaining popularity in this field where the system can operate with multiple inputs and outputs. It would be ideal for power generations which sizes are critical such as electric vehicle energy management and portable fuel cell power supply system in the application of military or aeronautic communication power management. Centralized control is desired because of the high number of power devices introducing potential power losses problems. Due to the appealing characteristics of multiport converter, a variety of topologies and control methods are introduced. Some researchers proposed a common dc bus to link the different dc sources. However the drawback of this topology is the complexity and low efficiency due to the multiple power conversion stages. An alternative multiport dc-dc converter system has also been studied which is different from the former one. The whole system is considered as a single power processing system with multiple ports. Hence, the overall system efficiency may be improved by eliminating the redundant power stages. A

high frequency transformer can be presented to be the solution due to its advantage of compactable size and possible multiple winding systems.

5.2 Multiport Bidirectional DC-DC Converters

A multiport converter structure with many ports to which sources or loads can be connected as shown in Fig. 5.1. The multiport topology has some advantages such as bidirectional power flow, centralized control between the ports, galvanic isolation, different voltage magnitudes of ports, and compact size of the converter. For example, in the applications of renewable energy regeneration systems, fuel cell system are always operated with accompany of low voltage batteries or supercapacitors. Because fuel cells have low response due to the electrochemical reactions, the power supplying by fuel cells cannot match transients of dynamic power. Hence, the deficiency or surplus power must be supplied by extra energy systems such as batteries or supercapacitors.

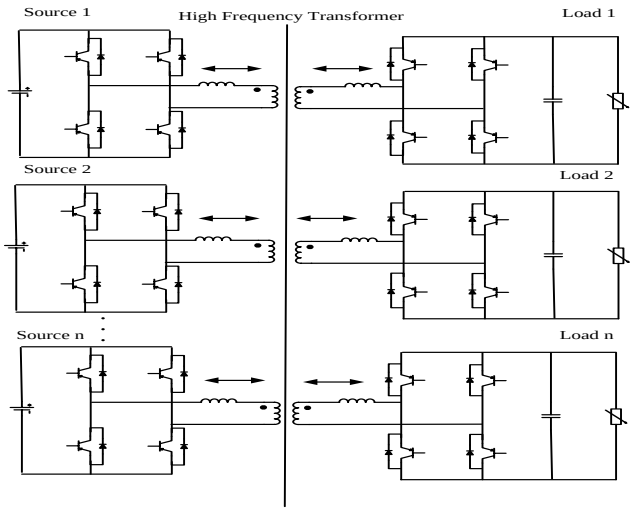

Fig. 5.1 Multiport bidirectional dc-dc converter structure

5.3 Analysis of Three-Port Bidirectional DC-DC Converter Using Harmonic Balance Technique

This section presents a three-port bidirectional dc-dc converter system as an extension of two-port bidirectional dc-dc converter system discussed in the former chapters. Compared with the well known averaging technique such as state space method, it has a greater advantage using harmonic balance technique to study the steady state performance and dynamic characteristics of three-port system.

As already studied, the equivalent of three-port dc-dc converter system has been shown in Fig. 5.2. It can be viewed as a network of inductors supplied by the voltage sources with phase shifted rectangular voltage waveforms according to the T model of the equivalent circuit in Fig. 5.2. The quantities of secondary and third port sides are referred to the primary side. Based on KVL,

$$(L_1 + L_m)pi_1 + L_m(pi_2' + pi_3') + r_1 i_1 = v_1 \tag{5.1}$$

$$(L_2' + L_m)pi_2' + L_m(pi_1' + pi_3') + r_2 i_2' = v_2' \tag{5.2}$$

$$(L_3' + L_m)pi_3' + L_m(pi_1' + pi_3') + r_3 i_3' = v_3' \tag{5.3}$$

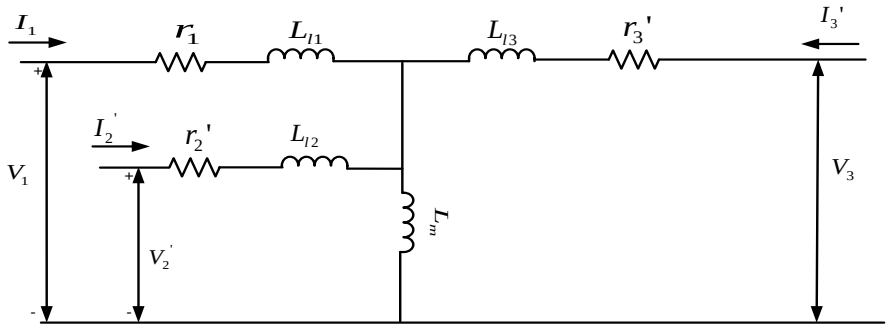

Fig. 5.2 Equivalent circuit of three-port bidirectional dc-dc converter

The capacitor and load model is represented by the following current equation:

$$CpV_{dcL} = -i_3' s_3 - \frac{V_{dcL}}{R} \tag{5.4}$$

The input voltage can be figure by

$$v_1 = V_{dcs1} s_1 \tag{5.5}$$

$$v_2' = V_{dcs2} s_2 \tag{5.6}$$

where i_1, i_2' and i_3' are the currents of each port, r_1, r_2 and r_3 are transformer resistances, L_1, L_2' and L_3' are transformer leakage inductances, L_m are transformer mutual inductance, C is output capacitance, R is the output resistive load, v_1, v_2' and v_3' are ac voltages of each port going through the single-phase converter. V_{dcs1}, V_{dcs2} and V_{dcL} are the dc voltages going into the single-phase converter. s_1, s_2 and s_3 are the switching functions for primary and secondary and third side converters.

The state variables and the switching functions are assumed to have average and ripple components. The switching function of single-phase converter is rectangular pulse with variable duty ratio and variable phase shift angle.

By using harmonic balance technique in Equations (5.1)- (5.6), all the state variables can be separated into two components which are average quantities and ripple quantities individually. All the state variables are expressed as

$$i_1 = I_{10} + \mathrm{Re}[I_1 e^{j\theta}] \tag{5.7}$$

$$i_2' = I_{20} + \mathrm{Re}[I_2 e^{j\theta}] \tag{5.8}$$

$$i_3' = I_{30} + \mathrm{Re}[I_3 e^{j\theta}] \tag{5.9}$$

$$V_{dcL} = V_{dc0} + \mathrm{Re}[V_{dc1} e^{j2\theta}] \tag{5.10}$$

$$s_1 = S_{10} + \mathrm{Re}[S_1 e^{j\theta}] \tag{5.11}$$

$$s_2 = S_{20} + \mathrm{Re}[S_2 e^{j\theta}] \tag{5.12}$$

$$s_3 = S_{30} + \mathrm{Re}[S_3 e^{j\theta}] \tag{5.13}$$

Substituting the equations above into dynamic Equations (5.1)-(5.6)

$$(L_1 + L_m)p(I_{10} + \mathrm{Re}[I_1 e^{j\theta}]) + L_m p(I_{20} + \mathrm{Re}[I_2 e^{j\theta}] + I_{30} + \mathrm{Re}[I_3 e^{j\theta}]) + r_1(I_{10} + \mathrm{Re}[I_1 e^{j\theta}]) = V_{dcs}(S_{10} + \mathrm{Re}[S_1 e^{j\theta}]) \tag{5.14}$$

$$(L_2' + L_m)p(I_{20} + \mathrm{Re}[I_2 e^{j\theta}]) + L_m p(I_{10} + \mathrm{Re}[I_1 e^{j\theta} + I_3 e^{j\theta}] + I_{30}) + r_2(I_{20} + \mathrm{Re}[I_2 e^{j\theta}]) = V_{dcs2}(S_{20} + \mathrm{Re}[S_2 e^{j\theta}]) \tag{5.15}$$

$$(L_3' + L_m)p(I_{30} + \mathrm{Re}[I_3 e^{j\theta}]) + L_m p(I_{10} + \mathrm{Re}[I_1 e^{j\theta} + I_2 e^{j\theta}] + I_{20}) + r_3(I_{30} + \mathrm{Re}[I_3 e^{j\theta}]) = V_{dcL0}(S_{30} + \mathrm{Re}[S_3 e^{j\theta}]) \tag{5.16}$$

The capacitor and load model is represented by the following current equation:

$$Cp(V_{dc0} + \mathrm{Re}[V_{dc1} e^{j2\theta}]) = -(I_{30} + \mathrm{Re}[I_3 e^{j\theta}]) * (S_{30} + \mathrm{Re}[S_3 e^{j\theta}]) - \frac{V_{dc0} + \mathrm{Re}[V_{dc1} e^{j2\theta}]}{R} \tag{517}$$

The input voltage of Port 1 can be calucated by

$$v_1 = V_{dcs1} * (S_{10} + \mathrm{Re}[S_1 e^{j\theta}]) \tag{5.18}$$

The input voltage of Port 2 can be gotten by

$$v_2' = V_{dcs2} * (S_{20} + \mathrm{Re}[S_2 e^{j\theta}]) \tag{5.19}$$

When the system comes into steady state, the derivatives of the state variables are all equal to zero. Also the average components of $I_{10}, I_{20}, I_{30}, S_{10}, S_{20}$ and S_{30} are all equal to 0. The peak value of fundamental components from ripple equations can be used to study the characteristic and performance of the system. Hence the peak fundamental component equations are used as below:

At steady state, $pI_1, pI_2', pI_3', pV_{dcL} = 0$

$$(r_1 + j\omega L_1)I_1 + j\omega L_m(I_1 + I_2'+I_3') = V_{dcs1}S_1 \tag{5.20}$$

$$(r_2 + j\omega L_2')I_2'+ j\omega L_m(I_1 + I_2'+I_3') = V_{dcs2}S_2 \tag{5.21}$$

$$(r_3 + j\omega L_3')I_3'+ j\omega L_m(I_1 + I_2'+I_3') = V_{dc0}S_3 \tag{5.22}$$

$$0 = -\frac{1}{2}\mathrm{Re}[I_3'S_3^*] - \frac{V_{dc0}}{R} \Rightarrow V_{dc0} = -\frac{1}{2}R*\mathrm{Re}[I_3'S_3^*] \tag{5.23}$$

Because out ac voltage V_3' contains the real value of the multiplication by two complex components, it is feasible to separate into *q* and *d* axis variables which can make equations of state variables in the linear way.

Set

$$I_1 = I_{q1} + jI_{d1} \tag{5.24}$$

$$I_2' = I_{q2} + jI_{d2} \tag{5.25}$$

$$I_3' = I_{q3} + jI_{d3} \tag{5.26}$$

$$S_1 = S_{q1} + jS_{d1} \tag{5.27}$$

$$S_2 = S_{q2} + jS_{d2} \tag{5.28}$$

$$S_3 = S_{q3} + jS_{d3} \tag{5.29}$$

Bring the complex expressions into the matrix above and separate them into real and imaginary part, rearrange the equations:

$$r_1 I_{q1} - \omega(L_1 + L_m)I_{d1} - \omega L_m I_{d2} - \omega L_m I_{d3} = V_{dcs1}S_{q1} \tag{5.30}$$

$$r_1 I_{d1} + \omega(L_1 + L_m)I_{q1} + \omega L_m I_{q2} + \omega L_m I_{q3} = V_{dcs1}S_{d1} \tag{5.31}$$

$$r_2' I_{q2} - \omega(L_2'+L_m)I_{d2} - \omega L_m I_{d1} - \omega L_m I_{d3} = V_{dcs2}S_{q2} \tag{5.32}$$

$$r_2' I_{d2} + \omega(L_2'+L_m)I_{q2} + \omega L_m I_{q1} + \omega L_m I_{q3} = -V_{dcs2}S_{d2} \tag{5.33}$$

$$r_3' I_{q3} - \omega(L_3'+L_m) I_{d3} - \omega L_m I_{d1} - \omega L_m I_{d2} = -\frac{1}{2} R[I_{q3} S_{q3} + I_{d3} S_{d3}] S_{q3} \tag{5.34}$$

$$r_3' I_{d3} + \omega(L_3'+L_m) I_{q3} + \omega L_m I_{q1} + \omega L_m I_{q2} = --\frac{1}{2} R[I_{q3} S_{q3} + I_{d3} S_{d3}] S_{d3} \tag{5.35}$$

The matrix can be gotten as follows:

$$\begin{bmatrix} r_1 & -\omega(L_1+L_m) & 0 & -\omega L_m & 0 & -\omega L_m \\ \omega(L_1+L_m) & r_1 & \omega L_m & 0 & \omega L_m & 0 \\ 0 & -\omega L_m & r_2 & -\omega(L_2'+L_m) & 0 & -\omega L_m \\ \omega L_m & 0 & \omega(L_2'+L_m) & r_2 & \omega L_m & 0 \\ 0 & -\omega L_m & 0 & -\omega L_m & \frac{1}{2} R S_{q3}^{\ 2} + r_3 & \frac{1}{2} R S_{q3} S_{d3} - \omega(L_3'+L_m) \\ \omega L_m & 0 & \omega L_m & 0 & \omega(L_3'+L_m) + \frac{1}{2} R S_{q3} S_{d3} & \frac{1}{2} R S_{d3}^{\ 2} + r_3 \end{bmatrix} \begin{bmatrix} I_{q1} \\ I_{d1} \\ I_{q2} \\ I_{d2} \\ I_{q3} \\ I_{d3} \end{bmatrix} = \begin{bmatrix} V_{dcs1} S_{q1} \\ V_{dcs1} S_{d1} \\ V_{dcs2} S_{q2} \\ V_{dcs2} S_{d2} \\ 0 \\ 0 \end{bmatrix}$$

(5.36)

Compared with the fundamental component of the system, the high order harmonic ripple components of the system can be calculated by the equations below. For the high order ripple components of capacitor side:

$$Cp(V_{dc0} + \mathrm{Re}[V_{dc1} e^{j2\theta}]) = -\mathrm{Re}[I_3 e^{j\theta}] * \mathrm{Re}[S_3 e^{j\theta}] - \frac{V_{dc0} + \mathrm{Re}[V_{dc1} e^{j2\theta}]}{R_l} \tag{5.37}$$

For the ripple part

$$\mathrm{Re}[CpV_{dc1} e^{j2\theta} + 2Cj\omega V_{dc1} e^{j2\theta}]) = -\frac{1}{2}\mathrm{Re}[I_3 S_3 e^{j2\theta}] - \frac{\mathrm{Re}[V_{dc1} e^{j2\theta}]}{R_l} \tag{5.38}$$

Delete $\mathrm{Re}[e^{j2\theta}]$ part, ripple peak value of high order components can be gotten as below:

$$CpV_{dc1} + 2C * j\omega V_{dc1} = -\frac{1}{2} I_3 S_3 - \frac{V_{dc1}}{R_l} \tag{5.39}$$

For the expression of switching function:

$$C_h = \frac{\sqrt{(\frac{4}{\pi h})^2 \sin(\frac{D}{2}\pi h) * 2}}{\sqrt{2}} = \frac{4}{\pi h}\sin(\frac{D}{2}\pi h) \tag{5.40}$$

The initial phase angle is expressed as follows:

$$\tan\phi_h = -\frac{b_h}{a_h} = \tan(\frac{\pi}{2} - h\phi) \tag{5.41}$$

So, $S_{ih} = C_{ih}e^{j\phi_h}$ (5.42)

For the ripple component of current at primary side:

$$\begin{aligned}&\mathrm{Re}[I_1 e^{j\theta}] * \mathrm{Re}[S_{11}e^{j\theta} + S_{13}e^{j3\theta}] = \frac{1}{2}\mathrm{Re}[I_1 S_{11}^{\ *}] + \frac{1}{2}\mathrm{Re}[I_1 S_{11}e^{j2\theta}] + \frac{1}{2}\mathrm{Re}[S_{13}I_1^{\ *}e^{j2\theta}] + \frac{1}{2}\mathrm{Re}[S_{13}I_1 e^{j4\theta}] \\ &= I_{dc0} + \mathrm{Re}[I_{dc2}e^{j2\theta} + I_{dc4}e^{j4\theta}]\end{aligned} \tag{5.43}$$

Delete $\mathrm{Re}[e^{j2\theta}]$ and $\mathrm{Re}[e^{j4\theta}]$ part, ripple peak value of high order components can be calculated as below:

$$I_{dc2} = \frac{1}{2}I_1 S_{11} + \frac{1}{2}S_{13}I_1^{\ *} \tag{5.44}$$

$$I_{dc4} = \frac{1}{2}I_1 S_{13} \tag{5.45}$$

Similarly, for the high peak ripple of high order components of secondary side:

$$I_{dc22} = \frac{1}{2}I_2 S_{21} + \frac{1}{2}S_{23}I_2^{\ *} \tag{5.46}$$

$$I_{dc24} = \frac{1}{2}I_2 S_{23} \tag{5.47}$$

5.4 Minimization of Three-Port Converter System

Optimization technique is the science of searching the best solutions under certain circumstances. Engineers make an effort to achieve the goals with minimum cost, greatest profit, the least energy wasted, and so on. The optimization technique can be viewed as a function of certain variables under some conditions. The ultimate objective is to find the maximum or minimum value of the desired function. In the design of multiport bidirectional dc-dc converter system, it is necessary to maximize the overall system efficiency. Therefore, it is of interest to find the optimum operating control conditions to minimize the wasted energy such as reactive power circulating inside the transformer. The minimization control strategy of three-port bidirectional dc-dc converter system is based on the phase shift and duty ratio control of the individual full bridge modules. As mentioned in the former chapter, when the real power is transferred between the two ports of bidirectional dc-dc converter, the reactive power is also being transferred at the same time only using phase shift control. If the magnitudes of voltages for each side can be varied using duty ratio control, more control freedoms can be introduced to realize the minimization of the overall system reactive power flow. Hence each full bridge converter is switched at a fixed frequency and operating a rectangular wave voltage v_1, v_2' and v_3'. The variety of phase shifts ϕ_1, ϕ_2 and ϕ_3 and duty ratios D_1, D_2 and D_3 result in desired power flow regulation among three ports, desired output voltage and controllable reactive power. The bidirectional power flow can be realized due to the lagging and leading of the phase angle compared between two ports and active bridges of all the ports. The high frequency transformer can step up or down the voltage level based

on the load requirements and makes the galvanic isolation. Also, the leakage inductances of each port winding play an important role in transferring the power among the three ports.

In the following sections, modeling of the three-port system, description of the minimization of the reactive power flow using langrange multiplier, and Gröbner basis introduction are reviewed, respectively.

5.4.1 Modeling of the Three-Port Bidirectional DC-DC Converter System

Conceptually, the equivalent circuit can be viewed as a grid of inductors including the leakage, external inductors and magnetizing inductance driven by controllable rectangular waveforms. The network can be represented on the three leakage inductances and mutual inductance to study the power flow of the three-port bidirectional dc-dc converter system. To illustrate the operation of the system, Fig. 5.3 shows the ideal simplified three-port system. The variable magnitude of voltage sources are phase shifted to regulate the corresponding power flow among the three ports. Hence the modeling of

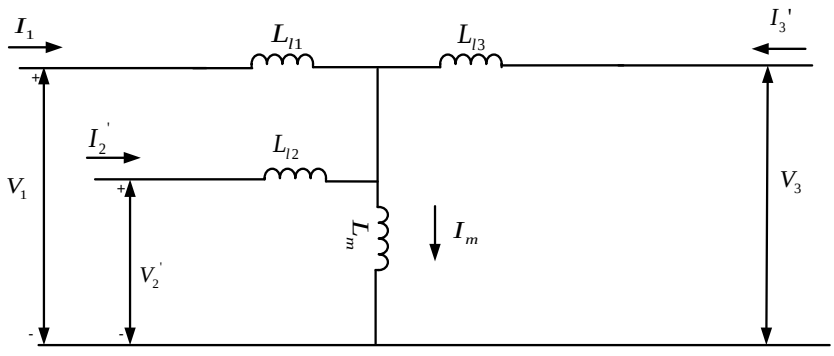

Fig. 5.3 Simplified model of equivalent circuit of three-port converter system

the three-port system can be analyzed based on the major power transferring components leakage inductances on each side. According to the descriptions above, it comes to the equations below:

$$j\begin{bmatrix} \omega(L_1+L_m) & \omega L_m & \omega L_m \\ \omega L_m & \omega(L_2+L_m) & \omega L_m \\ \omega L_m & \omega L_m & \omega(L_3+L_m) \end{bmatrix} * \begin{bmatrix} I_1 \\ I_2' \\ I_3' \end{bmatrix} = \begin{bmatrix} V_{dc1}S_1 \\ V_{dc2}'S_2 \\ V_{dc3}'S_3 \end{bmatrix} \tag{5.48}$$

Set $A = \begin{bmatrix} \omega(L_1+L_m) & \omega L_m & \omega L_m \\ \omega L_m & \omega(L_2+L_m) & \omega L_m \\ \omega L_m & \omega L_m & \omega(L_3+L_m) \end{bmatrix}$

$$A^{-1} = \begin{bmatrix} b_{11} & b_{12} & b_{13} \\ b_{21} & b_{22} & b_{23} \\ b_{31} & b_{32} & b_{33} \end{bmatrix}, if \det A \neq 0$$

Then, solve the equation above to get the current expression:

$$\begin{bmatrix} I_1 \\ I_2' \\ I_3' \end{bmatrix} = \frac{1}{j} A^{-1} \begin{bmatrix} V_{dc1}S_1 \\ V_{dc2}'S_2 \\ V_{dc3}'S_3 \end{bmatrix} = -j \begin{bmatrix} b_{11} & b_{12} & b_{13} \\ b_{21} & b_{22} & b_{23} \\ b_{31} & b_{32} & b_{33} \end{bmatrix} \begin{bmatrix} V_{dc1}S_1 \\ V_{dc2}'S_2 \\ V_{dc3}'S_3 \end{bmatrix} \tag{5.49}$$

The current I_i can be found as below:

$$I_i' = -j[b_{i1}V_{dc1}S_1 + b_{i2}V_{dc2}'S_2 + b_{i3}V_{dc3}'S_3] \tag{5.50}$$

Because the ac current contains real part and complex part, it is possible to decompose the state variables into *q* and *d* components, which can linearize the equation above. It is assumed that $I_i = I_{qi} + I_{di}$. Thus

$$I_{qi}' = [b_{i1}V_{dc1}S_{d1} + b_{i2}V_{dc2}'S_{d2} + b_{i3}V_{dc3}'S_{d3}] \tag{5.51}$$

$$I_{di}' = -[b_{i1}V_{dc1}S_{q1} + b_{i2}V_{dc2}'S_{q2} + b_{i3}V_{dc3}'S_{q3}] \tag{5.52}$$

5.4.2 Description of Minimization of Reactive Power Using Lagrange Multiplier

In this section, the optimal design of the three-port bidirectional dc-dc converter system is set forth for the minimal operating conditions to achieve the minimum reactive power flow among the three ports. The energy wasted during power transmission has a close relation to the value of the current in each port supplying into the transformer. Therefore, the problem of minimization of reactive power can be resolved through the minimization of the summation of currents circulating inside the transformer. Minimization of reactive power can significantly reduce the size and cost of the external inductors, capacitors, and rating of the power semiconductors. Also larger magnitudes of currents also cause the greater conductor size and more conduction losses.

Usually the input voltage of power source is the main power supply desired to be operated as full duty ratio. In addition, the phase angle of the primary side voltage can be set as reference angle which the secondary and third port voltage angles can be either leading or lagging compared with it. Hence, the duty ratio D_1 = 1 and Φ_1 = 0°. The switching function S_{q1} = 0 and S_{d1} = 1.27

From the Equations (5.51) and (5.52), the currents decomposition and *q-d* definition can be rewritten as

$$I_{qi}' = [1.27 b_{i1} V_{dc1} + b_{i2} V_{dc2}' S_{d2} + b_{i3} V_{dc3}' S_{d3}] \tag{5.53}$$

$$I_{di}' = -[b_{i2} V_{dc2} S_{q2} + b_{i3} V_{dc3}' S_{q3}] \tag{5.54}$$

where S_{q2}, S_{d2}, S_{q3} and S_{d3} are unknown variables

In a practical system, the power flow control can be implemented to regulate the ports' voltage, current, and power according to the system's specifications. If phase angle Φ_1 are set as reference, Φ_2 and Φ_3 are compared with Φ_1 either lagging or leading, Also duty ratio D_1 is fixed. Here the load port is power regulated. The real power P_3 can be desired and calculated as follows:

$$P_3 = V_3' I_3'^* = \mathrm{Re}[V_{dc3}'(S_{q3} + jS_{d3})(I_{q3}' - jI_{d3}')] = V_{dc3}'(S_{q3}I_{q3}' + S_{d3}I_{d3}') \tag{5.55}$$

Substituting S_{q1} and S_{d1} into the equation above,

$$P_3 = V_{dc3}'(S_{q3}[1.27b_{31}V_{dc1} + b_{32}V_{dc2}'S_{d2} + b_{33}V_{dc3}'S_{d3}] - S_{d3}[b_{32}V_{dc2}'S_{q2} + b_{33}V_{dc3}'S_{q3}] \tag{5.56}$$

Based on the KCL rule, the magnetizing current can be expressed as

$$I_m = I_1 + I_2 + I_3 \tag{5.57}$$

To produce the certain output power P_3 for a given input voltage V_1,there are numerous choices for I_{qi} and I_{di}, however the minimal value of the summation of the currents I_1, I_2,I_3, and I_m can be the solutions of the corresponding minimal reactive power circulating among the three ports:

$$I_1^2 + I_2^2 + I_3^2 + I_m^2 = (I_{q1} + I_{q2})^2 + (I_{q1} + I_{q3})^2 + (I_{q2} + I_{q3})^2 + (I_{d1} + I_{d2})^2 + (I_{d1} + I_{d3})^2 + (I_{d2} + I_{d3})^2 \tag{5.58}$$

The general form of solving an optimization problem subject to the constraints is defined

Minimize $$\min_{x \in R^n} f(x) \tag{5.59}$$

Subject to $$h_j(x) = 0, \text{ for } j = 1,2,...,m \tag{5.60}$$

$$g_j(x) \le 0, \text{ for } j = 1,2,...,n \tag{5.61}$$

All the functions above are assumed to be continuous at x which is an optimum under consideration. The Equations (5.56) and (5.58) the summation of the square of the

currents and the real power output of port three are nonlinear equations. It is clear that the process of determining the minimum value of summation of currents is to deal with the objective function with a set of unknown variables using nonlinear programming techniques to satisfy all constraints.

The control objective function of the minimization is shown as below. The reactive power minimization is formulated as

Minimize $\sum I^2 = (I_{q1} + I_{q2})^2 + (I_{q1} + I_{q3})^2 + (I_{q2} + I_{q3})^2 + (I_{d1} + I_{d2})^2 + (I_{d1} + I_{d3})^2 + (I_{d2} + I_{d3})^2$ (5.62)

Subject to the following:

The output power P_3 is the design specification. The control variables should be determined such that it generates the specified power at the output. The expression of the equality constraint is

$$P_3 = V_{dc3}'(S_{q3}[1.27b_{31}V_{dc1} + b_{32}V_{dc2}'S_{d2} + b_{33}V_{dc3}'S_{d3}] - S_{d3}[b_{32}V_{dc2}'S_{q2} + b_{33}V_{dc3}'S_{q3}] \quad (5.63)$$

The switching functions also have their own limits. The PWM pulse operated is rectangular waveforms. Using Fourier analysis, the switching functions of the fundamental component can be represented as

$$S_{qi} = \frac{4}{\pi}\sin(\frac{D_i}{2}\pi)\sin(\phi_i) \quad i = 1,2 \quad (5.64)$$

$$S_{di} = \frac{4}{\pi}\sin(\frac{D_i}{2}\pi)\cos(\phi_i) \quad i = 1,2 \quad (5.65)$$

where D_i is the duty ratio and Φ_i is phase shift angle.

So the inequality constraint can be constructed:

$$S_{q2}{}^2 + S_{d2}{}^2 \le (\frac{4}{\pi})^2 \tag{5.66}$$

$$S_{q3}{}^2 + S_{d3}{}^2 \le (\frac{4}{\pi})^2 \tag{5.67}$$

As can be seen, the mathematical models are characterized by nonlinear equations also called nonlinear programming problems. The Lagrange multiplier method is an elegant approach to obtain the solution to a constrained problem. In overview, it seems unreasonable to introduce some new additional unknown variables λ_i to solve the constrained problem. It is common sense that the fewer the unknown variables, the easier to get the solutions. The concept of Lagrange multiplier has been introduced in [55]. It is significant to express the ratio of the change in the objective function to the change in the constraint values. Therefore, the description of Lagrange function is stated

$$L(x,\lambda) = f(x) + \sum \lambda_j h_j(x) \tag{5.68}$$

If x is an optimum of the constrained problem, then it is necessary that $L_x = 0$ for some λ

$$L_x = f_x + \lambda h_x = 0 \tag{5.69}$$

λ designates the coefficients of linear combinations. Furthermore if *x* is a candidate solution by the necessary condition from Equation (5.68), then the sufficiency condition that must be satisfied is

$$T = L_{xx}(x,\lambda) + \beta h_x^T(x) h_x(x) > 0 \tag{5.70}$$

for some positive semi-definite values of β.

The significance of the sufficient condition lies in that without the constraint the problem can be extremized. The positive semi-definite matrix enables on the test for sufficiency.

From the analysis above, the optimization problem is composed of four unknown variables and four equations. The duty ratios D_2, Φ_2, D_3 and Φ_3 are control variables to be solved to get the minimum summation of the currents circulating inside the transformer under the specification of the output power and switching functions limits.

Let the Lagrangian be defined by

$$\begin{aligned} L &= f + \lambda_3 P_3 \\ &= \left\{(K_{11}+K_{21}) + (K_{12}+K_{22})S_{d2} + (K_{13}+K_{23})S_{d3}\right\}^2 + \left\{(K_{12}+K_{22})S_{q2} + (K_{13}+K_{23})S_{q3}\right\}^2 \\ &+ \left\{(K_{11}+K_{31}) + (K_{12}+K_{32})S_{d2} + (K_{13}+K_{33})S_{d3}\right\}^2 + \left\{(K_{12}+K_{32})S_{q2} + (K_{13}+K_{33})S_{q3}\right\}^2 \\ &+ \left\{(K_{21}+K_{31}) + (K_{22}+K_{32})S_{d2} + (K_{23}+K_{33})S_{d3}\right\}^2 + \left\{(K_{22}+K_{32})S_{q2} + (K_{23}+K_{33})S_{q3}\right\}^2 \\ &+ \lambda_3\left\{S_{q3}[K_{31}V_{dc3} + K_{32}V_{dc3}S_{d2} + K_{33}V_{dc3}S_{d3}] - S_{d3}[K_{32}V_{dc3}S_{q2} + K_{33}V_{dc3}S_{q3}] - P_3\right\} \end{aligned} \tag{5.71}$$

where K_{i1}, K_{i2} and K_{i3} are defined by

$$K_{i1} = 1.27 b_{i1} V_{dc1} K_{i2} = b_{i2} V_{dc2}, K_{i3} = b_{i3} V_{dc3}, i = 1,2,3 \tag{5.72}$$

5.4.3 Implementation of Lagrange Optimization Using Gröbner Basis

Numerical iterative methods can be used to solve the Lagrange optimization problems. However, they have some drawbacks such as sample-based searching computation and significance of the initial values. The objective function has to be processed by the sample step size and calculated iteratively starting from the initial value. Therefore, the global solutions highly rely on the selection of the initial values. That means the results have to be examined not only on one initial value but on many groups of the initial values. It will involve lots of time to compare the results. More over it turns out to be difficult to solve due to the change of the parameters or unknown variables.

The concept of the Gröbner basis (GB) [56] was introduced in 1965 by Austrian researcher Bruno Buchberger named after his advisor W. Gröbner. The GB provides a uniform approach to solving a wide range problems expressed in terms of sets of multivariate polunomials. GB method can be a powerful mathematical tool to solve the nonlinear polynomial equations. It can turn a group of high coupled equations into uncoupled equations based on the selection of different basis. Also, some coefficients of the nonlinear equations can be set as unknown except the original unknown variables. The influence of the coefficients of the system can be studied using Gröbner basis method whereas the numerical iterative methods cannot do the job.

To begin with the GB technique, the concepts of ideal and generating set have to be known at first. Set $k[x_1, x_2, ...x_n]$ as a polynomial ring over the field k. An ideal is defined as $I \subset k[x_1, x_2, ...x_n]$ under the conditions below

(i) $0 \in I$

(ii)if $f, g \in I$, then $f + g \in I$

(iii) if $f, g \in I$ and $h \in k[x_1, x_2, ..., x_n]$, then $hf \in I$

Another indication of the role played by ideal is the affine variety. If $f_1, f_2, ..., f_s$ and $g_1, g_2, ..., g_t$ are basis of the same ideal in $k[x_1, x_2, ...x_n]$, so that $\langle f_1, f_2, ..., f_s \rangle = \langle g_1, g_2, ..., g_t \rangle$, then $V(f_1, f_2, ..., f_s) = V(g_1, g_2, ..., g_t)$. It tells that the solutions of the finite polynomial equations are the same as that of the infinite polynomial. Hilbert basis gives the proof that for any ideal in polynomial rings there is more than one generating set. Therefore, for a given set F of polynomials, Buchberger introduced the GB algorithm to find out another set of G with certain nice properties such that

- F and G are equivalent.
- It would be much easier to solve the polynomial equations based on the set G but difficult for the original set of F.
- The solutions of G are same as the ones of F. They can be interpreted each other.

The first step of GB technique is the ordering on the terms in polynomials in $k[x_1, x_2, ...x_n]$. The success of GB algorithm depends on polynomials in one variable. To begin with, since a polynomial is a sum of monomials, it would be possible to arrange the terms in a polynomial unambiguously in either descending or ascending order. The definition of monomial ordering is for a given monomial:

$$m = x_1^{\alpha_1} x_2^{\alpha_2} x_3^{\alpha_3} x_4^{\alpha_4} = x^{\alpha} \tag{5.73}$$

where $x = x_1 x_2 \ldots x_n, \alpha = (\alpha_1, \alpha_2, \ldots \alpha_n)$.

Then for any relation on the set of monomial $x^{\alpha}, \alpha \in Z_{\geq 0}^n$, satisfying

$$Z_{\geq 0}^n = \left\{ (\alpha_1, \alpha_2, \cdots \alpha_n) \middle| \alpha \in Z_{\geq 0}^n \right\} \tag{5.74}$$

(i) $>$ relation is o total ordering on $Z_{\geq 0}^n$

(ii) If $\alpha > \beta$ and $\gamma \in Z_{\geq 0}^n$, then $\alpha + \gamma > \beta + \gamma$

(iii) $>$ is a well ordering on $Z_{\geq 0}^n$. It means that every nonempty subset of $Z_{\geq 0}^n$ has a smallest element under $>$

There are several monomial orders being used. The most common ones are lexicographic order, graded lex order, and graded reverse lex order.

(i) Lexico Order- Let $\alpha = (\alpha_1, \alpha_2, \alpha_n)$ and $\beta = (\beta_1, \beta_2, \beta_n) \in Z_{\geq 0}^n$. It is said $\alpha >_{lex} \beta$,

if in the vector difference $\alpha - \beta \in Z_{\geq 0}^{n}$, the left-most nonzero entry is positive. Write $x^{\alpha} >_{lex} \beta$

(ii) Graded Lexico Order - Let $\alpha, \beta \in Z_{\geq 0}^{n}$. It is said $\alpha >_{lex} \beta$, if $|\alpha| = \sum_{i=1}^{n} \alpha_i > |\beta| = \sum_{i=1}^{n} \beta_i$, or $|\alpha| = |\beta|$ and $\alpha >_{lex} \beta$

(iii) Graded reverse Lexico order - Let $\alpha, \beta \in Z_{\geq 0}^{n}$. It is said $\alpha >_{grevlex} \beta$, if $|\alpha| = \sum_{i=1}^{n} \alpha_i > |\beta| = \sum_{i=1}^{n} \beta_i$, or $|\alpha| = |\beta|$ and the rightmost nonzero entry of $\alpha - \beta \in Z_{\geq 0}^{n}$ is negative.

Another step of GB technique is the construction of S polynomial. It is the key to understand the derivation of the Buchberger algorithm. Before using S polynomial, some definitions have to be introduced.

(i) The multi-degree of f is

$$multi\deg(f) = \max(\alpha \in Z_{\geq 0}^{n} : a_{\alpha} \neq 0) \tag{5.75}$$

(ii) The leading coefficient of f is

$$LC(f) = a_{multi\deg(f)} \in k \tag{5.76}$$

(iii) The leading monomial of f is

$$LM(f) = x^{multi\deg(f)} \tag{5.77}$$

(iv) The leading term of f is

$$LT(f) = LC(f) \cdot LM(f) \tag{5.78}$$

By using the definitions above, the S polynomial is defined. Let $f, g \in k[x_1, x_2, ..., x_n]$ be nonzero polynomials, if $multi\deg(f) = \alpha$ and $multi\deg(g) = \beta$, then

$\gamma = (\gamma_1, \gamma_{2,} \cdots \gamma_n)$, where $\gamma_i = \max(\alpha_i, \beta_i)$ for each i. Call x^γ the least common multiple of $LM(f)$ and $LM(g)$, written $x^\gamma = LCM(LM(f), LM(g))$. The S-polynomial is written as

$$S(f,g) = \frac{x^\gamma}{LT(f)} \cdot f - \frac{x^\gamma}{LT(g)} \cdot g \tag{5.79}$$

After the S polynomial can be generated y any two polynomials, it can be used to check the following criterion of Bucberger for when a basis of ideal is a Gröbner basis.

The Theorem will be defined as follows: Let *I* be a polynomial ideal. Then a basis $G = \{g_1, g_2, \cdots g_t\}$ for *I* is a Gröbner basis for *I* if and only if for all pairs $i \neq j$, the reminder on divison of $S(g_i, g_j)$ by G is zero.

All the brief introductions come to the question: given an ideal $I \subset k[x_1, x_2, \cdots x_n]$, how can we actually construct a Gröbner basis for *I*? The Buchberger's algorithm gives an explanation as below. It can be calculated by using the following steps:

Input: $F = \{f_1, f_2, \cdots f_s\}$

Output: $G = \{g_1, g_2, \cdots g_t\}$ for I, with $F \subset G$

Step 1: $G = F$

Step 2: $G = G'$

Step 3: for each pair $\{p, q\}$, $p \neq q \in G$

Do $S := \overline{S(p,q)}^{G'}$

Check if $S \neq 0$, then $G = G \bigcup \{S\}$

Else if $S = 0$, G is the Gröbner basis

Step 4: find the minimal Gröbner basis that satisfies $LC(p)=1$ for all $p \in G$ and $LT(p) \notin \langle LT(G-\{p\}) \rangle$

Step 5: find reduced Gröbner basis. For all $p \in G$ satisfies $LC(p)=1$ and no monomial lies in $LT(G-\{p\}$

The calculation steps using to find GB above can be programmed and calculated using GB package of the software Maple environment. Here is an example to find out GB used to solve polynomial equations. Given a set of nonlinear equations as

$$\begin{cases} x^2+y^2+z^2=1 \\ x^2+z^2=y \\ x=z \end{cases} \tag{5.80}$$

Though the equations above can be solved directly, GB is used with respect to the lex order. The basis is

$$\begin{cases} g_1=x-z \\ g_2=-y+2z^2 \\ g_3=z^4+(1/2)z^2-1/4 \end{cases} \tag{5.81}$$

From the GB, it can be found some remarkable equation that *z* is obtained by solving the last equation in the GB, then substituting *z* into the second equation, variable *y* can be calculated. Further, bring *z* into the first equation, *x* can be solved. Also solutions of GB are not only real solutions which can only be gotten by using numerical iterative methods with the initial values. Hence, the GB technique provides a powerful analytical solution for the nonlinear equations. If one coefficient of the system is set as unknown parameter, it is visible how this parameter affects the system. Next, return to consider the

system of nonlinear polynomial equations which are composed of partial differential equations of Equation (5.71). They are listed

$$\frac{\partial L}{\partial S_{q2}} = Z_1 S_{q2} + Z_2 S_{q3} - Z_3 \lambda_3 S_{d3} \tag{5.82}$$

$$\frac{\partial L}{\partial S_{d2}} = Z_4 + Z_1 S_{d2} + Z_2 S_{d3} + Z_3 \lambda_3 S_{q3} \tag{5.83}$$

$$\frac{\partial L}{\partial S_{q3}} = Z_3 S_{q2} + Z_5 S_{q3} + \lambda_3 [Z_6 + Z_3 S_{d2}] \tag{5.84}$$

$$\frac{\partial L}{\partial S_{d3}} = Z_7 + Z_2 S_{d2} + Z_5 S_{d3} - Z_3 \lambda_3 S_{q2} \tag{5.85}$$

$$\frac{\partial L}{\partial \lambda_3} = Z_6 S_{q3} + Z_3 S_{q3} S_{d2} - Z_3 S_{q2} S_{d3} - P_3 \tag{5.86}$$

where $Z_1 = [2(K_{12} + K_{22})^2 + 2(K_{12} + K_{32})^2 + 2(K_{22} + K_{32})^2]$

$Z_2 = [2(K_{12} + K_{22})(K_{13} + K_{23}) + 2(K_{12} + K_{32})(K_{13} + K_{33}) + 2(K_{22} + K_{32})(K_{23} + K_{33})]$

$Z_4 = [2(K_{12} + K_{22})(K_{11} + K_{21}) + 2(K_{12} + K_{32})(K_{11} + K_{31}) + 2(K_{22} + K_{32})(K_{21} + K_{31})]$

$Z_3 = K_{32} V_{dc3}$

$Z_5 = [2(K_{13} + K_{23})^2 + 2(K_{13} + K_{33})^2 + 2(K_{23} + K_{33})^2]$

$Z_6 = K_{31} V_{dc3}$

$Z_7 = [2(K_{13} + K_{23})(K_{11} + K_{21}) + 2(K_{13} + K_{33})(K_{11} + K_{31}) + 2(K_{23} + K_{33})(K_{21} + K_{31})]$

Applying the GB method on the minimization problem above, the computation results are listed in Table 5.1.

The optimization tool package using numerical iteration in the software MATLAB environment can be used to verify the results gotten by GB method. To use the optimization toolbox package, the objective function needs to be defined. Also the constraint function also needs to be filed. The initial values chosen are $S_{q2} = 0$, $S_{d2} = 0$,

$S_{q3} = 0$, $S_{d3} = 0$. After that, using the optimization tool graphical user interface to run and get solutions, it takes seventeen steps to converge to the optimal solutions. Table 5.2 lists the values.

As is known, the solutions of the system by numerical iteration method highly depend on the selection of the initial values. In practical system, usually the initial conditions are unknown, especially during the transient of the system. If another group of initial conditions are selected, it is highly possible that the system can converge to another local optimal point whereas the GB method can give us global solutions including both real and imaginary solutions which can be used to study the influence of parameters on the system dynamics. Figure 5.3 shows the 3-D relationship of output power P_3 when varying control variables Φ_2, Φ_3 and D_3.

Further, Figure 5.4 shows the 3-D relationship of summation of circulating currents when varying control variables Φ_2, Φ_3 and D_3.

Table 5.1 Results from GB technique

Operating conditions of minimizing the circulating current	
$S_{q2} = 0$, $S_{d2} = 1.27$	$S_{q3} = 0.114$, $S_{d3} = 1.268$
$D_2 = 1$, $\Phi_2 = 0$	$D_3 = 1$, $\Phi_3 = 5$

Table 5.2 Results from numerical iteration method

Operating conditions of minimizing the circulating current	
$S_{q2} = 0$, $S_{d2} = 1.27$	$S_{q3} = 0.11$, $S_{d3} = 1.27$
$D_2 = 1$, $\Phi_2 = 0$	$D_3 = 1$, $\Phi_3 = 4$

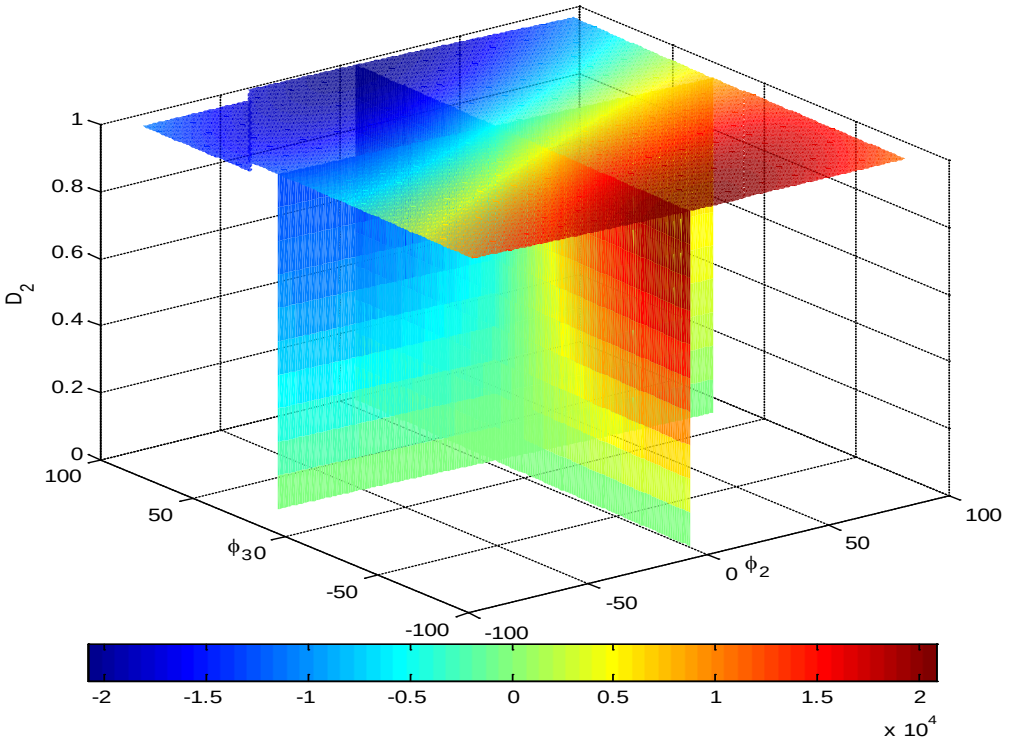

Fig. 5.3 Output power P_3 when varying Φ_2, Φ_3 and D_3

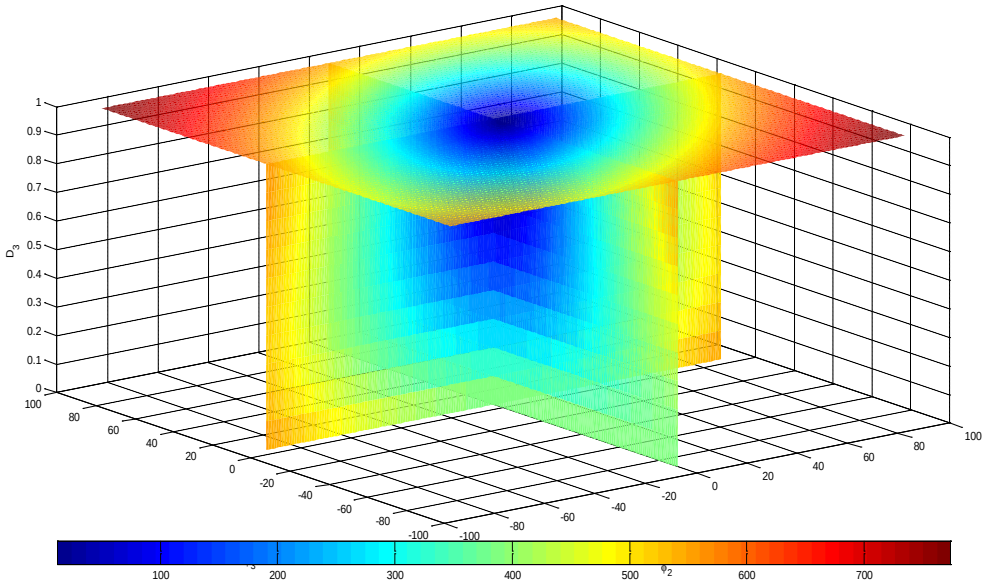

Fig. 5.4 Summation of Square of the currents I_1, I_2, I_3 and I_m

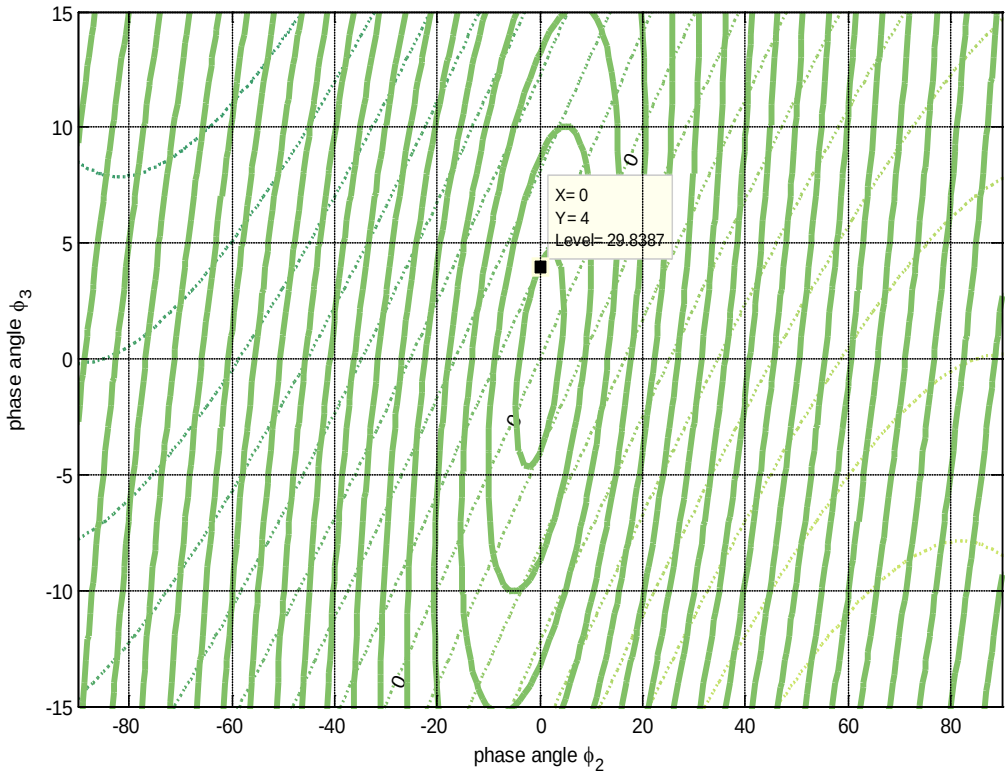

Fig. 5.5 Intersection point of optimal condition under min $\sqrt{\sum I_i^2}$ and P_3

The Fig. 5.5 shows the contour of P_3 and $\sqrt{\sum I_i^2}$, as can be seen the tangential point shows the optimal condition to achieve the minimum value of summations of the circulating currents $\sqrt{\sum I_i^2}$ under the desired output power P_3.

5.5 Simulation Model of Four-Port Bidirectional DC-DC Converter System

From the former study, the three-port bidirectional dc-dc converter system has been studied. It has a wide application such as one energy source, one energy backup and

the load system. The energy source could be any kinds of dc renewable source. The energy backup is usually selected among the batteries and supercapacitors.

In this section, a four-port bidirectional dc-dc converter system is presented. It is particular interesting for the on-site, small scale, residential power generation system where a variety of renewable energy sources are combined and many energy storage sources are available together. The subject is devoted to the design and analysis of a four-port isolated bidirectional dc-dc converter system shown in Fig. 5.6 feeding by an alternative energy source, a auxiliary energy storage, and two loads.

It aims to supply and distribute the power flow to the load side through four-port DAB system. The advantage of this topology is the battery system can provide fast response energy to load changes and also restore energy. It can supply multi loads at the

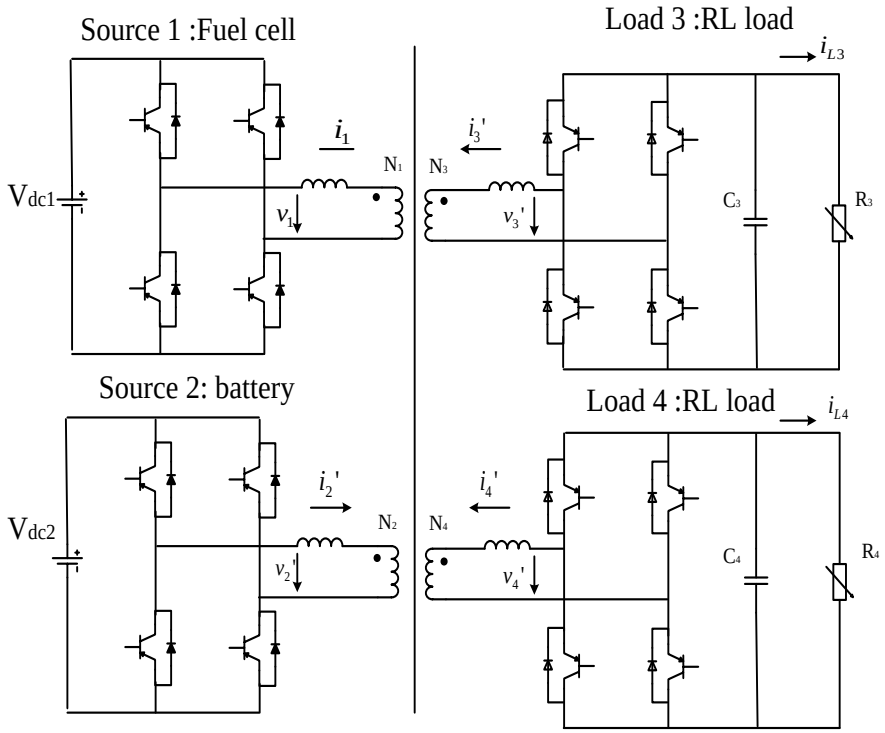

Fig. 5.6 Four-port isolated bidirectional dc-dc converter system

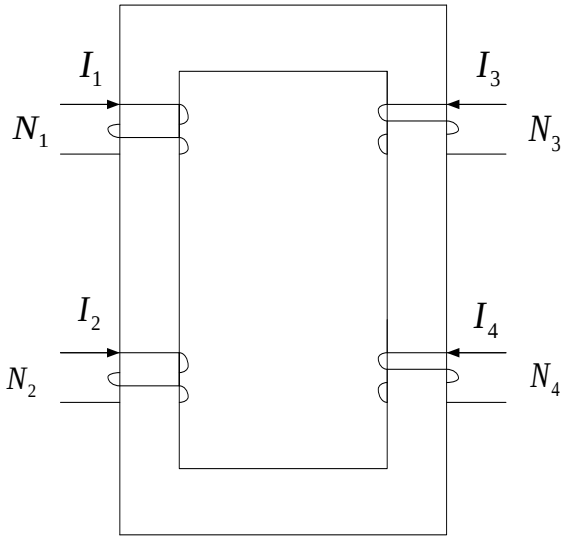

Fig. 5.7 Four-port magnetically coupled circuit

same time. Moreover, the compact high frequency transformer can isolate the source and load side in order to protect the expensive renewable source such as fuel cell appliance.

5.5.1 Modeling of the Four Winding Transformer System

Magnetically coupled electric circuits are crucial to the operation and modeling of multiport transformer system. The magnetic coupled circuit of four winding transformer system is shown in Fig. 5.7. Derivation of the equations for four-port transformer-fuel cell with battery power management system is laid out.

In general, the flux generated by each coil can be expressed into two parts: a leakage component and a magnetizing component with the positive direction based on right-hand rule.

The flux linking each coil can be expressed as below:

$$\phi_1 = \phi_{l1} + \phi_{m1} + \phi_{m2} + \phi_{m3} + \phi_{m4} \tag{5.87}$$

$$\phi_2 = \phi_{l2} + \phi_{m2} + \phi_{m1} + \phi_{m3} + \phi_{m4} \tag{5.88}$$

$$\phi_3 = \phi_{l3} + \phi_{m3} + \phi_{m1} + \phi_{m2} + \phi_{m4} \tag{5.89}$$

$$\phi_4 = \phi_{l4} + \phi_{m4} + \phi_{m1} + \phi_{m2} + \phi_{m3} \tag{5.90}$$

The general voltage equation is

$$V = rI + \frac{d\lambda}{dt} \tag{5.91}$$

Hence the voltage equation of each winding is expressed as

$$V_1 = r_1 I_1 + \frac{d\lambda_1}{dt} \qquad \lambda_1 = N_1 \phi_1 \tag{5.92}$$

$$V_2 = r_2 I_2 + \frac{d\lambda_2}{dt} \qquad \lambda_2 = N_2 \phi_2 \tag{5.93}$$

$$V_3 = r_3 I_3 + \frac{d\lambda_3}{dt} \qquad \lambda_3 = N_3 \phi_3 \tag{5.94}$$

$$V_4 = r_4 I_4 + \frac{d\lambda_4}{dt} \qquad \lambda_4 = N_4 \phi_4 \tag{5.95}$$

If saturation is neglected, the system is linear and fluxes can be determined:

$$\phi_{l1} = \frac{N_1 I_1}{R_{l1}} \qquad \phi_{m1} = \frac{N_1 I_1}{R_m} \tag{5.96}$$

$$\phi_{l2} = \frac{N_2 I_2}{R_{l2}} \qquad \phi_{m2} = \frac{N_2 I_2}{R_m} \tag{5.97}$$

$$\phi_{l3} = \frac{N_3 I_3}{R_{l3}} \qquad \phi_{m3} = \frac{N_3 I_3}{R_m} \tag{5.98}$$

$$\phi_{l4} = \frac{N_4 I_4}{R_{l4}} \qquad \phi_{m4} = \frac{N_4 I_4}{R_m} \tag{5.99}$$

where R_{l1}, R_{l2}, R_{l3} and R_{l4} are the reluctances of the leakage paths and R_m is the reluctance of the path of magnetizing flux.

Substituting (5.96) – (5.99) into (5.92) – (5.95),

$$\phi_1 = \frac{N_1 I_1}{R_{l1}} + \frac{N_1 I_1}{R_m} + \frac{N_2 I_2}{R_m} + \frac{N_3 I_3}{R_m} + \frac{N_4 I_4}{R_m} \tag{5.100}$$

$$\phi_2 = \frac{N_2 I_2}{R_{l2}} + \frac{N_2 I_2}{R_m} + \frac{N_1 I_1}{R_m} + \frac{N_3 I_3}{R_m} + \frac{N_4 I_4}{R_m} \tag{5.101}$$

$$\phi_3 = \frac{N_3 I_3}{R_{l3}} + \frac{N_3 I_3}{R_m} + \frac{N_1 I_1}{R_m} + \frac{N_2 I_2}{R_m} + \frac{N_4 I_4}{R_m} \tag{5.102}$$

$$\phi_4 = \frac{N_4 I_4}{R_{l4}} + \frac{N_4 I_4}{R_m} + \frac{N_1 I_1}{R_m} + \frac{N_2 I_2}{R_m} + \frac{N_3 I_3}{R_m} \tag{5.103}$$

Substituting (5.100) – (5.102) into (5.92)–(5.95),

$$\lambda_1 = \frac{N_1^{\,2} I_1}{R_{l1}} + \frac{N_1^{\,2} I_1}{R_m} + \frac{N_1 N_2 I_2}{R_m} + \frac{N_1 N_3 I_3}{R_m} + \frac{N_1 N_4 I_4}{R_m} \tag{5.104}$$

$$\lambda_2 = \frac{N_2^{\,2} I_2}{R_{l2}} + \frac{N_2^{\,2} I_2}{R_m} + \frac{N_2 N_1 I_1}{R_m} + \frac{N_2 N_3 I_3}{R_m} + \frac{N_2 N_4 I_4}{R_m} \tag{5.105}$$

$$\lambda_3 = \frac{N_3^{\,2} I_3}{R_{l3}} + \frac{N_3^{\,2} I_3}{R_m} + \frac{N_3 N_1 I_1}{R_m} + \frac{N_3 N_2 I_2}{R_m} + \frac{N_3 N_4 I_4}{R_m} \tag{5.106}$$

$$\lambda_4 = \frac{N_4^{\,2} I_4}{R_{l4}} + \frac{N_4^{\,2} I_4}{R_m} + \frac{N_4 N_1 I_1}{R_m} + \frac{N_4 N_2 I_2}{R_m} + \frac{N_4 N_3 I_3}{R_m} \tag{5.107}$$

Hence, define self inductances as

$$L_{11} = \frac{N_1^{\,2}}{R_{l1}} + \frac{N_1^{\,2}}{R_m} = L_{l1} + L_{m1}, L_{22} = \frac{N_2^{\,2}}{R_{l2}} + \frac{N_2^{\,2}}{R_m} = L_{l2} + L_{m2}, L_{33} = \frac{N_3^{\,2}}{R_{l3}} + \frac{N_3^{\,2}}{R_m} = L_{l3} + L_{m3}, L_{44} = \frac{N_4^{\,2}}{R_{l4}} + \frac{N_4^{\,2}}{R_m} = L_{l4} + L_{m4} \tag{5.108}$$

Mutual inductances come from

$$\frac{1}{R_m} = \frac{L_{m1}}{N_1^{\,2}} = \frac{L_{m2}}{N_2^{\,2}} = \frac{L_{m3}}{N_3^{\,2}} = \frac{L_{m4}}{N_4^{\,2}} \tag{5.109}$$

$$L_{12} = L_{21} = \frac{N_1 N_2}{R_m}, L_{13} = L_{31} = \frac{N_1 N_3}{R_m}, L_{14} = L_{41} = \frac{N_1 N_4}{R_m}, L_{23} = L_{32} = \frac{N_2 N_3}{R_m}, L_{34} = L_{43} = \frac{N_3 N_4}{R_m} \tag{5.110}$$

The flux linkages can be expressed in matrix:

$$\begin{bmatrix}\lambda_1\\ \lambda_2\\ \lambda_3\\ \lambda_4\end{bmatrix}=\begin{bmatrix}L_{11} & L_{12} & L_{13} & L_{14}\\ L_{21} & L_{22} & L_{23} & L_{24}\\ L_{31} & L_{32} & L_{33} & L_{34}\\ L_{41} & L_{42} & L_{43} & L_{44}\end{bmatrix}\begin{bmatrix}I_1\\ I_2\\ I_3\\ I_4\end{bmatrix} \tag{5.111}$$

Refer all the other 2, 3, 4 Coils to 1 side and use the same mutual inductance L_{m1}

$$\lambda_1 = L_{l1}I_1 + L_{m1}[I_1 + \frac{N_2}{N_1}I_2 + \frac{N_3}{N_1}I_3 + \frac{N_4}{N_1}I_4] \tag{5.112}$$

$$\lambda_2 = L_{l2}I_2 + L_{m2}[I_2 + \frac{N_1}{N_2}I_1 + \frac{N_3}{N_2}I_3 + \frac{N_4}{N_2}I_4] \tag{5.113}$$

$$\lambda_3 = L_{l3}I_3 + L_{m3}[I_3 + \frac{N_1}{N_3}I_1 + \frac{N_2}{N_3}I_2 + \frac{N_4}{N_3}I_4] \tag{5.114}$$

$$\lambda_4 = L_{l4}I_4 + L_{m4}[I_4 + \frac{N_1}{N_4}I_1 + \frac{N_2}{N_4}I_2 + \frac{N_3}{N_4}I_3] \tag{5.115}$$

$$I_2' = \frac{N_2}{N_1}I_2, \quad I_3' = \frac{N_3}{N_1}I_3, \quad I_4' = \frac{N_4}{N_1}I_4 \tag{5.116}$$

$$L_{m2} = \frac{N_2^{\,2}}{N_1^{\,2}}L_{m1}, L_{m3} = \frac{N_3^{\,2}}{N_1^{\,2}}L_{m1}, L_{m4} = \frac{N_4^{\,2}}{N_1^{\,2}}L_{m1} \tag{5.117}$$

Substitute (5.112) – (5.115) using (5.116) and (5.117):

$$\lambda_1 = L_{l1}I_1 + L_{m1}[I_1 + I_2' + I_3' + I_4'] \tag{5.118}$$

$$\lambda_2' = L_{l2}'I_2' + L_{m1}[I_1 + I_2' + I_3' + I_4'] \tag{5.119}$$

$$\lambda_3' = L_{l3}'I_3' + L_{m1}[I_1 + I_2' + I_3' + I_4'] \tag{5.120}$$

$$\lambda_4' = L_{l4}'I_4' + L_{m1}[I_1 + I_2' + I_3' + I_4'] \tag{5.121}$$

where

$$\lambda_2' = \frac{N_1}{N_2}\lambda_2, \ \lambda_3' = \frac{N_1}{N_3}\lambda_3, \ \lambda_4' = \frac{N_1}{N_4}\lambda_4 \tag{5.122}$$

$$L_{l2}' = L_{l2}(\frac{N_1}{N_2})^2, L_{l3}' = L_{l3}(\frac{N_1}{N_3})^2, L_{l4}' = L_{l4}(\frac{N_1}{N_4})^2 \tag{5.123}$$

Hence the equations of four winding transformer system can be expressed as below:

$$V_1 = r_1 I_1 + \frac{d\lambda_1}{dt} \tag{5.124}$$

$$V_2' = r_2' I_2' + \frac{d\lambda_2'}{dt} \tag{5.125}$$

$$V_3' = r_3' I_3' + \frac{d\lambda_3'}{dt} \tag{5.126}$$

$$V_4' = r_4' I_4' + \frac{d\lambda_4'}{dt} \tag{5.127}$$

where

$$V_2' = \frac{N_1}{N_2} V_2,\ V_3' = \frac{N_1}{N_3} V_3,\ V_4' = \frac{N_1}{N_4} V_4 \tag{5.128}$$

$$r_2' = (\frac{N_1}{N_2})^2 r_2, r_3' = (\frac{N_1}{N_3})^2 r_3, r_4' = (\frac{N_1}{N_4})^2 r_4 \tag{5.129}$$

5.5.2 Simulation Model of the Four-Port Bidirectional DAB System

The equivalent circuit of four-port DAB system is shown in Fig. 5.8. Rearrange the voltage Equations (5.118) – (5.123) derived from the former section. The dynamic equations of the system can be expressed as follows:

$$(L_{l1} + L_m) pi_1 + L_m (pi_2' + pi_3' + pi_4') + r_1 i_1 = v_1 \tag{5.130}$$

$$(L_{l2}' + L_m) pi_2' + L_m (pi_1 + pi_3' + pi_4') + r_2 i_2' = v_2' \tag{5.131}$$

$$(L_{l3}' + L_m) pi_3' + L_m (pi_1 + pi_2' + pi_4') + r_3 i_3' = v_3' \tag{5.132}$$

$$(L_{l4}' + L_m) pi_4' + L_m (pi_1 + pi_2' + pi_3') + r_4 i_4' = v_4' \tag{5.133}$$

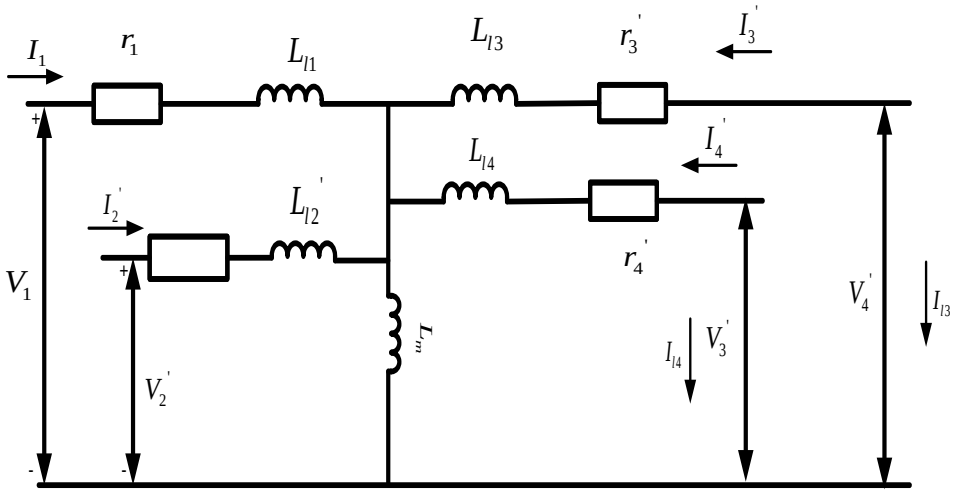

Fig. 5.8 Equivalent circuit with Coil 1 as the reference coil

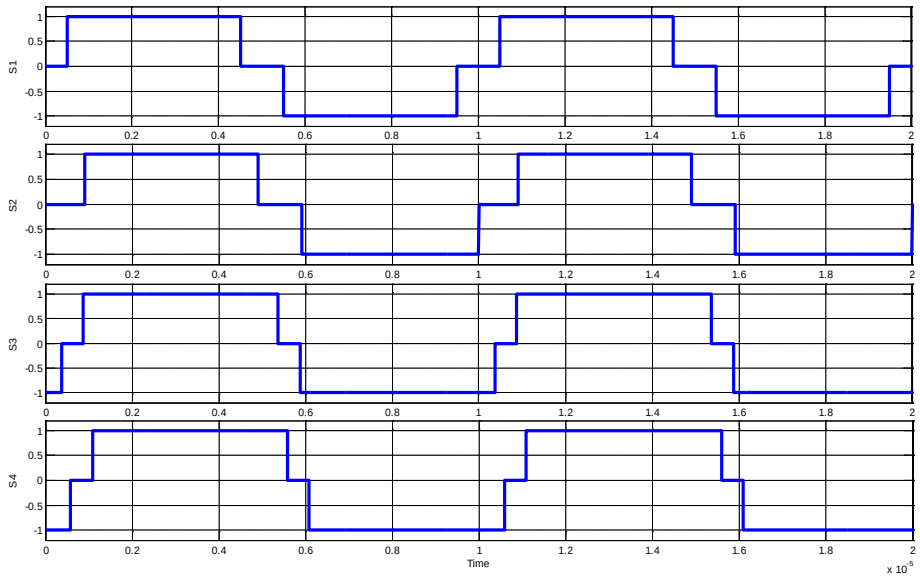

Fig. 5.9 Description of phase shift and duty variation of switching functions

For increasing the degrees of freedom, both duty ratio and phase displacement can be regulated in switching function. The rectangular waveform with duty variation and phase shift control is shown in Fig. 5.9.

The general ac output voltage can be expressed as follows:

$$V = V_{dc} \cdot (S_{ap} - S_{bp}) \tag{5.134}$$

Define

$$S_i = S_{api} - S_{bpi} \tag{5.135}$$

The input voltage can be derived by

$$v_1 = V_{dc1} * S_1 \tag{5.136}$$

$$v_2' = V_{dc2} * S_2 \tag{5.137}$$

The general capacitor and load model for Ports 3 and 4 is represented by the following current equation:

$$C_3 p V_{dcL3} = -i_3' * S_3 - \frac{V_{dcL3}}{R_3} \tag{5.138}$$

$$C_4 p V_{dcL3} = -i_3' * S_3 - \frac{V_{dcL3}}{R_3} \tag{5.139}$$

where i_1, i_2', i_3' and i_4' are the currents of each port. r_1, r_2, r_3 and r_4 are transformer resistances L_1, L_2', L_3' and L_4' are transformer leakage inductances. L_m is transformer mutual inductance, C is output capacitance, R_1 and R_2 is the output resistive load. V_1, V_2', V_3', and V_4' are ac voltages of each port going through the single-phase converter. V_{dcs1}, V_{dcs2}, $V_{dcl1,}$ and V_{dcl2} are the dc voltages going into the single-phase converter. S_1, S_2, $S_{3,}$ and S_4 are the switching functions for primary and secondary and third side converters. The parameters of four winding high frequency transformer are given in Table 5.3.

The study case is chosen as a two load system supplied with two sources. The load side capacitors' values are C_3=4700μF and C_4=6000μF. The resistive loads are

R_3=5Ω and R_4=10Ω. In this simulation case, the duty ratios and phase angles of each port are listed in Table 5.4.

The simulation results are as shown in Fig. 5.10, Fig. 5.11 and Fig. 5.12.

The output Port 3 and Port 4 dc voltages V_{dc3} and V_{dc4} are expressed as follows:

Table 5.3 Parameters for the four winding transformer

	Winding 1	Winding 2	Winding 3	Winding 4
Resistance	0.03 Ω	0.005Ω	0.002Ω	0.005Ω
Leakage inductance	210μH	4950nH	550nH	4500nH
Mutual inductance	1mH	1mH	1mH	1mH
Turn ratio	1	3/20	1/20	3/20

Table 5.4 Parameters of control variables for four DAB converter system

Control parameters	Port 1	Port 2	Port 3	Port 4
Duty ratio (Di)	D_1=0.8	D_2=0.8	D_3=0.8	D_3=0.8
Phase angle (Φ_i)	Φ_1=0°	Φ_2=15°(lagging)	Φ_3=30°(lagging)	Φ_4=45°(lagging)

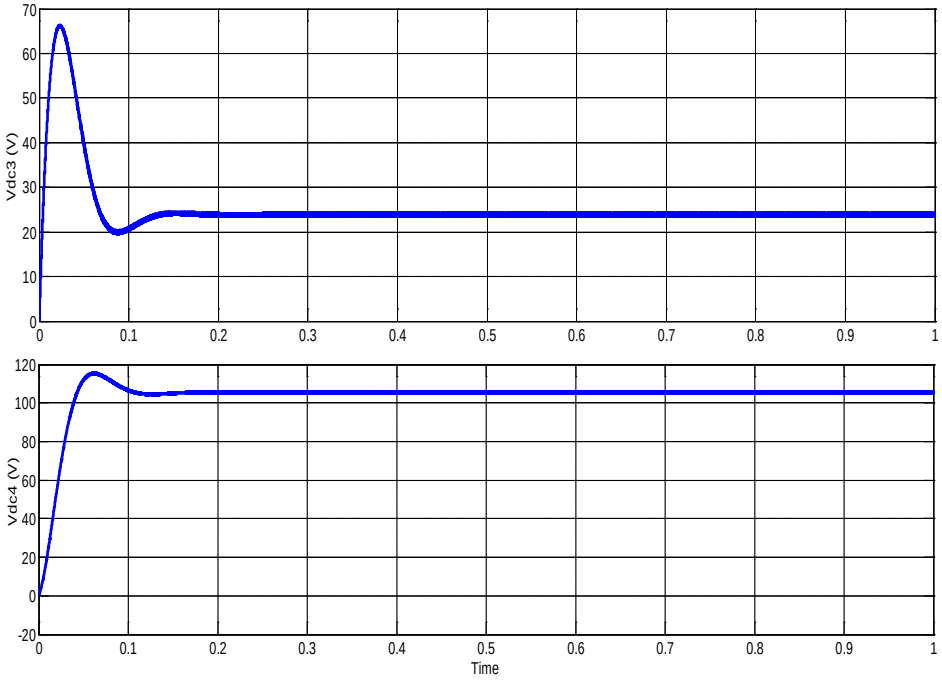

Fig. 5.10 DC output voltages of Port 3 and Port 4

The ac voltages between phase leg points for V_1, V_2', V_3' and V_4' are shown:

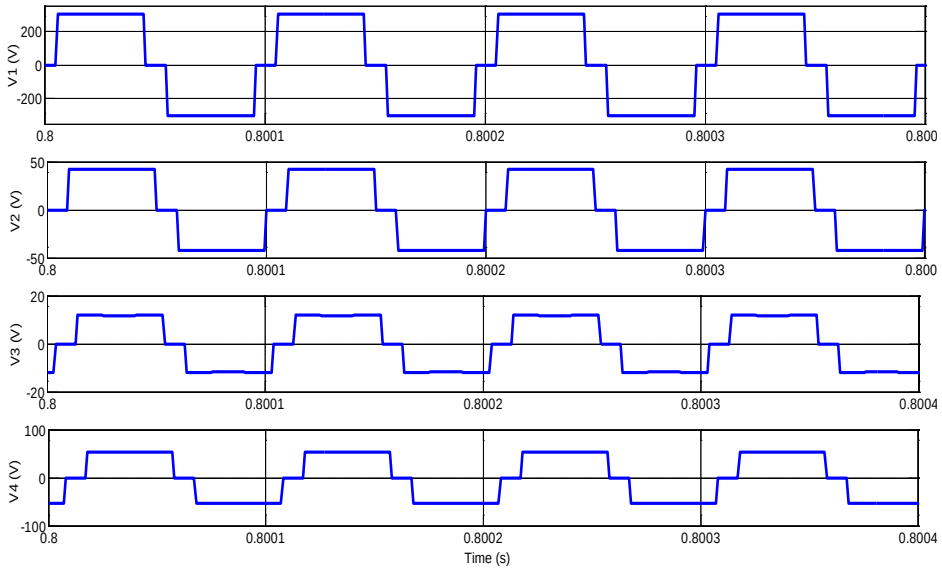

Fig. 5.11 Output voltages for four single-phase converters

The ac port currents going through transformer i_1, i_2', i_3' and i_4' are shown:

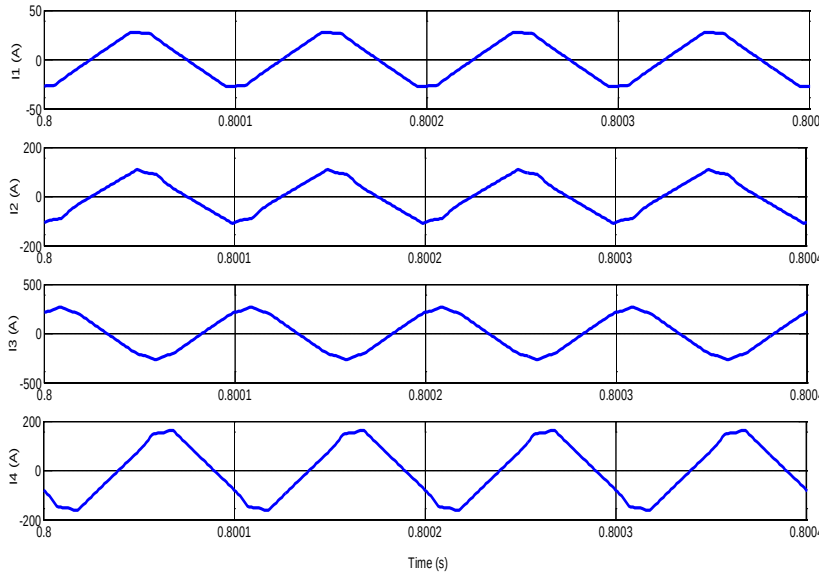

Fig. 5.12 Output currents of four single-phase converters

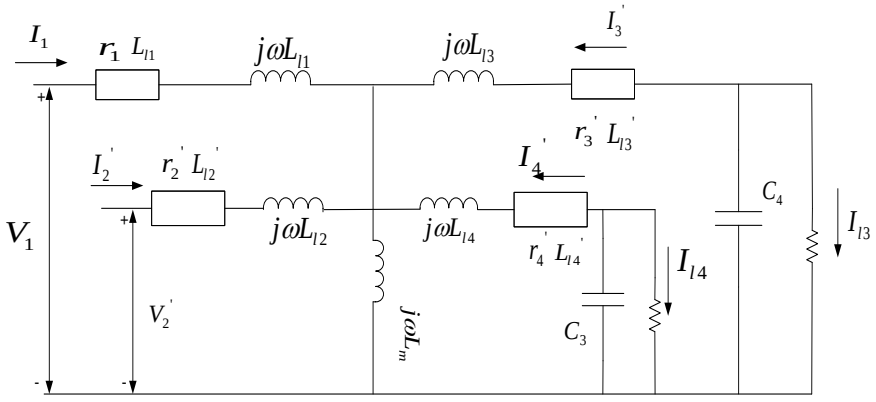

Fig. 5.13 Equivalent circuit of four-port DAB system based on steady state

5.5.3 Steady State Analysis of the Four-Port Bidirectional DAB System Using HBT

Using HBT method introduced in Chapter 4, the steady state results of the four-port DAB system can be analyzed. The state variables and the switching functions are assumed to have average and ripple components. The switching function of single-phase

converter is rectangular pulse with variable duty ratio and variable phase shift angle. The equivalent circuit can be drawn in Fig. 5.13.

For the four-port transformer side:

$$(L_1+L_m)pI_1+L_m(pI_2^{'}+pI_3^{'}+pI_4^{'})+(r_1+j\omega(L_1+L_m))I_1+j\omega L_m(I_2^{'}+I_3^{'}+I_4^{'})=V_1 \quad (5.140)$$

$$(L_2^{'}+L_m)pI_2^{'}+L_m(pI_1^{'}+pI_3^{'}+pI_4^{'})+(r_2+j\omega(L_2^{'}+L_m))I_2^{'}+j\omega L_m(I_1+I_3^{'}+I_4^{'})=V_2^{'} \quad (5.141)$$

$$(L_3^{'}+L_m)pI_3^{'}+L_m(pI_1^{'}+pI_2^{'}+pI_4^{'})+(r_3+j\omega(L_3^{'}+L_m))I_3^{'}+j\omega L_m(I_1+I_2^{'}+I_4^{'})=V_3^{'} \quad (5.142)$$

$$(L_4^{'}+L_m)pI_4^{'}+L_m(pI_1^{'}+pI_2^{'}+pI_3^{'})+(r_4+j\omega(L_4^{'}+L_m))I_4^{'}+j\omega L_m(I_1+I_2^{'}+I_3^{'})=V_4^{'} \quad (5.143)$$

Based on the KCL rule, the Capacitor 3's voltage can be expressed as

$$\begin{aligned} C_3p(V_{d30}+\mathrm{Re}[V_{d31}e^{j2\theta}]) &= -\mathrm{Re}[I_3^{'}e^{j\theta}]*\mathrm{Re}[S_3e^{j\theta}]-\frac{V_{d30}+\mathrm{Re}[V_{d31}e^{j2\theta}]}{R_3} \\ &= -\frac{1}{2}(\mathrm{Re}[I_3^{'}S_3^{*}]+\mathrm{Re}[I_3^{'}S_3e^{j2\theta}])-\frac{V_{d30}+\mathrm{Re}[V_{d31}e^{j2\theta}]}{R_3} \end{aligned} \quad (5.144)$$

$$\Rightarrow \begin{cases} 2C_3pV_{d30} = -\mathrm{Re}[I_3^{'}S_3^{*}]-\dfrac{V_{d30}}{R_3} \\ 2C_3pV_{d31}+4C_3j\omega V_{d31} = -I_3^{'}S_3-\dfrac{V_{d31}}{R_3} \end{cases} \quad (5.145)$$

Based on the KCL rule, the Capacitor 4's voltage can be expressed as

$$\begin{aligned} C_4p(V_{d40}+\mathrm{Re}[V_{d41}e^{j2\theta}]) &= -\mathrm{Re}[I_4^{'}e^{j\theta}]*\mathrm{Re}[S_4e^{j\theta}]-\frac{V_{d40}+\mathrm{Re}[V_{d41}e^{j2\theta}]}{R_4} \\ &= -\frac{1}{2}(\mathrm{Re}[I_4^{'}S_4^{*}]+\mathrm{Re}[I_4^{'}S_4e^{j2\theta}])-\frac{V_{d40}+\mathrm{Re}[V_{d41}e^{j2\theta}]}{R_4} \end{aligned} \quad (5.146)$$

$$\Rightarrow \begin{cases} 2C_4pV_{d40} = -\mathrm{Re}[I_4^{'}S_4^{*}]-\dfrac{V_{d40}}{R_4} \\ 2C_4pV_{d41}+4C_4j\omega V_{d41} = -I_4^{'}S_4-\dfrac{V_{d41}}{R_4} \end{cases} \quad (5.147)$$

When the system comes into steady state, the derivatives of the state variables are equal to zero. Also the average components of I_{10}, I_{20}, I_{30}, I_{40}, S_{10}, S_{20}, S_{30}, S_{40} are equal to 0. The peak value of fundamental components from ripple equations can be used to study the characteristic of the system. Hence, the peak fundamental component equations are used as below:

All pI_1, pI_2, pI_3, pI_4, pV_{dc30}, pV_{dc31}, pV_{dc40}, pV_{dc41} are all equal to 0

$$(r_1 + j\omega L_1)I_1 + j\omega L_m(I_1 + I_2^{'} + I_3^{'} + I_4^{'}) = V_1 \tag{5.148}$$

$$(r_2 + j\omega L_2^{'})I_2^{'} + j\omega L_m(I_1 + I_2^{'} + I_3^{'} + I_4^{'}) = V_2^{'} \tag{5.149}$$

$$(r_3 + j\omega L_3^{'})I_3^{'} + j\omega L_m(I_1 + I_2^{'} + I_3^{'} + I_4^{'}) = V_3^{'} \tag{5.150}$$

$$(r_4 + j\omega L_4^{'})I_4^{'} + j\omega L_m(I_1 + I_2^{'} + I_3^{'} + I_4^{'}) = V_4^{'} \tag{5.151}$$

For Capacitor 3:

$$V_{d30} = -R_3 * \mathrm{Re}[I_3^{'} S_3^{*}] \tag{5.152}$$

For Capacitor 4:

$$V_{d40} = -R_4 * \mathrm{Re}[I_4^{'} S_4^{*}] \tag{5.153}$$

Substitute V_3', V_4' in terms of capacitor voltage

$$V_3^{'} = (V_{d30} + \mathrm{Re}[V_{d31} e^{j2\theta}]) * \mathrm{Re}[S_3 e^{j\theta}] \tag{5.154}$$

$$V_4^{'} = (V_{d40} + \mathrm{Re}[V_{d41} e^{j2\theta}]) * \mathrm{Re}[S_4 e^{j\theta}] \tag{5.155}$$

Also the source voltage V_1', V_2' are expressed as follows:

$$V_1 = V_{dc1}\,\mathrm{Re}[S_1 e^{j\theta}] \tag{5.156}$$

$$V_2 = V_{dc2}\,\mathrm{Re}[S_2 e^{j\theta}] \tag{5.157}$$

After bringing all the voltage into steady state equations, the following equations come about:

$$(r_1 + j\omega L_1)I_1 + j\omega L_m(I_1 + I_2^{'} + I_3^{'} + I_4^{'}) = V_{dc1} \cdot S_1 \tag{5.158}$$

$$(r_2 + j\omega L_2^{'})I_2^{'} + j\omega L_m(I_1 + I_2^{'} + I_3^{'} + I_4^{'}) = V_{dc2} \cdot S_2 \tag{5.159}$$

$$(r_3 + j\omega L_3^{'})I_3^{'} + j\omega L_m(I_1 + I_2^{'} + I_3^{'} + I_4^{'}) = -R_3 \cdot \mathrm{Re}[I_3^{'}S_3^{*}] \cdot S_3 \tag{5.160}$$

$$(r_4 + j\omega L_4^{'})I_4^{'} + j\omega L_m(I_1 + I_2^{'} + I_3^{'} + I_4^{'}) = -R_4 * \mathrm{Re}[I_4^{'}S_4^{*}] \cdot S_4 \tag{5.161}$$

The steady state variables matrix of four-port DAB system can be derived:

$$\begin{bmatrix} r_1 + j\omega(L_1 + L_m) & j\omega L_m & j\omega L_m & j\omega L_m \\ j\omega L_m & r_2 + j\omega(L_2 + L_m) & j\omega L_m & j\omega L_m \\ j\omega L_m & j\omega L_m & r_3 + j\omega(L_3 + L_m) & j\omega L_m \\ j\omega L_m & j\omega L_m & j\omega L_m & r_4 + j\omega(L_4 + L_m) \end{bmatrix} \begin{bmatrix} I_1 \\ I_2^{'} \\ I_3^{'} \\ I_4^{'} \end{bmatrix} = \begin{bmatrix} V_{dc1} \cdot S_1 \\ V_{dc2} \cdot S_2 \\ -R_3 \cdot \mathrm{Re}[I_3^{'}S_3^{*}] \cdot S_3 \\ -R_4 \cdot \mathrm{Re}[I_4^{'}S_4^{*}] \cdot S_4 \end{bmatrix} \tag{5.162}$$

Because out ac voltage V_3'contains the real value of the multiplication by two complex components, it is feasible to separate into q and d axis variables which can make equations of state variables in the linear way.

Set

$$I_i = I_{qi} + jI_{di} \tag{5.163}$$

$$S_i = S_{qi} + jS_{di} \tag{5.164}$$

Also as the Fourier analysis of rectangular waveform is derived and shown in (4.37) and (4.38) in Chapter 4, the switching functions of the fundamental component can be represented as:

$$S_{qi} = \frac{4}{\pi}\sin(\frac{D_i}{2}\pi)\sin(\Phi_i) \tag{5.165}$$

$$S_{di} = \frac{4}{\pi}\sin(\frac{D_i}{2}\pi)\cos(\Phi_i) \tag{5.166}$$

where D is the duty ratio and Φ is phase shift angle.

Hence the Equations (5.158) –(5.161) can be rearranged in terms of *q* and *d* components:

$$r_1 + j\omega L_1(I_{q1} + jI_{d1}) + j\omega L_m[I_{q1} + I_{q2} + I_{q3} + I_{q4} + j(I_{d1} + I_{d2} + I_{d3} + I_{d4})] = V_{dc1}(S_{q1} + jS_{d1}) \tag{5.167}$$

$$r_2 + j\omega L_2(I_{q2} + jI_{d2}) + j\omega L_m[I_{q1} + I_{q2} + I_{q3} + I_{q4} + j(I_{d1} + I_{d2} + I_{d3} + I_{d4})] = V_{dc2}(S_{q2} + jS_{d2}) \tag{5.168}$$

$$\begin{aligned} &r_3 + j\omega L_3(I_{q3} + jI_{d3}) + j\omega L_m[I_{q1} + I_{q2} + I_{q3} + I_{q4} + j(I_{d1} + I_{d2} + I_{d3} + I_{d4})] \\ &= -R_3 * \mathrm{Re}[(I_{q3} + jI_{d3}) * (S_{q3} - jS_{d3})^*] * (S_{q3} + jS_{d3}) \end{aligned} \tag{5.169}$$

$$\begin{aligned} &r_4 + j\omega L_4(I_{q4} + jI_{d4}) + j\omega L_m[I_{q1} + I_{q2} + I_{q3} + I_{q4} + j(I_{d1} + I_{d2} + I_{d3} + I_{d4})] \\ &= -R_4 * \mathrm{Re}[(I_{q4} + jI_{d4}) * (S_{q4} - jS_{d4})^*] * (S_{q4} + jS_{d4}) \end{aligned} \tag{5.170}$$

Separate the equations above into real and imaginary part.

The steady state variables of separate q and d matrix can be gotten as follows:

$$\begin{bmatrix} r_1 & -\omega(L_1+L_m) & 0 & -\omega L_m & 0 & -\omega L_m & 0 & -\omega L_m \\ \omega(L_1+L_m) & r_1 & \omega L_m & 0 & \omega L_m & 0 & \omega L_m & 0 \\ 0 & -\omega L_m & r_2 & -\omega(L_2+L_m) & 0 & -\omega L_m & 0 & -\omega L_m \\ \omega L_m & 0 & \omega(L_2+L_m) & r_2 & \omega L_m & 0 & \omega L_m & 0 \\ 0 & -\omega L_m & 0 & -\omega L_m & r_3+R_3 S_{q3}^{\ 2} & -\omega(L_3+L_m)+R_3 S_{q3} S_{d3} & 0 & -\omega L_m \\ \omega L_m & 0 & \omega L_m & 0 & \omega(L_3+L_m)+R_3 S_{q3} S_{d3} & r_3+R_3 S_{d3}^{\ 2} & \omega L_m & 0 \\ 0 & -\omega L_m & 0 & -\omega L_m & 0 & -\omega L_m & r_4+R_4 S_{q4}^{\ 2} & -\omega(L_4+L_m)+R_4 S_{q4} S_{d4} \\ \omega L_m & 0 & \omega L_m & 0 & \omega L_m & 0 & \omega(L_4+L_m)+R_4 S_{q4} S_{d4} & r_4+R_4 S_{d4}^{\ 2} \end{bmatrix} \bullet \begin{bmatrix} I_{q1} \\ I_{d1} \\ I_{q2} \\ I_{d2} \\ I_{q3} \\ I_{d3} \\ I_{q4} \\ I_{d4} \end{bmatrix} = \begin{bmatrix} V_{dc1} S_{q1} \\ V_{dc1} S_{d1} \\ V_{dc2} S_{q2} \\ V_{dc2} S_{d2} \\ 0 \\ 0 \\ 0 \\ 0 \end{bmatrix} \tag{5.171}$$

Using the steady state matrix above, it is applied to compute the dc output load voltage and output power by varying the phase shift angle of load Port 4 under several fixed phase angle of load Port 3. The current, dc voltage and power can be calculated. The parameters are given: Port1: V_{dc1}=300V, Φ_1=0°, D_1=0.8. Port 2: V_{dc2}=42V, D_2=0.8,

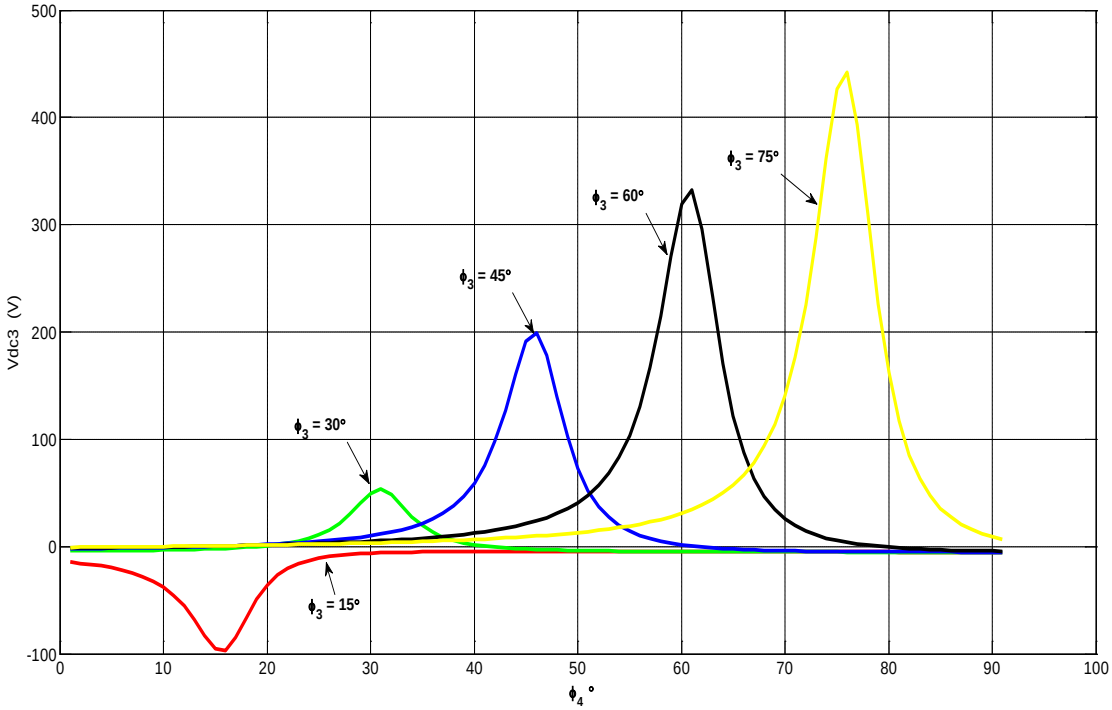

Fig. 5.14 DC voltage V_{dc3} of Port 3 by varying Φ_4 from 0° to 90° when fixed Φ_3=45°

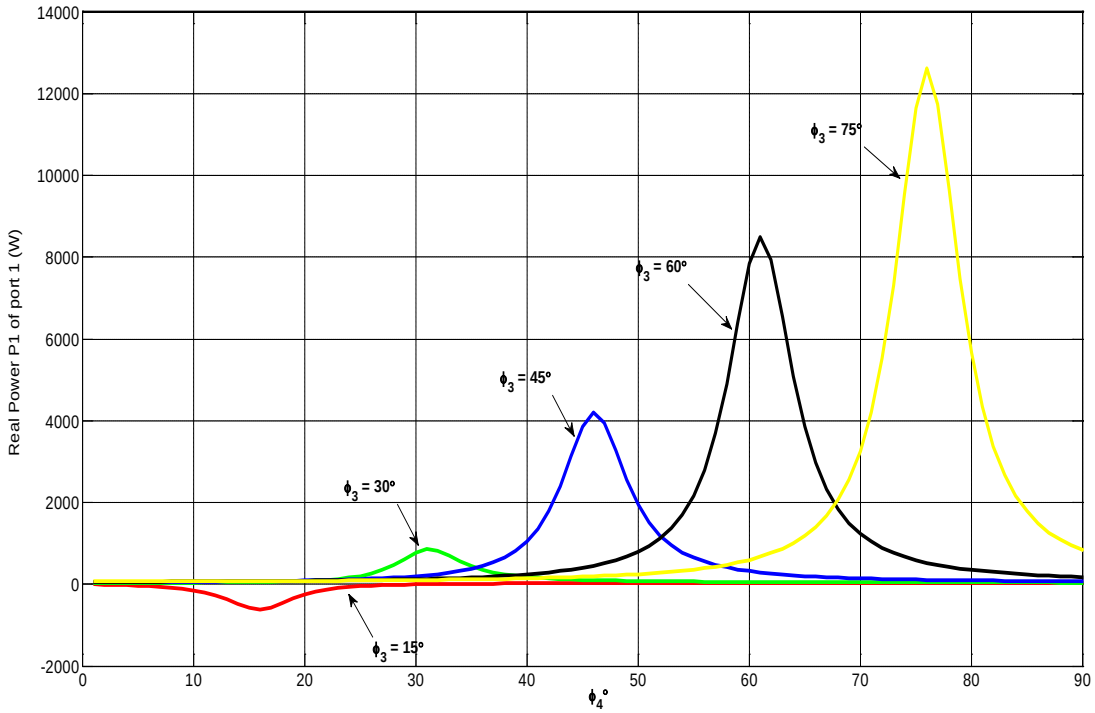

Fig. 5.15 Real Power P_1 of Port 1 by varying Φ_4 from 0° to 90° when fixed Φ_3=45°

Φ_2=30° (lagging). Port 3: R_3=5Ω, D_3=0.8, Φ_3=15°, 30°, 45°, 60°, 75° (lagging). Port 4: R_4=10Ω, D_4=0.8, vary Φ_4 from 0° to 90°.

By varying the phase angle when fixed duty ratio of each converter, it is possible to solve the matrix above to get the steady state solutions as shown below. The steady state analysis based on the output load voltage V_{dc3} and V_{dc4}, real input and output power P_1, P_2 are laid out. The influence of phase shift angle $\Phi_4$dc on output voltage V_{dc3} and the input power are shown from Fig. 5.14 to Fig. 5.15.

From the these figures, it can be observed that the value of real power flow becomes larger as phase shift is increasing to some point. After the specific angle, the real power input will be decreased. It clearly shows that the system can draw more reactive power when phase shift angle is leading. To minimize the reactive power in the system, it is better to set a constraint region for phase shift angle which can get minimum loss. Therefore limiting the phase angle range, it can increase the overall system efficiency.

5.5.4 Minimization of Reactive Power for Four-Port DAB Converter System

In the former sections, the optimal design of three-port bidirectional DAB converter system was carried out to acquire the operating control conditions to achieve the minimum reactive power flow among the three ports. The results are verified with simulation results. In this section, the problem of minimization of reactive power can be extended to be applied in four-port DAB converter system. Although the equations of

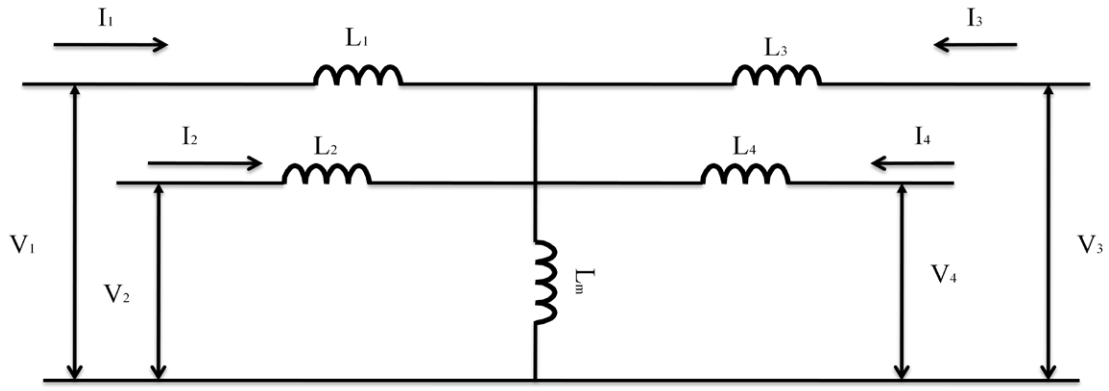

Fig. 5.16 Equivalent circuit of four-port bidirectional dc-dc converter

system are complex, the regulation of the minimal circulating current can still be carried out by using HBT and Lagrange method.

Usually the input voltages of power sources are main power supply desired to be operated as full duty ratio such as fuel cell system. Also, there is an auxiliary power storage source such as battery or supercapacitor. Two loads can be either fed at the same time or supplied separately based on the control command. Within this small scale renewable energy system, the power at each port can be controlled by the phase angle either leading or lagging compared with the reference angle and the duty cycles of each port voltage. The equivalent circuit of the four-port DAB system is shown in Fig. 5.16. Based on the equivalent circuit of four-port DAB system, the steady state equations using HBT can be derived as follows:

$$j\begin{bmatrix} \omega(L_1+L_m) & \omega L_m & \omega L_m & \omega L_m \\ \omega L_m & \omega(L_2+L_m) & \omega L_m & \omega L_m \\ \omega L_m & \omega L_m & \omega(L_3+L_m) & \omega L_m \\ \omega L_m & \omega L_m & \omega L_m & \omega(L_4+L_m) \end{bmatrix} \cdot \begin{bmatrix} I_1 \\ I_2 \\ I_3 \\ I_4 \end{bmatrix} = \begin{bmatrix} V_{dc1}S_1 \\ V_{dc2}S_2 \\ V_{dc3}S_3 \\ V_{dc4}S_4 \end{bmatrix} \tag{5.172}$$

where

$$A=\begin{bmatrix} \omega(L_1+L_m) & \omega L_m & \omega L_m & \omega L_m \\ \omega L_m & \omega(L_2+L_m) & \omega L_m & \omega L_m \\ \omega L_m & \omega L_m & \omega(L_3+L_m) & \omega L_m \\ \omega L_m & \omega L_m & \omega L_m & \omega(L_4+L_m) \end{bmatrix} \tag{5.173}$$

The inverse of the matrix can be expressed in symbolic way

$$A^{-1}=\begin{bmatrix} b_{11} & b_{12} & b_{13} & b_{14} \\ b_{21} & b_{22} & b_{23} & b_{24} \\ b_{31} & b_{32} & b_{33} & b_{34} \\ b_{41} & b_{42} & b_{43} & b_{44} \end{bmatrix}, if \ \det A \neq 0 \tag{5.174}$$

Then, the current at each port can be derived

$$\begin{bmatrix} I_1 \\ I_2 \\ I_3 \\ I_4 \end{bmatrix}=\frac{1}{j}A^{-1}\begin{bmatrix} V_{dc1}S_1 \\ V_{dc2}S_2 \\ V_{dc3}S_3 \\ V_{dc4}S_4 \end{bmatrix}=\frac{1}{j}\begin{bmatrix} b_{11} & b_{12} & b_{13} & b_{14} \\ b_{21} & b_{22} & b_{23} & b_{24} \\ b_{31} & b_{32} & b_{33} & b_{34} \\ b_{41} & b_{42} & b_{43} & b_{44} \end{bmatrix}\begin{bmatrix} V_{dc1}S_1 \\ V_{dc2}S_2 \\ V_{dc3}S_3 \\ V_{dc4}S_4 \end{bmatrix} \tag{5.175}$$

The general expression of port current I_i can be found as below:

$$I_i=-j[b_{i1}V_{dc1}S_1+b_{i2}V_{dc2}S_2+b_{i3}V_{dc3}S_3+b_{i4}V_{dc4}S_4] \tag{5.176}$$

Similarly, as is carried out before, it is possible to decompose the state variables into *q* and *d* components. It is assumed that $I_i = I_{qi}+I_{di}$. Hence,

$$I_{qi}=[b_{i1}V_{dc1}S_{d1}+b_{i2}V_{dc2}S_{d2}+b_{i3}V_{dc3}S_{d3}+b_{i4}V_{dc1}S_{d4}] \tag{5.177}$$

$$I_{di}=-[b_{i1}V_{dc1}S_{q1}+b_{i2}V_{dc2}S_{q2}+b_{i3}V_{dc3}S_{q3}+b_{i4}V_{dc4}S_{q4}] \tag{5.178}$$

In the study case, the voltage type energy source such as fuel cell is considered as the main power supply and desired to be operated as full duty ratio. Also the phase angle of the primary side voltage can be set as reference angle which the secondary and third port voltage angles can be either leading or lagging; therefore, the duty ratio and phase

angle of the major power supply Port 1 can be $D_1 = 1$ and $\Phi_1 = 0°$. Correspondingly, the switching function $S_{q1} = 0$ and $S_{d1} = 1.27$.

$$I_{qi} = 1.27 b_{i1} V_{dc1} + b_{i2} V_{dc2} S_{d2} + b_{i3} V_{dc3} S_{d3} + b_{i4} V_{dc4} S_{d4} \tag{5.179}$$

$$I_{di} = -[b_{i2} V_{dc2} S_{q2} + b_{i3} V_{dc3} S_{q3} + b_{i4} V_{dc4} S_{q4}] \tag{5.180}$$

where S_{q2}, S_{d2}, S_{q3}, S_{d3}, $S_{q4,}$ and S_{d4} are unknown.

In a practical system, the power flow of the load side can be regulated to the system's specifications. The objective is to manage the output power of each load port. Therefore the realpower P_3 can be calculated as follows:

$$P_3 = V_3 I_3^{*} = \mathrm{Re}[V_{dc3}(S_{q3} + jS_{d3})(I_{q3} - jI_{d3})] = V_{dc3}(S_{q3} I_{q3} + S_{d3} I_{d3}) \tag{5.181}$$

Substituting S_{q1} and S_{d1} into the equation above,

$$P_3 = V_{dc3} S_{q3}[1.27 b_{31} V_{dc1} + b_{32} V_{dc2} S_{d2} + b_{33} V_{dc3} S_{d3} + b_{34} V_{dc4} S_{d4}] - V_{dc3} S_{d3}[b_{32} V_{dc2} S_{q2} + b_{33} V_{dc3} S_{q3} + b_{34} V_{dc4} S_{q4}] \tag{5.182}$$

The real power P_4 can be calculated as follows:

$$P_4 = V_4 I_4^{*} = \mathrm{Re}[V_{dc4}(S_{q4} + jS_{d4})(I_{q4} - jI_{d4})] = V_{dc4}(S_{q4} I_{q4} + S_{d4} I_{d4}) \tag{5.183}$$

Similarly, substituting S_{q1} and S_{d1} into the equation above

$$P_4 = V_{dc4} S_{q4}[1.27 b_{41} V_{dc1} + b_{42} V_{dc2} S_{d2} + b_{43} V_{dc3} S_{d3} + b_{44} V_{dc4} S_{d4}] - V_{dc3} S_{d3}[b_{42} V_{dc2} S_{q2} + b_{43} V_{dc3} S_{q3} + b_{44} V_{dc4} S_{q4}] \tag{5.184}$$

Based on the KCL rule, the mutual inductance is equal to

$$I_m = I_1 + I_2 + I_3 + I_4 \tag{5.185}$$

If the summation of the currents I_1, I_2, I_3 and I_m, is minimized the objective function can be derived as

$$I_1^{\,2} + I_2^{\,2} + I_3^{\,2} + I_4^{\,2} + I_m^{\,2} = (I_1 + I_2)^2 + (I_3 + I_4)^2 + (I_1 + I_3)^2 + (I_2 + I_4)^2 + 2I_2 I_3 + 2I_1 I_4 \tag{5.186}$$

For this system, it is also formulated with some constraints imposed on the control variables. The Lagrange optimization of such problem has to be carried out within the limits of these constraints. Using Equations (5.59) – (5.61), the function of Lagrange can be defined. The control objective function of the minimization is shown as below. The reactive power minimization is formulated as

$$\begin{aligned}
&F = I_1^{\,2} + I_2^{\,2} + I_3^{\,2} + I_4^{\,2} + I_m^{\,2} = (I_1 + I_2)^2 + (I_3 + I_4)^2 + (I_1 + I_3)^2 + (I_2 + I_4)^2 + 2I_2I_3 + 2I_1I_4 \\
&= I_{q1}^{\,2} + I_{q2}^{\,2} + I_{q3}^{\,2} + I_{q4}^{\,2} + (I_{q1} + I_{q2} + I_{q3} + I_{q4})^2 + I_{d1}^{\,2} + I_{d2}^{\,2} + I_{d3}^{\,2} + I_{d4}^{\,2} + (I_{d1} + I_{d2} + I_{d3} + I_{d4})^2 \\
&= (I_{q1} + I_{q2})^2 + (I_{q3} + I_{q4})^2 + (I_{q1} + I_{q3})^2 + (I_{q2} + I_{q4})^2 + 2I_{q2}I_{q3} + 2I_{q1}I_{q4} \\
&+ (I_{d1} + I_{d2})^2 + (I_{d3} + I_{d4})^2 + (I_{d1} + I_{d3})^2 + (I_{d2} + I_{d4})^2 + 2I_{d2}I_{d3} + 2I_{d1}I_{d4}
\end{aligned} \tag{5.187}$$

Subject to equality constraints where are Equations (5.183) and (5.184). Also, the inequality constraints are the maximum magnitude of the switching functions as can be seen in (5.64) – (5.65). Therefore the description of Lagrange function is stated as

$$\begin{aligned}
&L = f + \lambda_3 P + \lambda_4 P_4 \\
&= \{(K_{11} + K_{21}) + (K_{12} + K_{22})S_{d2} + (K_{13} + K_{23})S_{d3} + (K_{14} + K_{24})S_{d4}\}^2 \\
&+ \{(K_{31} + K_{41}) + (K_{32} + K_{42})S_{d2} + (K_{33} + K_{43})S_{d3} + (K_{34} + K_{44})S_{d4}\}^2 \\
&+ \{(K_{11} + K_{31}) + (K_{12} + K_{32})S_{d2} + (K_{13} + K_{33})S_{d3} + (K_{14} + K_{34})S_{d4}\}^2 \\
&+ \{(K_{21} + K_{41}) + (K_{22} + K_{42})S_{d2} + (K_{23} + K_{43})S_{d3} + (K_{24} + K_{44})S_{d4}\}^2 \\
&+ 2[K_{21} + K_{22}S_{d2} + K_{23}S_{d3} + K_{24}S_{d4}][K_{31} + K_{32}S_{d2} + K_{33}S_{d3} + K_{34}S_{d4}] \\
&+ 2[K_{11} + K_{12}S_{d2} + K_{13}S_{d3} + K_{14}S_{d4}][K_{41} + K_{42}S_{d2} + K_{43}S_{d3} + K_{44}S_{d4}] \\
&+ \{(K_{12} + K_{22})S_{q2} + (K_{13} + K_{23})S_{q3} + (K_{14} + K_{24})S_{q4}\}^2 \\
&+ \{(K_{32} + K_{42})S_{q2} + (K_{33} + K_{43})S_{q3} + (K_{34} + K_{44})S_{q4}\}^2 \\
&+ \{(K_{12} + K_{32})S_{q2} + (K_{13} + K_{33})S_{q3} + (K_{14} + K_{34})S_{q4}\}^2 \\
&+ \{(K_{22} + K_{42})S_{q2} + (K_{23} + K_{43})S_{q3} + (K_{24} + K_{44})S_{q4}\}^2 \\
&+ 2[K_{22}S_{q2} + K_{23}S_{q3} + K_{24}S_{q4}][K_{32}S_{q2} + K_{33}S_{q3} + K_{34}S_{q4}] \\
&+ 2[K_{12}S_{q2} + K_{13}S_{q3} + K_{14}S_{q4}][K_{42}S_{q2} + K_{43}S_{q3} + K_{44}S_{q4}] \\
&+ \lambda_3\{V_{dc3}S_{q3}[K_{31} + K_{32}S_{d2} + K_{33}S_{d3} + K_{34}S_{d4}] - V_{dc3}S_{d3}[K_{32}S_{q2} + K_{33}S_{q3} + K_{34}S_{q4}] - P_3\} \\
&+ \lambda_4\{V_{dc4}S_{q4}[K_{41} + K_{42}S_{d2} + K_{43}S_{d3} + K_{44}S_{d4}] - V_{dc4}S_{d4}[K_{42}S_{q2} + K_{43}S_{q3} + K_{44}S_{q4}] - P_4\}
\end{aligned} \tag{5.188}$$

where K_{i1}, K_{i2}, K_{i3} and K_{i43} are defined by,

$$K_{i1} = 1.27 b_{i1} V_{dc1} K_{i2} = b_{i2} V_{dc2}, K_{i3} = b_{i3} V_{dc3}, K_{i4} = b_{i4} V_{dc4}, i = 1,2,3,4 \quad (5.189)$$

The optimization tool box in MATLAB is used here to solve the problem stated above. From the analysis above, the optimization problem is composed of six unknown variables. The duty ratios D_2, Φ_2, D_3, Φ_3, D_4 and Φ_4 are control variables to be solved to get the minimum summation of the currents circulating inside the transformer under the specification of the output power and switching functions limits. The parameters of four winding high frequency transformer are given in Table 5.5.

If the desired output power P_3 is 1000 W and the output power P_4 is 500 W. The results of control variables to get minimal reactive power are listed in Table 5.6.

Table 5.5 Parameters for the four winding transformer

	Winding 1	Winding 2	Winding 3	Winding 4
Turn ratio	1	3/20	3/20	1/20
Leakage inductance	21μH	0.495μH	0.495μH	0.055μH
Mutual inductance	1mH	1mH	1mH	1mH
Voltage	300V	42V	42V	12V
Operating frequency	100kHz	100kHz	100kHz	100kHz

Table 5.6 Results from GB technique

Operating conditions of minimizing the circulating current	
$S_{q2} = 0.005$, $S_{d2} = 1.27$	$D_2 = 1$, $\Phi_2 = 0^{\circ}$
$S_{q3} = 0.231$, $S_{d3} = 1.252$	$D_3 = 0.99$, $\Phi_3 = 10^{\circ}$
$S_{q4} = 0.163$, $S_{d4} = 1.263$	$D_4 = 1$, $\Phi_4 = 7^{\circ}$

CHAPTER 6

IMPLEMENTATION OF THE DAB CONVERTER SYSTEM

6.1 Introduction

In this chapter, the design of the proposed bidirectional dc-dc DAB converter system is presented and the core components design procedure detailed. The topology of the DAB converter system has been already introduced in the former sections. Several analytic methods have been used to study the steady state and dynamic performance of the system. The structure of the DAB converter system is composed of single-phase full bridge converters including the power stage design and drive circuit design. Also, high frequency transformer and extra inductors are the key components to transfer the corresponding desired power. The peripheral of the control system contains DSP microcontroller, current and voltage sensors.

This converter should be used in middle power operation such as 500 W to 2 KW. The transformer is needed for boosting or isolating the input voltage from the secondary and third port voltages. High switching frequency is preferred to reduce the volume of the transformer core and size of the wires. Also, an extra inductor needs to be considered to meet the desired power transfer based on the power flow formulas. Additionally, the duty ratio and phase-shift control technique is introduced using DSP system. Hence in this chapter, the prototype of the hardware unit is design and the procedures of the key components are also included.

6.2 The Design of Power Stage and Driver Circuit

The primary goal of the DAB converter system is to generate the output voltage as twice the input voltage. The input voltage level is around 30 V. After the primary full H-bridge single-phase converter, the input dc voltage is converter to ac voltage with the maximum magnitude of 1.27 times of dc magnitude. Hence, the secondary side ac voltage should be around 80 V.

The semiconductor device is one of the most critical components in the DAB converter system. The proper selection of the device can be cost effective and improve the system's efficiency and durability. The most available parts in the market are IGBTs and power MOSFETs. IGBT is preferably used in the high voltage high current situation because the voltage drop of the IGBT is constant when the device is conducting. When the system is operating in high voltage situation, the voltage drop would be kept the same. Other than power MOSFET, its voltage drop is proportional to the current and drain-source resistance $R_{ds\text{-}on}$ which is like a resistor. Hence MOSFET is suitable for the low power application when the current is not that high like the situations of IGBT.

The selection of the MOSFET is based on the reasonable price, lower drain source resistance, and ease of the implementations on the PCB boards. The discrete is chosen here because of the comparatively low cost to the half-bridge or full-bridge MOSFET modules. Among the different company's MOSFETs, STP40NF10 [52] is a 100 V, 50 A discrete MOSFET module with TO-220 package. Due to the available PCB milling machine in the lab, the MOSFETs have to be used as through-hole designs. The copper

board used is two layers. The MOSFETs will be soldered on board. They are screwed on the heat sink below.

The schematic of the individual full-bridge inverter is shown in Fig. 6.1 below. It is composed of four discrete MOSFETs (STP40NF10), heat sink, terminal connecter and two-layer copper board. The drain-source resistance $R_{ds\text{-}on}$ is 25m Ohm which is acceptable in the proposed system.

There are some considerations while a full H-bridge Power MOSFET is designed. First of all, the gate voltage signal going to MOSFET gate must be clear and the transition between high and low must be as fast as possible. The higher the change of dV/dt and current dI/dt, the less power loss can be achieved. Also, the protection circuit needs to be considered in case of the shoot through of the high voltage. The PCB layout of the presented schematic above is shown in Fig. 6.2.

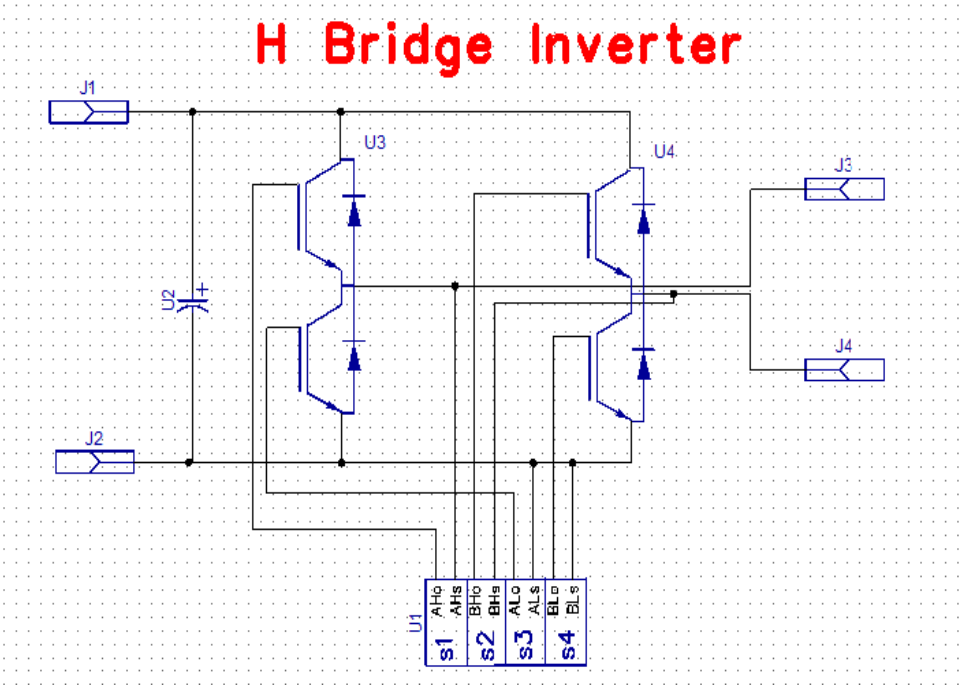

Fig. 6.1 Schematic of the individual single-phase inverter

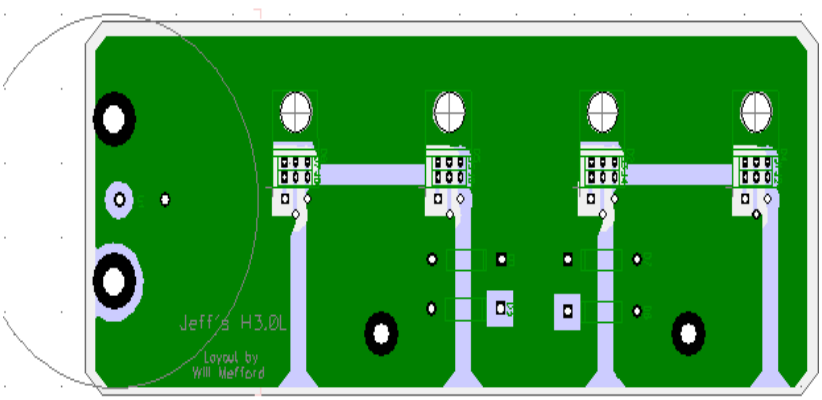

Fig. 6.2 PCB layout of the individual single-phase inverter

The driver circuit design is based on the gate driver MC 33153 [53]. It is an IGBT gate driver which can also be used for MOSFET operation. The gate voltage can be acquired from the output of the driver circuit output. The power supply voltage to MOSFET gate should be 18 V recommended by the application note of MC 33153. The waveform of gate signal is either 0 V or 18 V. So the function of the driver should draw the digital DSP input signals with 3.3 V cleanly and generate output gate voltage signal as 18 V. Based on the above specifications, Fig. 6.3 shows the picture of the built power stage set.

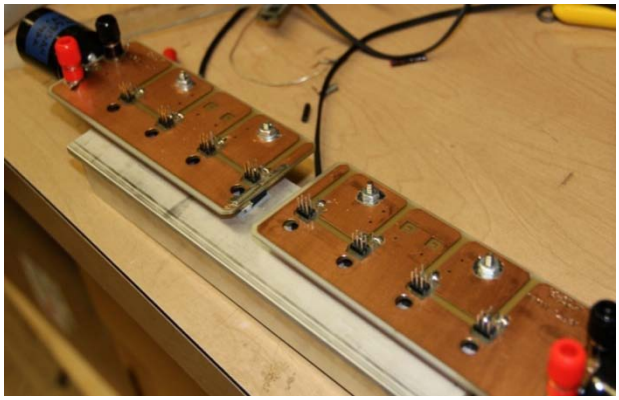

Fig. 6.3 picture of designed power stage of DAB system

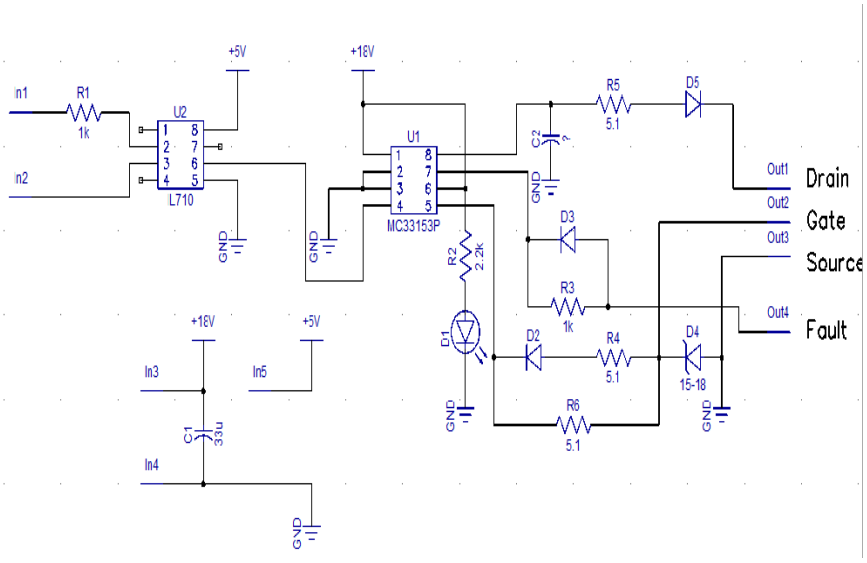

Fig. 6.4 Schematic of the MC33153 gate driver circuit

The connection between DSP and drive circuit must inserte opto-couplers to isolate and protect the DSP system if there are any high spikes of the voltages or currents. TLP 621 is selected to meet the frequency of operation up to 25 kHz. It cannot cause the delay of the input signals. The schematic and PCB layout circuit of gate driver are shown in Fig. 6.4 and Fig. 6.5.

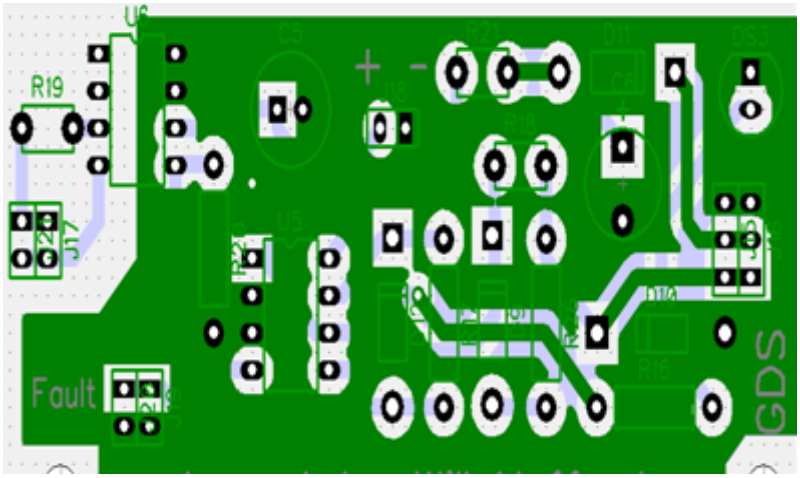

Fig. 6.5 PCB layout of the MC33153 gate driver circuit

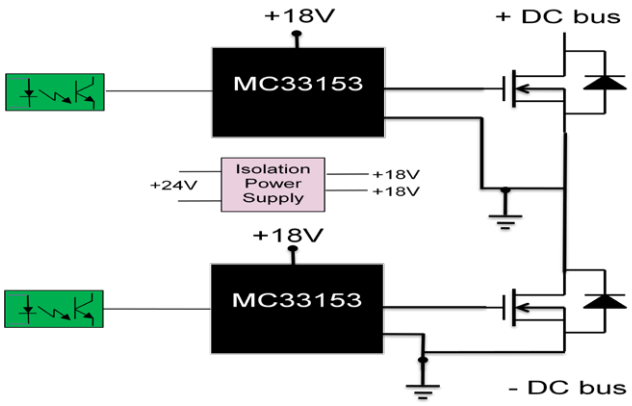

Fig. 6.6 Configuration of the MC33153 gate driver's operation

For the design of the turn on resistor and turn off resistor of the gate driver circuit, the criteria for $R_{G\text{-}on}$ selection are large enough to damp the ringing and to reduce the noise and small enough to accelerate turn-on process and reduce the turn-on loss. Also, the criteria for $R_{G\text{-}off}$ selection are large enough to limit the discharge current to be less than the sink current capability of the gate driver and small enough to reduce turn-off delay. The configuration of the driver circuit operation is shown in Fig. 6.6. The picture of the designed MOSFET driver circuit is shown in Fig. 6.7.

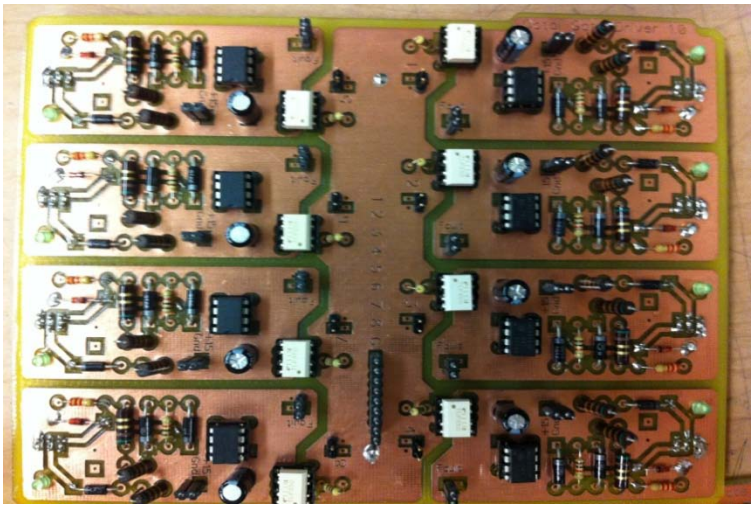

Fig. 6.7 Picture of the designed PCB driver circuit

In the applications of H-bridge system, it may exist that the currents flowing through the power semiconductor devices exceed the desired capabilities. If the devices are not protected again these overcurrents, they may be destroyed. Usually the primary choice would be fuses connected in series with the main input circuit. However, the fuses cannot act fast enough to disconnect the circuit and the power devices may have been destroyed. Hence, the overcurrent protection can be detected by using the default protection function from the driver MC33153. A low resistance current shunt (5 Ω) can be used to sense the emitter current. When there is a high inrush current coming through, the short circuit discerned function is implemented by the second comparator with a high trigger voltage. The short circuit signal is latched and appears at the Fault output. After the signals from each driver circuit are detected, they are sent back to DSP controller and all the switches should be turned off until the reset button is pressed again. The protection circuit designed is shown in Fig. 6.8 below.

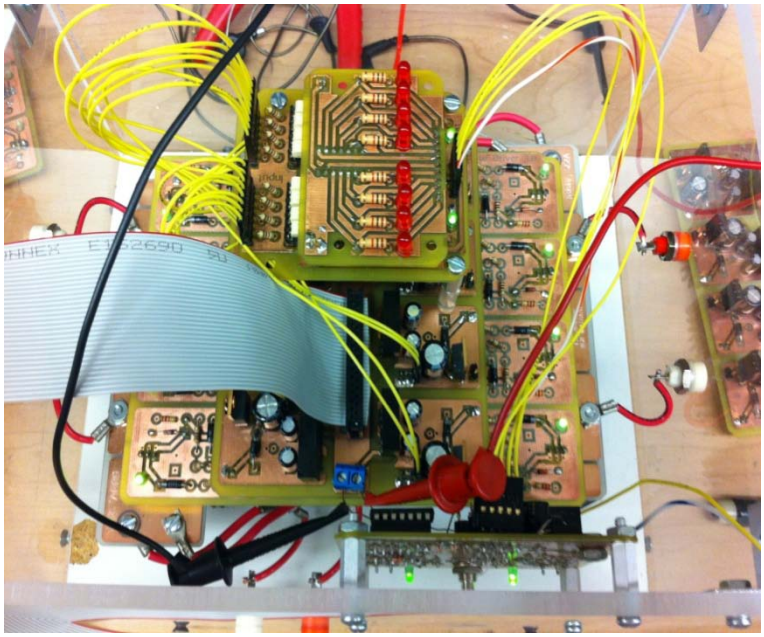

Fig. 6.8 Snapshot of the over current protection circuit

(a)

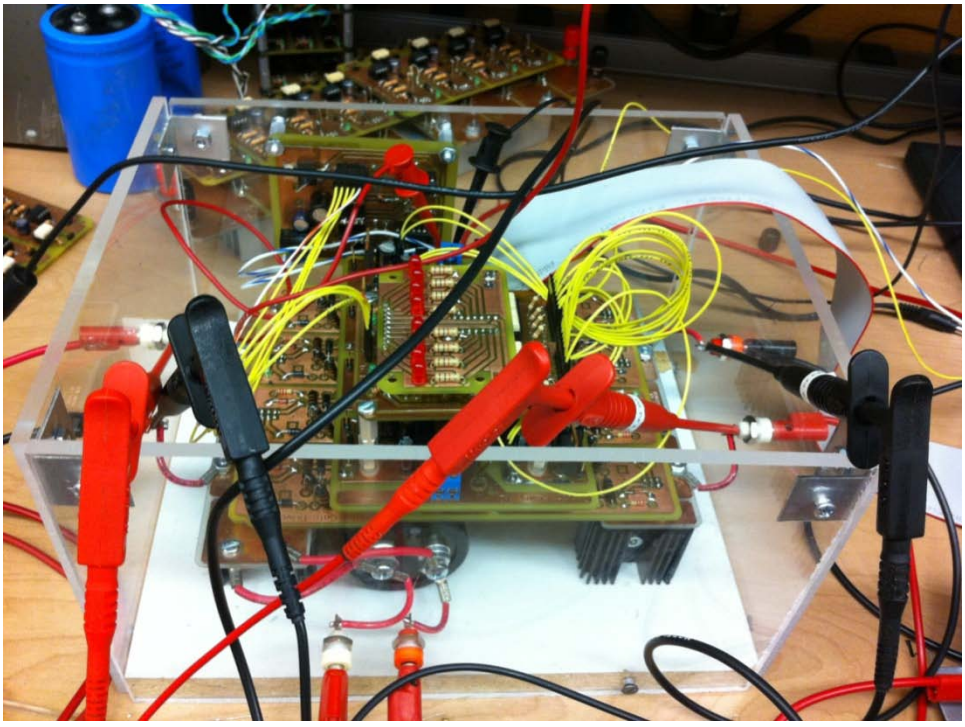

(b)

Fig. 6.9 Snapshot of the prototype system, showing (a) the full bridge module, (b) the completely assembled power conversion system

The photograph of the prototype is displayed in Fig. 6.9. Fig, 6.9(a) shows the two full bridge converter system. The completely assembled system with protection circuit is shown in Fig. 6.9 (b), where the power stages with heat sink are mounted on the white board, the driver circuits, isolated power supplies, and protection circuits are connected on the top of the power stages.

Before giving the power supply to the H-bridge circuit, it is necessary to check if the power MOSFET can work at all. The single-phase inverter circuit is shown in Fig. 6.10. Switch the rotary knob of Fluke MULTIMETER to diode test. Push the blue button to dc volts selection. Connect the multi-meter from the "+" port to A_o and "+" port to B_o port, if the MOSFET works well, it should display OL state. By reversing the connection, it should display the voltage drop of anti-parallel diode. Similarly, check the connection of A_o port to "-" port and B_o port to "-"port. Also check the connection from "+" port to "-" port. It should display OL state and 0.45 V for reverse connection.

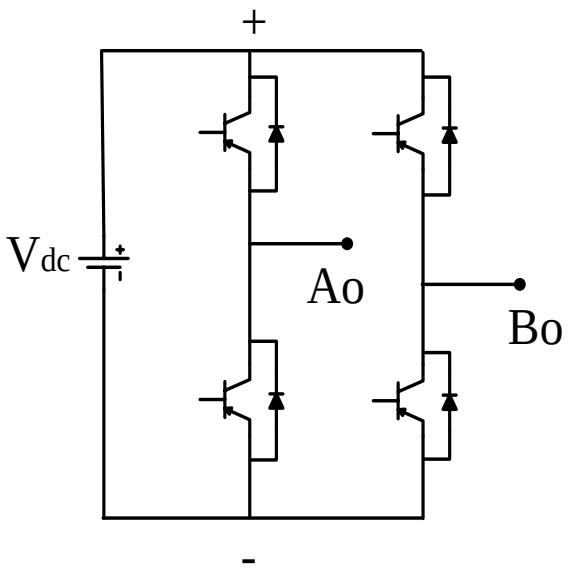

Fig. 6.10 Single H-bridge inverter circuit

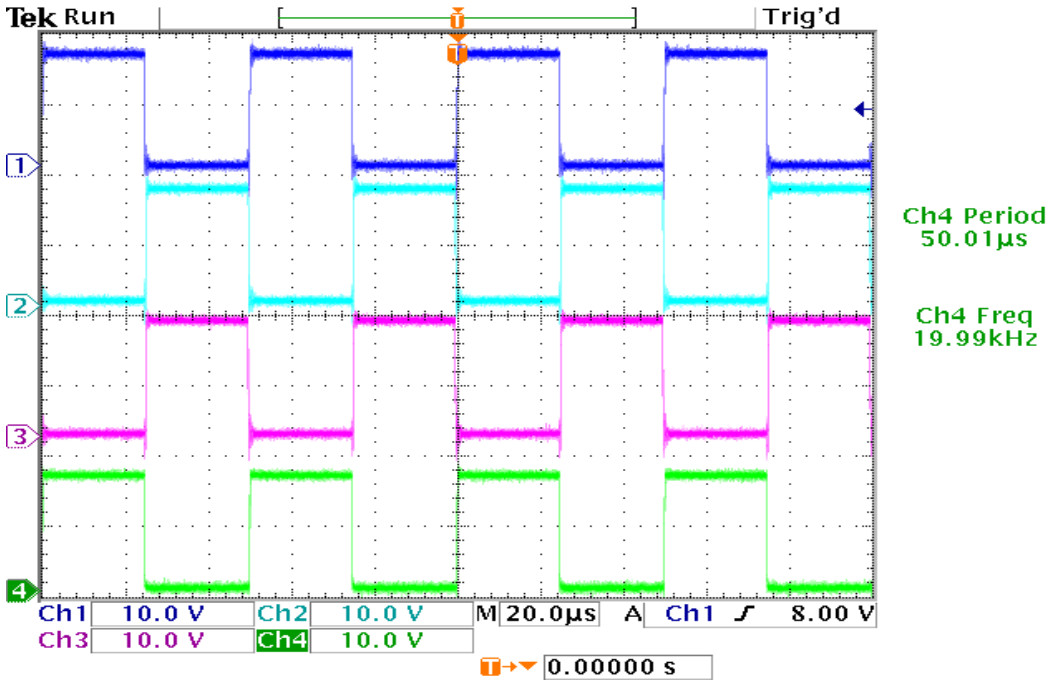

Fig. 6.11 Hardware test result demonstrating gate voltage V_G

The test results are from the built prototype circuit. It is composed of MC33153 driver and Power stage circuit. As can be seen from Fig. 6.11, the device drain-to-source voltage waveforms are very clean. The waveforms show the gate voltage V_G 18 V operating well.

6.3 High Frequency Transformer Design

The design of the high frequency transformer has a significant influence on the overall weight, power conversion efficiency, and the cost of the DAB converter system. So it is necessary to design a small, efficient transformer. As is known, increasing the frequency and core loss is a tradeoff situation to confront. If the operating frequency is increasing, the size of the core and wire will be smaller but the core losses will be

increased and the influence of EMI interference will become more serious. Hence, the design of the high frequency transformer should transfer the rated power and converter the voltage at reasonable core and copper losses. Also, EMI should be prevented as much as possible. Because EMI can cause the disconnected communication between DSP control system and power stage. This can cause the damage of the semiconductor's devices. In this section, a two-port high frequency transformer is presented.

A high frequency transformer is the key component to connect individual ports together and voltages based on the specifications. In this section, a detailed step by step design of high frequency transformer is stated. The design includes the determination of variables such as core dimensions, wire gauge, and turn number. Usually the following part is the list of the specifications of the transformer to be designed shown in Table 6.1.

Table 6.1 Specifications of the 20k Hz high frequency transformer

Description	Parameters
Rated power	P=1000 W
Input voltage	V1 = 24 V
Output voltage	V2 = 48 V
Switching frequency	f = 20 kHz
Temperature	T = 40°C
Efficiency	$\eta = 0.98$
Flux density	$B_m = 0.3$Tesla
Waveform coefficient	$K_f = 4$
Current density coefficient @40°C	Kj = 534
Window utilization factor	$K_u = 0.4$

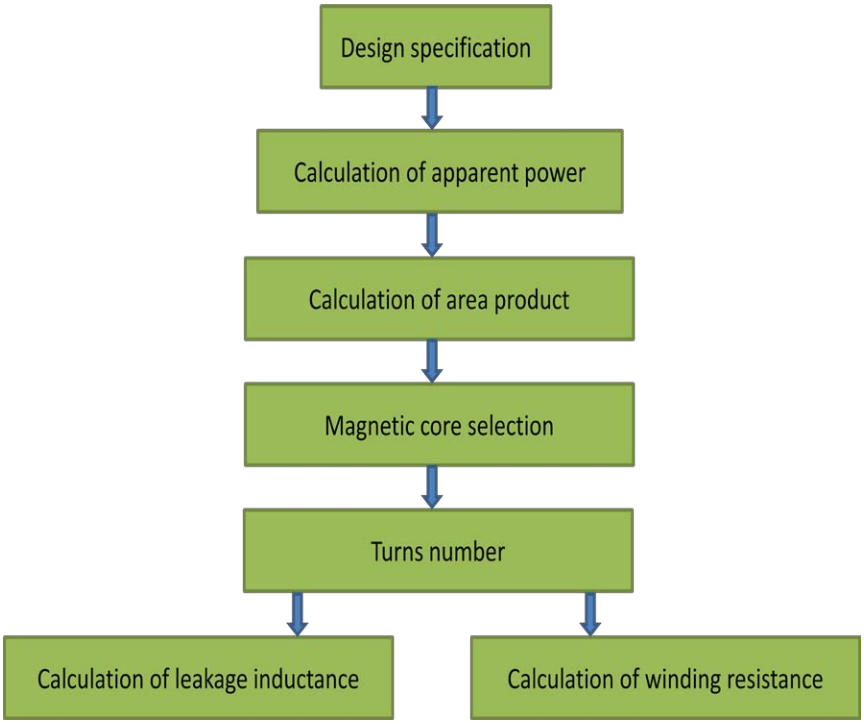

Fig. 6.12 Flow chart of the conventional design method

Traditionally, in conventional design, the first step is to calculate the apparent power. After that, the size and type of the magnetic core will be selected based on geometric factor of the core such as window utilization, waveform coefficient, operating frequency, etc. When core is selected, winding turns number and wire sizes can be determined and, with theses values decides, the transformer can be built. The general procedure of the tradition design method is shown in Fig 6.12.

This traditional method is mainly for the initial design of the transformer. The selection of the core size is based on the equation of inequality. Hence, it can be redesigned to get closer to the optimal operating condition. The first step is to calculate the apparent power as below:

Step 1: Calculate the apparent power using Equation (6.1)

$$P_t = P_m + P_\Sigma \tag{6.1}$$

$$P_t = 1000/0.98 + 1000 = 2020W \tag{6.2}$$

Step 2: Calculate the area product using (6.3) and the result is in Equation (6.4)

$$A_p = \left| \frac{P_t * 10^4}{K_f B_m f K_u K_j} \right| \tag{6.3}$$

$$A_p = \left| \frac{2020 \cdot 10^4}{4 \cdot 0.3 \cdot 10000 \cdot 0.4 \cdot 534} \right| = 10.522 cm^4 \tag{6.4}$$

After A_p has been determined, the geometry of the transformer can be evaluated. The criteria of the selection of core is that the area product of the core is at least greater than the area product calculated by the apparent power. Among the different cores available in the market, EE ferrite core may be the one of the most efficient cores due to its larger window area and high magnetic permeability coupled with low electrical conductivity. Due to the available EE ferrite cores in the market, the specifications of the EE ferrite core chosen are listed in Table 6.2.

Table 6.2 Specifications of the magnetic core

Parameters	EE ferrite core 65/32/27
Area product Ap, cm4	29.9 cm4
Mean length per turn MLT, cm	14.7 cm
Core window area Wa, cm2	5.54cm2
Core cross-section area Ae, cm2	5.4 cm2
Winding fill factor Ku	0.4

Step 3: Calculate the number of primary turns using (6.5) and the result is shown:

$$N_p = \left| \frac{V_p \cdot 10^4}{K_f B_m f A_e} \right| turns \tag{6.5}$$

$$N_p = \left| \frac{30.55 * 10^4}{4 * 0.3 * 10^4 * 5.4} \right| = 4.715 turns \tag{6.6}$$

Step 4: Calculate the current of primary winding using (6.7) and the result is shown as below:

$$I_p = \frac{P_o}{V_p \eta} \tag{6.7}$$

$$I_p = \frac{1000}{30.55 * 0.98} = 33.4A \tag{6.8}$$

Step 5: Determine the current density J using K_j as below:

$$J = K_j A_p{}^y \ (A/cm^2) \tag{6.9}$$

$$J = 534 * 29.9^{-0.12} = 355.19 \ (A/cm^2) \tag{6.10}$$

Step 6: Determine the bare wire size $A_{w(B)}$ for the primary windings:

$$A_{w(B)} = \frac{I_p}{J} \ (cm^2) \tag{6.11}$$

$$A_{w(B)} = \frac{33.4}{355.19} = 0.094 \ (cm^2) = 94 * 10^{-3} (cm^2) \tag{6.12}$$

Litz wire is selected here to reduce the eddy current circulating inside the normal wire. The 200 strands 36 AWG is chosen here. It is equivalent to normal wire No. 12 AWG which is close to the value calculated above.

Step 7: Calculate the primary winding resistance:

$$R_p = (MLT) N_p (\mu\Omega / cm) \tag{6.13}$$

$$R_p = (14.7) * 4.715 * (32.9 * 10^{-6}) = 0.0023\Omega \tag{6.14}$$

Step 8: Determine the primary copper loss $P_{p:}$

$$P_p = I_P{}^2 R_p \tag{6.15}$$

$$P_p = 33.4^2 \cdot 0.0023 = 2.56W \tag{6.16}$$

Step 9: Determine the number of the secondary turns N_s:

$$N_s = \frac{N_P V_s}{V_p} \tag{6.17}$$

$$N_s = \frac{4.715 \cdot 60}{30.55} = 9.43 turns \tag{6.18}$$

Step 10: Determine the secondary current I_s:

$$I_s = \frac{P_o}{V_s \eta} \tag{6.19}$$

$$I_s = \frac{P_o}{V_{s1} \eta} = \frac{1000}{61 \cdot 0.98} = 16.7\,A \tag{6.20}$$

Step 11: Calculate the bare size A_w for the secondary windings:

$$A_{w(B)} = \frac{I_p}{J}\,(cm^2) \tag{6.21}$$

$$A_{ws1(B)} = \frac{I_{p1}}{J} = \frac{16.7}{355.19} = 0.0471 = 47.1 \cdot 10^{-3} (cm^2) \tag{6.22}$$

The 27 strands 30 AWG is chosen here. It is equivalent to normal wire No. 15 AWG which is close to the value calculated above.

Step 12: Calculating the secondary winding resistance:

$$R_s = (MLT) N_s (\mu\Omega / cm) \tag{6.23}$$

$$R_s = (14.7) \cdot 9.43 \cdot (32.710^{-6}) = 0.0045\Omega \tag{6.24}$$

Hence, the primary design parameters are achieved. The next step is to measure the leakage inductance and mutual inductance of the built transformer.

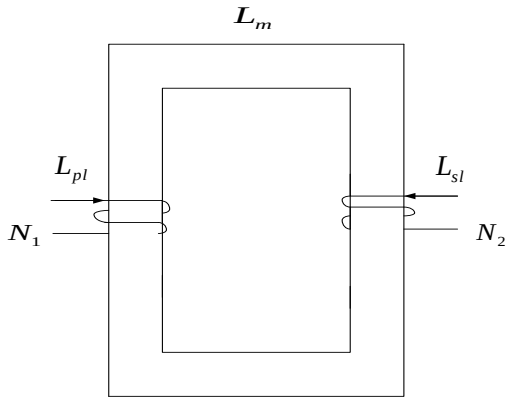

Fig. 6.13 Design schematic of 1 kW high frequency transformer

The Fig. 6.13 above shows the winding geometry of two-port transformer. The inductance of primary side is composed of self leakage inductance and mutual inductance. The secondary side winding also has self leakage inductance and mutual inductance. As shown in the example below, the method of measuring leakage inductance and mutual inductance are described clearly. Let the secondary side open connect two windings of the primary side, one can get the measured inductance $L_{me1/}$:

$$L_{me1} = L_{pl} + L_m \tag{6.25}$$

Because the mutual inductance is way greater than the leakage inductance $L_m >> L_{pl}$

$$L_{me1} \approx L_m \tag{6.26}$$

Let the secondary side shortly connect and make the primary side windings open, one can get the measured inductance L_{me2}:

$$L_{me2} = L_{pl} + (L_m // n^2 L_{pl}) \approx L_{pl} + n^2 L_{pl} \tag{6.27}$$

As turn ratio is known, another equation must be solved:

$$\frac{L_{pl}}{n^2} = L_{sl} \tag{6.28}$$

Table 6.3 Specifications of the built transformer

Measured parameter	Value
Input resistance r_1	0.03Ω
Input leakage inductance L_{pl}	5.85 μH
Output resistance r_2	0.005Ω
Output leakage inductance L_2	1.35 μH
Mutual inductance L_m	185μH

The measured values of built transformer are shown in Table 6.3. By using (6.24), (6.25) and (6.26), one can solve L_{pl}, L_{sl} The following is the picture of the transformer shown in Fig. 6.14.

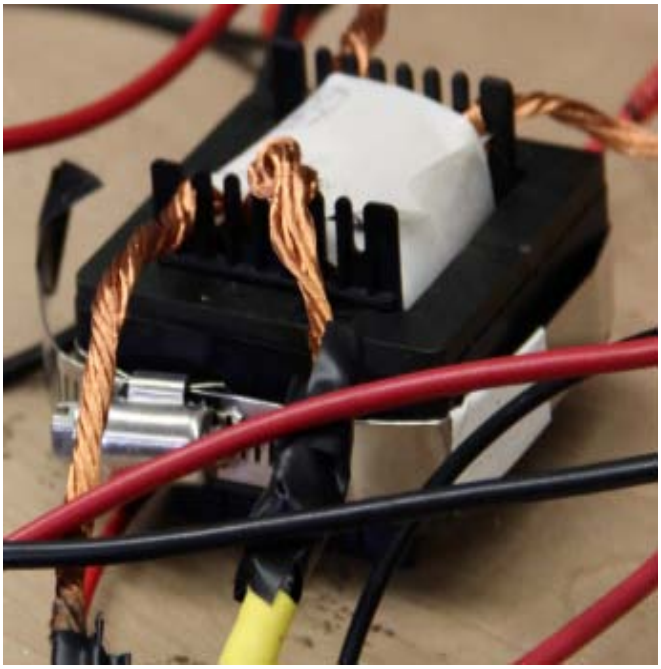

Fig. 6.14 1 kW high frequency transformer

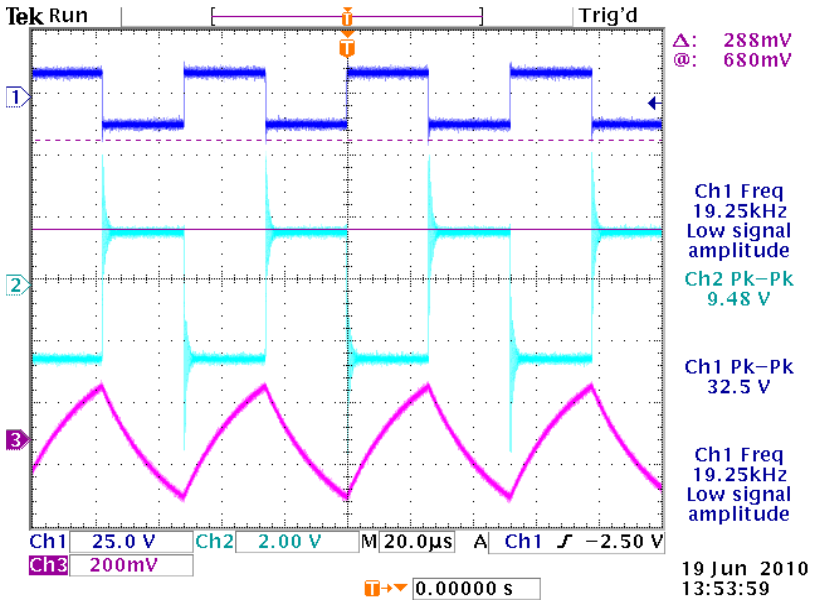

Fig. 6.15 Primary and Secondary voltages measured

The experimental data of the primary voltage and secondary voltage and ac current flowing through transformer is shown in Fig. 6.15. Fig. 6.16 and Fig. 6.17 show the transient change of the switching voltage for up and down side.

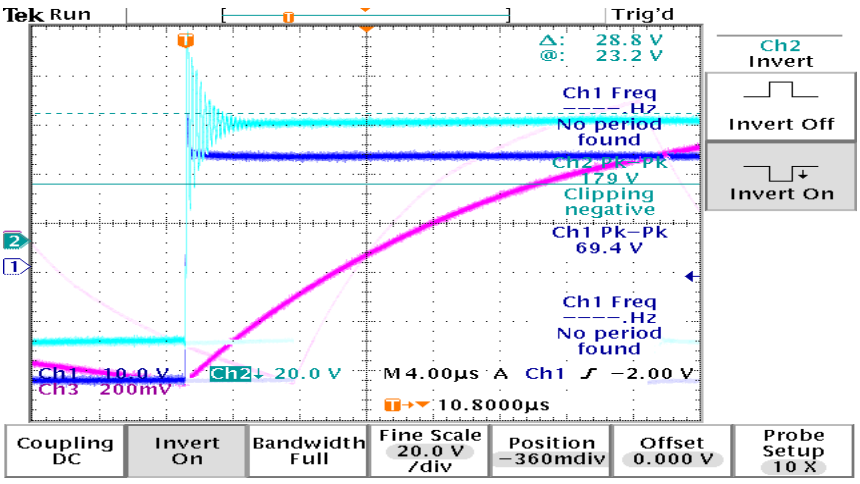

Fig. 6.16 Transient change of up side

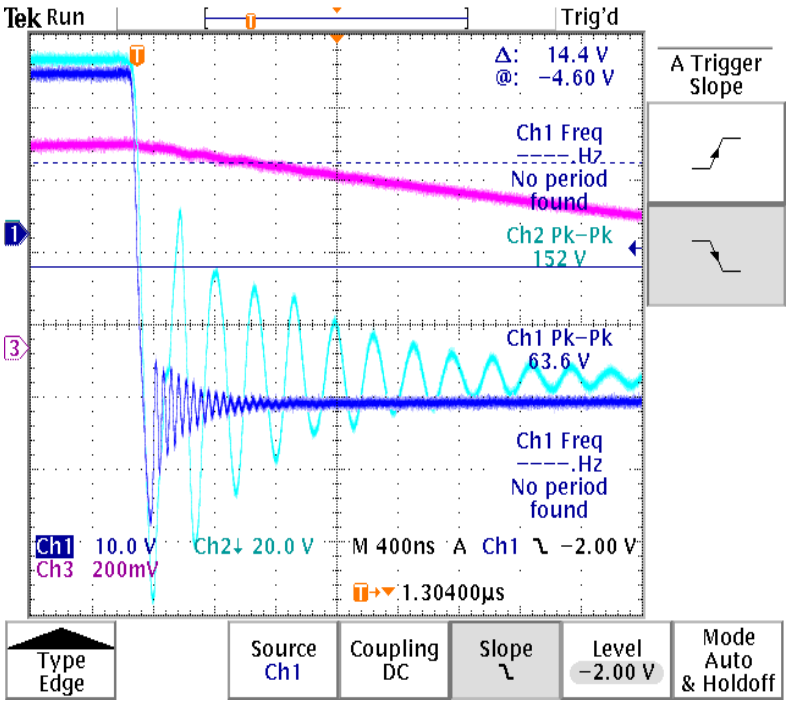

Fig. 6.17 Transient change of low-side

As can be seen from the figures above, the transformer is operating at 10 kHz and step up the input voltage to twice as the output side which is expected.

6.4 Inductor Design

The auxiliary inductor is necessary to be added to the primary side of the transformer. The inductance in the operation of high frequency transformer DAB system is critical. When the system is operating at high frequency, the inductance composed of leakage inductance and extra inductance is taking an important role in managing the power flow between the primary and secondary side shown in Fig. 6.18.

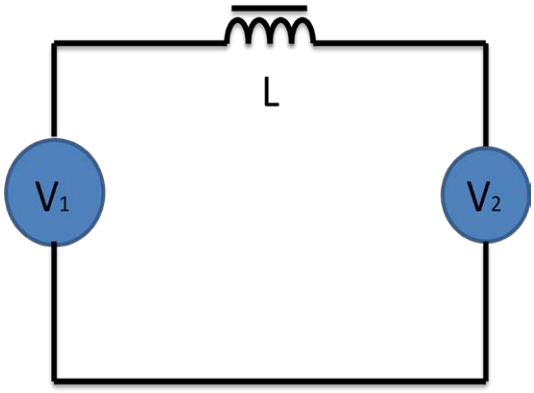

Fig. 6.18 Inductance *L* in the operation of the proposed DAB system

The inductance *L* determines the maximum transient power the power source can supply. Because of the design of high frequency transformer, the leakage inductance is smaller and cannot be enough to handle the required power flow. It can result in a higher peak current. So it is necessary to add an external inductance to the proposed system. Hence, it should be designed such that it delivers the output power. The ac inductor is designed using the following procedure [54]. The specifications of are listed in Table 6.4.

Table 6.4 Specifications of the auxiliary inductor

Parameters	Value
Applied voltage V	25 V
Line current A	40 A
Line frequency Hz	20 kHz
Current density amp/cm^2	300 amp/cm^2
Efficiency η	90%

Step 1: Calculate the apparent power P_t of the inductor L:

$$P_t = V_l I_l = 25 \cdot 40 = 1000W \tag{6.29}$$

Step 2: Calculate the area product A_p:

$$A_p = \frac{VA(10^4)}{K_f K_u B_{ac} fJ} = \frac{25 \cdot 50 \cdot 10^4}{4.44 \cdot 0.4 \cdot 10000 \cdot 0.4 \cdot 300} = 5.86cm^4 \tag{6.30}$$

Step 3: Select EE core 55/28/21-3C85. It can handle the area product calculated.

Step 4: Calculate the number of inductor turns, N_L:

$$N_L = \frac{V_L 10^4}{K_f B_{ac} fA_c} = \frac{25 * 10^4}{4.44 * 0.3 * 10000 * 3.53} = 5.31turns \tag{6.31}$$

Step 5 Calculate the inductive reactance X_L:

$$X_L = \frac{V_L}{I_{Lc}} = 50 = 0.5 \tag{6.32}$$

Step 6 Calculate the required inductance L:

$$L = \frac{X_L}{2\pi f} = \frac{0.5}{2\pi * 10000} = 7.9\mu H \tag{6.33}$$

The leakage inductance is about 2.7 μH. So the extra inductance should be made about 5 μH. Fig. 6.19 shows the built inductor with 5 μH.

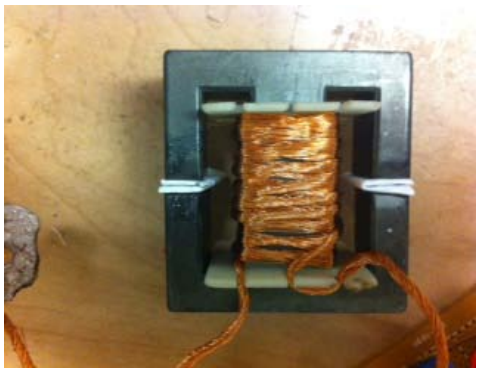

Fig. 6.19 5 μH auxiliary inductor

6.5 Implementation of DSP

The proposed phase shift PWM generation scheme for the DAB converter system is implemented with DSP controller system from Texas Instruments (TI) C2000 family. The phase shift PWM pulses are generated directly from an internal time event using TM320SF2812 shown in Fig. 6.20. This digital is usually a digital pulse with binary amplitude (0, 1). One (1) is usually 3.3 V and 0 is 0 V. All digital I/O ports can be grouped into Group GPIO A, B, D, E, F, and G. These GPIO ports mean general purpose input output. Also, for each single physical pin it can be used for two or three different special functions. The functions here are specified as PWM generation.

All six GPIO ports are controlled by their own multiplex register called GPxMUX. Writing 0 to the bit means choosing normal digital I/O function. Setting 1 to the bit means selecting special function also called primary function. When the digital I/O function is selected, then the register group GPxDIR defines the direction of I/O. writing 0 to pin means input. On (1) is chosen as output.

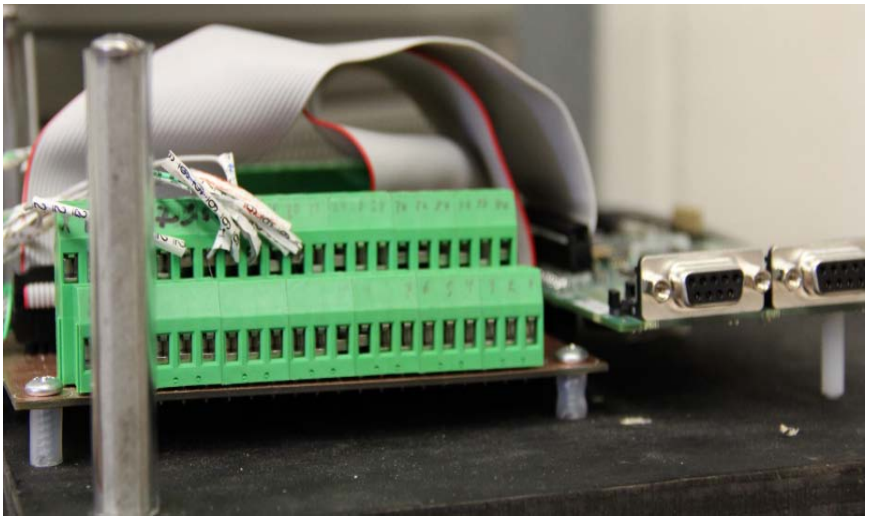

Fig. 6.20 DSP TM320SF 2812 control system

The CPU clock module is driven by an external crystal clock. The inner PLL circuit generates the speed by using the registers PCLKCR and HISPCP. Also, a watchdog timer has the function of resetting the C28x if the CPU crashes. The watchdog is always alive when DSP is power up so it must be taken care of. One of the simplest ways is to disable it. The register WDCR can be used to finish the setup. Also, the register SCSR controls whether the watchdog causes a Reset or an interrupt request.

The event manager (EV) shown in Fig. 6.21 is a unit that can be used in time-based procedures. The event manager timers units are usually called Time 1, 2, 3, and 4. These timers are completely different than CPU core Timers 0, 1, and 2. First, they have a 16-bit counter unit, whereas a core timer is a 32-bit register. Secondly, an EV can be used to generate hardware signals directly from an internal time event. This digital event is usually a digital pulse with binary amplitude 0 and 1. One (1) is usually 3.3 V and 0 is 0 V. With the help of logic of EV, we can modify the frequency of and shape of signals called PWM.

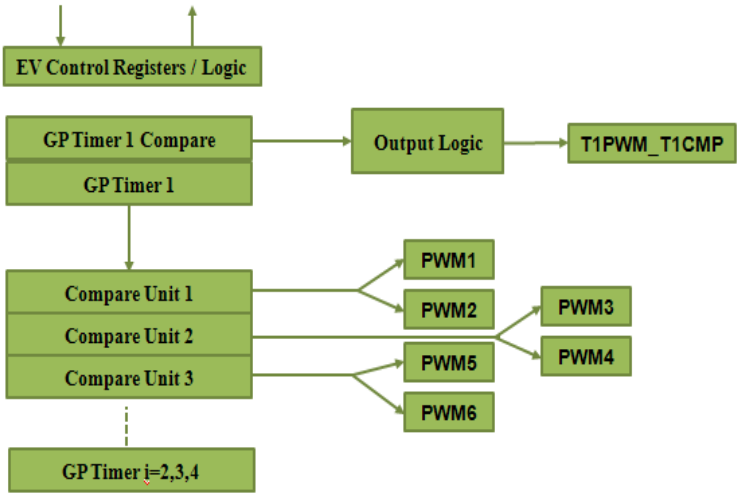

Fig. 6.21 Event manager system of DSP 2812

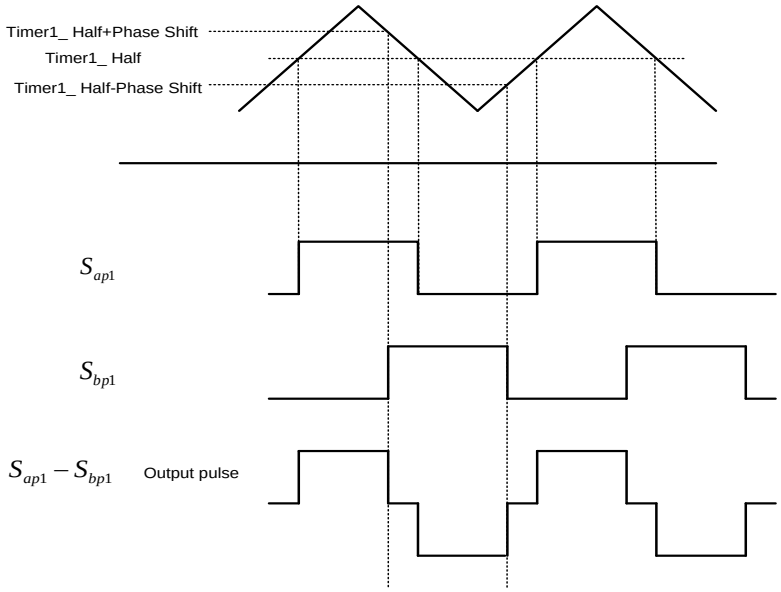

Fig. 6.22 Realization of the phase shifts by DSP 2812

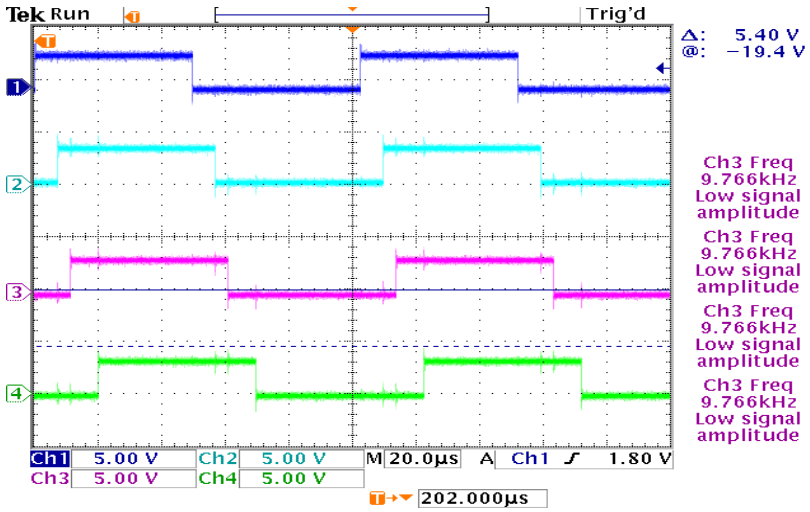

Fig. 6.23 10 kHz phase shift square wave PWM with 0°, 15°, 30°, and 60°

After setting all the registers, the first goal is to generate 10 kHz square wave PWM with phase shift 0°, 15°, 30°, and 60°. It can be shown in Fig. 6.23.

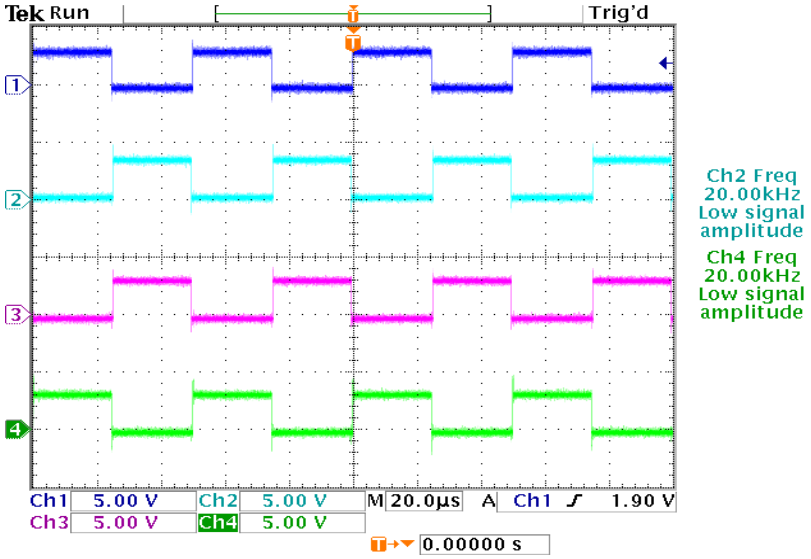

Fig. 6.24 20 kHz phase shift square wave PWM with 180° phase shift

A two pair of 20 kHz PWM signals with duty ratio cycles of 50% and a phase shift of 180° shown in Fig. 6.24 are generated which can be used to turn on the four switches for one single-phase inverter.

After generating the phase shift PWM. The output voltage can be expressed as

$$V_{ac} = V_{dc}(S_{ap} - S_{bp}) \tag{6.34}$$

If S_{ap} and S_{bp} are operated as phase shift PWM pulses. The output ac voltage waveform should be rectangular PWM waveforms.

Another issue of implementing the gate signals to the single-phase inverter is the upper and lower side cannot be turned on at the same time for each bridge. For each bridge, the upper and lower side cannot be turned on at the same time. The dreaded condition called shoot-through can cause the damage of both driver circuit and power stage. The high-side input logical signal cannot be turned off whenever the low-side input logic signal is commanded on in spite of the state of high-side signal. The turn on time is

much faster than the turn off time. When the high-side is commanded off, the falling edge cannot be going to zero simultaneously. At this moment the low-side is turned on. So it is possible that the rising edge of low-side will conflict with falling edge of high-side which causes the happening of shoot-through. The dead band to be added to the gate signals are shown in Fig. 6.25.

Therefore DSP even manager's register DBTCONA can add adjustable dead time to either rising or falling edge of the PWM signals. Here a 2% (500nS) dead band between upper and lower leg is added and shown in Fig. 6.26.

The test result below is from the built prototype circuit. It is composed of MC33153 driver circuit and MOSFET power stage circuit. As can be seen from Fig. 6.27, the device drain-to-source voltage waveforms are very clean. The blue waveform shows the ac output voltage V_{AB} at 36 V from the inverter. The green waveform shows the gate voltage V_G 18 V operating well. The individual full bridge's output voltage V_{AB} can be operated till 60 V and the waveform is still clean.

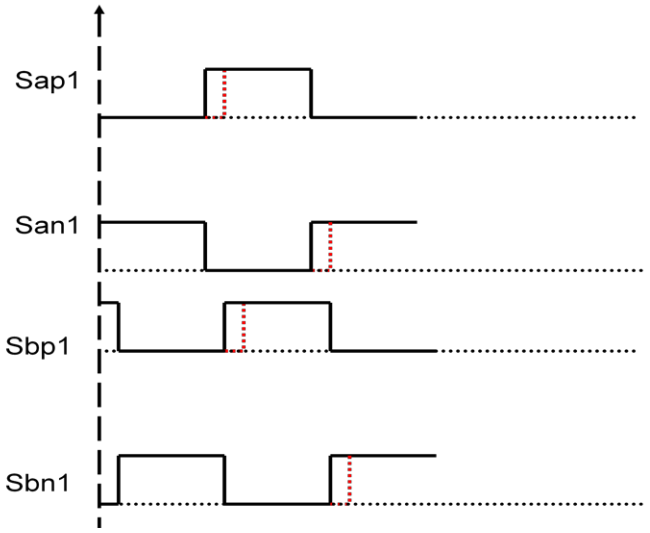

Fig. 6.25 Influence of the dead band time on each gate signals

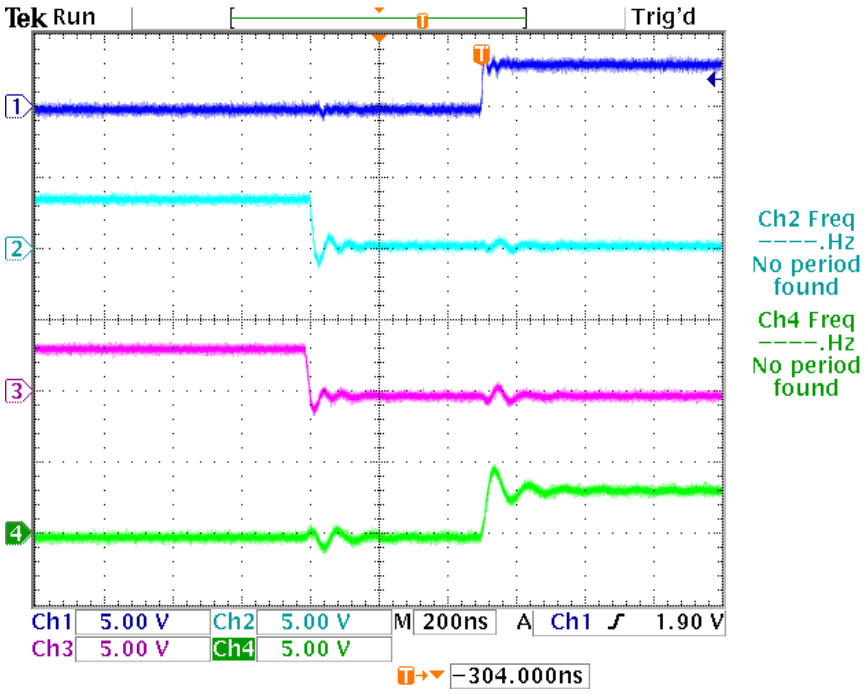

Fig. 6.26 Two pair of Complementary signals with 2% period dead band

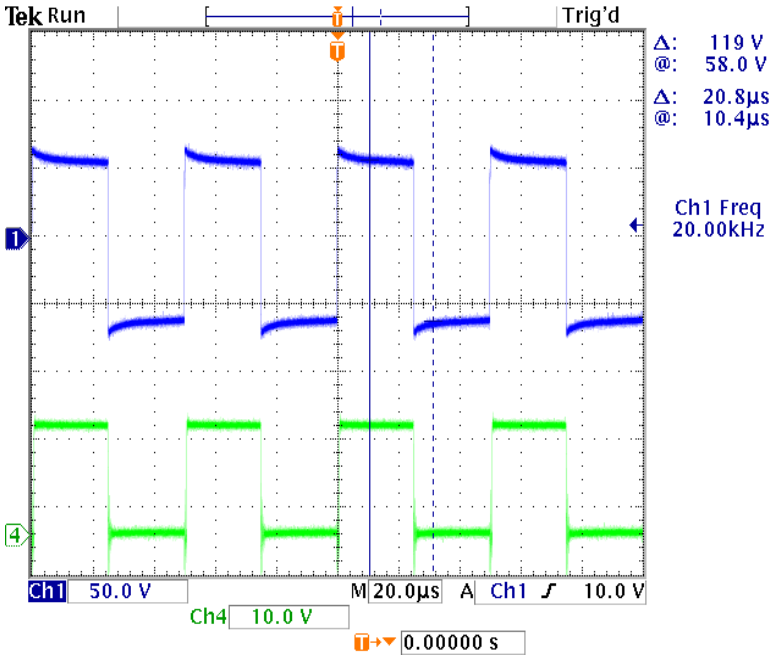

Fig. 6.27 Hardware test result of H-bridge showing output voltage V_{AB} and gate voltage V_G

As can be seen from Fig. 6.28, the waveform shows the ac output voltage V_{AB} at 23 V from the inverter with 60 degree phase shift.

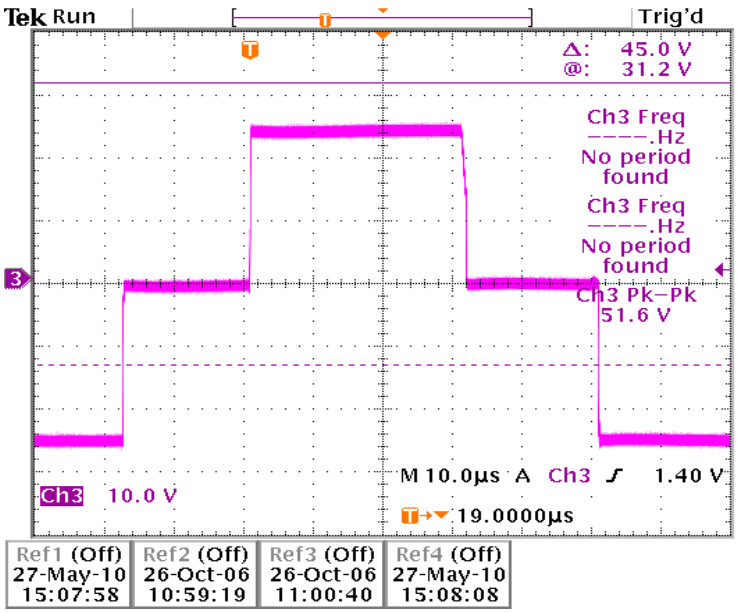

Fig. 6.28 60° phase shift rectangular PWM ac voltage waveform

CHAPTER 7

EXPERIMENTAL VERIFICATION OF THE PROPOSED DAB CONVERTER SYSTEM

7.1 Introduction

In this chapter, the duty cycle and phase shift control method for the proposed DAB converter system is checked experimentally. The specification of the converter system is described in the former chapter. The purposed of the experimental set-up and testing it to analyze the theoretical results and optimal operation topologies derived using HBT. The two-port DAB converter system is examined first in the following section.

7.2 Measurements of the Two-Port DAB Converter System

The proposed measurement of the two-port DAB converter system is to check how the real power and reactive power correspond by varying different duty ratios of each full bridge and phase shifts between two full bridges to some specific output power and voltage level. The input voltage level is around 25 V. After inverted by the primary full bridge converter, the output ac voltage would be related with given duty ratio and a constant gain which is 1.27 times of the dc input voltage. Similarly, the output voltage can be also regulated by the controlled duty ratio.

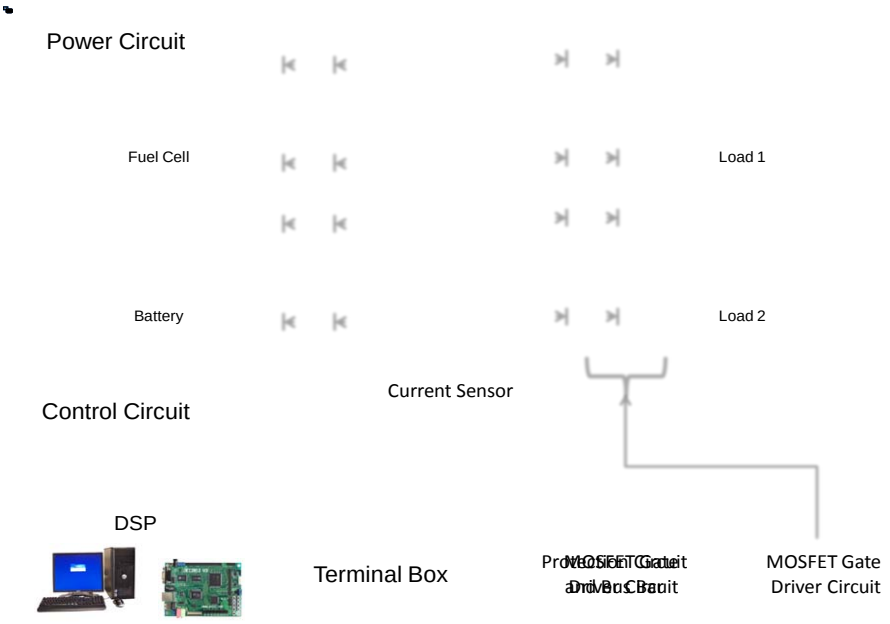

Fig. 7.1 Schematic of the two-port DAB converter system

The schematic of the two-port DAB converter system is shown in Fig. 7.1 above including the control and current sensing system. The DSP micro controller generates phase shift PWM signals to the gate drives. Before the system is operating functionally, the protection circuit needs to be reset and clear the faults to make the system run. After the faults are clear first, the switches on the power stages are turned on and off by the amplified and isolated gate signals from the gate drive circuit. The power supply and load are connected with each full bridge. The phase shift angle control is also done by DSP 28335. The current sensor is connected in series with the primary side of the transformer. Hence, the input ac current can be measured, and the power can be calculated by multiplying the output ac voltage and current. The snapshot of the hardware system is shown in Fig. 7.2.

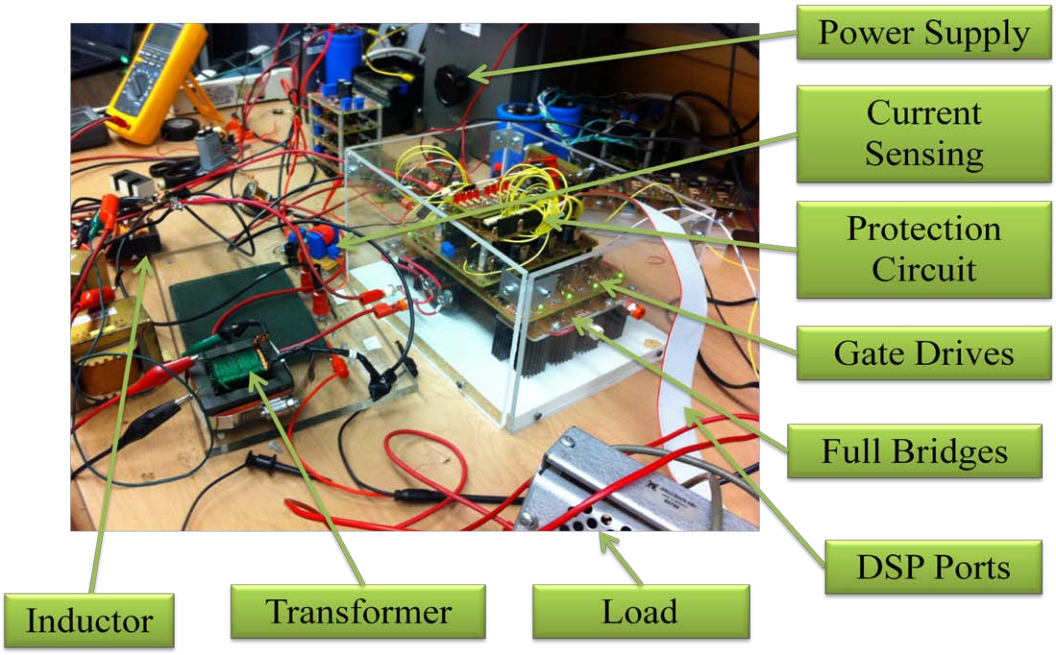

Fig. 7.2 Photograph of the two-port DAB converter system

7.2.1 Steady State Operation with Phase Shift Control Only

To illustrate the steady state operating waveforms, measurements results of the voltage generated by each full-bridge (v_1 and v_2) and the corresponding input current waveform (i_1) at a variety of operating points are shown from Fig. 7.3 to Fig. 7.5. The instantaneous input power (p_1) is also calculated. The laboratory prototype is rated at maximum power 500 W at 20 kHz switching frequency. The load R_L is a 42 Ω resistor. The converters are operated at full duty ratios first to check the effect of phase shift angle on the real and reactive power flow of the DAB system. To prove the simulation results received from HBT the real power and reactive power are increased when the phase shift is increasing. In Fig. 4.3, the study cases are reused for the experiments when duty ratio D_1 =1, D_2 = 1 and the phase shift angles 30°, 60°, and 90°.

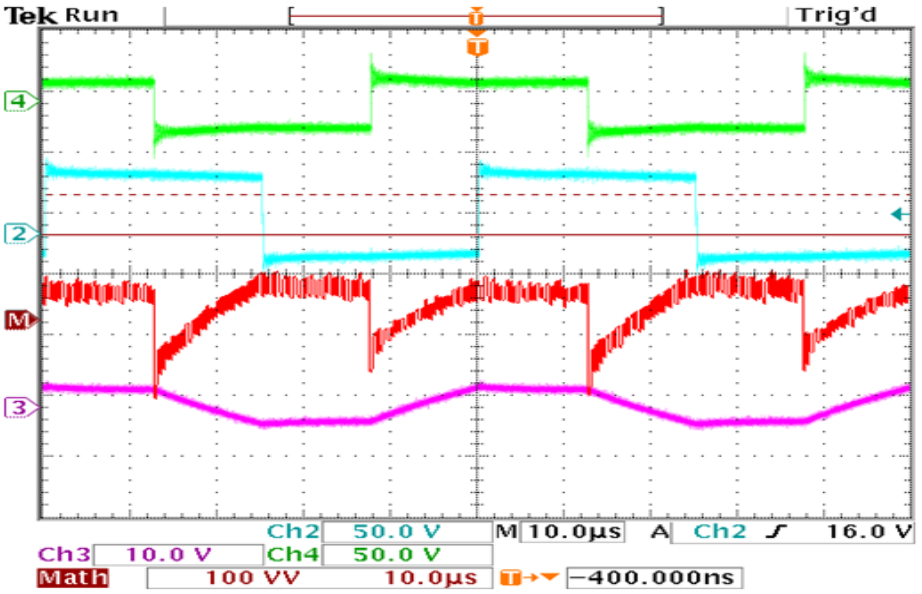

Fig. 7.3 Experimental results of the steady state operation of the two-port DAB converter with $D_1 = 1$, $D_2 = 1$ $\Phi = 90°$, showing from top (4) Input ac voltage v_1 (50V/div); (2) Output voltage v_2 (50V/div); (M) Input instantaneous power P_1 (100VV/div); (3) Input ac current i_1 (10V/div).

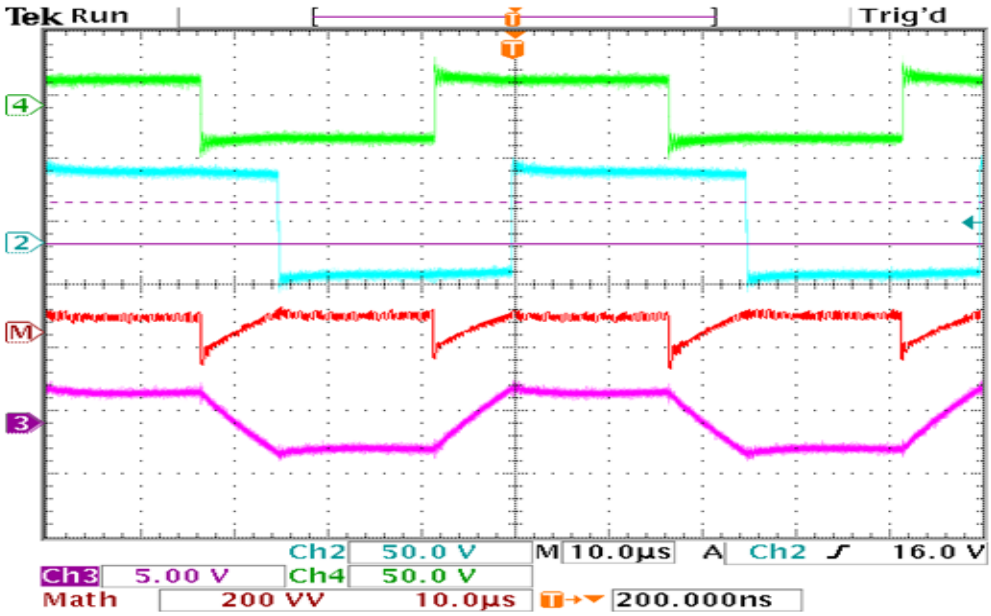

Fig. 7.4 Experimental results of the steady state operation of the two-port DAB converter with $D_1 = 1$, $D_2 = 1$ $\Phi = 60°$, showing from top (4) Input ac voltage v_1 (50V/div); (2) Output voltage v_2 (50V/div); (M) Input instantaneous power P_1 (100VV/div); (3) Input ac current i_1 (10V/div)

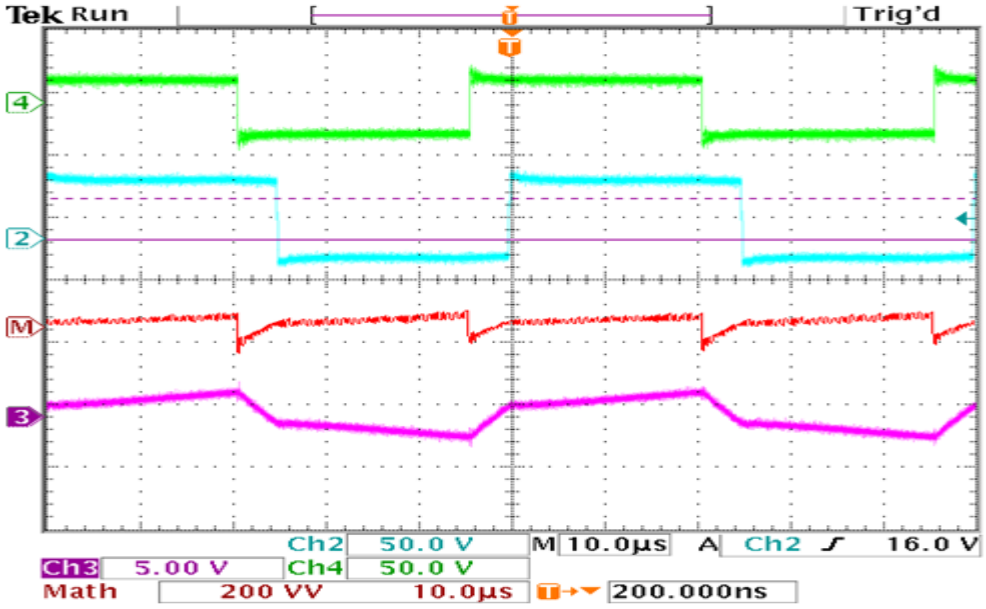

Fig. 7.5 Experimental results of the steady state operation of the two-port DAB converter with $D_1 = 1$, $D_2 = 1$ $\Phi = 30°$, showing from top (4) Input ac voltage v_1 (50V/div); (2) Output voltage v_2 (50V/div); (M) Input instantaneous power P_1 (625W/div); (3) Input ac current i_1 (10V/div).

The power flow in response to the phase shift angle can be well explained both from the theoretical analysis and experimental results. The current transducer from LEM used is LA 55-P/SP1. The current rating is 50 A and the measuring resistance used is 50Ω. There are eight turns used on the current sensor. The proportional relationship between real current value and voltage measured by the oscilloscope is 2.5 times for 1 V. When the phase shift angle is increased from 30°, 60°, to 90°, as can be seen from the red color input instantaneous power, the input real power is increasing and achieving the maximum value at 90°.

When the input voltage is positive at beginning, the current i_1 is negative, it means the reactive power is transferred which it is not desired. Also, Fig. 7.6 tells that the multiplication of the dynamic input voltage and current determines the magnitude of real

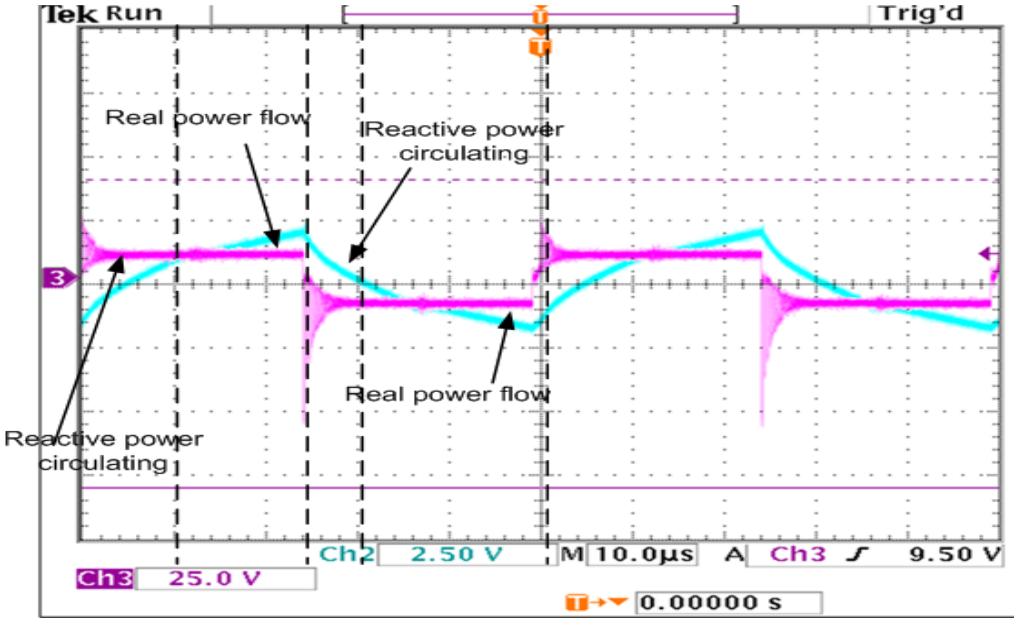

Fig. 7.6 Experimental results showing the real power and reactive power transferred, showing from top (4) Input ac voltage v_1 (50V/div); (2) Output voltage v_2 (50V/div); (M) Input instantaneous power P_1 (625W/div); (3) Input ac current i_1 (10V/div).

power and reactive power transferred. When the input voltage v_1 is positive at beginning, the current i_1 is negative, it means the reactive power is transferred which it is not desired. When the input voltage is positive and current is positive, it means the real power is transferring from the primary side to the load side. So there is unexpected reactive power circulating inside the transformer.It tells that the real power is transferred; however, at the same time the reactive power is also increasing. Hence, it can be analyzed that if the duty ratios of each full-bridge can be also changed the reactive power can be reduced and minimized while keep the input power unchanged.

7.2.2 Steady State Operation with Duty Ratios and Phase Shift Control

In order to gain more degrees of freedom for reducing the overall system losses, the duty ratio control of the full bridge output voltages v_1 and v_2 are introduced in addition to the traditional phase shift control as shown in the former section. The duty ratio range is from 0 to 1 and the control range of phase shift angle is from 0 to $\pi/2$. For controlling the DAB converter system, the traditional phase shift control can only affect the real power flow of the two ports. But, at the same time the voltages on each side and the reactive power cannot be regulated due to the limit of the control freedom.

With both duty cycle variations and phase shift change, the magnitude of the voltages and reactive power can be regulated. Fig. 7.5 shows the ac voltage v_1 and v_2 can both be regulated based on the desired specifications.

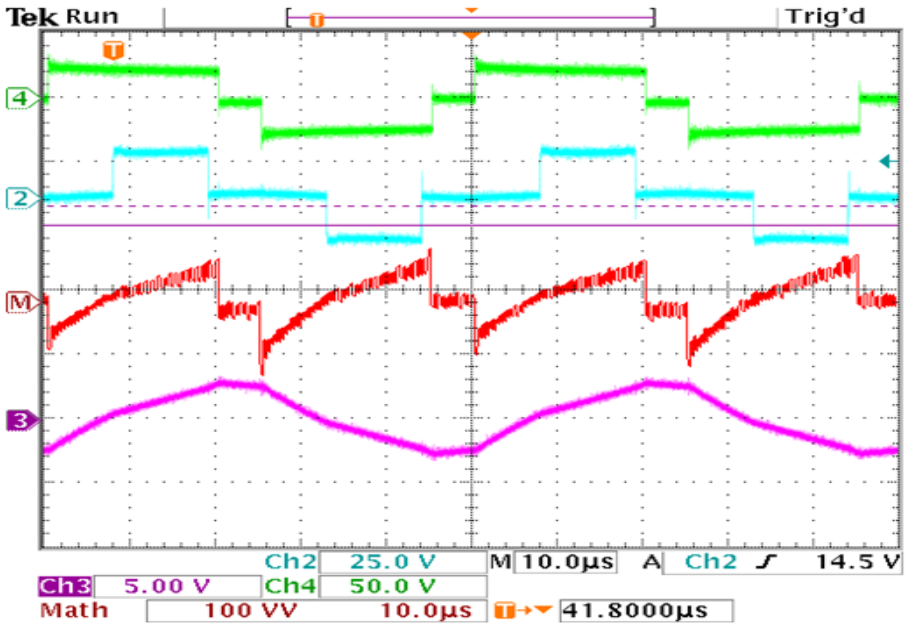

Fig. 7.7 Experimental results of the steady state operation of the two-port DAB converter with $D_1 = 0.8$, $D_2 = 0.6$ $\Phi = 90°$, showing from top (4) Input ac voltage v_1 (50V/div); (2) Output voltage v_2 (50V/div); (M) Input instantaneous power P_1 (625W/div); (3) Input ac current i_1 (10V/div).

The previous theoretical analysis on the minimization of the reactive power in Chapter 4.4 is verified by the following experimental setup where the control parameters are derived from the Equation (4.83). With the electrical parameters given in the Chapter 4.4, Fig. 7.6 shows the measured steady state operation results, showing the voltage between the phase leg midpoints for each full bridge and the current flowing into the primary side of the transformer.

As can be seen, the input instantaneous power is examined to check the real and reactive power. The positive side of the red color line above the average is the real power and the negative side below the average is the reactive power. The circulating reactive power inside the high frequency transformer can be minimized.

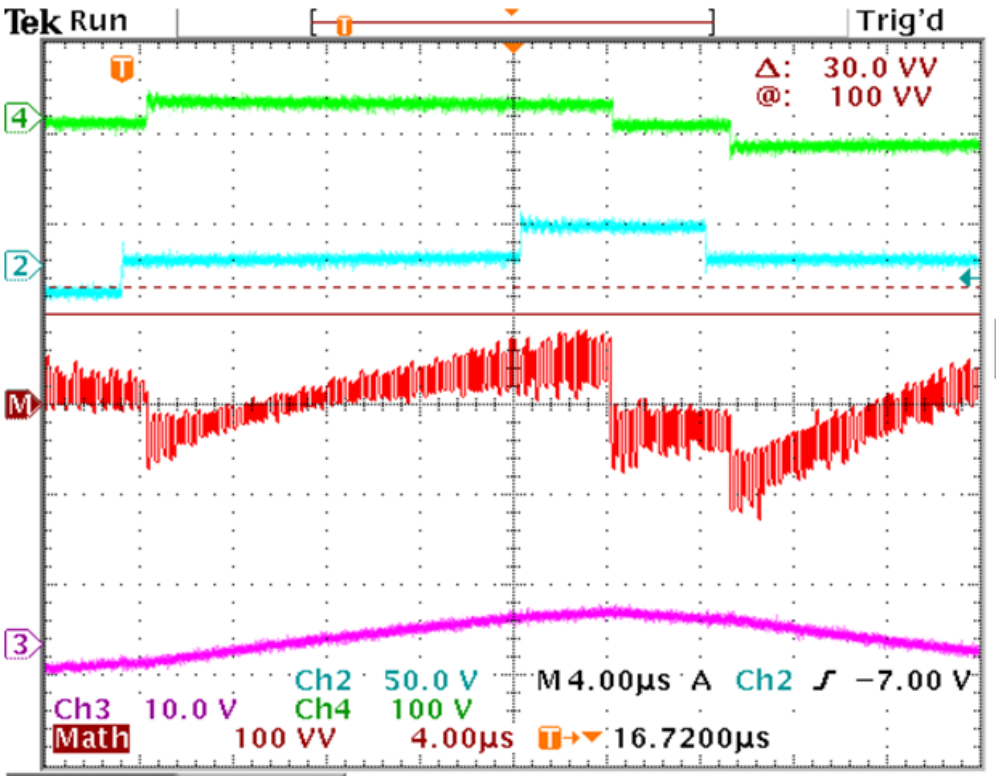

Fig. 7.8 Experimental results of the steady state operation of the two-port DAB converter with $D_1 = 0.8$, $D_2 = 0.26$ $\Phi = 20°$, showing from top (4) Input ac voltage v_1 (50V/div); (2) Output voltage v_2 (50V/div); (M) Input instantaneous power P_1 (625W/div); (3) Input ac current i_1 (10V/div).

CHAPTER 8

CONCLUSION AND FUTURE WORK

8.1 Conclusion

This research work is dedicated to studying the steady state analysis and control of overall system efficiency optimization for two-port and multiport bidirectional DAB converter systems. The dissertation is concluded as follows:

1. In this dissertation, the extensive modeling and analysis using the state space method for two-port bidirectional DAB converter system. The objective is to ease the problem by simplifying the equations and the closed form solutions can be acquired based on different modes of operation. The state space method is a powerful mathematical tool which can make the nonlinear power switching system to be approximated as a linear system. Based on the state space method, the effect of the dead time between upper and lower switches on the DAB system has been introduced. The operation stages considering the dead time intervals are laid out to study the voltage drop of the semiconductor device. Furthermore, the small signal analysis of the two-port DAB converter system is derived clearly.
2. The approach using the converter switching functions and harmonic balance technique (HBT) to modeling and analyzing the DAB system is proposed. The method can predict not only the steady state characteristics of state variables but also even the ripple quantities. The ripple capabilities of filter capacitor

and inductor design can be calculated. Therefore, the size of the filter components can be reduced. A new control strategy from the macroscopic perspective based on the state variables derived from the HBT is used to minimize the reactive power caused by current circulating inside the transformer. This method uses Lagrange multiplier to minimize the objective function which is the least summation of the squares of the currents. The separate state variable equations generated using HBT is used to determine the minimum loss operation of proposed two-port DAB converter system.

3. To further address the advantage of HBT method, it can be also extended into multiport DAB converter system compared with the well-known averaging techniques such as state space method where the state variable matrix would be too complex to solve. Hence, HBT is a powerful method used in the analysis of three-port DAB converter system. Moreover, to solve the problem of minimizing the reactive power circulating inside the transformer for three-port DAB converter system, a mathematical tool called Gröbner basis is firstly introduced to solve the Lagrange multiplier problem with equality and inequality constraints. The proposed approach is compared with numerical iterative method using optimization tool box from software MATLAB.
4. The extensive study of steady state performance of the four-port DAB system is carried out. Also, the investigation of the dynamic simulation of the four-port DAB converter system with various load and two power sources is analyzed by varying operating control variables.

5. The step-by-step hardware design of the proposed two-port DAB and multiple port DAB converter systems is shown clearly. The schematic and PCB layout of the individual single-phase full bridge including the power stage, driver circuit, and protection circuit are given. The procedures of designing the high frequency transformer and auxiliary inductor are carried out. Also, the implementation of PWM phase shift waveforms are included using the digital signal processor (DSP).
6. The traditional phase shift control experimental results of the proposed two-port DAB system are shown to verify the steady state analysis derived from HBT. The reactive power cannot be regulated using the traditional method. Hence, the experiments of both duty cycle and phase shift control method for the proposed DAB converter systems illustrate that the circulating reactive power inside the high frequency transformer can be minimized.

8.2 Future Work

This dissertation contributes to using HBT as a powerful tool to study the steady state characteristics and dynamic performance for the family of bidirectional dual active bridge converter system. It can be extended to analyze some other topologies such as half-bridge converter system, bidirectional three-phase converter systems for the future researchers to work on. Based on the results of this work, recommendations for future research are suggested:

- Analysis of the dynamic behavior of two-port DAB converter system has been studied. The interest would be to design the corresponding ac components controller designer based on natural reference frame.
- Further research in the control design of multiport converters needs to be studied extensively. New decoupling control topologies should be designed.
- The hardware design for the multiport converters can be further optimized. For example, the high frequency transformer design can be used optimization method or even newer structure such as planar style can be introduced. The size of single-phase full bridge converter can be further reduced and the system should be less wired connected to achieve higher overall system efficiency
- The present work can be extended to three-phase bidirectional converter system to get higher power density.

REFERENCES

[1] G. Spagnuolo, G. Petrone, S. V. Araujo, C. Cecati, E. Friis-Madsen, E. Gubia, D. Hissel, M. Jasinski, W. Knapp, M. Liserre, P. Rodriguez, R. Teodorescu, and P. Zacharias, "Renewable Energy Operation and Conversion Schemes," *IEEE Industrial Electronics Magazine*, vol. 4, issue 1, Mar. 2010, pp. 38-51.

[2] J. M. Guerrero, F. Blaabjerg, T. Zhelev, K. Hemmes, E. Monmasson, S. Jemei, M. P. Comech, R. Granadino, and J. I. Frau, "Distributed Generation: Toward a New Energy Paradigm," *IEEE Industrial Electronics Magazine*, Vol. 4, Issue 1, Mar. 2010, pp. 52-64.

[3] Saifur Rahman, "Green Power: What Is It and Where Can We Find It?" *IEEE Power and Energy Magazine*, Vol. 1, Issue 1, Jan.-Feb., 2003, pp. 30-37.

[4] L. A. Barroso, H. Rudrick, F. Sensfuss, and P. Linares, "The Green Effect" *IEEE Power and Energy Magazine*, Vol. 8, Issue 5, Sept.-Oct., 2010, pp. 22-35.

[5] M. Liserre, T. Sauter, and J. Y. Hung, "Future Energy Systems: Integrating Renewable Energy Sources into the Smart Power Grid Through Industrial Electronics," *IEEE Industrial Electronics Magazine*, Vol. 4, Issue 1, Mar., 2010, pp. 18-37.

[6] J. Bebic, R. Walling, K. O'Brien, and B. Kroposki, "The Sun Also Rises" *IEEE Power and Energy Magazine*, Vol. 7, Issue 3, May-Jun., 2003, pp. 45-54.

[7] M. Shahidehpour and F. Schwarts, "Don't Let the Sun Go Down on PV," *IEEE Power and Energy Magazine*, Vol. 2, Issue 3, May-Jun., 2004, pp. 40-48.

[8] P. Thounthong, B. Davat, S. Rael, and P. Sethakul, "Fuel Cell High-Power Applications," *IEEE Industrial Electronics Magazine*, Vol. 3, Issue 1, Mar., 2009, pp. 32-46.

[9] Chuanhong Zhao, Simon D. Round, and Johann W. Kolar, "An Isolated Three-Port Bidirectional DC-DC Converter With Decoupled Power Management," *IEEE Trans. Power Electron.*, Vol. 23, No. 5, Sept. 2008, pp. 2443-2453.

[10] Haimin Tao, Andrew Kotsopoulos, Jorge L. Duarte, and Marcel A. M. Hendrix, "Tranformer-Coupled Multiport ZVS Bidirectional DC-DC Converter With Wide Input Range," *IEEE Trans. Power Electron.*, Vol. 23, No. 2, Mar. 2008, pp. 771-781.

[11] Hua Bai and Chris Mi, "Eliminate Reactive Power and Invrease System Efficiency of Isolated Bidirectional Dual-Active-Bridge DC-DC Converters Using Novel-

Dual-Phase-Shift Control," *IEEE Trans. Power Electron.*, Vol. 23, No. 6, Nov. 2008, pp. 2905-2913.

[12] Haimin Tao, Jorge L. Duarte, and Marcel A. M. Hendrix, "Three-Port Triple-Half-Bridge Bidirectional Converter With Zero-Voltage Switching," *IEEE Trans. Power Electron.*, Vol. 23, No. 2, Mar. 2008, pp. 782-792.

[13] Jorge L. Duarte, Marcel Hendrix, and Marcelo Godoy Simoes, "Three-Port Bidirectional Converter for Hybrid Fuel Cell Systems," *IEEE Trans. Power Electron.*, Vol. 22, No. 2, Mar. 2007, pp. 480-487.

[14] Rajesh Gopinath, Sangsun Kim, Jae-Hong Hahn, Prasad N. Enjeti, Mark B. Yeary, and Jo. W. Howze, "Development of a Low Cost Fuel Inverter System With DSP Control," *IEEE Trans. Power Electron.*, Vol. 19, No. 5, pp. Sept. 2004, 1256-1262.

[15] Changrong Liu, Amy Ridenour, and Jih-Sheng(Jason) Lai, "Modeling and Control of a Novel Six-Leg Three-Phase High-Power Converter for Low Voltage Fuel Cell Applications," *IEEE Trans. Power Electron.*, Vol. 21, No. 5, pp. Sept. 2006, 1292-1300.

[16] H. Matsuo, W. Lin, F. Kurokawa, T. Shigemizu, and N. Watanabe, "Characteristics of The Multiple-Input DC-DC Converter," *IEEE Trans. Ind. Electron.*, Vol. 51, No. 3, Jun. 2004, pp. 625-631.

[17] Lizhi Zhu, "A Novel Soft-Commutating Isolated Boost Full-Bridge ZVS-PWM DC-DC Converter for Bidirectional High Power Applications," *IEEE Trans. Power Electron.*, Vol. 21, No. 2, pp. Mar. 2006, 422-429.

[18] Mohamed Z. Youssef, Humberto Pinheiro, and Parveen K. Jain, "Self-Sustained Phase Shift Modulated Resonant Converters: Modeling, Design, and Performance," *IEEE Trans. Power Electron.*, Vol. 21, No. 2, Mar. 2006, pp. 401-414.

[19] Dehong Xu, Chuanhong Zhao, and Haifeng Fan, "A PWM Plus Phase-Shift Control Bidirectional DC-DC Converter," *IEEE Trans. Power Electron.*, Vol. 19, No. 3, pp. May. 2004, 666-675.

[20] Hua Bai, Chunting Chris Mi, and Sonya Gargies, "The Short-Time-Scale Transient Processes in High-Voltage and High-Power Isolated Bidirectional DC-DC Converters," *IEEE Trans. Power Electron.*, Vol. 23, No. 6, pp. Nov. 2008, 2648-2656.

[21] Sung Young Kim, Ilsu Jeong, Kwanghee Nam, and Hong-Seok Song, "Three-Port Full Bridge Converter Application as a Combined Charger for PHEVs," *IEEE Vehicular Power and Propulsion Conference*, Sept. 2009, pp. 461-465.

[22] B. G. Dobbs and P. L. Chapman, "A Multiple-Input DC-DC Converters Topology," *IEEE Power Electronics Letters*, Vol. 1, No. 1, Mar. 2003, pp. 6-9.

[23] D. Liu and H. Li, "A ZVS bi-directional DC-DC converter for multiple energy storage elements," *IEEE Trans. Power Electron.*, Vol.21, No. 5, Sept. 2006, pp. 1513-1517.

[24] H. Al-Atrash F. Tian, and I. Bataresh, "Tri-model half-bridge converter topology for three-port interface" *IEEE Trans. Power Electron.*, Vol.22, No. 1, Jan. 2007, pp.341-345.

[25] H. Tao, A. Kotsopoulos, J. L Duarte, and M. A. M. Hendrix, "Family of multiport bidirectional DC-DC converters," *IEE Proceeding Electric Power Applications*, Vol. 153, No. 3, May 2006, pp. 451-458.

[26] Hariharan Krishnaswami and Ned Mohan, "Three-Port Series-Resonant DC-DC Converter to Interface Renewable Energy Sources With Bidirectional Load and Energy Storage Ports," *IEEE Trans. Power Electron.*, Vol. 24, No. 10, Oct. 2009, pp 2289-2297.

[27] German G. Oggier, Guillermo O. Garcia, and Alejandro R. Oliva, "Switching Control Strategy to Minimize Dual Active Bridge Converter Losses," *IEEE Trans. Power Electron.*, Vol. 24, No. 7, Jul, 2009, pp 1826-1837.

[28] De Doncker, R. W., Divan, D. M., and Kheraluwala, M. H., "A Three-Phase Soft-Switched High-Power Density DC/DC Converter for High-Power Applications," *IEEE Transactions on Industry Applications*, Vol. 27, No.1, Jan. 1991, pp. 63-73.

[29] M. H. Kheraluwala, R. W. Gascogine, D. M. Divan and E.D. Baumann, "Performance characterization of a high-power dual active bridge dc-to-dc converter," *IEEE Transactions on Industry Applications*, Vol. 28. Nov. 1992, pp. 1294-1301.

[30] C. Mi H. Bai C. Wang, and S.Gargies, "Operation, design and control of dual H-Bridge-Based Isolated Bidirectional DC-DC Converter," *IET Power Electron.*, Vol.1. No.4. Mar. 2008, pp. 507-517.

[31] Florian Krismer and Johann W. Kolar, "Accurate Power Loss Model Derivation of a High Current Dual Active Bridge Converter for an Automotive Application," *IEEE Trans. Ind. Electron.*, Vol. 57, No. 3, Mar. 2010, .pp 881-891.

[32] C. Zhao, S. D. Round and J. W. Kolar, "Full-order Averaging Modelling of Zero-Voltage-Switching Phase-Shift Bidirectional DC-DC Converters," *IET Power Electron.*, Vol.3. No.3. Apr. 2010, pp. 400-410.

[33] Chen Chi-Tsong. *Linear System Theory and Design*, Oxford, New York.

[34] Zhijun Qian, Osama Abdel-Rahman and Issa Batarseh, “An Integrated Four-Port DC/DC Converter for Renewable Energy Applications,” *IEEE Trans. Power Electron.*, Vol.25, No. 7, Jul. 2010, pp. 1877-1887.

[35] German G. Oggier, Guilermo O. Garcia and Alejandro R. Oliva, “Modulation Strategy to Operate the Dual Active Bridge DC-DC Converter Under Soft-Switching in the Whole Operating Range,” *IEEE Trans. Power Electron.*, Vol.26, No. 4, Apr. 2011, pp. 1228-1236.

[36] Mario Cacciato, Alfio Consoli, Rosario Attansio, and Francesco Gennaro, “Soft-Switching Converter with HF Transformer for Grid-Connected Photovoltaic Systems,” *IEEE Trans. Ind. Electron.*, Vol.57, No. 5, May. 2010, pp. 1678-1686.

[37] Yanhui Xie, Reza Ghaemi, Jing Sun, and James S. Freudenberg, “Implicit Model Predictive Control of A Full Bridge DC/DC Converter,” *IEEE Trans. Power Electron.*, Vol.24, No. 12, Dec. 2009, pp. 2704-2713.

[38] Yanhui Xie, Jing Sun, and James S. Freudenberg, “Power Flow Characterization of a Bidirectional Galvanically Isolated High-Power DC/DC Converter Over a Wide Operating Range,” *IEEE Trans. Power Electron.*, Vol.25, No. 1, Jan. 2010, pp. 54-66.

[39] Hua Bai, Ziling Nie, and Chris Mi, “Experimental Comparison of Traditonal Phase-Shift, Dual-Phase-Shift, and Model Based Control of Isolated Bidirectioanl DC-DC Converters,” *IEEE Trans. Power Electron.*, Vol.25, No. 6, Jun. 2010, pp. 1444-1449.

[40] Morten Nymand and Michael A. E Andersen, “High-Efficiency Isolated Boost DC-DC Converter for High-Power Low-Voltage Fuel-Cell Applications,” *IEEE Trans. Ind. Electron.*, Vol.57, No. 2, Feb. 2010, pp. 505-514.

[41] Dipankar De and Venkataramanan Ramanarayanan “A Proportional Multiresonant Controller for Three-Phase Four-Wire High-Frequency Link Inverter.,” *IEEE Trans. Power Electron.*, Vol.25, No. 4, Apr. 2010, pp. 899-906.

[42] D. De V. Ramanarayanan, “Improved Utilization of an HF Transformer in DC-AC Application,” *IET Power Electron.*, Vol.4. Iss. 5. May. 2008, pp. 508-515.

[43] Junggi Lee, Kwanghee Nam, Seoho Choi, and Soonwoo Kwon, “Loss-Minimizing Control of PMSM With the Use of Polynomial Approximations,” *IEEE Trans. Power Electron.*, Vol.24, No. 4, Apr. 2009, pp. 1071-1081.

[44] Georgios D. Demetriades, “On Small-Signal Analysis and Control of the Single and the Dual-Active Bridge Topologies,” *Ph.D. Dissertation*, Royal Institute of Technology, Stockholm, Sweden, Mar. 2005.

[45] Haimin Tao, “Integration of Sustainable Energy Sources through Power Electronic Converters in Small Distributed Electricity Generation Systems,” Eindhoven, Netherland, Jan.,2008

[46] N. Kryloff and N. Bogoliuboff, *Introduction to Nonlinear Mechanics*, Princeton University Press, Princeton, NJ,1943

[47] E. M. Baily, “Steady State Harmonic Analysis of Nonlinear Networks,” *Ph.D. Dissertation*, Stanford University, Stanford, CA, 1968.

[48] J. C. Lindenlaub, “An Approach for Finding the Sinusoidal Steady State Response of Nonlinear Systems,” *Proc. 7th Annual Allerton Conf. Circuit and System Theory*, 1969, pp. 323-327.

[49] M. S., Nakhla and J. Vlach, “A Picewise Harmonic Balance Technique for Determination of Periodic Response of Nonlinear Systems,” *IEEE Trans. Circuits Syst.*, CAS-23, Feb. 1976, pp. 85-91.

[50] Leon Chus, Charles A. Desoer, and Ernest S. Kuh, *Linear and Nonlinear Circuits*, Mcgraw-Hill Book Company, 1987.

[51] Ned Mohan, Tore M. Undeland, and William P. Robins, *Power Electrionics*, John Wiley & Sons, Inc, 1995.

[52] *STP40NF10 data sheet*, Rev. 5, STMicroelectronics Corporation, 2010.

[53] *MC33153 data sheet*, Rev. 3, On Semiconductor Corporation, 2011.

[54] Colonel Wm T. Mclyman, *Transformer and Inductor Design Handbook*, 1978.

[55] James A. Momoh, *Electric Power System Applications of Optimization*, Marcel Dekker, 2001.

[56] D. Cox, J. Little, and D. O’Shea, *Ideals, Varieties and Algorithms: An Introduction to Computational Algebraic Geometry and Commutative Algebra* (second edition), Springer Science+Business Media, Inc., 2005

[57] F. Krismer, S. Round, and J. W. Kolar, “Performance Optimization of a High Current Dual Active Bridge with A Wide Operating Voltage Range,” *Power Electronics Specialists Conference*, Jun. 2006, pp. 1-7.

[58] Sangtaek Han and Deepak Divan, “Dual Active Bridge Buck-Boost Converter,” *Energy Conversion Congress and Exposition*, Sept. 2009, pp. 2905-2911.

[59] Yushi Miura, Masato Kaga, Yasuhisa Horita, and Toshifumi Ise, “Bidirectional Isolated Dual Full-Bridge DC-DC Converter with Active Clamp for EDLC,” *Energy Conversion Congress and Exposition*, Sept. 2010, pp. 1136-1143.

[60] Sangtaek Han and Deepak Divan, “Bi-Directional DC/DC Converter for Plug-in Hybrid Electric Vehicle (PHEV) Applications,” *Energy Conversion Congress and Exposition*, Feb. 2008, pp. 784-789.

[61] G. Guidi, M. Pavlovsky, A. Kawamura, T. Imakubo, and Y. Sasaki, “Improvement of Light Load Efficiency of Dual Active Bridge DC-DC Converter by Using Dual Leakage Transformer and Variable Frequency,” *Energy Conversion Congress and Exposition*, Sept. 2010, pp. 830-837.

[62] Alberto Rodriguez Alonso, Javier Sebastian, Diego G. Lamar, Marta M. Hernando and Aitor Vazquez, “An Overall tudy of a Dual Active Bridge for Bidirectional DC/DC Conversion,” *Energy Conversion Congress and Exposition*, Sept. 2010, pp. 1129-1135.

[63] Haifeng Fan and Hui Li, “A Novel Phase-Shift Bidirectional DC-DC Converter with an Extended High-Efficiency Range for 20KVA Solid State Transformer,” *Energy Conversion Congress and Exposition*, Sept. 2010, pp. 3870-3876.

[64] Chuanhong Zhao, Simon Round and Johann W. Kolar, “Buck and Boost Start-up Operation of a Three-Port Power Supply for Hybrid Vehicle Application,” *Power Electronics Specialists Conference*, Jan. 2005, pp. 1851-1857.

[65] Zhan Wang and Hui Li, “Three-phase Bidirectional DC-DC Converter with Enhanced Current Sharing Capability,” *Energy Conversion Congress and Exposition*, Sept. 2010, pp. 1116-1122.

[66] Zhijun Qian, Osama Abdel-Rahman, Hussam Al-Atrash, and Issa Batarseh “Modeling and Control of Three-Port DC/DC Converter Interface for Satellite Applications,” *IEEE Trans. Power Electron.*, Vol.25, No. 3, Mar. 2010, pp. 637-649.

[67] Diogenes D. Molina Cardizo, Juan Carlos Balda, Derik Trowler, and H. Alan Mantooth, “Novel Nonlinear Control of Dual Active Bridge Using Simplified Converter Model,” *Applied Power Electronics Conference and Exposition*, Feb. 2010, pp. 321-327.

[68] D. Segaran, B. P. McGrath, and D. G. Holmes, “Adaptive Dynamic Control of a Bi-Directional DC-DC Converter,” *Energy Conversion Congress and Exposition*, Sept. 2010, pp. 1442-1449.

[69] Sangtaek Han, Imayavaramban Munuswamy, and Deepak Divan, “Preventing Transformer Saturation in Bi-Directional Dual Active Bridge Buck-Boost DC/DC

Converters," *Energy Conversion Congress and Exposition*, Sept. 2010, pp. 1450-1457.

[70] Mario Cacciato, Alfio Consoli, Vittorio Crisafulli, Gianni Vitale, and Nunzio Abbate "A New Resonant Active Clamping Technique for Bidirectional Converters in HEVs," *Energy Conversion Congress and Exposition*, Sept. 2010, pp. 1436-1441.

[71] Yi Wang, S. W. H. de Haanm, and J. A. Ferria "Design of Low-Profile Nanocrystalline Transformer in High-Current Phase-Shifted DC-DC Converter," *Energy Conversion Congress and Exposition*, Sept. 2010, pp. 2177-2181.

[72] Zhe Zhang, Ole C. Thomsen, Michael A. E. Anderson, Jacob D. Schmidt, and Henning R. Nielsen "Analysis and Design of Bi-directional DC-DC Converter in Extened Run Time DC UPS System Based on Fuel Cell and Supercapacitor," *Applied Power Electronics Conference and Exposition*, Feb. 2009, pp. 714-719.

VITA

Jianfu Fu was born on May 9, 1984, in Anshan, China. He completed his Bachelor's Degree from Northeast Forestry University in July 2005. In July 2007, he received Master of Science degree in Harbin Institute of Technology. Since September 2007, he joined Tennessee Technological University, Cookeville, Tennessee, and received Ph.D. degree in Engineering in May 2012.